Statistical properties in the quasi-continuum of atomic nuclei

Ann-Cecilie Larsen
Department of Physics
University of Oslo
May, 2008

Dissertation presented for the degree of
Philosophiae Doctor (PhD) in Physics

Preface

In 1911, Rutherford discovered the existence of the atomic nucleus, which was later confirmed through the experiments of Geiger and Marsden. A new branch of science, nuclear physics, started to develop. In the 1940s and 1950s, it was revealed that protons and neutrons, which are the constituents of the nucleus, were not fundamental, but built up of even smaller particles later called quarks and gluons. However, some of the most fundamental problems of nuclear physics such as the exact nature of the force that holds the nucleus together, are yet unsolved. In recent years, a huge effort has been made to understand the basic force between the quarks and gluons, and attempts have been made to describe nuclear properties from first principles. However, the complex nature of the nuclear force makes this task extremely hard. The status of today is that nuclear physics still lacks a coherent theoretical formulation that would enable us to analyze and interpret all nuclear phenomena in a fundamental way.

The aim of this thesis is to provide a tiny bit of new insight into the broad and diverse field of nuclear physics by presenting experimental observations on statistical properties of medium-mass nuclei at high temperatures. This has long been the main research field of the nuclear physics group at the Oslo Cyclotron Laboratory, where the experiments were performed. In the experiments, the nuclei were excited to high-energy quantum levels and the decay from these levels were studied by means of statistical methods. This thesis will show that statistical methods are applicable in the energy region of interest, even for relatively small systems such as a nucleus, provided that the nucleus is brought to a sufficiently high temperature and that the time scale is large enough for the nucleus to equilibrate before emitting radiation. The results are especially interesting from an astrophysical point of view, as the nuclear structure close to the particle separation energies influences strongly the nucleosynthesis processes that take place in extreme stellar environments such as supernovae.

Acknowledgments

First, my superb supervisors John B. Rekstad and Sunniva Siem deserve a heap of thanks for always being inspiring, supportive and helpful. Many thanks for all the nuclear physics discussions, and your proofreading of this thesis. I am indebted to John for helping me out with methodical details and lots of questions, and to Sunniva who did a great job with all the administrative issues in addition to the scientific and social part. You are clever and talented nuclear scientists, and I have learnt so much from you.

I am deeply grateful to the whole nuclear physics group at the Oslo Cyclotron Laboratory. You make the working day easy and pleasant. It is always fun to go together to conferences and experiments abroad. Special thanks to my room mate Naeem U. H. Syed for all nice discussions and conversations. Many thanks to Rositsa Chankova, Finn Ingebretsen, Svein Messelt, and Stein Ødegård for taking shifts during the experiments and your helpful comments. Finn, thanks for lending me the Peanuts cartoons. Many thanks to Alexander Bürger for the careful reading of this thesis, that was of great help. Also, I would like to thank Hilde T. Nyhus and Heidi K. Toft that helped me baking birthday cakes and freed me from boring committee meetings in the stressful and critical time when the thesis was finished.

I am very thankful to the excellent engineers of the Cyclotron Laboratory, Eivind A. Olsen and Jon C. Wikne for their outstanding work keeping the cyclotron and the lab computers in good shape, and for providing great experimental conditions during the campaigns. I have learned much from you, especially which knobs one should and should *not* touch at the cyclotron control panel.

I am indebted to Andreas Schiller and Alexander Voinov from Ohio University. You have both been of tremendous help and have been deeply involved in this project, and I have learnt so much from you. I am also grateful to Steve M. Grimes and all the collaborators at Ohio University. I would like to express my gratitude to Undraa Agvaanluvsan and Lee Bernstein at Lawrence Livermore National Laboratory, Emel Algin from Osmangazi University, and Gary E. Mitchell from North Carolina State University for your contributions, support and illuminating discussions. Special thanks to Tom Lönnroth from Åbo Akademi University for letting me be responsible for the vanadium data. You were always the winner of the night-shift competition during the experiments. I hope you will find some time to build more model trains.

Finally, I wish to give many thanks to my dear family. I am grateful to

my parents, Ann-Vilde and Hans-Peder, and my sister Beate, for their love and support through all these years. Magne, I cannot thank you enough for all your help in every aspects and stages of this work. You have the knowledge of every detail of the experimental setup and the analysis, and you have a deep insight in nuclear physics. From now on, since the thesis is finished and there should be no more working late at night, I promise to take our dog Romeo out in the morning.

Ann-Cecilie Larsen

May 7, 2008

Contents

List of Figures

List of Tables

Chapter 1

Introduction

Low-energy nuclear physics describes atomic nuclei in terms of nucleons as the relevant degrees of freedom. The carriers of the force between the nucleons are thought to be light mesons, in particular the π and ρ mesons. *Ab initio* calculations based on, e.g, the shell model, are able to describe the observed nuclear quantum numbers such as energy levels, spin and parity with good accuracy for nuclei and excitation energies where there are relatively few quantum energy levels accessible. Transition strengths and branching ratios are also often well reproduced.

However, as the excitation energy increases, the density of energy levels becomes so high that it is impractical or even impossible to resolve individual levels. This is the region of the quasi-continuum, squeezed in between the discrete region where levels are easily resolved with state-of-the-art spectroscopy measurements, and the continuum region, where the levels are overlapping and thus not possible to separate. The onset of quasi-continuum varies from nucleus to nucleus, and is in general at higher excitation energy for light nuclei and nuclei with nucleon numbers close to or equal a magic number – that is, a filled major shell[1].

In the region of quasi-continuum, the precise location of levels and strengths of individual transitions between those levels is of much lesser importance than in the discrete region. The mixing that occurs due to small, residual interactions dilutes the purity of, in principle, simple excitations formulated in terms of approximate quantum numbers. The strength of these excitations is then distributed over many energy levels. Therefore, statistical concepts such as average values and fluctuations around those values become the physically relevant quantities.

Two very important, statistical quantities applied in the quasi-continuum,

---

[1] The magic numbers representing shell closures are 2, 8, 20, 28, 50, 82, and 126 [1].

is the nuclear level density and the γ-ray strength function. These average quantities can be regarded as the counterparts of the energy levels and transition strengths in the discrete region. Local deviations from a smooth behaviour in the level density and the strength function imply global structure changes in the nucleus, such as breaking of nucleon Cooper pairs or collective excitation modes such as the scissors mode.

However, it has has proven to be a difficult task to get experimental information on the level density and the γ-ray strength function in the medium and high excitation-energy region. The nuclear physics group at the Oslo Cyclotron Laboratory (OCL) has developed a method (the so-called Oslo method) to extract level density and γ-ray strength function from first-generation γ-ray spectra for excitation energies between the ground state and the neutron (proton) binding energy [2, 3, 4]. This unique technique has provided experimental evidence for the sequential breaking of nucleon Cooper pairs [5] and an M1 scissors mode pygmy resonance in rare-earth nuclei [6, 7]. Also, a strongly enhanced strength function at low γ energies has been discovered in several Fe and Mo isotopes [8, 9].

The main object of this thesis is to investigate how the level density and the γ-ray strength function develop in medium-mass nuclei, and to test the Oslo method on nuclei with neutron or proton numbers near or at magic numbers. Therefore, the nuclei studied here are $^{44,45}_{21}$Sc [10, 11], $^{50,51}_{23}$V [12], and $^{93-98}_{42}$Mo [9, 13]. The Sc nuclei are close to the proton shell $Z = 20$, while the neutrons are filling the $f_{7/2}$ shell half-way. The situation is opposite in ^{50,51}V, with 23 protons and with a closed or almost closed $N = 28$ shell for ^{51}V and ^{50}V, respectively. Moving to a region of heavier nuclei, the Mo isotopes considered in this thesis have neutron numbers near the $N = 50$ shell closure. Shell effects are therefore expected to manifest themselves in the level density through structures and an overall lower level density than for mid-shell nuclei. Such features will be looked for in the presented experimental data.

When it comes to the γ-ray strength functions, it is an open question whether the low-energy enhancement seen in the Fe and Mo isotopes is a feature related to specific structures in these nuclei, or if it is a general behaviour of nuclei in a certain mass region. This issue has been addressed in the present work.

The thesis is organized as follows: Chapter 2 gives a historic overview of theoretical and experimental achievements concerning level densities and γ-ray strength functions. In Chapter 3, the experimental equipment and some details of the performed experiments are given, and the data analysis is briefly described. The Oslo method is explained and discussed in Chapter 4. Chapter 5 includes reprints of five published articles. Finally, conclusions and an outlook will be given in Chapter 6.

Chapter 2

Nuclear structure and γ-ray strength in the quasi-continuum

The excitation-energy region between the discrete regime (where the nuclear states have well-defined quantum numbers), and the continuum region (where individual levels cannot be resolved due to minuscule or vanishing level spacings), is defined as the quasi-continuum. Here, the nucleus undergoes a transition from an ordered phase at low excitation energy to a more chaotic behaviour as the energy is increased. Nuclei in this transitional excitation-energy region might be most appropriately described by average quantities like the level density and the γ-ray strength function. The level density, averaged over a specific excitation-energy bin, replaces the counting of discrete levels, while the γ-ray strength function inherits the role that transition probabilities are playing at low excitation energies.

2.1 The level density

The level density is defined as the number of quantum energy levels accessible at a specific excitation energy, within a given energy bin. The level density gives direct information on thermodynamic properties of the nuclear system, see Appendix A for a brief introduction to thermodynamic concepts and quantities.

The first theoretical attempt to describe nuclear level densities was done by H. Bethe in 1936 [15]. In his fundamental and pioneering work, Bethe described the nucleus as a gas of non-interacting fermions moving freely in equally spaced single-particle orbits. The level density was obtained by the inverse Laplace transformation of the partition function determined from Fermi statistics. Bethe's original results yielded a level density function

$$\rho(E) = \frac{\sqrt{\pi}}{12} \frac{\exp(2\sqrt{aE})}{a^{1/4}E^{5/4}}, \tag{2.1}$$

for an excitation energy E, and where a is the level-density parameter given by

$$a = \frac{\pi}{6}(g_{\mathrm{p}} + g_{\mathrm{n}}). \tag{2.2}$$

The terms g_{p} and g_{n} are the single-particle level density parameters for protons and neutrons, respectively, which are expected to be proportional to the mass number A. In fact, Bethe's consideration of the nucleus to be a Fermi gas of free protons and neutrons confined to the nuclear volume gives

$$a = \alpha A. \tag{2.3}$$

The constant α has been found to be about $1/8 - 1/10$ by fitting to experimental data.

The Bethe expression predicts an exponential increase in the level density with the square-root of the excitation energy and level-density parameter. This has been found to be qualitatively true, although important factors such as pairing correlations, collective phenomena and shell effects are not included. Refined versions of the original Fermi gas formula take into account these effects by employing free parameters that are adjusted to fit experimental data on level spacings obtained from neutron and/or proton resonance experiments. A. Gilbert and A. G. W. Cameron [16] proposed the following level-density formula in 1965:

$$\rho(U) = \frac{\sqrt{\pi}}{12} \frac{\exp(2\sqrt{aU})}{a^{1/4}U^{5/4}} \frac{1}{\sqrt{2\pi}\sigma}. \tag{2.4}$$

Here, U is the shifted excitation energy, $U = E - \Delta_{\mathrm{p}} - \Delta_{\mathrm{n}}$, where Δ_{p} and Δ_{n} are the pairing energy for protons and neutrons, respectively. The spin cutoff parameter σ is given by

$$\sigma^2 = g\langle m^2 \rangle T, \tag{2.5}$$

where $g = g_{\mathrm{p}} + g_{\mathrm{n}}$ relate to the level density parameter as in Eq. (2.2), $\langle m^2 \rangle \approx 0.146A^{2/3}$ is the mean-square magnetic quantum number for single-particle states, and the temperature is given by

$$T = \sqrt{U/a}. \tag{2.6}$$

Another expression of the level density for excitation energies between $0 - 10$ MeV is obtained from the constant-temperature (CT) model [16],

$$\rho(E) = \frac{1}{T}\exp[(E - E_0)/T], \tag{2.7}$$

where E is the excitation energy, and the free parameters T and E_0 are connected to a constant nuclear temperature (in contrast to Eq. (2.6)) and an energy shift, respectively.

A variant of the shifted Gilbert-Cameron expression given in Eq. (2.4) is the back-shifted Fermi gas (BSFG) model [17], where the level-density parameter and energy shift are considered as free parameters, allowing for a reasonable fit to experimental data over a wider range of energies[1]. Also, phenomenological methods were developed to describe the energy dependence of the parameter a.

In 2005, T. von Egidy and D. Bucurescu [18] published a new compilation of systematics of nuclear level-density parameters. In their approach, they determined a new set of phenomenological level density parameters for the BSFG and CT model by fitting the latest data on low-excitation-energy levels and neutron resonance spacings at the neutron binding energies for 310 nuclei between ^{19}F and ^{251}Cf. Then they studied the variations of these parameters for the set of nuclei, and observed correlations with other physical observables leading to the determination of simple formulas that describe the main features of the empirical parameters. For the BSFG model, the following expressions were used for the level density and the spin cutoff parameter:

$$\rho(E) = \frac{\exp[2\sqrt{a(E - E_1)}]}{12\sqrt{2}\sigma a^{1/4}(E - E_1)^{5/4}} \tag{2.8}$$

and

$$\sigma^2 = 0.0146A^{5/3}\frac{1 + \sqrt{1 + 4a(E - E_1)}}{2a}. \tag{2.9}$$

The level-density parameter a and energy shift E_1 were treated as free parameters to be fitted to experimental data.

The expression for σ is based on the rigid-body value for the nuclear moment of inertia,

$$\mathcal{I} = \frac{2}{5}\frac{m_0 r_0^2}{\hbar^2}A^{5/3}, \tag{2.10}$$

---

[1] The shift $\Delta_p + \Delta_n$ turns out to be too large, so it is 'back-shifted' by subtracting a parameter C_1 [17].

where m_0 is the nucleon mass and r_0 is the nuclear radius parameter, and the nuclear temperature is described as

$$T = \frac{1 + \sqrt{1 + 4a(E - E_1)}}{2a}. \tag{2.11}$$

From the relation

$$\sigma^2 = \mathcal{I}T, \tag{2.12}$$

we obtain the expresion given in Eq. (2.9). Although Eq. (2.11) has been shown to be mathematically incorrect in [16], the authors of [18] found Eq. (2.9) to be most adequate in the excitation-energy region considered in their work.

Other semi-empirical level density models have also been developed, such as the model by Kataria, Ramamurthy and Kapoor (KRK), which accounts for shell effects in terms of the ground-state shell correction to the nuclear binding energy, and the Generalized Superfluid (GSF) model introduced by Ignatyuk and others. As these models will not be used in this thesis, the reader is referred to [19] and references therein for further information.

Although the above-mentioned semi-empirical expressions give reasonable agreement with experimental data on, e.g., neutron resonance spacings, they are not able to describe fine structures in the level density caused by pair breaking, shell effects etc. Also, any extrapolation to nuclei far from the valley of stability where little or no experimental data are known could be highly uncertain. In order to have a predictive power, level densities should ideally be calculated from microscopic models based on first principles and fundamental interactions.

For a detailed, microscopic description of the nuclear level density, one should solve the exact many-body eigenvalue problem

$$\hat{H} |\Psi\rangle = E |\Psi\rangle, \tag{2.13}$$

where the Hamiltonian is given by

$$\hat{H} = \sum_{i=1}^{A} -\frac{\hbar^2}{2m}\nabla_i + \sum_{i<j}^{A} v(i,j) \tag{2.14}$$

assuming a two-body character of the nucleon interaction, and where i represents all relevant coordinates and quantum numbers of the ith nucleon. The nuclear wave function for A nucleons is given as

$$|\Psi\rangle = |\Psi(1, ..., A)\rangle. \tag{2.15}$$

This is a simplified, non-relativistic treatment where three-body and higher-order contributions are neglected. However, this has turned out to be a tremendous challenge for mid-mass and heavy nuclei as the dimension of the problem grows rapidly with the number of nucleons. For example, using the interactive shell model to simplify the Hamiltonian and provide an orthogonal basis for single-particle wave functions, the required model space is many orders of magnitude larger than spaces in which conventional diagonalization methods can be applied. It is therefore of great importance to introduce methods where level density can be calculated approximately without loosing too much of the desired microscopic details.

One such method is the shell model Monte Carlo approach as applied by Y. Alhassid *et al*. [20, 21, 22]. Here, thermal averages are taken over all possible states of a given nucleus. Two-body correlations are fully taken into account within the model space[2]. These calculations show very promising results and are often in good agreement with experimental data. The drawback is that they are very time consuming.

Another statistical approach, starting from mean-field theory, is presented by P. Demetriou and S. Goriely [23]. Here, a global, microscopic prescription of the level density is derived based on the Hartree-Fock-BCS (HFBCS) ground-state properties (single-particle level scheme and pairing force). Combinatorial models have also been developed [24], which, like the HFBCS plus statistical model, give almost equally good agreement with experimental data as obtained with phenomenological BSFG formulae. A global combinatorial model has been combined with an updated deformed Hartree-Fock-Bogolyubov model by S. Hilaire and S. Goriely [25], where the combinatorial predictions provide the non-statistical limit that by definition cannot be described by any statistical approach. Another advantage of this combined model is that the parity dependence of the level density is obtained in addition to the energy and spin dependence. Globally, the new model of [25] predicts s- and p-wave neutron resonance spacing data within a factor of two.

When it comes to measuring level densities experimentally, several methods have been developed and applied in various excitation-energy regions. At low excitation energies it is possible to determine the level density by counting the discrete levels from databases such as the Table of Isotopes [26] and ENSDF [27]. However, this method quickly becomes unreliable when the level density reaches about 50 levels per MeV.

---

[2] The complete *pf* shell and the $0g_{9/2}$ orbit are included in calculations of nuclei from iron to germanium [21]).

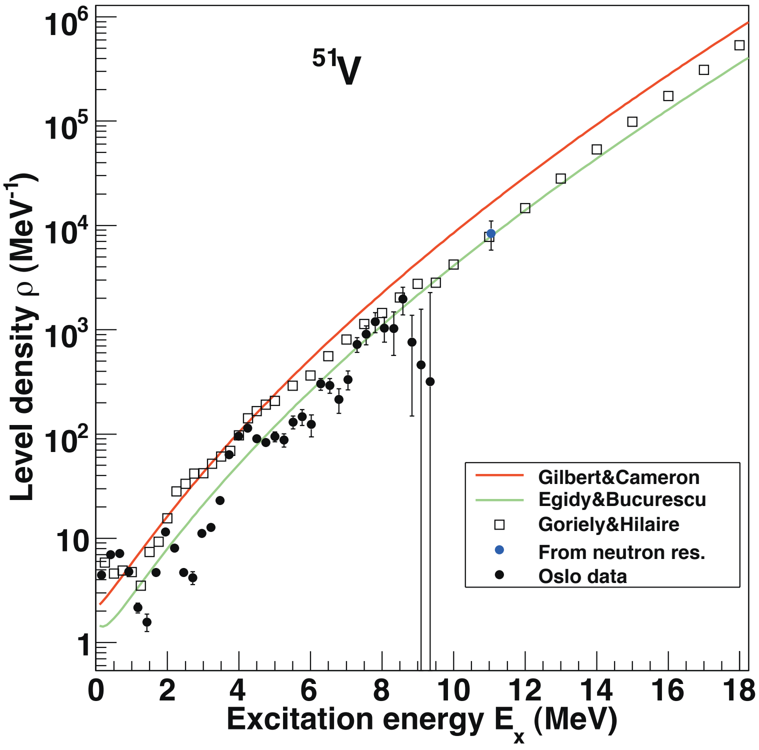

Figure 2.1: The level density of ^{51}V calculated with two parameterizations of the back-shifted Fermi gas model (colored lines, [17, 18]), and from the work of S. Hilaire and S. Goriely (white squares, [25]) compared to the experimental level density from OCL (black dots, [12]).

At the neutron (proton) separation energy, the numbers of s- and p-wave neutron (proton) resonances within the energy range of the incoming neutron (proton) reveal the level spacing between the states reached in the capture reaction [19]. This is the method of choice for determining parity- and spin-projected level density at and slightly above the neutron (proton) separation energy. Obviously, the method is not applicable at other energies, and corrections are needed for missing resonances or contaminating resonances with higher ℓ values.

Another appreciable method is the Hauser-Feshbach modelling of evaporation spectra [28]. This method can be applied to the quasi-continuum and produces reliable level density functions, including fine structures. However, care has to be taken so that the underlying assumptions of the Hauser-Feshbach theory are met by choosing appropriate reactions, beam

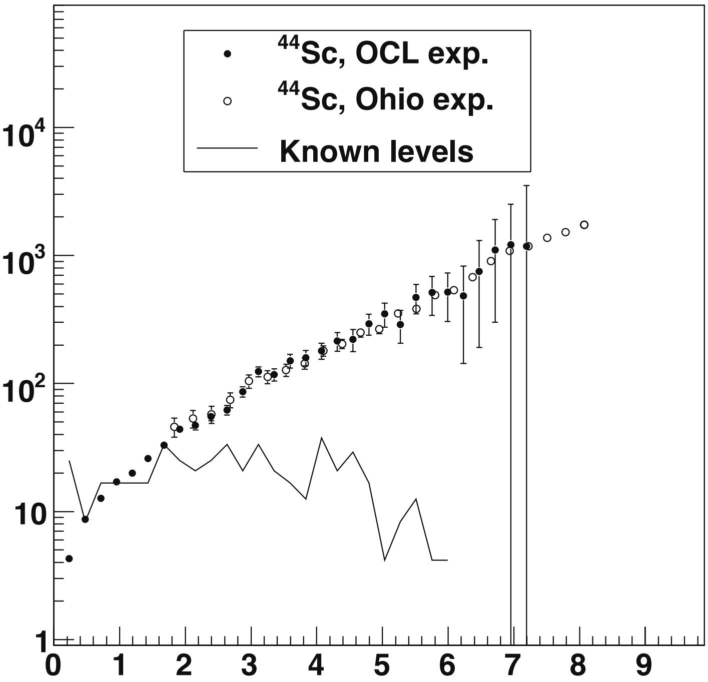

Figure 2.2: The level density of ^{44}Sc obtained from Hauser-Feshbach modelling of α-evaporation spectra (open circles) and from a statistical analysis of primary-γ spectra (black circles), see [11].

energies, ejectile angles and so on. Also, *a priori* knowledge of particle transmission coefficients is needed.

In the Ericsson regime (excitation energies $3-4$ MeV above the neutron separation energy for heavy nuclei), the level density can be determined from a fluctuation analysis of total neutron cross sections [29]. This method relies on specific assumptions concerning how level density can be extracted from cross-section fluctuations. In particular, level widths, level spacings and the experimental resolution must follow a certain hierarchy, which is only fulfilled in certain energy regions. Also the restriction to very specific reactions limits the usefulness of this method.

A recent method to measure the level density has been developed by the Oslo nuclear physics group [2, 3, 4]. This method, called the Oslo method, is based on a statistical analysis of primary-γ spectra extracted from various excitation-energy bins. The extracted level density of ^{51}V is shown in Fig. 2.1, where it is compared with calculated level densities from the back-shifted Fermi gas model, and the calculations of [25]. The Oslo method determines the functional form of the level density between the discrete region and the neutron (or proton) separation energy, and has about the same precision in providing information on fine structures as the Hauser-Feshbach modelling of evaporation spectra, see Fig. 2.2. It is however necessary to use information on discrete levels and neutron (proton) resonances in order to obtain the correct slope and absolute value of the level density.

2.2 The γ-ray strength function

Gamma-ray strength functions characterize the average electromagnetic properties of excited nuclei, which means that they are closely connected to radiative decay and photo-absorption processes. They are also called radiative strength functions [30] and photon strength functions [31] in the literature. They can be directly associated with reduced transition probabilities, see Appendix B for details on this subject.

The original definition of a model-independent γ-ray strength function is (Bartholomew *et al.* [32]):

$$f_{XL}(E_\gamma) = \frac{\langle \Gamma_{\gamma\ell} \rangle}{(E_\gamma^{2L+1} D_\ell)} \,. \tag{2.16}$$

Here, $f_{XL}(E_\gamma)$ is the γ-ray strength for electromagnetic character X, multipolarity L, and γ-ray energy E_γ, $\langle \Gamma_{\gamma\ell} \rangle$ is the average radiative width and D_ℓ is the resonance spacing for ℓ-wave resonances (usually s- or p-wave) determined from average resonance capture (ARC) neutron experiments. This is the "downward" strength function related to the γ decay. The photo-excitation ("upward") strength function is determined by the average photo-absorption cross section $\langle \sigma_{XL}(E_\gamma) \rangle$ summed over all possible spins of final states [19, 31, 33]:

$$f_{XL}(E_\gamma) = \frac{1}{(2L+1)(\pi\hbar c)^2} \frac{\langle \sigma_{XL}(E_\gamma) \rangle}{E_\gamma^{(2L-1)}} \,. \tag{2.17}$$

Based on Fermi's golden rule and the principle of detailed balance, the "upward" and "downward" γ-ray strength function correspond to each other provided that the same states are populated.

The γ-ray strength function f_{XL} is related to the γ-ray transmission coefficient $\mathcal{T}_{XL}$ by

$$\mathcal{T}_{XL}(E_\gamma) = 2\pi E_\gamma^{(2L+1)} f_{XL}(E_\gamma)\,. \tag{2.18}$$

Therefore, γ-ray strength functions are important for the description of the γ emission channel in nuclear reactions. This is an almost universal channel since γ rays, in general, may accompany emission of any other emitted particle. Like the particle transmission coefficients that emerge from the optical model, γ-ray transmission coefficients enter the Hauser-Feshbach model for calculation of the competition between photon emission with other particles.

The simplest model for the strength function, the single-particle model of Blatt and Weisskopf [34], results in energy-independent strength functions. This has been long known to be a too simple picture – collective excitations must also be taken into account. For instance, the well-known giant electric dipole resonance (GEDR) that strongly influences the strength function has been observed throughout the periodic table with great regularity. This resonance is believed to stem from harmonic vibrations where protons and neutrons oscillate off-phase against each other, and is therefore called an *isovector* collective excitation mode. Other giant resonances have been discovered as well, such as the giant magnetic dipole resonance (GMDR), which is built of spin-flip transitions between $\ell \pm 1/2$ subshells, and the *isoscalar* giant electric quadrupole resonance (GEQR) originated from surface oscillations where the protons and neutrons are distorted in two orthogonal directions. For more information on giant resonances in general, see M. N. Harakeh and A. van der Woude [35].

There is also experimental evidence for other types of collective excitation modes, namely the so-called pygmy resonances, which are small compared to the corresponding giant resonances. Examples of such small resonances are the M1 scissors mode, where, in a macroscopic view, the proton and neutron clouds act like a pair of scissor blades "clipping" against each other, and the E1 pygmy resonance caused by a "skin" created by excess neutrons oscillating against an $N = Z$ core.

In the following, some of the standard models for the E1 strength function will be described. For details regarding the determination of various constants etc., and also for a description of the models of the M1 spin-flip and E2 isoscalar resonance, see Appendix C.

The Brink-Axel hypothesis [30, 36] has been widely used to describe collective excitation modes, and in particular the GEDR. The hypothesis states that collective excitations built on excited states have the same properties as those built on the ground state; that is, the probability of γ decay is only dependent on the γ-ray energy and not on the temperature of the final state. This strong assumption leads to a Lorentzian shape of the giant resonances. For the GEDR, the Standard Lorentzian (SLO) is given as[3] [19]

$$f_{\mathrm{E1}}(E_\gamma) = \frac{1}{3\pi^2\hbar^2c^2}\frac{\sigma_r\Gamma_r^2E_\gamma}{(E_\gamma^2-E_r^2)^2+\Gamma_r^2E_\gamma^2} \tag{2.19}$$

in units of MeV^{-3}. Here, the Lorentzian parameters σ_r (in mb), Γ_r (in MeV) and E_r (in MeV) are the peak cross section, width and centroid energy of the GEDR, respectively. This form gives a very accurate description of photo-absorption data of mid-mass and heavy nuclei close to the resonance maximum. However, the SLO model significantly underestimates the γ-ray strength function for $E_\gamma \lesssim 1$ MeV. Also, the SLO model tends to overestimate experimental data such as capture cross sections and average radiative widths in heavy nuclei (see [19] and references therein).

In the work of Kadmenskiĭ, Markushev and Furman (KMF) based on Fermi liquid theory [37], a temperature dependency on the final states T_f is incorporated in the description of the GEDR:

$$f_{\mathrm{E1}}^{\mathrm{KMF}}(E_\gamma,T_f) = \frac{1}{3\pi^2\hbar^2c^2}\frac{0.7\sigma_r\Gamma_r^2(E_\gamma^2+4\pi^2T_f^2)}{E_r(E_\gamma^2-E_r^2)^2} \tag{2.20}$$

Here, the temperature-dependent width of the GEDR is given by

$$\Gamma_{KMF}(E_\gamma,T_f) = \frac{\Gamma_r}{E_r^2}(E_\gamma^2+4\pi^2T_f^2), \tag{2.21}$$

where the first term reflects the spreading of particle-hole states into more complex configurations, and the second term accounts for collisions between quasiparticles. This temperature inclusion made it possible for the authors of [37] to reproduce quite accurately the experimental strength function of ^{144}Nd [38] in the region $E_\gamma = 0.2-7$ MeV. Also, the KMF model gives good agreement with capture cross sections and average radiative widths. However, using a variable temperature of the final states contradicts the Brink-Axel hypothesis. This could in principle be mended if a constant temperature is applied instead. Another problem with the KMF model is the divergence at the resonance centroid energy that makes it impossible to describe both the high- and low-energy part of the E1 strength function.

---

[3] The constant $1/(3\pi^2\hbar^2c^2) = 8.674\cdot10^{-8}$ mb^{-1}MeV^{-2}.

Several attempts have been made to implement the behavior of the strength function at low and high γ energies simultaneously. The Generalized Lorentzian (GLO) model as proposed by J. Kopecky and R. E. Chrien [39] consists of two terms: a Lorentzian with a temperature-dependent width according to Eq.(2.21), and the non-zero limit when $E_\gamma \to 0$ as described in [37]:

$$f_{\mathrm{E1}}^{\mathrm{GLO}}(E_\gamma, T_f) = \frac{1}{3\pi^2\hbar^2c^2}\sigma_r\Gamma_r \left[E_\gamma \frac{\Gamma_{KMF}(E_\gamma, T_f)}{(E_\gamma^2 - E_r^2)^2 + E_\gamma^2\Gamma_{KMF}^2(E_\gamma, T_f)} \right. \\ \left. + 0.7\frac{\Gamma_{KMF}(E_\gamma = 0, T_f)}{E_r^3} \right]. \tag{2.22}$$

The GLO model gives reasonable agreement with data on capture cross sections and primary γ-ray spectra from ARC measurements for nearly spherical nuclei. For nuclei with a large ground-state deformation in the mass region $A = 150 - 170$, the GLO model underestimates the observed strength calculated from primary γ rays. Therefore, an Enhanced Generalized Lorentzian (EGLO) model has been proposed [19, 40], where a generalization of the temperature-dependent width is introduced as follows:

$$\Gamma_{\mathcal{K}}(E_\gamma, T_f) = \mathcal{K}(E_\gamma)\frac{\Gamma_r}{E_r^2}(E_\gamma^2 + 4\pi^2T_f^2), \tag{2.23}$$

where the empirical function $\mathcal{K}(E_\gamma)$ given by

$$\mathcal{K}(E_\gamma) = \kappa + (1-\kappa)\frac{E_\gamma - E_0}{E_r - E_0} \tag{2.24}$$

relates the width in Eq. (2.21) to the collisional damping width in the Fermi liquid theory. The factor κ depends on the model adopted for the level density, while E_0 is a constant set to 4.5 MeV (see [19] and Appendix C).

From a theoretical point of view, there are problems with both the SLO and the (E)GLO models despite the good agreement of the latter with experimental results. As described in [19] and references therein, the shapes of the (E)GLO and SLO models are inconsistent with the general relationship between the γ-ray strength function of heated nuclei and the imaginary part of the nuclear response function to the electromagnetic field. Also, the damping width of the EGLO model is proportional to the collisional component of the damping width in the infinite Fermi liquid in which only the collisional (two-body) relaxation is considered. It is however necessary to also include the contribution from the fragmentation (one-body) width stemming from the nucleon motion in a self-consistent mean field. This fragmentation width is almost independent of the temperature, and is not included in the (E)GLO model, while the temperature-independent width in the SLO model only accounts for the fragmentation, but not for collisional damping.

These shortcomings can be avoided using refined closed-form models such as the Modified Lorentzian (MLO) [19, 41, 42] given by

$$f_{\mathrm{E1}}^{\mathrm{MLO}}(E_\gamma, T_f) = \frac{1}{3\pi^2\hbar^2c^2}\mathcal{L}(E_\gamma, T_f)\sigma_r\Gamma_r\frac{E_\gamma\Gamma(E_\gamma, T_f)}{(E_\gamma^2 - E_r^2)^2 + E_\gamma^2\Gamma^2(E_\gamma, T_f)}. \quad (2.25)$$

Equation (2.25) is consistent with the principle of detailed balance, and is obtained by calculating the average radiative width of nuclei with microcanonically distributed initial states. The term

$$\mathcal{L}(E_\gamma, T_f) = \frac{1}{1 - \exp(-E_\gamma/T_f)} \quad (2.26)$$

is a scaling factor that determines the enhancement of the γ-ray strength function in a heated nucleus as compared to a cold nucleus. This quantity can be interpreted as the average number of one-particle $-$ one-hole states excited by an electromagnetic field with frequency $\omega = E_\gamma/\hbar$, and is only important for low-energy γ rays [19]. The semi-empirical damping width is expressed as

$$\Gamma(E_\gamma, T_f) = \Gamma_C(E_\gamma, T_f) + \Gamma_F(E_\gamma), \quad (2.27)$$

where Γ_C represents the collisional damping width and Γ_F simulates the fragmentation component of the total damping width (see Appendix C for more details).

Another approach for the E1 strength function is the Generalized Fermi Liquid (GFL) model as proposed by S. F. Mughabghab and C. L. Dunford [43] and slightly modified in [19]. The GFL model depends on the final temperature T_f and the deformation parameter β_2, and is given by

$$f_{\mathrm{E1}}^{\mathrm{GFL}}(E_\gamma, T_f, \beta_2) = \frac{1}{3\pi^2\hbar^2c^2}\sigma_r\Gamma_r\frac{\mathcal{K}_{\mathrm{GFL}}E_\gamma\Gamma_m(E_\gamma, T_f)}{(E_\gamma^2 - E_r^2)^2 + \mathcal{K}_{\mathrm{GFL}}E_\gamma^2\Gamma_m^2(E_\gamma, T_f)}, \quad (2.28)$$

$$\mathcal{K}_{\mathrm{GFL}} = \sqrt{\frac{1 + F_1'/3}{1 + F_0'}}, \quad (2.29)$$

where F_0' and F_1' are the Landau-Migdal parameters of the quasi-particle interaction in the isovector channel of the Fermi system. According to [19], the term $\mathcal{K}_{\mathrm{GFL}} E_\gamma^2 \Gamma_m^2(E_\gamma, T_f)$ is added in the denominator to avoid singularity at the resonance centroid energy. Equation (2.28) is thus an extension of the original expression given in [43]. Quite similar to the width in Eq. (2.27), the width Γ_m is given by a sum of a collisional damping width Γ_C and the term Γ_{dq} that simulates the fragmentation width:

$$\Gamma_m(E_\gamma, T_f) = \Gamma_C(E_\gamma, T_f) + \Gamma_{\mathrm{dq}}(E_\gamma, \beta_2). \tag{2.30}$$

The Hybrid Formula proposed by S. Goriely in Ref. [44] is another model that is able to simultaneously describe the low-energy and high-energy part of the γ-ray strength function. The form of the Hybrid Formula as given in [19] is:

$$f_{\mathrm{E1}}^{\mathrm{HF}}(E_\gamma, T_f) = \frac{1}{3\pi^2\hbar^2c^2}\sigma_r\Gamma_r \frac{E_\gamma \Gamma_h(E_\gamma, T_f)}{(E_\gamma^2 - E_r^2)^2 + E_\gamma^2 \Gamma_r \Gamma_h(E_\gamma, T_f)}, \tag{2.31}$$

where

$$\Gamma_h(E_\gamma, T_f) = \mathcal{K}_{\mathrm{GFL}} \Gamma_r \frac{E_\gamma^2 + 4\pi^2 T_f^2}{E_\gamma E_r}. \tag{2.32}$$

All expressions discussed so far need to be generalized for deformed nuclei, where the deformation leads to a splitting of the GEDR into two components corresponding to two oscillation frequencies, one for each principal axis. The E1 strength function in deformed nuclei is thus defined as the sum of two components, each with the corresponding centroid energy $E_{r,j}$, damping width $\Gamma_{r,j}$ and peak value of the photo-absorption cross section $\sigma_{r,j}$ where $j = 1$ and $j = 2$ correspond to collective vibrations along and perpendicular to the symmetry axis (see Appendix C for further details). In Fig. 2.3, model calculations are shown for the E1 strength function of ^{51}V, and it is seen how the models might deviate significantly at the low- and high-energy tails of the GEDR. The models of the M1 and E2 resonance briefly described in Appendix C are also included in the figure.

As for the level density, a microscopic treatment of the strength function is necessary to obtain information on the underlying nuclear structure and to have predictive power throughout the nuclear chart. For example, structures due to the scissors mode and neutron skin oscillations are not dealt with in a comprehensive way in the models described so far. Also, any extrapolation of the GEDR, GMDR and GEQR systematics for the resonance centroid energy, maximum cross section and damping width to exotic nuclei far from the β-stability line is highly questionable. Calculations based on, e.g., the random-phase approximation (RPA) have proven to be superior to the semi-classical approaches in predictive power.

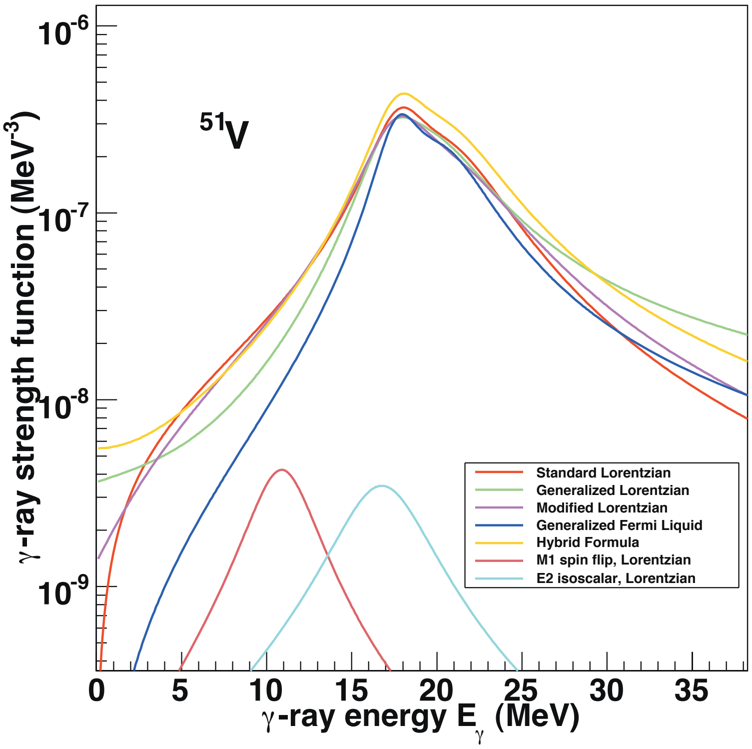

Figure 2.3: Various theories for the E1 strength in ^{51}V (see text) and the M1 spin-flip and E2 isoscalar resonance.

Several publications have been dedicated to the microscopic description of γ-ray strength functions. S. Goriely and E. Khan presented in Ref. [45] large-scale calculations based on the quasi-particle RPA (QRPA) model [46] to generate excited states on top of the HF+BCS ground state. To account for the damping of the collective motion, the GEDR is empirically broadened by folding the QRPA resonance strength with a Lorentzian function. These calculations were performed for more than 6000 nuclei with $8 \leq Z \leq 110$. It is shown that the QRPA provides a quite accurate description of the GEDR centroid and the fraction of the energy-weighted sum rule exhausted by the E1 mode (see [35] for a thorough treatment of radiative sum rules).

Another approach to treat the collective modes microscopically, is the quasi-particle multiphonon (QPM) model introduced by F. Andreozzi, F. Knapp, N. Lo Iudice, A. Porrino, and J. Kvasil [47]. Within this model, the nuclear eigenvalue problem given in Eq. (2.13) is solved exactly in a multiphonon space, where the basis states are generated via the Tamm-Dancoff Approximation (TDA) [46]. The calculations in Ref. [47] are compared with experimental data on low-lying negative parity states in ^{16}O, showing a fairly good agreement when three phonons ($3\hbar\omega$) are included. It appears that the isovector GEDR, which is harmonic, is not affected by the choice of number of phonons included. However, the strength distribution of the isoscalar GEQR is very sensitive to the size of the multiphonon space; if three phonons are included, much more fragmentation is induced compared to the case when only one phonon or two phonons are included. The same is true for octupole modes.

The by far largest contribution of experimental information on the γ-ray strength function is from photoabsorption measurements[4]. To measure photoabsorption, most often photoneutron cross sections, which provide a good substitute for photoabsorption cross sections, are measured. Photoneutron (or photoproton) cross-section measurements are dominated by E1 radiation, and are limited to energies above the neutron (proton) separation energy. Also, the absorption cross sections can only be measured on ground states or on very long-lived isomeric states. These measurements are traditionally performed by guiding a beam of photons to impinge on a thick target (typically several grams) of the nucleus that is under study. The photons can be of bremsstrahlung type from a betatron or a synchrotron facility, or produced by the in flight annihilation of fast positrons from a linear accelerator giving a quasi-monoenergetic photon beam although still containing some bremsstrahlung components [50, 51]. More recently, the inverse Compton-scattering technique has been utilized to produce true quasi-monoenergetic photon beams (see, e.g., Ref. [52] and references therein).

To measure the γ-ray strength function below the particle-emission threshold, photon scattering on isolated levels has been utilized. In the so-called Nuclear Resonance Fluorescence (NRF) method, the spins, parities, branching ratios and reduced transition probabilities of the excited states can be extracted in a model-independent way [53]. Polarization and angular correlation measurements allow the separation of transitions into E1, M1, and E2 transitions, usually with very good precision [54]. However, the method is selective with respect to strong transitions, and experimental thresholds might hamper the determination of an *average* transition strength as represented by the γ-ray strength function [6, 7, 55]. Never-

---

[4] See, e.g., the atlas of ground-state photoneutron and photoabsorption cross sections by S. S. Dietrich and B. L. Berman [48], and the Centre for Photonuclear Experiments Data [49].

theless, this method was able to confirm the experimental evidence for a new, low-lying magnetic dipole mode [53] first discovered in (e,e′) experiments [56] on rare-earth nuclei. Also, a thorough study of the E1 pygmy resonance in the ^{40,44,48}Ca isotopes and in $N = 82$ nuclei using photon scattering (γ,γ') reactions has been presented by A. Zilges *et al.* [57]. Here, a summed $B(\mathrm{E1}\uparrow)$ strength of up to 1% of the Thomas-Reiche-Kuhn sum rule [35] for the total E1 strength was found for the pygmy resonance.

Another way of measuring γ-ray strength functions below the neutron separation energy, is by radiative neutron (or proton) capture reactions into compound states in the final nucleus [39, 58, 59]. From such experiments, both average total radiative widths of neutron resonances and individual transition strengths from one or several neutron resonances to one or several lower-lying discrete states can be obtained. Such primary γ-rays are averaged manually to get the γ-ray strength function, unless ARC neutrons were used, covering a wider range of energy and including many resonances. In the case of the total radiative widths, the γ-ray strength is obtained by integrating a modeled spectral distribution of γ rays which is constructed from trial γ-ray strength functions and level densities. In the analysis of individual transition strengths, corrections can be applied for, e.g., experimental bias and non-statistical effects. The advantage of measuring individual transition strengths is that since the spin and parity of both the initial and final states are known, E1, M1, and E2 γ-ray strength functions can be obtained separately. The method is however limited in energy in that it provides averages of transitions with energies in the order of $\sim 1-2$ MeV below the neutron separation energy.

Yet another approach in determining the γ-ray strength experimentally, is the spectrum-fitting method (see Ref. [60] and references therein). Within this method, a total γ-cascade spectrum is fitted in terms of trial γ-ray strength functions and level densities. This method has been used extensively for γ spectra following, e.g, fusion-evaporation reactions in the search for the temperature response of the giant electric dipole resonance and can cover a wide range of temperatures and spins. A special development of the spectrum-fitting method is the two-step cascade (TSC) or (n,2γ) method, where experimentally, only two-step cascades which connect neutron resonances and discrete low-lying levels with definite parity and spin are recorded. In this manner, the method trades flexibility in terms of applicable nuclear reactions, and temperature and spin regions with sensitivity to γ-ray strength functions of different multipolarities [6, 8, 55]. The disadvantage of all spectrum-fitting methods is that the level density remains a large source of systematic uncertainty, unless it is known *a priori*.

The Oslo method makes it possible to extract the γ-ray strength through the statistical analysis of excitation-energy indexed primary γ-ray spectra [4, 61]. This method is probably the most reliable method in terms of possible systematic errors to produce a total γ-ray strength function in the energy region below the neutron separation energy. It is therefore entirely complementary to the measurement of photoneutron and photoproton cross sections. The method is able to reveal fine structures, however, it does not provide absolute values and the γ-ray strength function has to be normalized to the average total radiative neutron resonance width. In several cases, the results from the Oslo method have been validated by their successful application to the spectrum-fitting method of total and two-step cascades [6, 8]. Also, the results after normalization to the average total radiative neutron resonance width are shown to be in excellent agreement with extrapolations of γ-ray strength from photoneutron cross-section measurements as well as individual transition strengths from neutron resonances [14].

Chapter 3

Experimental details and data analysis

3.1 Introduction

The experiments were performed at the Oslo Cyclotron Laboratory (OCL) at the University of Oslo. The cyclotron at the OCL is the heart and workhorse of the research centre SAFE (Centre for Accelerator Based Research and Energy Physics), which was established by the University of Oslo in June 2005, merging the nuclear physics group, the nuclear chemistry group, and the energy research group.

The Oslo cyclotron is an MC-35 Scanditronix model delivering pulsed light-ion beams, see Table 3.1 for a list of available beams. The molybdenum data were taken in February and June 2002, the vanadium data in November 2002, and the scandium experiment was carried out in September 2004. In all experiments, a ^{3}He beam was used. For details on the targets, see Table 3.2. In order to prevent pileup in the detectors, the beam current was limited to $\approx 1-2$ nA. The experiments were run for about six days.

Ion	Charge state	Energy range (MeV)	Intensity (μA)
Proton	^{1}H$^+$	2-35	100
Deuteron	^{2}H$^+$	4-18	100
Helium-3	^{3}He^{++}	6-47	50
Helium-4 (α)	^{4}He^{++}	8-35	50

Table 3.1: Beams available at the Oslo Cyclotron Laboratory.

Target	Enrichment	Thickness (mg/cm^2)	Reactions	Beam energy (MeV)
^{45}Sc†	99.9%	3.4	^{45}Sc(^{3}He,$\alpha\gamma$)^{44}Sc ^{45}Sc(^{3}He,^{3}He$'\gamma$)^{45}Sc	38
^{51}V†	99.8%	2.3	^{51}V(^{3}He,$\alpha\gamma$)^{50}V ^{51}V(^{3}He,^{3}He$'\gamma$)^{51}V	30
^{94}Mo	92%	2.7	^{94}Mo(^{3}He,$\alpha\gamma$)^{93}Mo ^{94}Mo(^{3}He,^{3}He$'\gamma$)^{94}Mo	30
^{96}Mo	96.7%	1.9	^{96}Mo(^{3}He,$\alpha\gamma$)^{95}Mo ^{96}Mo(^{3}He,^{3}He$'\gamma$)^{96}Mo	30
^{98}Mo	97.0%	2.0	^{98}Mo(^{3}He,$\alpha\gamma$)^{97}Mo ^{98}Mo(^{3}He,^{3}He$'\gamma$)^{98}Mo	45

† Natural targets.

Table 3.2: Targets and reactions used for the experiments studied in this thesis.

The following nuclei will be studied in this thesis: ^{44,45}Sc, ^{50,51}V, and $^{93-98}$Mo. The selected reactions are listed in Table 3.2. The experimental equipment used in the experiment is described in the following sections.

3.2 Experimental setup

The experimental setup at the OCL is shown in Fig. 3.1. The cyclotron is situated in the inner hall, the cyclotron hall, where it delivers the light-ion beam in pulses with a typical frequency of about 8 MHz for ^{3}He ions. The beam from the cyclotron is bent 90° by an analysing magnet into the experimental hall, giving an energy resolution of typically 60 keV of the beam after this magnet[1]. In addition, slits and quadrupole magnets in the beam line allow for collimation and further focusing of the beam, respectively. When the beam reaches the target placed in the centre of the detector array CACTUS (see next section), the diameter of the beam is collimated to about $1 - 2$ mm.

---

[1] The analysing magnet is a so-called doubly-focusing magnet, focusing in both the vertical and horizontal direction. The result of ~60 keV resolution (full width half maximum, FWHM) is obtained with a 38-MeV ^{3}He beam and with 2 mm wide slits in front of the analysing magnet, which has a radius of 1 m.

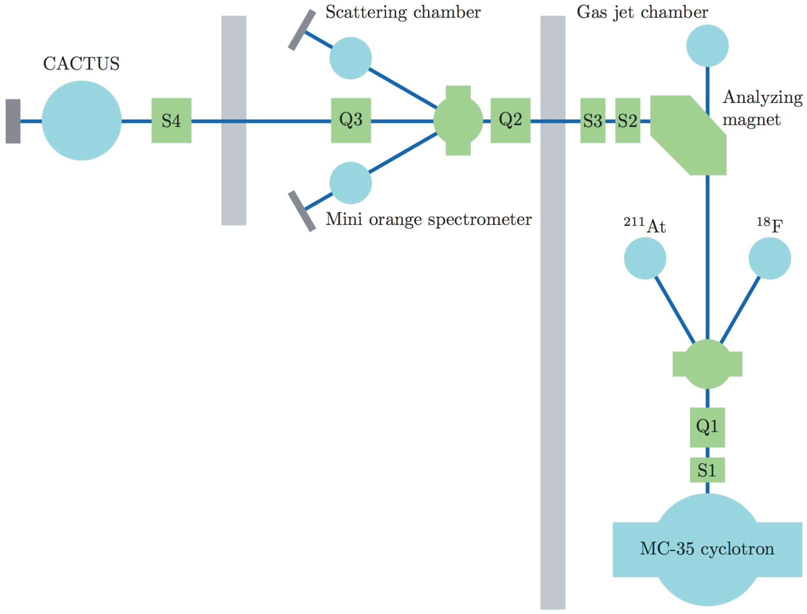

Figure 3.1: Experimental setup at the Oslo Cyclotron Laboratory. The $Q1 \ldots Q4$ are guadrupole magnets, the $S1 \ldots S4$ are slits. The beam dumps marked with ^{211}At and ^{18}F are stations for producing the radioactive isotopes ^{211}At and ^{18}F for medical use and research.

3.2.1 CACTUS

The multi-detector array CACTUS [62] is utilised for measuring particle-γ coincidences. The γ-rays are detected with 28 $5'' \times 5''$ NaI(Tl) detectors mounted on a spherical frame surrounding the target and the particle telescopes, see Fig. 3.2. The NaI(Tl) crystals are collimated with lead collimators, so that their diameter is reduced from 12.7 cm to 7 cm. The solid angle coverage of the collimated NaI(Tl) detectors is estimated to be 17.7% of 4π from $\Omega = \frac{NA}{4\pi R^2}$, where $N = 28$ is the number of detectors, $A = \pi r^2$ is the collimated front area of one detector with radius r = 3.5 cm, and R = 22 cm is the distance of the NaI(Tl) detectors from the target.

The total efficiency was measured to be 15.2% for the 1332-keV γ transition in ^{60}Co. The efficiency was determined by measuring a singles-γ spectrum of a ^{60}Co source with a Ge detector placed in a long distance ($\approx$ 50 cm) from the source. Then, a coincidence requirement was set for the Ge detector and the NaI(Tl)s, so that either the 1173-keV or the 1332-keV transition was measured by the Ge detector or the NaI(Tl)s. The area (counts) reduction in the full-energy peak of the 1173-keV transition of the Ge coincidence spectrum compared to the singles-γ spectrum gave the ef-

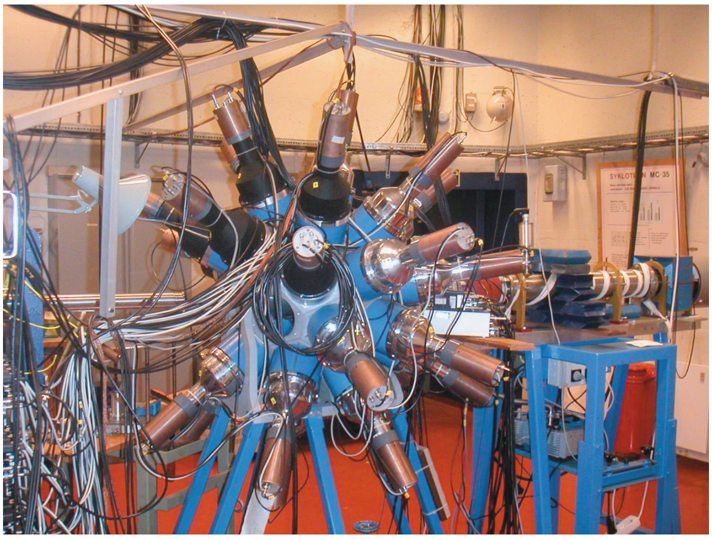

Figure 3.2: The multi-detector array CACTUS.

ficiency of the NaI(Tl)s:

$$\varepsilon_{\mathrm{tot}}^{\mathrm{NaI}}(1332\,\mathrm{keV}) = \frac{N_{\mathrm{coinc}}^{\mathrm{Ge}}(1173\,\mathrm{keV})}{N_{\mathrm{singles}}^{\mathrm{Ge}}(1173\,\mathrm{keV})}, \tag{3.1}$$

where $\varepsilon_{\mathrm{tot}}^{\mathrm{NaI}}$ is the total efficiency of the 28 NaI(Tl)s for $E_\gamma = 1332$ keV, N_{coinc} is the number of counts in the 1173-keV coincidence full-energy peak, and N_{singles} is the number of counts in the 1173-keV singles full-energy peak of the Ge detector.

The resolution of the NaI(Tl) detectors is $\sim$ 7% FWHM for the 1332-keV line. A 2 mm copper absorber is placed in front of each γ detector to suppress X-rays. To reduce crosstalk[2], a 3 mm lateral lead shielding surrounds each NaI(Tl) crystal.

For the runs on the vanadium target, a 60% Ge detector was placed in backward direction in order to monitor the range of spins populated in the (^{3}He,α) and (^{3}He,^{3}He$'$) reactions. It also helped to ensure that the correct nuclei were studied – the good energy resolution allows for the identification of well-known γ transitions in the specific nuclei. The electronics setup allows for three Ge detectors; however, normally only one is used during an experiment.

---

[2] Crosstalk occurs when a γ ray interacts with one of the detectors and then scatters into another detector. Then, there is a non-negligible probability for the γ ray to be measured by two or more detectors within the detector response time, giving false γ signal.

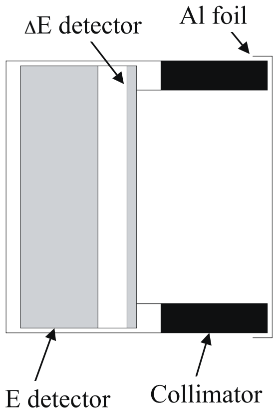

Figure 3.3: Schematic drawing of a Si particle telescope.

The charged particles produced in the nuclear reaction are detected by eight Si $\Delta E - E$ telescopes mounted inside the CACTUS frame. The ΔE counters have a thickness of $\sim$ 140 μm, and the E counters are 1500 μm thick. The particle telescopes are placed 5 cm from the target in the forward direction at an angle of 45° with respect to the beam axis. A 15 μm thick Al foil is placed in front of the particle telescopes in order to stop δ electrons that are emitted from the target foil when the beam is passing through it. The particle detectors were collimated to reduce the uncertainty in the outgoing angle and thereby in the energy of the ejectile. The eight particle telescopes cover 0.2% of 4π when using collimators of 3 mm diameter, as done in the Mo, V, and Sc experiments. The average energy resolution is $\approx$ 200 $-$ 300 keV as determined from the FWHM of the elastic ^{3}He peak.

3.2.2 Electronics and data acquisition

At present, the electronics at the OCL is placed partly in the experimental room and partly in the computer room, see Fig. 3.4 and Fig. 3.5. The pulses from the particle and Ge detector(s) are first amplified with preamplifiers mounted close to the detectors, and then sent to timing filter amplifier (TFA) units where fast timing signals are filtered out, amplified and inverted (Fig. 3.4). The signals are also sent to main amplifiers and directly to their corresponding analog-to-digital converters (ADCs). The timing signals are further processed by constant fraction discriminators (CFDs) to obtain essentially walk-free, fast logic signals. For simplicity, the signals

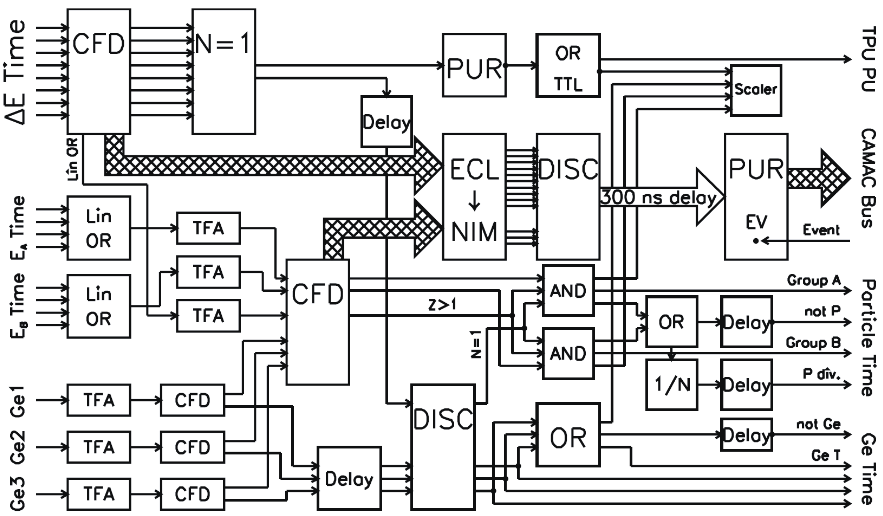

Figure 3.4: Block diagram of the electronics setup in the experimental room, taken from Ref. [63].

from the eight particle end counters are put in groups of four (E_A Time and E_B Time), added by a linear fan in (Lin OR) and processed together (Group A and B). The ΔE detector time signals (ΔE Time) are connected to a multiplicity unit with the setting $N = 1$, which produces a gate signal if one and only one ΔE detector was hit. In addition, a summed, attenuated analog output of the ΔE timing CFD (Lin OR) is fed into a TFA, where it is amplified and then used for a common threshold setting ($Z > 1$). In this way, it is possible, if desired, to suppress events where protons or electrons[3] hit the ΔE detectors.

All the ΔE-detector CFDs are connected to a pile-up rejection module (PUR). This module takes the logic signal from the multiplicity unit and stretches it for ≈ 1 µs, and if another pulse arrives within this time interval, the PUR gives an inverted logic signal to indicate a pile-up event. Then the pile-up signal is sent to a VME trigger pattern unit (TPU), where the event is marked as pileup.

The coincidence events of the ΔE and E detectors are made by requiring three conditions:

1. Exactly one ΔE detector is hit.
2. The signal of the ΔE detector is larger than the common threshold setting ($Z = 1$).

---

[3] Fast electrons and protons with $Z = 1$ deposit only a small fraction of their energy in the ΔE counters.

3. At least one E detector is hit.

This is done by a coincidence unit (AND) checking whether the E detector CFD signal, the multiplicity unit signal, and the $Z > 1$ CFD signal are in coincidence with each other. Unfortunately, there is neither a hardware condition that the ΔE and E detector of the same particle telescope are hit, nor that only one E detector gave a signal. However, since the particle multiplicity and the beam current are relatively low, this does not introduce severe problems, and can also be checked during offline data sorting.

A scaler serves as a counter for several unit signals, such as the coincidence rate of the particle telescopes and the summed rate of the Ge detectors. Since the elastically scattered ^{3}He particles produce a high count rate due to the large Rutherford cross section, every other event is rejected with a $(1/N)$ module with the setting $N = 2$ unless a γ-ray detector is hit; thus, the particle singles spectrum is divided by two (shown as 'P div.' output in Fig. 3.4).

The electronics setup in the computer room is displayed in Fig. 3.5. The timing signals from the NaI(Tl) detectors (NaI Time) are processed by CFD units. The coincidence of the signals from the particle telescopes and the γ-ray detectors is first tested with a gated discriminator (DISC) shown in the upper part of Fig. 3.5. The DISC is vetoed unless a particle counter gives a signal. Then, if a coincidence is measured, a logic signal is sent to start a time-to-digital converter (TDC). Another branch, delayed by 200 ns, is used to stop the TDC. The gate generators (GG) connected to the DISC create a gate signal for the analog-to-digital converters (ADC) for the NaI(Tl) detectors (ADC NaI) and the Ge detectors (ADC Ge1/2/3/T). The other logic units connected to the DISC are used to (i) identify which particle-telescope group is in coincidence with the γ ray(s) (NaI OR, Ge OR, γ OR, γ+p OR, A OR (AND), B OR (AND), Delay), and subsequently send a gate signal to open the particle-telescope ADC, (ii) start the Ge-detector time-to-amplitude converter (TAC) which, with the ADC GeT unit, works as a TDC (Ge OR), and (iii) set flags in the VME trigger pattern units (TPU), which control the readout of the digitized data.

In Table 3.3 all the hit patterns for the TPUs are listed. TPU1 handles the particle telescopes and the Ges, while TPU2 and TPU3 deal with the NaI(Tl) detectors. The virtual TPU4 is not a real module, but is created by the sorting program (see next two sections) in order to show in which detectors pile-up events occured. For simplicity, the control of the NIM-ADCs by VME-ADC controllers, and the control of the CAMAC crate by a CAMAC-branch driver are not shown in Fig. 3.5. The VME crate ac-

Bit #	TPU 1	TPU 2	TPU 3	TPU 4 (virtual, for pile up)
0	Group A	NaI(Tl) 1	NaI(Tl) 17	ΔE 1
1	Singles	NaI(Tl) 2	NaI(Tl) 18	ΔE 2
2	Group B	NaI(Tl) 3	NaI(Tl) 19	ΔE 3
3	Coincidence	NaI(Tl) 4	NaI(Tl) 20	ΔE 4
4	Ge 1	NaI(Tl) 5	NaI(Tl) 21	ΔE 5
5		NaI(Tl) 6	NaI(Tl) 22	ΔE 6
6	Ge 2	NaI(Tl) 7	NaI(Tl) 23	ΔE 7
7		NaI(Tl) 8	NaI(Tl) 24	ΔE 8
8	Ge 3	NaI(Tl) 9	NaI(Tl) 25	Ge 1
9		NaI(Tl) 10	NaI(Tl) 26	Ge 2
10	Ge time	NaI(Tl) 11	NaI(Tl) 27	Ge 3
11		NaI(Tl) 12	NaI(Tl) 28	
12		NaI(Tl) 13	NaI(Tl) 29	
13		NaI(Tl) 14	NaI(Tl) 30	
14		NaI(Tl) 15	NaI(Tl) 31	E_A
15		NaI(Tl) 16	NaI(Tl) 32	E_B

Table 3.3: Hit patterns for the TPUs.

commodates connections to the SUN-Sparc station via a BIT3 Sun Sbus to VMEbus interface.

Each event is constructed on an event-by-event basis by the program Eventbuilder+ [64], running on a CES RIO2 single board processor in the VME crate with a PowerPC 604r @ 300 MHz CPU running LynxOS. The event structure is similar to that of Fig. 4.2 in Ref. [64]; the event starts with a 16-bit word, were bits 12–15 are set to indicate the start of a new event. The bits 0–11 describe the total event length. The next two words denote which TPU is read and its pattern word, respectively. The follow words contain the data (energy, time) of the corresponding detector(s). Then the next TPU is read and so on, until all information of this particular event is recorded. The events are then put in buffers with a length of 32768 words. When a buffer is full, it is transferred to the Sun SPARC computer, where the data acquisition program Sirius+ [64] writes the event buffer to disk. While waiting for buffers, the program sorts events on-line for monitoring the experiment.

The hit patterns of the TPUs displayed in Table 3.3 indicate whether the corresponding detector has data. When sorting the data files off-line with the program Offline+ [65], an event matrix is generated so that the user can access energies and times from this matrix in the sorting user routine.

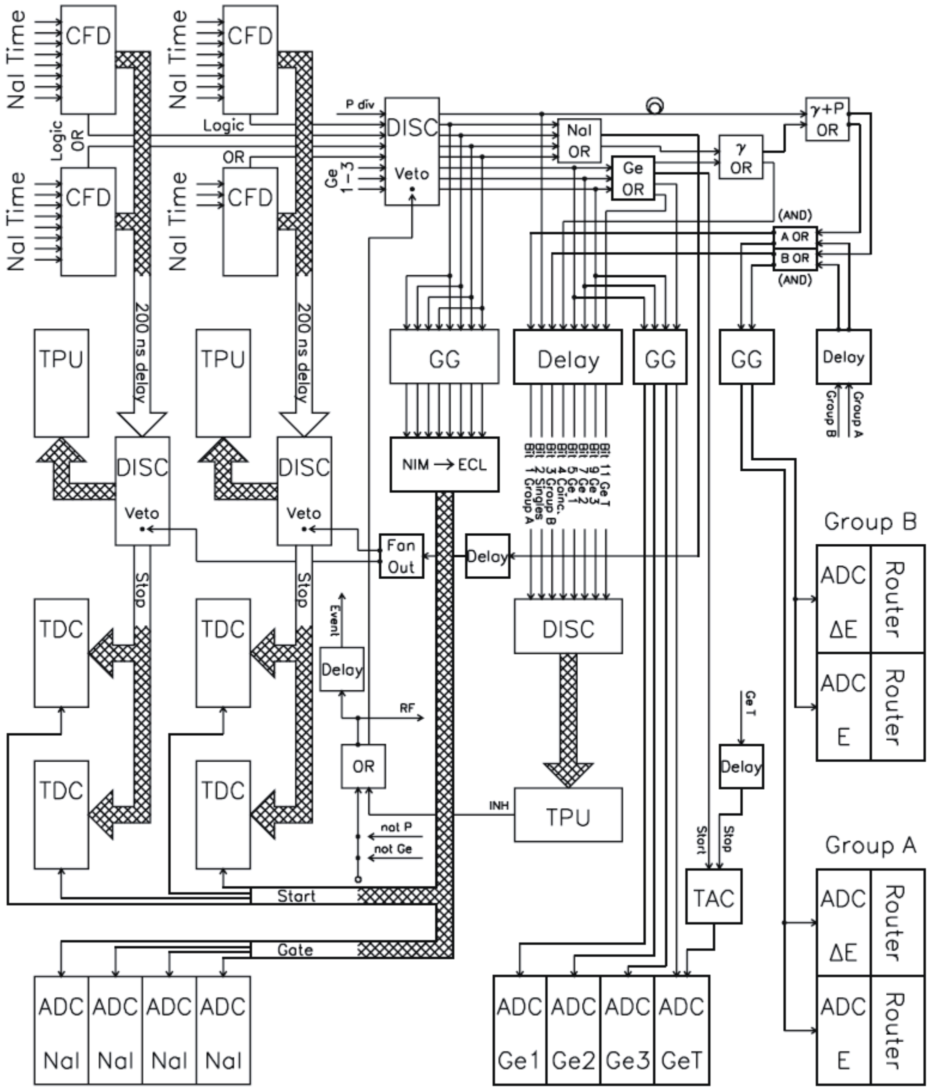

Figure 3.5: Block diagram of the electronics setup in the computer room, taken from Ref. [63].

3.3 Data analysis

In this section, the data analysis applied on the event files will be briefly discussed, as well as the techniques involved to obtain a coincidence matrix with γ-decay spectra for each given excitation energy.

3.3.1 Selected reactions

As previously described, the ^{3}He beam energy used for the experiments discussed here is between $30 - 45$ MeV. Letting these ^{3}He ions impinge on the targets, several reaction channels are opened, such as (^{3}He,xnγ), (^{3}He,dγ), (^{3}He,xn$\alpha\gamma$), and (^{3}He,^{3}He$'\gamma$). The reactions of interest for this study were the inelastic scattering (^{3}He,^{3}He$'\gamma$) and the (^{3}He,$\alpha\gamma$) pick-up reaction as shown in Table 3.2. As there are no neutron detectors present in the experimental setup, and it is necessary to measure all the ejectiles' energies in order to precisely determine the initial excitation energy of the target nucleus, the highest excitation energy for which the γ spectra can be used is the neutron binding energy B_n. If a proton is emitted, the proton binding energy B_p plus the Coulomb barrier is the excitation limit. In Table 3.4, the proton and neutron binding energies for all the nuclei studied in this work are shown, together with the Coulomb barrier for proton emission and the reaction Q value in the case where the nuclei are populated through the (^{3}He,$\alpha\gamma$) reaction. The Coulomb barrier for the proton is given by

$$U_{\text{Coul}} = \frac{e^2}{4\pi\epsilon_0}\frac{Z_{\text{p}}Z_{\text{target}}}{R_{\text{p}} + R_{\text{target}}}, \tag{3.2}$$

where the factor $e^2/4\pi\epsilon_0 = 1.44\,\text{MeV}\cdot\text{fm}$, the sum of the radii $R_{\text{p}} + R_{\text{target}} = r_0(A_{\text{p}}^{1/3} + A_{\text{target}}^{1/3})$ with $r_0 \approx 1.25$ fm, and Z_{p}, Z_{target} are the electric charge of the proton and the target nucleus, respectively.

The maximum angular momentum transfer ℓ_{max} possible in the reactions can roughly be estimated using the classical expression

$$\left|\vec{\ell}\right| = |\vec{r} \times \vec{p}| = rmv\sin\theta. \tag{3.3}$$

For $\theta = 90^\circ$, we have

$$\ell = R_{\text{target}}m_{^3\text{He}}v = r_0 A_{\text{target}}^{1/3} m_{^3\text{He}}\sqrt{\frac{2E_k}{m_{^3\text{He}}}}, \tag{3.4}$$

where the relation

$$E_k = \frac{1}{2}mv^2 \tag{3.5}$$

Nucleus	I^π	B_p (MeV)	B_n (MeV)	Coulomb barrier (MeV)	Q value (MeV)
^{44}Sc	2^+	6.696	9.700	5.34	9.255
^{45}Sc	$7/2^-$	6.889	11.32	5.31	-
^{50}V	6^+	7.949	9.332	5.66	9.526
^{51}V	$7/2^-$	8.061	11.05	5.63	-
^{93}Mo	$5/2^+$	7.643	8.070	8.75	10.90
^{94}Mo	0^+	8.490	9.678	8.72	-
^{95}Mo	$5/2^+$	8.632	7.369	8.70	11.42
^{96}Mo	0^+	9.298	9.154	8.67	-
^{97}Mo	$5/2^+$	9.226	6.821	8.65	11.94
^{98}Mo	0^+	9.794	8.643	8.62	-

Table 3.4: Neutron and proton binding energies, ground-state spin/parity, Coulomb barriers, and Q values for the nuclei under study.

for the kinetic energy E_k of the ^{3}He projectile has been utilized. Using $r_0 \approx 1.25$ fm, $A_{\text{target}} = 98$, $E_k = 45$ MeV, $m_{^3\text{He}} = 2809.41$ MeV$/c^2$ and $\hbar c = 192.329$ MeV $\cdot$ fm gives

$$\ell_{\text{max}} \approx 15\hbar \tag{3.6}$$

for the target nucleus ^{98}Mo. Of course, to get a more precise estimate for the expected spin window populated, one should perform more realistic reaction calculations based on reaction theory such as the distorted wave Born approximation (DWBA, see [1, 66]), taking into account the quantum nature of the impinging ion and the target nucleus, and also the geometry, as the particle telescopes are placed 45° with respect to the beam axis. Previous experiments [67] and DWBA calculations [68] have shown that for the (^{3}He,α) reaction, the pick-up of neutrons with high ℓ-values are preferred. For the nuclei Sc, V, and Mo, the spin range of states populated by the direct reactions is typically $2\hbar \leq I \leq 6\hbar$.

3.3.2 Coincidence technique

As displayed in Figs. 3.4 and 3.5, the electronics setup consists of a *fast* branch that treats the timing information, and a *slow* branch that ensures the best possible handling of the energy information [69]. The time between the detection of a particle and one or more γ-rays is registered by TDCs for the NaI(Tl) detectors and a TAC plus an ADC for the Ge detector. By setting gates on the prompt peak in the measured time spectra when sorting the data offline, the true coincident events were obtained, i.e. the particle and the γ-rays are detected within a narrow time interval. The present electronics setup has a time window of 200 ns, which means that the master gate signal set by the particle (start of the TDCs/TAC) has a duration of 200 ns.

Figure 3.6 shows the time spectrum from the ^{51}V(^{3}He,$\alpha\gamma$)^{50}V, and the gates chosen for the random background (left) and the prompt peak (right). The time resolution is determined by the FWHM of the prompt peak, which is in this case about 17 ns. The gated area of the peak to the left gives the number of random coincidences, and in addition the events where γ-rays from a reaction stemming from one beam burst are detected in coincidence with particles from a reaction produced by the next beam burst. Roughly, the true number of coincidences can be obtained by subtracting the events in the random peak from the prompt peak. Therefore, during the offline data sorting, events that fall into the random gate will be decremented and events in the prompt gate will be incremented, while everything else is rejected.

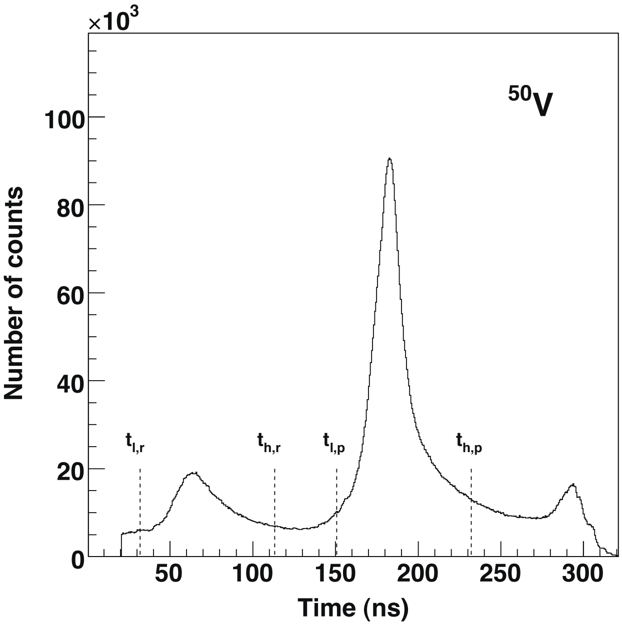

Figure 3.6: The time spectrum of ^{50}V. The dashed lines indicate lower ($t_{l,r}$, $t_{l,p}$) and upper ($t_{h,r}$, $t_{h,p}$) gates on the random and prompt peak, respectively.

3.3.3 Particle–γ matrix

In order to obtain the particle energy vs. γ-ray energy matrix, each individual particle telescope and NaI(Tl) detector is calibrated with a linear calibration

$$E = a_0 + a_1 \cdot \mathrm{ch}, \tag{3.7}$$

where E is the energy, a_0 is the constant shift, a_1 is the dispersion and ch is the channel number in the spectrum. When all detectors are properly calibrated, one can add the data of all the particle telescopes together, and likewise the NaI(Tl) spectra.

The particle telescopes allow for particle identification by utilizing the fact that the energy loss of a charged particle per unit length in a medium is a function of the charge and the mass of the penetrating particle according to the Bethe-Bloch formula [69]. The penetration depth or range as a function of the particle's kinetic energy differs for each charged particle due to their different charge and mass numbers. A given particle will therefore lose a different amount of its energy in the ΔE and E detectors as a function of its total kinetic energy. Such a plot of the energy deposited in the ΔE detector vs. the energy deposited in the E detector is shown in Fig. 3.7, with characteristic banana-shaped curves for each type of particle.

The particle-identification technique described above makes it possible to gate on a specific particle type utilizing its unique range curve in the Si detectors. By gating on the ^{3}He and α particles event-by-event in the offline sorting procedure in addition to the gates on the time spectrum, the ^{3}He–γ and α–γ coincidence events can be extracted. Figure 3.8 shows the α–γ coincidence matrix of the ^{45}Sc(^{3}He,$\alpha\gamma$)^{44}Sc reaction.

The α–γ coincidence matrix in Fig. 3.8 displays characteristic features such as the diagonal where the excitation energy equals the γ-ray energy $E = E_\gamma$. The strong population of yrast states in many excitation-energy bins is shown as intense, vertical lines in the matrix at low γ-ray energy. In the region of excitation energies around $8 - 9$ MeV, the γ-ray multiplicity is seen to be drastically reduced. In this region, the excitation energy is high enough so that proton/neutron emission starts to compete with γ-ray emission, and the nucleus with $A - 1$ is populated.

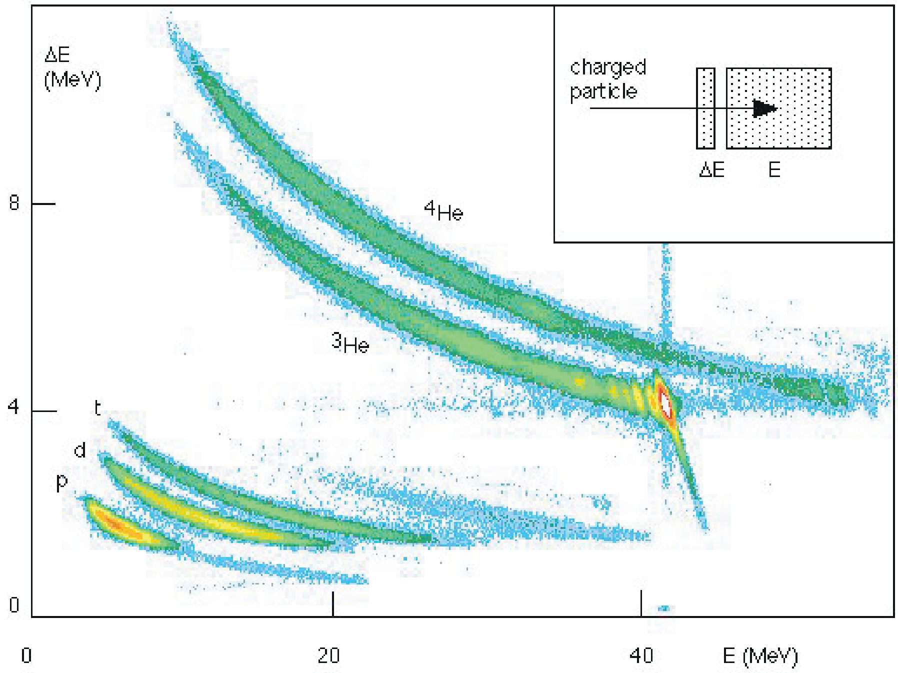

Figure 3.7: Identification of the ejectiles (bananas) by plotting the energy deposited in the thin ΔE detector versus the energy deposited in the thick E detector of the Si particle telescopes (insert).

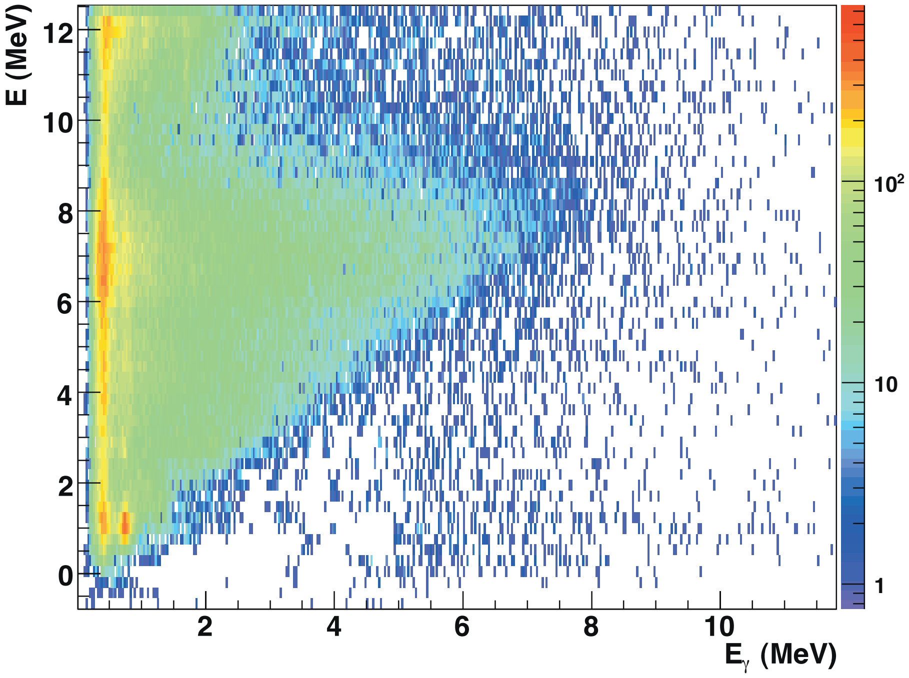

Figure 3.8: Alpha–γ coincidence matrix of ^{44}Sc. The energy of the α particle is transformed into excitation energy E of the residual nucleus using the reaction kinematics and the Q-value.

Chapter 4

The Oslo method

Based on the particle-γ coincidence matrix that is obtained by tagging the measured γ rays with the corresponding particle energy, the Oslo group has developed a method to unfold the γ-ray spectra by means of the response functions of the CACTUS array. In this way, the γ-ray spectra for each excitation energy are corrected for the single- and double escape peak, the annihilation peak, the Compton events, and the detector efficiency [2]. From the unfolded γ-ray spectra, the first γ-rays emitted in the decay cascades from each excitation energy are extracted utilizing a subtraction procedure called the 'first-generation method' [3]. This matrix of primary γ-rays contains information on the level density and the average γ-ray transition probability, which are extracted simultaneously through an iterative procedure with a global fit to the experimental first-generation matrix [4]. Together, these three methods are called the Oslo method.

4.1 Unfolding the γ-ray spectra

The response function of a γ-ray detector depends on the various interactions with matter that the photons can undertake: Compton scattering, photoelectric absorption, and pair production. Ideally, the original γ-ray is fully absorbed and is found in the full-energy peak in the γ-ray spectrum. However, since Compton-scattered photons and one or both of the annihilation photons can escape from the detector and thus deposit only part of the full energy, it is necessary to correct the observed γ-ray spectra for such incompletely detected photons. Additional background from backscattered annihilation and Compton γ-rays in the surroundings of the experimental setup give rise to peak structures at 511 and $\approx$ 200 keV, respectively.

To obtain proper γ-ray spectra, one in principle needs to know the response of the detector for all incident γ-ray energies. In practice, however, one is limited to several well-known γ lines from calibration sources such as ^{152}Eu, ^{60}Co, and ^{137}Cs, and in addition γ lines from in-beam experiments. It is therefore mandatory to choose an appropriate procedure to interpolate between the response functions of the monoenergetic γ-rays to get the response function of all γ energies. The technique used here is explained in detail in Ref. [2], where a folding iteration method called the Compton subtraction method is applied in order to construct full-energy γ spectra. A brief outline of the method is given in the following.

First, the detector response functions $R(E, E_\gamma)$, where E is the actual amount of energy deposited in the detector, are established for available incident γ-ray energies E_γ. In total, ten response functions have been measured for monoenergetic γ lines ranging from 122 to 15 110 keV [2]. These spectra are the basis for interpolating to intermediate full energy γ-ray peaks. This interpolation is easily done for the peak structures, that is, the full energy (f), single escape (s), double escape (d), and annihilation (a) peaks, by adding a Gaussian distribution at the interpolated peak position with proper intensity and width. However, the interpolation of the Compton background is more complicated, as the observed Compton background response functions have different maximum energy depending on their respective full energy values. Therefore, the interpolation operates along a set of curves forming a fan, connecting the same channels in the lower end and the highest channels in the upper end of the spectra, see Fig. 4.1. A γ-ray that is scattered at an angle θ transfers an energy E to the electron as given by

$$E = E_\gamma - \frac{E_\gamma}{1 + \frac{E_\gamma}{m_e c^2}(1 - \cos\theta)}, \tag{4.1}$$

where m_e is the electron mass and c is the speed of light. As a reasonable approach, the Compton background is thus interpolated between channels having the same Compton scattering angle θ (see Fig. 4.1).

Having the appropriate response matrix $\mathbf{R}$ at hand, the unfolding procedure can be applied on the experimental γ-ray spectra. The folding iteration method takes advantage of the fact that folding is easy and fast to perform. Each matrix element R_{ij} of the response matrix $\mathbf{R}$ is defined as the response in channel i when the detector is hit by γ-rays with an energy corresponding to channel j. For each incident γ-ray energy channel j, the response function is normalized so that $\sum_i R_{ij} = 1$. The folding is then

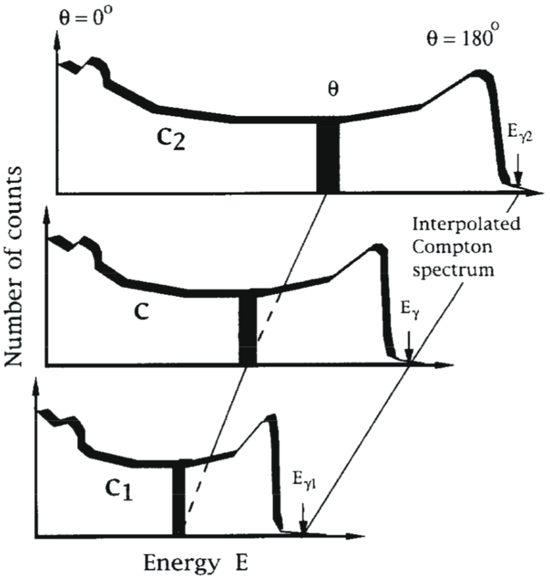

Figure 4.1: The interpolation of the Compton part of the measured response functions c_1 and c_2, illustrating the increase of $\Delta\theta$ with the full energy E_γ.

expressed as

$$f = \mathbf{R}u, \tag{4.2}$$

or, explicitly,

$$\begin{pmatrix} f_1 \\ f_2 \\ \vdots \\ f_N \end{pmatrix} = \begin{pmatrix} R_{11} & R_{12} & \dots & R_{1N} \\ R_{21} & R_{22} & \dots & R_{2N} \\ \vdots & \vdots & \dots & \vdots \\ R_{N1} & R_{N2} & \dots & R_{NN} \end{pmatrix} \begin{pmatrix} u_1 \\ u_2 \\ \vdots \\ u_N \end{pmatrix}. \tag{4.3}$$

Here, f and u represent the folded and unfolded spectra, respectively. Thus by obtaining better and better trial spectra for u, those trial functions can be folded with the corresponding response functions and compared with the observed γ spectrum, hereby denoted r. In practice, the folding iteration method is carried out as follows:

1. As the first trial function u^0 for the unfolded spectrum, the observed spectrum r is used:
$$u^0 = r. \tag{4.4}$$
2. The first folded spectrum f^0 is then calculated,
$$f^0 = \mathbf{R}u^0. \tag{4.5}$$

3. The next trial function u^1 is obtained by adding the difference spectrum $r - f^0$ as a correction to the original trial function u^0:

$$u^1 = u^0 + (r - f^0). \tag{4.6}$$

4. The new trial function u^1 is folded again to get the next f^1, which again is used to generate the next trial function:

$$u^2 = u^1 + (r - f^1), \tag{4.7}$$

   and so on until $f^i \sim r$, where i is the iteration index.

Typically, ten iterations ($i = 10$) are sufficient to get a folded spectrum that agrees with the observed spectrum within the experimental uncertainties. However, the obtained unfolded spectrum $u^{10} = u$ exhibits strong oscillations and fine structures, which give artificially a better resolution of u than the experimental resolution. This problem is mended by the Compton subtraction method [2].

The starting point for the Compton subtraction method is the unfolded spectrum u resulting from the folding iteration method as described above, hereby denoted u_0. This spectrum is used to create the expected contributions from the full energy u_{f}, single escape u_{s}, double escape u_{d}, and annihilation u_{a} part of the original, observed spectrum:

$$u_{\mathrm{f}}(i) = p_{\mathrm{f}}(i)u_0(i), \tag{4.8}$$

$$u_{\mathrm{s}}(i - i_{511}) = p_{\mathrm{s}}(i)u_0(i), \tag{4.9}$$

$$u_{\mathrm{d}}(i - i_{1022}) = p_{\mathrm{d}}(i)u_0(i), \tag{4.10}$$

$$u_{\mathrm{a}}(i_{511}) = \sum_i p_{\mathrm{a}}(i)u_0(i), \tag{4.11}$$

where i_{511} and i_{1022} represent the channels with energies 511 and 1022 keV, respectively. The factors $p_{\mathrm{f}}(i)$, $p_{\mathrm{s}}(i)$, $p_{\mathrm{d}}(i)$, and $p_{\mathrm{a}}(i)$ are the probabilities for an event in channel i to be a photo peak, single escape, double escape, or annihilation event, respectively (see Table 1 in Ref. [2]). The probabilities are normalized so that

$$\sum_i p_{\mathrm{f}}(i) + p_{\mathrm{s}}(i) + p_{\mathrm{d}}(i) + p_{\mathrm{a}}(i) + p_{\mathrm{c}}(i) = 1, \tag{4.12}$$

where $p_{\mathrm{c}}(i)$ is the probability for a Compton event in channel i.

The u_{a} spectrum, originally with all its counts in channel i_{511}, must be smoothed with the experimental resolution denoted 1.0 FWHM in order to get the energy resolution of the observed spectrum. The energy resolution of the spectra u_f, u_s, and u_d is determined by the resolution of the observed spectrum (1.0 FWHM) and the response matrix (0.5 FHWM) giving[1] $\sqrt{1.0^2 - 0.5^2}$ FWHM $= 0.87$ FWHM. Therefore, an additional smoothing of 0.5 FWHM is done to get a spectrum with the experimental resolution of 1.0 FWHM: $\sqrt{0.87^2 + 0.5^2}$ FWHM ≈ 1.0 FWHM.

The Compton background spectrum[2] $c(i)$ can now be found by subtracting the components u_f, u_s, u_d, and u_a from the experimentally observed spectrum $r(i)$:

$$c(i) = r(i) - v(i), \tag{4.13}$$

where

$$v(i) = u_\mathrm{f} + u_\mathrm{s} + u_\mathrm{d} + u_\mathrm{a}. \tag{4.14}$$

The extracted Compton spectrum $c(i)$ displays strong oscillations of the same order as the experimental spectrum $r(i)$. To be able to preserve the experimental, statistical fluctuations, an additional, rather strong smoothing of 1.0 FWHM is applied on the spectrum $c(i)$, justified by the fact that this spectrum should be a slowly varying function of energy. The total smoothing of $c(i)$ is then $\sqrt{2}$ FWHM.

To obtain the unfolded energy spectrum u_unf of full-energy peaks, the smoothed Compton spectrum c and the peaks u_s, u_d, and u_a are subtracted from the observed spectrum r:

$$u_\mathrm{unf}(i) = r(i) - c(i) - u_\mathrm{s}(i - i_{511}) - u_\mathrm{d}(i - i_{1022}) - u_\mathrm{a}(i_{511}). \tag{4.15}$$

Finally, the true γ-ray energy distribution is calculated, correcting u_unf for the full energy probability p_f and the energy-dependent total γ-ray detection efficiency ϵ_tot:

$$U_\mathrm{unf}(i) = \frac{u_\mathrm{unf}(i)}{p_\mathrm{f}(i)\epsilon_\mathrm{tot}(i)}. \tag{4.16}$$

Here, ϵ_tot is taken from Table 1 in Ref. [2]. In addition, ϵ_tot is multiplied with the energy-dependent cutoff function reflecting the individual detector's discriminator level. Typically, the experimental energy threshold is about 100-200 keV with a width of $\approx$ 100 keV.

Figure 4.2 shows an example of the resulting α–γ coincidence matrix of ^{44}Sc, where all γ-ray spectra for each excitation-energy bin are unfolded

---

[1] Assuming that the spectra f, r, and u follow a Gaussian behavior, we have $(\delta f)^2 = (\delta r)^2 + (\delta u)^2$, giving $\delta u = \sqrt{(\delta f)^2 - (\delta r)^2}$.

[2] This Compton spectrum also contains the backscattering peak at $\approx$ 200 keV stemming from Compton backscattered γ-rays of the surroundings, in addition to other background events such as X-rays.

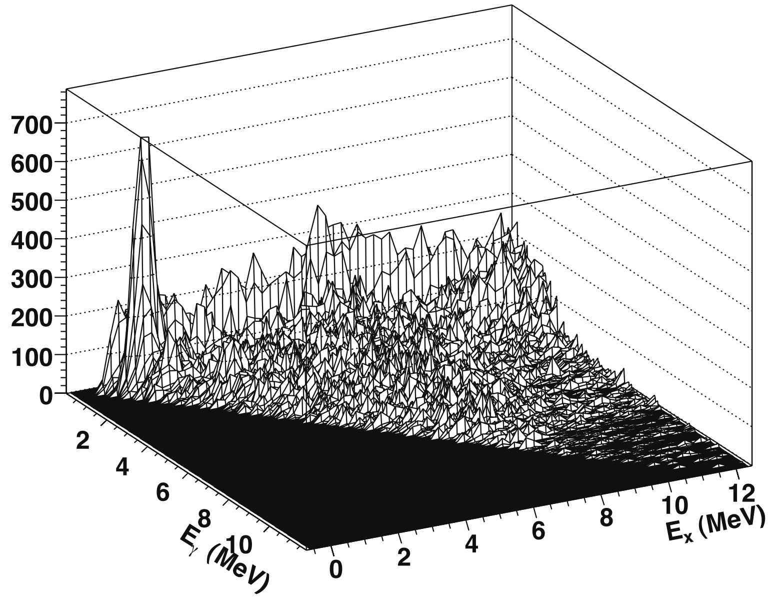

Figure 4.2: Unfolded α–γ coincidence matrix of ^{44}Sc.

using the above-described method. A fraction of the matrix is displayed in Fig. 4.3, where a projection of the γ-ray spectra has been performed for excitation energies between 5.5–6.5 MeV. As is seen from Fig. 4.3 by comparing the original and the folded spectrum, the unfolding procedure works very well.

4.2 Distribution of first-generation γ rays

In general, the γ decay from highly excited states involves a cascade of transitions. The measured γ spectra will contain contributions from all decay steps, since the γ decay in the quasi-continuum is generally very fast ($\approx 10^{-15}$ s) and as no timing technique is able to determine the order of the γ-rays that belonged to a specific cascade. As the generations of γ rays are not well separated in energy either, it is difficult to get hold of the distribution of primary γ-rays in this excitation-energy region.

The nuclear physics group at the OCL has developed a subtraction method to extract the primary (first-generation) γ-rays from the quasi-continuum γ-ray spectra measured for each excitation-energy bin. The method is described in detail in Ref. [3], and its main features will be

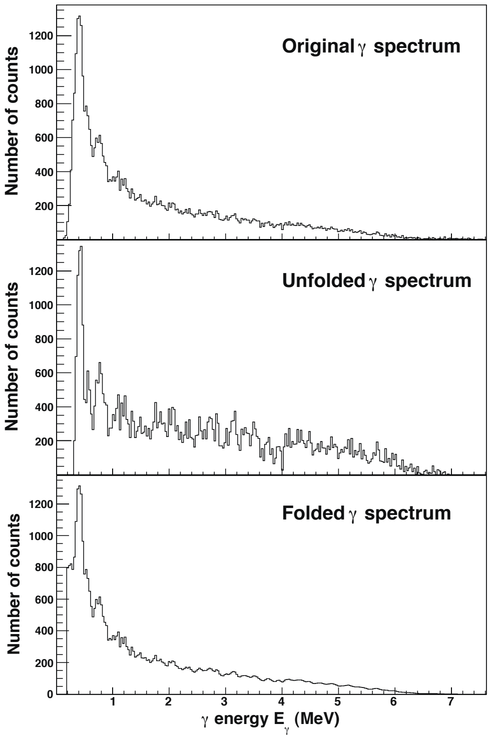

Figure 4.3: Original (top), unfolded (middle) and folded γ spectrum of ^{44}Sc for excitation energy between 5.5 − 6.5 MeV.

sketched here.

The main assumption of the first-generation method is that the γ decay from any excitation-energy bin is independent on how the nucleus was excited to this bin. In other words, the decay routes are the same whether they were initiated directly by the nuclear reaction or by γ decay from higher-lying states. This assumption is automatically fulfilled when states have the same cross section to be populated by the two processes, since γ branching ratios are properties of the levels themselves. Even if different states are populated, the assumption is still valid for statistical γ decay, which only depends on the γ-ray energy and the number of accessible final states. Here, in the region of high level density, the nucleus seems to attain a compound-like system before emitting γ-rays even though the direct reactions (^{3}He,α) and (^{3}He,^{3}He$'$) are utilized. This is because the reaction time, and thus the time it takes to create a complete compound state, is $\approx 10^{-18}$s, while the typical life time of states in the quasi-continuum is $\approx 10^{-15}$s. Therefore, it is reasonable to assume that the nucleus has thermalized prior to γ decay.

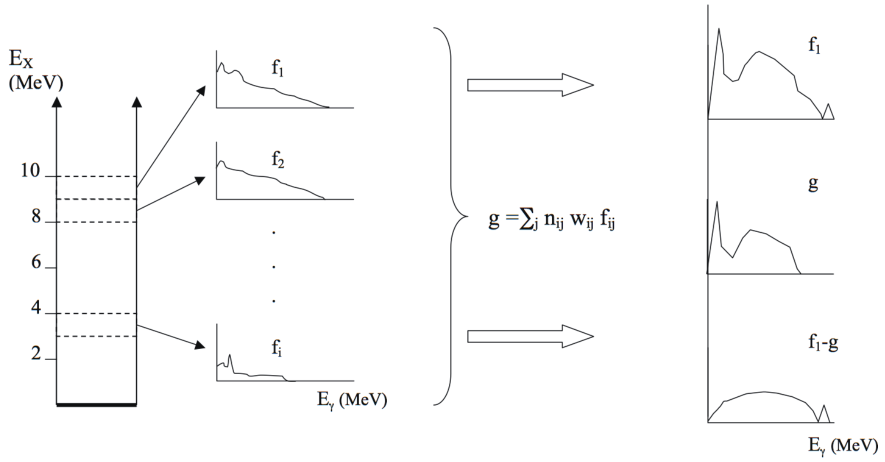

Figure 4.4: Illustration of the principle of the first-generation method (see text).

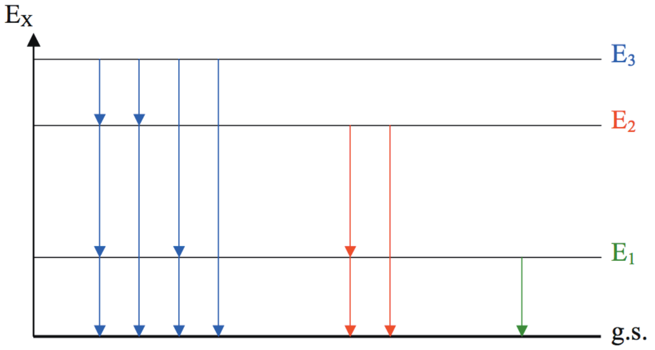

Figure 4.5: A hypothetical γ-decay cascade. The first-generation γ rays from level E_3 can be obtained by subtracting the γ spectra from the levels E_2 and E_1.

The method is illustrated in Fig. 4.4. For each excitation-energy bin i (typically $120 - 240$ keV wide), a γ-ray spectrum f_i is projected out from the total particle–γ coincidence matrix, which is generated as described in Sec. 3.3.3 and unfolded as explained in Sec. 4.1. The unfolded spectra f_i are made of all generations of γ rays from all possible cascades decaying from the excited levels within the bin i. Now, we utilize the fact that the spectra $f_{j<i}$ for all the underlying energy bins j contain the same γ transitions as f_i *except* the first γ rays emitted, since they will bring the nucleus from the states in bin i to underlying states in the energy bins j. This is shown for one specific, hypothetical cascade in Fig. 4.5, where it is easily seen that by subtracting the γ spectra from the levels E_2 and E_1, the first-generation spectrum of level E_3 is found. The picture of Fig. 4.5 is of course oversimplified. In reality, one has to take into account the different cross

sections for populating the levels in the various energy bins i and also the different intensities (branching ratios) of the primary γs. Therefore, the first-generation spectrum h_i is found by

$$h_i = f_i - g_i, \tag{4.17}$$

where g_i is a weighted sum of all spectra

$$g_i = n_{i1}w_{i1}f_1 + n_{i2}w_{i2}f_2 + \ldots + n_{ij}w_{ij}f_j = \sum_j n_{ij}w_{ij}f_j. \tag{4.18}$$

Here, the unknown coefficients w_{ij} (with $\sum_j w_{ij} = 1$) represent the probability of the decay from bin i to bin j. In other words, w_{ij} is the weighting coefficient or branching ratio of each primary γ-ray depopulating level i. In this sense, the w_{ij} values correspond directly to the first-generation spectrum h_i.

The coefficients n_{ij} are correcting factors for the different cross sections of populating level i and the underlying levels j, and are determined so that the total area of each spectrum f_i multiplied by n_{ij} corresponds to the same number of cascades. This can be done in two ways [3]:

- Singles normalization. The singles-particle cross section is proportional to the number of populated states and thus to the number of decay cascades. We denote the number of counts measured for bin i and j in the singles spectrum S_i and S_j, respectively. The normalization factor n_{ij} that should be applied to the spectrum f_j is then given by

  $$n_{ij} = \frac{S_j}{S_i}. \tag{4.19}$$

- Multiplicity normalization. The average γ-ray multiplicity $\langle M \rangle$ can be obtained in the following way [70]: Assume an N-fold population of an excited level E. The decay from this level will result in N γ-ray cascades, where the ith cascade contains M_i γ rays. The average γ-ray energy $\langle E_\gamma \rangle$is equal to the total energy carried by the γ rays divided by the total number of γ rays:

  $$\langle E_\gamma \rangle = N \cdot \frac{E}{\sum_{i=1}^{N} M_i} = \frac{E}{\frac{1}{N}\sum_{i=1}^{N} M_i} = \frac{E}{\langle M \rangle}. \tag{4.20}$$

  Then, the average multiplicity is simply given by

  $$\langle M \rangle = \frac{E}{\langle E_\gamma \rangle}. \tag{4.21}$$

The average γ-ray multiplicity $\langle M_i \rangle$ can thus easily be calculated for each excitation-energy bin i. Let the area (or total number of counts) in spectrum f_i be denoted by $A(f_i)$. Then the singles particle cross section S_i is proportional to the ratio $A(f_i)/\langle M_i \rangle$, and the normalization coefficient n_{ij} that should be applied to bin i when subtracting bin j is

$$n_{ij} = \frac{A(f_i)/\langle M_i \rangle}{A(f_j)/\langle M_j \rangle} = \frac{\langle M_j \rangle A(f_i)}{\langle M_i \rangle A(f_j)}. \tag{4.22}$$

In order to choose between the two normalization methods, one needs to consider the actual experimental conditions. For example, if the nucleus studied has an isomeric state that has a longer life time than the time range of the TDCs, the γ decay from this state will not be measured in coincidence with the outgoing particle. This was the case for the nucleus ^{44}Sc, which has an isomer at $E = 271.13$ keV with a half-life of 58.6 hours [26]. Therefore, the multiplicity normalization was applied for the Sc nuclei. In general, the two normalization methods give very similar results.

In cases where the multiplicity is well determined, an area consistency check can be applied to Eq. 4.17. Assume that a small correction has to be introduced by substituting g_i by αg_i, where α is close to unity. The area of the first-generation γ spectrum is then

$$A(h_i) = A(f_i) - \alpha A(g_i), \tag{4.23}$$

and corresponds to a γ-ray multiplicity of one unit. Since the number of primary γ rays in the spectrum f_i equals $A(f_i)/\langle M_i \rangle$, $A(h_i)$ is also given by

$$A(h_i) = A(f_i)/\langle M_i \rangle. \tag{4.24}$$

Combining Eqs. (4.23) and (4.24) yields

$$\alpha = (1 - 1/\langle M_i \rangle)\frac{A(f_i)}{A(g_i)}. \tag{4.25}$$

The α parameter can be varied to get the best agreement of the areas $A(h_i)$, $A(f_i)$ and $A(g_i)$ within the following restriction: $\alpha = 1.00 \pm 0.15$; that is, the correction should not exceed 15%. If a greater correction is necessary, then improved weighting functions w_{ij} should be determined instead.

As mentioned before, the weighting coefficients w_{ij} correspond directly to the first-generation spectrum h_i, and this close relationship makes it possible to determine w_{ij} (and thus h_i) through a fast converging iteration procedure [3]:

1. Apply a trial function w_{ij}.
2. Deduce h_i.
3. Transform h_i to w_{ij} by giving h_i the same energy calibration as w_{ij}, and normalizing the area of h_i to unity.
4. If $w_{ij}(\text{new}) \approx w_{ij}(\text{old})$, convergence is reached and the procedure is finished. Otherwise restart from step 2.

Tests of the convergence properties of the procedure have shown that excellent agreement is achieved between the exact solution (from simulated spectra) and the trial function w_{ij} already after three iterations [3]. Usually, about 10 iterations are performed on experimental spectra.

To demonstrate how well the first-generation procedure works, Fig. 4.6 shows the total, unfolded γ spectrum, the second and higher generations γ-ray spectrum and the first-generation spectrum of ^{45}Sc for excitation energy between $E = 5.5 - 6.5$ MeV. The first-generation spectrum has a continuum-like, bell-shaped form indicating that the γ decay is dominated by statistical processes in the region $E_\gamma = 1.4 - 6.5$ MeV. However, by looking at the lower panel of Fig. 4.6, it is clear that the main assumption of the subtraction method is not fulfilled for $E_\gamma \lesssim 1.4$ MeV. In this region, some strong, low-energy transitions were not subtracted correctly. This means that the levels from which these transitions originate are populated more strongly from higher excited levels through γ emission, than directly by inelastic ^{3}He scattering. Therefore, only data for $E_\gamma > 1.6$ MeV is used in the further analysis. Similar considerations are done for the V and Mo nuclei.

4.3 Extraction of level density and γ-ray strength function

For compound reactions, the following assumption has been shown to be valid: the relative probability for decay into any specific set of final states is independent of the means of formation of the compound nucleus; in other words, the compound nucleus can share its excitation energy on a relatively large number of nucleons and thus "forgets" the way of formation (see, e.g., Refs. [1, 75]). The subsequent decay of the compound states will mainly be governed by statistical rules. Therefore, the decay probability $P(E, E_\gamma)$ of a γ-ray with energy E_γ decaying from a specific excitation-energy E is proportional to the level density $\rho(E_\mathrm{f})$ at the final excitation

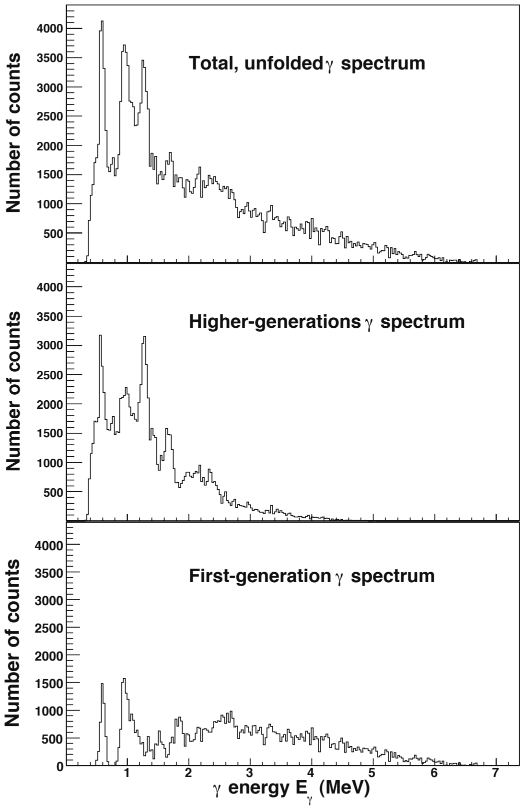

Figure 4.6: Unfolded, total γ-ray spectrum, second and higher-generation γ-ray spectrum and first-generation γ-ray spectrum of ^{45}Sc for excitation energy between $5.5 - 6.5$ MeV.

energy $E_{\mathrm{f}} = E - E_\gamma$, and the γ-ray transmission coefficient $\mathcal{T}(E_\gamma)$:

$$P(E, E_\gamma) \propto \rho(E_{\mathrm{f}})\mathcal{T}(E_\gamma). \tag{4.26}$$

The essential assumption the above relation is based on is that the nuclear reaction can be described as a two-stage process, where a compound state is first formed before it decays in a manner that is independent of the mode of formation [75, 76]. This is believed to be fulfilled at high excitation energy, even though the direct reactions (^{3}He,α) and (^{3}He,^{3}He$'$) are used, as already discussed in Sec. 4.2. Equation (4.26) can also be compared with Fermi's golden rule:

$$\lambda = \frac{2\pi}{\hbar} \left|\langle \mathrm{f} \,|\hat{H}_{\mathrm{int}}|\, \mathrm{i}\rangle\right|^2 \rho(E_{\mathrm{f}}), \tag{4.27}$$

where λ is the decay rate of the initial state $|\mathrm{i}\rangle$ to the final state $|\mathrm{f}\rangle$, and $\hat{H}_{\mathrm{int}}$ is the transition operator. In Eq. 4.26, an ensemble of initial and final states within each excitation-energy bin is considered, and thus the average decay properties of a set of initial states to a set of final states.

The γ-ray transmission coefficient $\mathcal{T}(E_\gamma)$ in Eq. 4.26 is independent of the excitation energy, and thus the nuclear temperature according to the generalized Brink-Axel hypothesis [30, 36], which states that collective excitation modes built on excited states have the same properties as those built on the ground state. This hypothesis is violated when high temperatures and/or spins are involved in the nuclear reactions, as shown for GEDR excitations in Ref. [60] and references therein. However, since both the temperature reached and the spins populated are rather low for the experiments in this work, these dependencies are assumed to be of minor importance in the excitation-energy region of interest here.

To extract the level density and the γ-ray transmission coefficient, an iterative procedure [4] is applied to the first-generation γ matrix $P(E, E_\gamma)$. The basic idea of this method is to minimize

$$\chi^2 = \frac{1}{N_{\text{free}}} \sum_{E=E^{\min}}^{E^{\max}} \sum_{E_\gamma=E_\gamma^{\min}}^{E} \left(\frac{P_{\text{th}}(E, E_\gamma) - P(E, E_\gamma)}{\Delta P(E, E_\gamma)} \right)^2, \tag{4.28}$$

where N_{free} is the number of degrees of freedom, and $\Delta P(E, E_\gamma)$ is the uncertainty in the experimental first-generation γ-ray matrix. The experimental matrix of first-generation γ-rays is normalized [4] such that for every excitation-energy bin E, the sum over all γ energies E_γ from some minimum value $E_\gamma^{\min}$ to the maximum value $E_\gamma^{\max} = E$ at this excitation-energy bin is unity:

$$\sum_{E_\gamma=E_\gamma^{\min}}^{E} P(E, E_\gamma) = 1. \tag{4.29}$$

The first-generation γ-ray matrix can theoretically be approximated by

$$P_{\text{th}}(E, E_\gamma) = \frac{\rho(E - E_\gamma)\mathcal{T}(E_\gamma)}{\sum_{E_\gamma=E_\gamma^{\min}}^{E} \rho(E - E_\gamma)\mathcal{T}(E_\gamma)}. \tag{4.30}$$

The input (experimental) matrix $P(E, E_\gamma)$ and the output (theoretical) matrix $P_{\text{th}}(E, E_\gamma)$ of ^{50}V are displayed in Fig. 4.7. The limits set in the first-generation matrix for extraction are also shown. These limits are chosen to ensure that the data utilized are from the statistical excitation-energy region ($E^{\min}$, $E^{\max}$) and that no γ lines stemming from, e.g., yrast transitions, which might not be subtracted correctly in the first-generation method, are used in the further analysis ($E_\gamma^{\min}$). Every point of the ρ and $\mathcal{T}$ functions is assumed to be an independent variable, so that the reduced χ^2 of

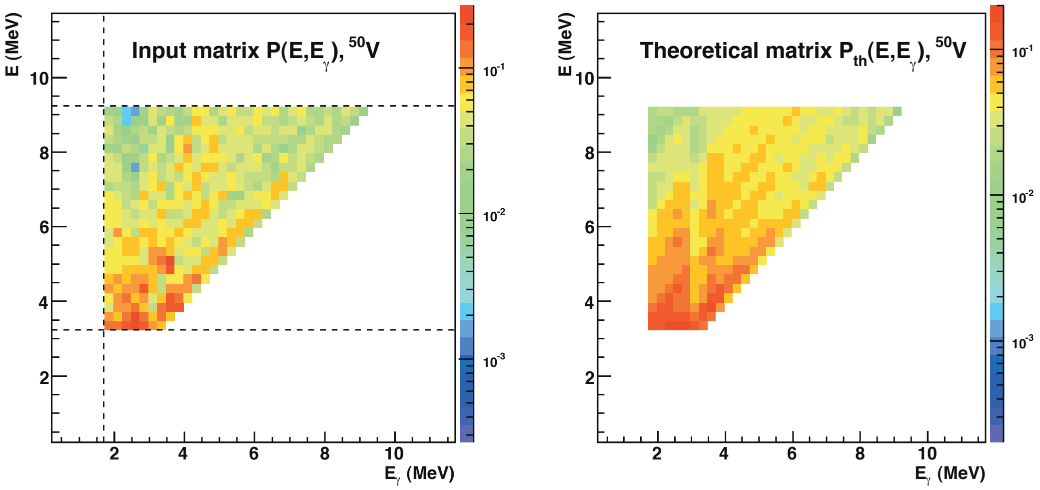

Figure 4.7: The experimental first-generation matrix $P(E, E_\gamma)$ of ^{50}V (left) and the calculated one (right) from the iteration procedure of A. Schiller *et al.* [4]. The dashed lines show the limits set in the experimental first-generation matrix.

Eq. (4.28) is minimized for every argument $E - E_\gamma$ and E. The quality of the procedure when applied to ^{50}V is shown in Fig. 4.8, where the experimental first-generation spectra for various initial excitation energies are compared to the least-χ^2 solution. In general, the agreement between the experimental data and the fit is very good.

The globalized fitting to the data points only gives the functional form of ρ and $\mathcal{T}$. In fact, it has been shown [4] that if one solution for the multiplicative functions ρ and $\mathcal{T}$ is known, one may construct an infinite number of other functions, which give identical fits to the $P(E, E_\gamma)$ matrix by

$$\begin{aligned} \tilde{\rho}(E - E_\gamma) &= A \exp[\alpha(E - E_\gamma)]\, \rho(E - E_\gamma), & (4.31)\\ \tilde{\mathcal{T}}(E_\gamma) &= B \exp(\alpha E_\gamma) \mathcal{T}(E_\gamma). & (4.32) \end{aligned}$$

Therefore the transformation parameters α, A and B, which correspond to the physical solution, remain to be found.

4.3.1 Normalizing the level density

In order to determine the correction α to the slope of the level density and the γ-ray transmission coefficient, and to determine the absolute value A of the level density in Eq. (4.31), the ρ function is adjusted to fit the number of known discrete levels at low excitation energy and neutron (or proton)

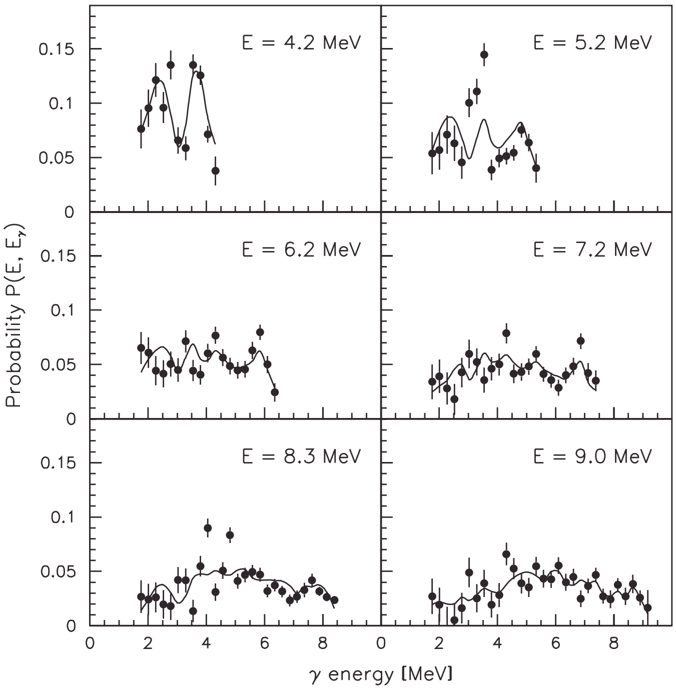

Figure 4.8: Experimental first-generation γ spectra (data points with error bars) at six different initial excitation energies (indicated in the figure) compared to the χ^2 fit (solid lines) for ^{50}V. The fit is performed simultaneously on the entire first-generation matrix of which the six displayed spectra are a fraction.

resonance data at high excitation energy. This normalization is shown for ^{44}Sc in Fig. 4.9. The data point at high excitation energy (open square in Fig. 4.9) is calculated in the following way according to [4]: The starting point are the Eqs. (4) and (5) of Ref. [16]:

$$\rho(U,J) = \frac{\sqrt{\pi}}{12}\frac{\exp(2\sqrt{aU})}{a^{1/4}U^{5/4}}\frac{(2J+1)\exp\left[-(J+1/2)^2/2\sigma^2\right]}{2\sqrt{2\pi}\sigma^3}, \tag{4.33}$$

$$\rho(U) = \frac{\sqrt{\pi}}{12}\frac{\exp(2\sqrt{aU})}{a^{1/4}U^{5/4}}\frac{1}{\sqrt{2\pi}\sigma}, \tag{4.34}$$

where $\rho(U,J)$ is the level density for a given spin J, and $\rho(U)$ is the level density for all spins (Eq. (4.34) is identical to Eq. (2.4)). The level-density parameter a and the spin cutoff parameter σ is taken from Ref. [18]. Let I be the spin of the target nucleus in a neutron resonance experiment. The average neutron resonance spacing $D_{\ell=0}$ for s-wave neutrons with

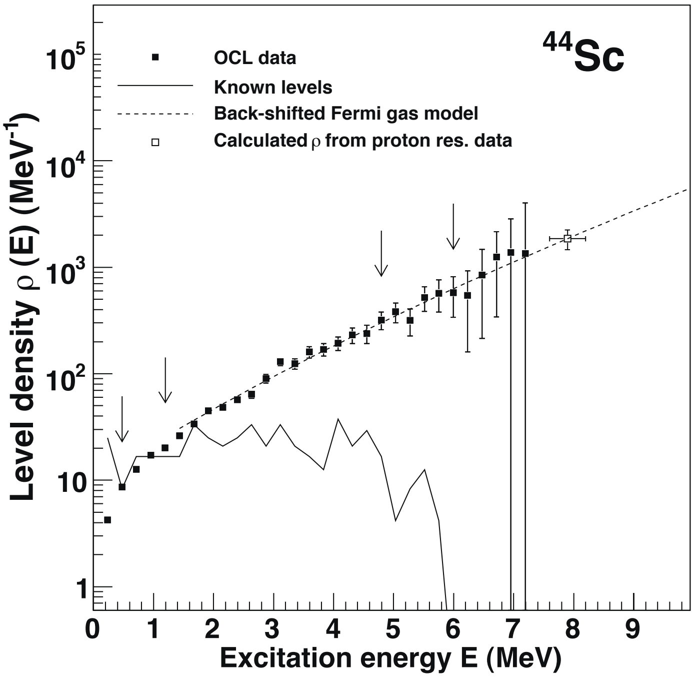

Figure 4.9: Normalization procedure of the level density (data points) of ^{44}Sc. The data points between the arrows are normalized to known levels at low excitation energy (solid line) and to the level density at the proton binding energy (open square) using an interpolation with the Fermi-gas level density (dashed line).

spin/parity $1/2^+$ can be written as

$$\frac{1}{D_0} = \frac{1}{2}\left[\rho(B_n, J = I + 1/2) + \rho(B_n, J = I - 1/2)\right], \tag{4.35}$$

because all levels with spin $J = I \pm 1/2$ are accessible in neutron resonance experiments, and it is assumed that both parities contribute equally to the level density at the neutron binding energy B_n. Combining Eqs. (4.33) to (4.35) with $U = B_n$, one finds the total level density at the neutron binding energy to be

$$\rho(B_n) = \frac{2\sigma^2}{D_0} \cdot \frac{1}{(I+1)\exp\left[-(I+1)^2/2\sigma^2\right] + \exp\left[-I^2/2\sigma^2\right]}, \tag{4.36}$$

where σ is calculated at B_n using Eq. (2.9).

Since the data only reach up to excitation energies around $B_n - E_\gamma^{\mathrm{min}}$, an interpolation is made between the Oslo data and $\rho(B_n)$ using the back-shifted Fermi gas model of Ref. [18], as shown in Fig. 4.9.

4.3.2 Normalizing the γ-ray transmission coefficient

The slope of the γ-ray transmission coefficient $\mathcal{T}(E_\gamma)$ has already been determined through the normalization of the level density as explained in the previous section. The remaining constant B in Eq. (4.32) gives the absolute normalization of $\mathcal{T}$, and is determined using information from neutron resonance decay on the average total radiative width $\langle\Gamma_\gamma\rangle$ at B_n according to Ref. [61].

The starting point is Eq. (3.1) of Ref. [59],

$$\langle\Gamma_\gamma(E,I,\pi)\rangle = \frac{1}{2\pi\rho(E,I,\pi)}\sum_{XL}\sum_{I_\mathrm{f},\pi_\mathrm{f}}\int_{E_\gamma=0}^{E} \mathrm{d}E_\gamma \mathcal{T}_{XL}(E_\gamma)\rho(E-E_\gamma,I_\mathrm{f},\pi_\mathrm{f}), \tag{4.37}$$

where $\langle\Gamma_\gamma(E,I,\pi)\rangle$ is the average total radiative width of levels with energy E, spin I and parity π. The summation and integration are going over all final levels with spin I_f and parity π_f that are accessible through γ transitions with energy E_γ, electromagnetic character X and multipolarity L. Assuming that the main contribution to the experimental $\mathcal{T}$ is from dipole radiation ($\ell = 1$), it can be expressed as

$$B\mathcal{T}(E_\gamma) = B\sum_{XL}\mathcal{T}_{XL}(E_\gamma) \approx B\left[\mathcal{T}_{\mathrm{E1}}(E_\gamma) + \mathcal{T}_{\mathrm{M1}}(E_\gamma)\right], \tag{4.38}$$

from which the total, experimental γ-ray strength function can easily be calculated from Eq. (2.18):

$$f(E_\gamma) = \frac{1}{2\pi E_\gamma^3} B\mathcal{T}(E_\gamma). \tag{4.39}$$

Further, we also assume that there are equally many accessible levels with positive and negative parity for any excitation energy and spin, so that the level density is given by

$$\rho(E-E_\gamma, I_\mathrm{f}, \pm\pi_\mathrm{f}) = \frac{1}{2}\rho(E-E_\gamma, I_\mathrm{f}). \tag{4.40}$$

Now, by combining Eqs. (4.37), (4.38) and (4.40), the average total radiative width of neutron s-wave capture resonances with spins $I_t \pm 1/2$ expressed in terms of $\mathcal{T}$ is obtained:

$$\begin{aligned}\langle\Gamma_\gamma(B_n, I_t \pm 1/2, \pi_t)\rangle = & \frac{B}{4\pi\rho(B_n, I_t \pm 1/2, \pi_t)} \int_{E_\gamma=0}^{B_n} \mathrm{d}E_\gamma \mathcal{T}_{XL}(E_\gamma) \\ & \times \rho(B_n - E_\gamma) \sum_{J=-1}^{1} g(B_n - E_\gamma, I_t \pm 1/2 + J),\end{aligned} \tag{4.41}$$

where I_t and π_t are the spin and parity of the target nucleus in the (n,γ) reaction and $\rho(B_n - E_\gamma)$ is the experimental level density. Note that the factor $1/\rho(B_n, I_t \pm 1/2, \pi_t)$ equals the neutron resonance spacing D_0. The spin distribution of the level density is given by [16]:

$$g(E, I) = \frac{2I+1}{2\sigma^2} \exp\left[-(I+1/2)^2/2\sigma^2\right]. \tag{4.42}$$

The spin distribution is normalized so that $\sum_I g(E, I) \approx 1$. The experimental value of $\langle\Gamma_\gamma\rangle$ at B_n is then the weighted sum of the level widths of states with $I_t \pm 1/2$ according to Eq. (4.41). From this expression the normalization constant B can be determined as described in Ref. [61]. However, some considerations must be done before normalizing according to Eq. (4.41).

Methodical difficulties in the primary γ-ray extraction prevent determination of the function $\mathcal{T}(E_\gamma)$ for $E_\gamma < E_\gamma^{\min}$ as discussed previously. In addition, the data at the highest γ-energies in the interval $B_n - E_\gamma^{\min} \leq E_\gamma \leq B_n$ suffer from poor statistics. Therefore, $\mathcal{T}$ is extrapolated with an exponential function, as demonstrated for ^{51}V in Fig. 4.10. The contribution of the extrapolation to the total radiative width given by Eq. (4.41) does not normally exceed 15%, thus the errors due to a possibly poor extrapolation are expected to be of minor importance [61].

4.4 Possible uncertainties in the normalization procedures

4.4.1 The spin distribution

The quantity $\rho(B_n)$ is calculated assuming a bell-like spin distribution according to [16] given by Eq. (4.42) and using a model for the spin cutoff parameter σ taken from [16] in the case of the Mo and V nuclei, and from [18] for the Sc isotopes. Both these assumptions could in principle be a

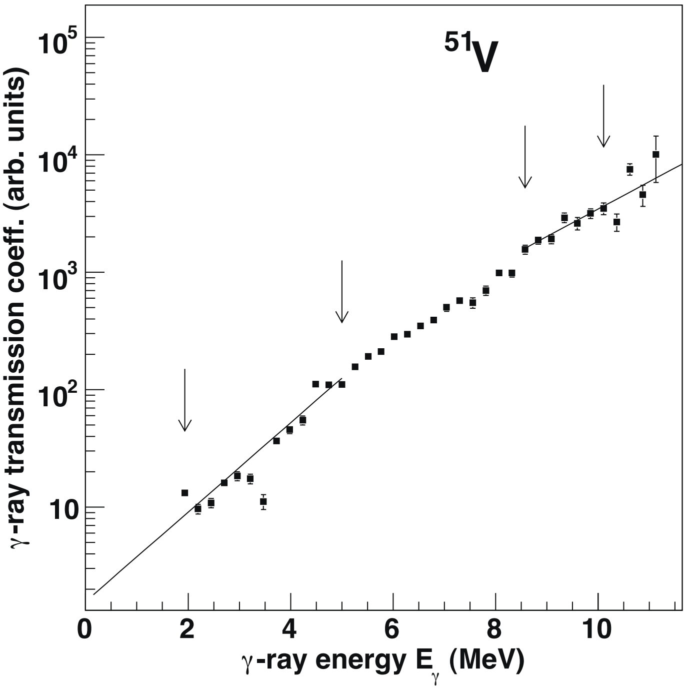

Figure 4.10: Extrapolation of the γ-ray transmission coefficient of ^{51}V. The data points between the arrows in the low and high γ-energy regions are utilized to fit the exponential functions to the data.

source of uncertainty, as it is hard or even impossible to measure the total spin distribution experimentally at high excitation energy.

In Fig. 4.11 various spin distributions for ^{44}Sc are shown, calculated at an excitation energy of 8.0 MeV. In the two upper panels, the spin distribution of [16] has been used, but with the expression for the spin cutoff parameter of [16] given in Eq. (2.5) in panel a) and the formalism of [18] (Eq. (2.9)) in panel b). In panel c) the spin distribution the spin-dependent level densities of [23] are shown. Here, the authors also have assumed a bell-shaped spin distribution according to Eqs. (7) and (8) in [23]. It is clear from the figure that the spin distributions in panel b) and c) give a broader spin distribution and a centroid shifted to higher spins compared to the one in panel a).

In panel d), the spin distribution of the calculated spin- and parity-dependent level density of [25] briefly discussed in Sec. 2.1 is shown. There are no underlying assumptions for the spin distribution in these calculations. It is seen from this distribution that there is a significant difference

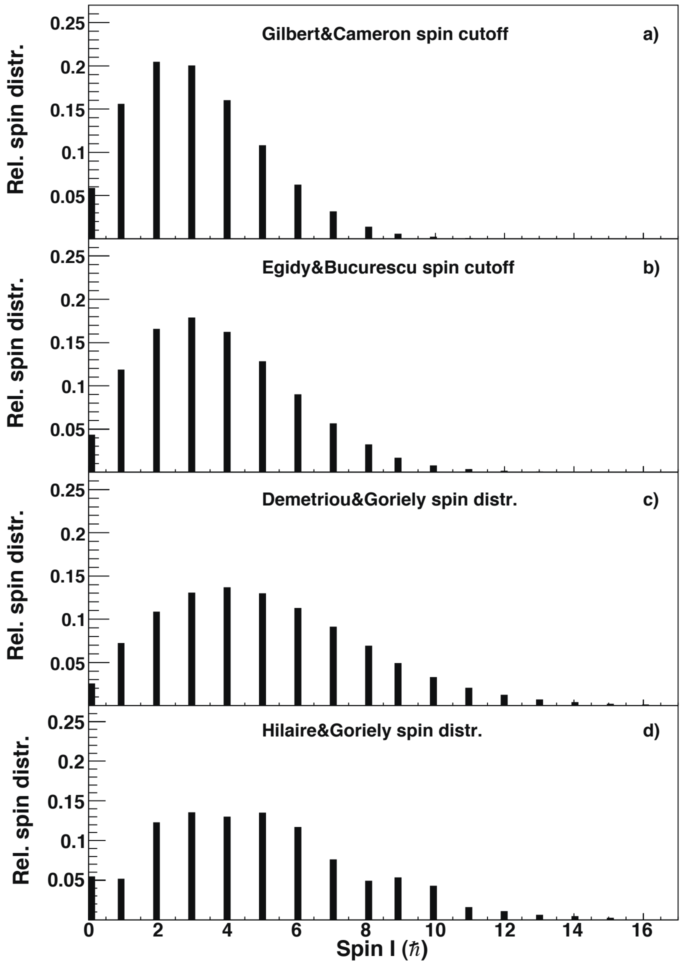

Figure 4.11: Relative spin distributions calculated for $E = 8.0$ MeV of ^{44}Sc (see text).

in the relative numbers of states with spin 0 and 1. The normalization method for the level density described above is especially sensitive to such variations at low spin if the neutron resonance spacing D_0 is measured from a neutron capture reaction where the target nucleus is even-even, that is, with zero ground-state spin. Then the states reached in neutron capture can only have spin $1/2^+$, and the number of all other states must be estimated using a certain spin cutoff parameter, introducing a larger uncertainty in the calculated $\rho(B_n)$. Therefore it is preferred to calculate $\rho(B_n)$ from both D_0 and D_1 resonance spacings if possible, since in the latter, also states with $3/2^-$ are reached for target nuclei with $I^\pi = 0^+$, and will therefore decrease this uncertainty.

4.4.2 The parity distribution

As described above, for both the normalization of the level density and the γ-ray transmission coefficient the assumption of equally many levels with positive and negative parity is used. For the level density, this assumption is likely to be approximately valid since it is utilized for the calculation of $\rho(B_n)$, which is at relatively high excitation energies for the nuclei considered in this work (see Table 3.4). For the nuclei ^{44,45}Sc and $^{93-98}$Mo, this assumption has been investigated by calculating the parity distribution with the code 'Micro' presented in [10]. Using ρ_+ and ρ_- to denote the level density with positive and negative parity levels, the parity asymmetry α is defined as [71]

$$\alpha = \frac{\rho_+ - \rho_-}{\rho_+ + \rho_-}, \tag{4.43}$$

which gives -1 and 1 for only negative and positive parities, respectively, and 0 when both parities are equally represented.

The resulting parity distributions are shown in Figs. 4.12 and 4.13 for the Sc and Mo isotopes. It is seen in Fig. 4.12 that α is close to zero for $E \approx 10$ MeV for both ^{44,45}Sc, in excellent agreement with the findings of [71]. By inspecting the $2^+/2^-$ level densities in ^{58}Ni and ^{90}Zr (Ref. [72] and references therein), one sees that this is also the case for these nuclei. However, the calculations for the Mo isotopes indicate a majority of levels with positive parity, even at excitation energies around 8 MeV, in conflict with the ^{90}Zr data and the calculations of [25].

To investigate the impact of the assumption of parity symmetry on the calculations of $\rho(B_n)$, the ratio ρ_+/ρ_- as a function of the parity asymmetry α is defined from Eq. (4.43) as

$$\frac{\rho_+}{\rho_-} = \frac{1+\alpha}{1-\alpha}. \tag{4.44}$$

Inserting $\alpha \approx 0.3$ found in the calculations on ^{93}Mo, we get

$$\rho_+ \approx 2 \cdot \rho_-, \tag{4.45}$$

which means that the assumption of equally many positive and negative parity levels are clearly not fulfilled in the 'Micro' calculations.

The parity distribution should be taken into account when calculating $\rho(B_n)$ for cases where the parity asymmetry is large. If one assumes that the spin- and parity-projected level density $\rho(E, J, \pi)$ can be described by [73]

$$\rho(E, J, \pi) = \rho(E) \cdot g(E, J) \cdot \mathcal{P}(E, \pi), \tag{4.46}$$

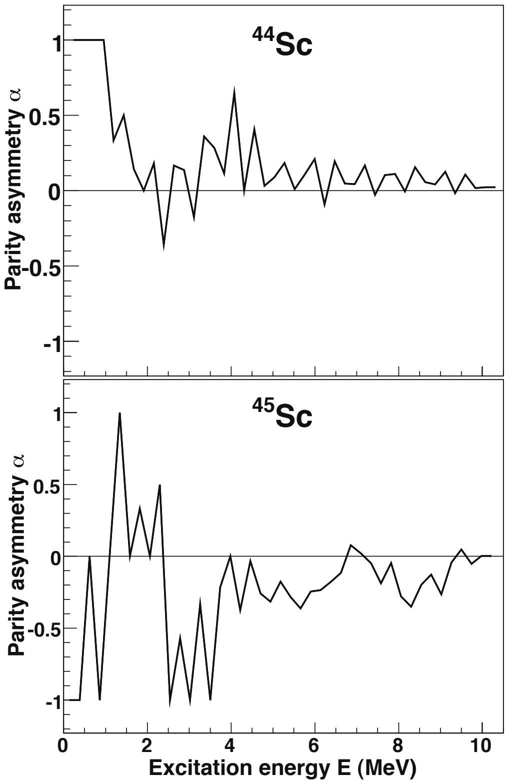

Figure 4.12: Parity distributions as a function of excitation energy calculated for ^{44,45}Sc (see text).

where $\rho(E)$ is the total level density at excitation energy E, $g(E, J)$ is the spin distribution given by Eq. (4.42), and $\mathcal{P}(E, \pi)$ is the parity projection factor. According to Eq. (4.35), we get

$$\frac{1}{D_0} = \rho(B_n) \cdot g(B_n, J = I \pm 1/2) \cdot \mathcal{P}(B_n, \pi_t) \qquad (4.47)$$

for the neutron resonance spacing at B_n reaching states with parity $\pi_t \cdot (-1)^\ell = \pi_t$ for s-wave neutrons having $\ell = 0$. Now, defining the level density of levels with the same parity π_g as the ground state of the nucleus as ρ_g, and the level density of levels with parity π_s opposite to the ground state of the nucleus as ρ_s, we obtain [73]

$$\mathcal{P}_g \equiv \mathcal{P}(E, \pi = \pi_g) = \frac{\rho_g}{\rho} = \frac{1}{1 + \xi}, \qquad (4.48)$$

$$\mathcal{P}_s \equiv \mathcal{P}(E, \pi = \pi_s) = \frac{\rho_s}{\rho} = \frac{1}{1 + 1/\xi}, \qquad (4.49)$$

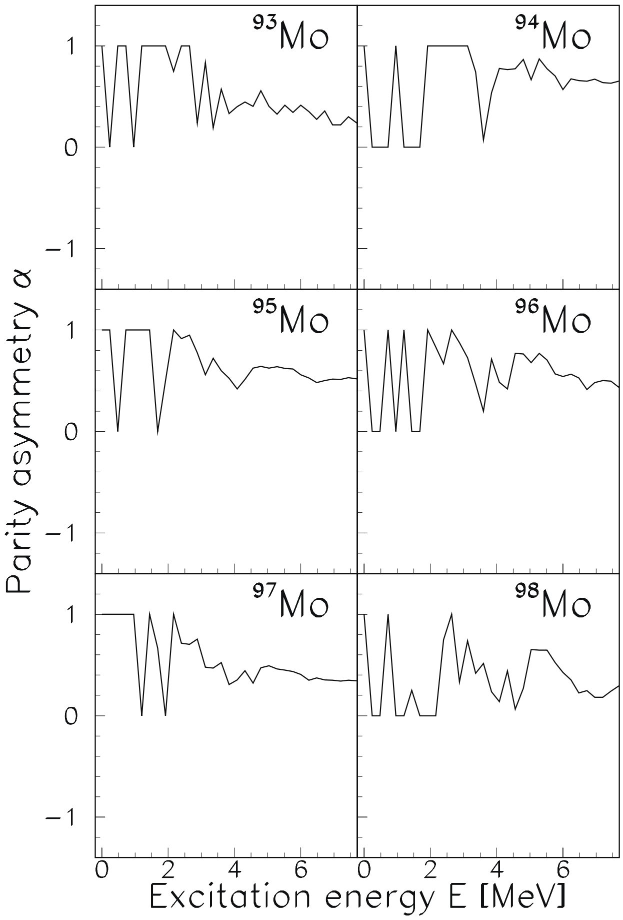

Figure 4.13: Parity distributions as a function of excitation energy calculated for $^{93-98}$Mo (see text).

with

$$\xi = \frac{\rho_s}{\rho_g}. \tag{4.50}$$

Further,

$$\frac{1}{D_0} = \rho(B_n)\,[g(B_n, J = I + 1/2) + g(B_n, J = I - 1/2)]\,\mathcal{P}_g(B_n) \tag{4.51}$$

$$= \rho(B_n)\,[g(B_n, J = I + 1/2) + g(B_n, J = I - 1/2)]\,\frac{1}{1+\xi}, \tag{4.52}$$

which gives

$$\rho(B_n) = \frac{\sigma^2}{D_0} \frac{1+\xi}{(I+1)\exp\left[-(I+1)^2/2\sigma^2\right] + I\exp\left[-I^2/2\sigma^2\right]}, \tag{4.53}$$

using Eq. (4.42). In the future, the expression given in Eq. (4.53) should be used for the calculation of $\rho(B_n)$ instead of Eq. (4.35) if the parity asymmetry is known, and especially if the parity asymmetry at B_n is large. The estimation of the factor ξ should be based on experimental data, or on realistic calculations if such data are not available.

The assumption of equally distributed levels with positive and negative parity influence also the normalization of the γ-ray transmission coefficient. To take into account the parity distribution, one can modify Eq. (4.40) according to Eq. (4.46) so that

$$\rho(E-E_\gamma, I_\mathrm{f}, \pm\pi_\mathrm{f}) = \rho(E-E_\gamma) \cdot g(E-E_\gamma, I_\mathrm{f}) \cdot \mathcal{P}_g(E-E_\gamma, \pi_\mathrm{f}). \tag{4.54}$$

Instead of Eq. (4.41), one finds

$$\begin{aligned}\langle\Gamma_\gamma(B_n, I_t \pm 1/2, \pi_t)\rangle = & \frac{B}{2\pi\rho(B_n, I_t \pm 1/2, \pi_t)} \int_{E_\gamma=0}^{B_n} \mathrm{d}E_\gamma \mathcal{T}_{XL}(E_\gamma) \\ & \times \rho(B_n - E_\gamma) \sum_{J=-1}^{1} g(B_n - E_\gamma, I_t \pm 1/2 + J) \mathcal{P}_g(B_n - E_\gamma, \pi_\mathrm{f}),\end{aligned} \tag{4.55}$$

where $\mathcal{P}_g$ now must be evaluated for every argument $B_n - E_\gamma$.

4.5 Robustness test of the Oslo method

The nucleus ^{96}Mo has become a benchmark for other experimental groups trying to verify or falsify the upbend structure seen in the γ-ray strength function [9]. For ^{96}Mo, it has been discovered that the extraction of the first-generation spectra used in Ref. [9] was not performed in an optimal way, and therefore the data sets from the reactions ^{96}Mo(^{3}He,^{3}He$'\gamma$)^{96}Mo and ^{97}Mo(^{3}He,$\alpha\gamma$)^{96}Mo have recently been reanalyzed [74]. The two main reasons for reanalyzing these data are explained in the following.

In the previous analysis, the γ-ray energies close or below the strong 778.2 keV $2^+ \rightarrow 0^+$ ground-state band transition were included, and this transitional region in the experimental (E, E_γ) matrix were not properly subtracted in the first-generation procedure. These γ-ray energies are now excluded from the further analysis.

The second point concerns the estimate of the γ-ray multiplicity as function of excitation energy, which was used for the normalization procedure in the first-generation method as explained in Sec. 4.2. In the previous analyses, the statistical multiplicity at excitation energy E was estimated by introducing a lower γ-ray threshold E_0 and an effective excitation energy $E - E_{\mathrm{entry}}$ giving

$$\langle M_\gamma^{\mathrm{stat}} \rangle = (E - E_{\mathrm{entry}})/\langle E_\gamma \rangle_{>E_0}, \tag{4.56}$$

where $\langle E_\gamma \rangle_{>E_0}$ is the average energy of the γ spectrum for $E_\gamma > E_0$. The E_{entry} parameter mimics the excitation energy at which the statistical γ-ray transitions enter the ground-state band. This treatment is applicable to rare earth nuclei, where the CACTUS efficiency for the lowest ground state band transitions, typically the $4^+ \to 2^+$ and the $2^+ \to 0^+$ transitions, is low. However, for ^{96}Mo the energy of the lowest ground-state band transitions are detected with high efficiency, as the first excited state is at $E = 778.2$ keV [26]. Therefore, in the present analysis the straightforward expression for the total γ-ray multiplicity

$$\langle M_\gamma^{\mathrm{tot}} \rangle = E/\langle E_\gamma \rangle, \tag{4.57}$$

is used, where the excitation energy is simply divided by the average energy of the γ spectrum as in Eq. (4.21).

In Figs. 4.14 and 4.15 the reanalyzed level densities and γ-ray strength functions are compared with previous data [9, 13]. Note that the error bars include statistical errors only. A very good resemblance between the pick-up reaction and the inelastic scattering reaction is seen. The reanalyzed level densities are very similar to the previous ones, and the same is true for the γ-ray strength functions, except that the upbend is less pronounced due to the exclusion of the 778.2 keV transition. This gives further confidence in the robustness and stability of the Oslo method, as different ways of performing the analysis give very similar results.

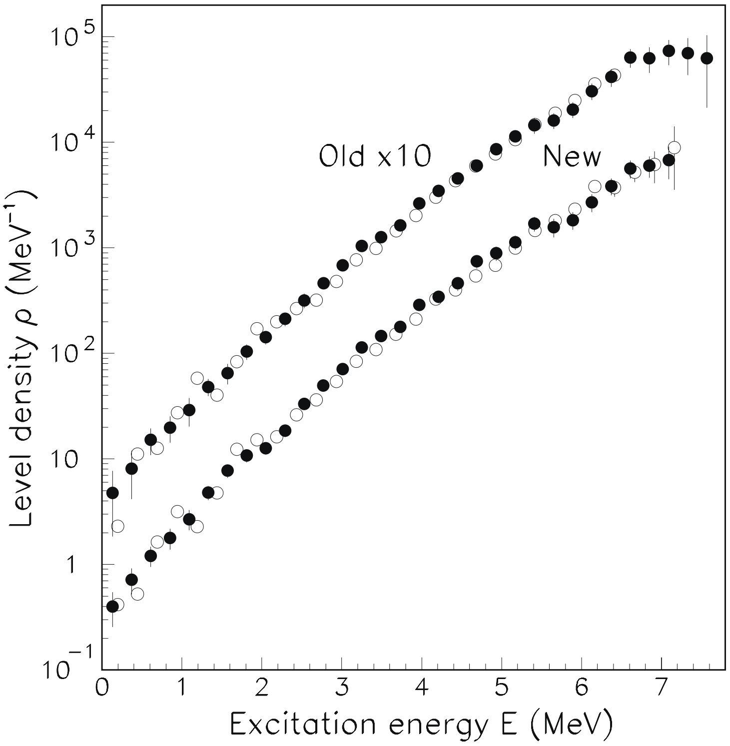

Figure 4.14: Experimental level densities of ^{96}Mo from the (^{3}He,α) (filled circles) and the (^{3}He,^{3}He′) (open circles) reaction. The data from the new analysis is compared with previously published data [13].

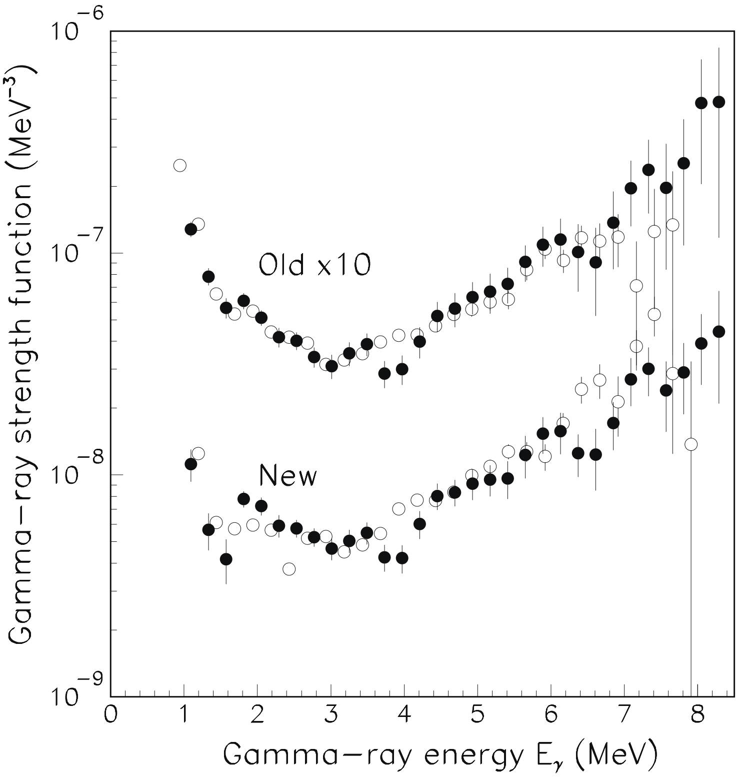

Figure 4.15: Experimental γ-ray strength functions of ^{96}Mo from the (^{3}He,α) (filled circles) and the (^{3}He,^{3}He′) (open circles) reaction. The data from the new analysis is compared with previously published data [9].

Chapter 5

Papers

The following papers are included in this thesis:

1. M. Guttormsen, R. Chankova, U. Agvaanluvsan, E. Algin, L.A. Bernstein, F. Ingebretsen, T. Lönnroth, S. Messelt, G.E. Mitchell, J. Rekstad, A. Schiller, S. Siem, A.C. Sunde[1], A. Voinov and S. Ødegård, *Radiative strength functions in* $^{93-98}$Mo, Phys. Rev. C **71**, 044307 (2005).

2. R. Chankova, A. Schiller, U. Agvaanluvsan, E. Algin, L. A. Bernstein, M. Guttormsen, F. Ingebretsen, T. Lönnroth, S. Messelt, G. E. Mitchell, J. Rekstad, S. Siem, A. C. Larsen, A. Voinov, and S. W. Ødegård, *Level densities and thermodynamical quantities of heated* $^{93-98}$Mo *isotopes*, Phys. Rev. C **73**, 034311 (2006).

3. A. C. Larsen, R. Chankova, M. Guttormsen, F. Ingebretsen, T. Lönnroth, S. Messelt, J. Rekstad, A. Schiller, S. Siem, N. U. H. Syed, A. Voinov, and S. W. Ødegård, *Microcanonical entropies and radiative strength functions of* ^{50,51}V, Phys. Rev. C **73**, 064301 (2006).

4. A. C. Larsen, M. Guttormsen, R. Chankova, F. Ingebretsen, T. Lönnroth, S. Messelt, J. Rekstad, A. Schiller, S. Siem, N. U. H. Syed, and A. Voinov, *Nuclear level densities and* γ*-ray strength functions in* ^{44,45}Sc, Phys. Rev. C **76**, 044303 (2007).

5. A. V. Voinov, S. M. Grimes, A. C. Larsen, C. R. Brune, M. Guttormsen, T. Massey, A. Schiller, S. Siem, and N. U. H. Syed, *Level densities of* ^{44}Sc *and* ^{47}Ti *from different experimental techniques*, Phys. Rev. C **77**, 034613 (2008).

---

[1] I changed my last name from 'Sunde' to 'Larsen' in 2006.

5.1 Brief introduction to the papers

Paper 1 and 2: The Mo isotopes

The motivation for the Mo experiments was primarily to test the Oslo method in the mass region near the $N = 50$ shell closure. Also, as the ground-state deformation parameter β_2 goes down from 0.17 in ^{98}Mo to 0.11 in ^{92}Mo [19], one would expect to see deformation effects in both the level density (decreasing $\rho(E)$ as the deformation decreases) and the γ-ray strength function (decreasing $f(E_\gamma)$ as the deformation decreases since the tail of the GEDR is expected to decrease when approaching spherical nuclear shape).

In paper 1, the γ-ray strength functions of $^{93-98}$Mo were studied through the analysis of the measured (^{3}He,^{3}He$'\gamma$) and (^{3}He,$\alpha\gamma$) reactions as described in Chapters 3 and 4. It was found that the γ-ray strength functions agreed well with the low-energy tail of the GEDR for γ-ray energies larger than about 3 MeV. However, below $E_\gamma \approx 3$ MeV, an increase of the strength functions was found for all nuclei, similar to the behavior previously discovered in ^{56,57}Fe [8]. This feature was found to be present at all initial excitation energies between $5-8$ MeV.

In paper 2, the level densities of $^{93-98}$Mo were investigated and analyzed within the framework of thermodynamics. It was found that the level density decreased when approaching the $N = 50$ shell closure. For example, $\rho(6\,\mathrm{MeV}) \approx 4000\,\mathrm{MeV}^{-1}$ for ^{98}Mo, while $\rho(6\,\mathrm{MeV}) \approx 1400\,\mathrm{MeV}^{-1}$ for ^{94}Mo. Also, the level densities of ^{93,94}Mo display more structures than the heavier Mo isotopes.

Thermodynamic quantities such as entropy, temperature, and heat capacity were deduced using both the microcanonical and canonical ensemble, and signatures of phase transitions were looked for (see Appendix B). The difference in the microcanonical entropies of $^{93-94}$Mo were found to be close to zero, while for $^{97-98}$Mo it was about $1k_B$. These observations were qualitatively explained considering the available single-particle orbits in the two cases. The canonical heat capacities showed an S-like functional form that might indicate a pairing phase transition, consistent with shell-model Monte Carlo simulations.

Paper 3: The V isotopes

In light of the successful application of the Oslo method on Fe and Mo nuclei, ^{51}V with $N = 28$ was chosen for the next experimental campaign at OCL. Now, the enhancement in the γ-ray strength function at low γ-

ray energies had been discovered not only in ^{56,57}Fe, but also in all the Mo isotopes studied in paper 1. One could therefore suspect that this feature was not singular for Fe and Mo due to some specific nuclear-structure effects in these nuclei, but rather could be a general feature, perhaps some sort of low-energy resonance, in a certain mass region.

The level densities and γ-ray strength functions of ^{50,51}V measured using the Oslo method on the (^{3}He,^{3}He$'\gamma$) and (^{3}He,$\alpha\gamma$) coincidence spectra. The level density of ^{51}V showed distinct structures and bumps at excitation energies up to $\approx$ 4.5 MeV, interpreted as effects of the $N = 28$ shell closure that inhibit the neutrons from participating in the creation of levels until the excitation energy is high enough to let the neutrons cross the shell gap. Microcanonical entropies were deduced from the level densities, and the entropy difference were found to be about $1.2k_B$. The γ-ray strength functions resembled the ones in Fe and Mo, with a good agreement with the low-energy GEDR tail at high γ-ray energies and an enhancement at low γ-ray energies.

Paper 4 and 5: The Sc isotopes

Going even further down in mass number and approaching the $Z = 20$ major shell, the level densities and γ-ray strength functions of the nuclei ^{44,45}Sc were extracted from the (^{3}He,^{3}He$'\gamma$) and (^{3}He,$\alpha\gamma$) data taken at OCL. The results were presented in paper 4. The level densities of both nuclei turned out to be much less structured than for ^{51}V, in spite of them having only one proton above the $Z = 20$ shell. However, the neutrons are mid-shell in the $1f_{7/2}$ orbit, and, apparently, produce a rather smooth behavior of the level density function. The level densities were compared with calculations performed with a microscopic combinatorial model called 'Micro', where BCS quasi-particles are scattered randomly into Nilsson single-particle levels, and collective states were schematically added. The agreement with this very simple model was satisfactory, especially for ^{44}Sc. Also the average number of broken Cooper pairs and the parity asymmetry were extracted from the calculations. The γ-ray strength functions were compared to (γ,n) and (γ,p) data and to the theoretical GEDR tail, and a good agreement was again found at γ-ray energies above 4 MeV. The γ-ray strength functions are seen to increase for γ-ray energies below 4 MeV, and this upbend structure is shown to be independent of initial excitation energy for $E = 4.5 - 9.3$ MeV in ^{45}Sc. Thus, the existence of this structure has been established in twelve nuclei from four different elements (Sc, V, Fe and Mo).

The motivation for the particle-evaporation experiment at Ohio University presented in paper 5 was twofold. First, since the normalization of the level density in ^{44}Sc was based on proton resonances with no distinction of $\ell = 0, 1$, this normalization might prove wrong even though a reasonable agreement was found with the level density and strength function of ^{45}Sc. By performing a particle-evaporation experiment for the compound reaction ^{45}Sc(^{3}He,α)^{44}Sc, where the α particles were measured in *backward* angles, the level density could be extracted using a Hauser-Feshbach model to describe the measured evaporation spectra. This method, which is briefly described in Chapter 2, will give the slope of the level density directly without any input from auxiliary data except the particle transmission coefficients determined from optical potential models. Thus, an independent check of the slope of the ^{44}Sc level density and strength function could be obtained.

Second, the overall agreement between the level density of ^{56}Fe previously measured at OCL and Ohio University was very good [28]. Therefore, we wanted to see if this was also the case for ^{44}Sc. The results presented in paper 5 was very encouraging, as the slope of the level density utilized in the OCL data was verified, and the agreement between the OCL and Ohio data were excellent (see also Fig. 2.2). The reliability of the Oslo method is thus further strengthened.

5.2 Paper 1: Radiative strength functions in $^{93-98}$Mo

PHYSICAL REVIEW C **71**, 044307 (2005)

Radiative strength functions in $^{93-98}$Mo

M. Guttormsen,[1,*] R. Chankova,[1] U. Agvaanluvsan,[2] E. Algin,[2,3,4,5] L. A. Bernstein,[2] F. Ingebretsen,[1] T. Lönnroth,[6]
S. Messelt,[1] G. E. Mitchell,[3,4] J. Rekstad,[1] A. Schiller,[2] S. Siem,[1] A. C. Sunde,[1] A. Voinov,[7,8] and S. Ødegård[1]
[1]*Department of Physics, University of Oslo, N-0316 Oslo, Norway*
[2]*Lawrence Livermore National Laboratory, L-414, 7000 East Avenue, Livermore, California 94551*
[3]*North Carolina State University, Raleigh, North Carolina 27695*
[4]*Triangle Universities Nuclear Laboratory, Durham, North Carolina 27708*
[5]*Department of Physics, Osmangazi University, Meselik, Eskisehir, 26480 Turkey*
[6]*Department of Physics, Åbo Akademi, FIN-20500 Turku, Finland*
[7]*Department of Physics and Astronomy, Ohio University, Athens, Ohio 45701*
[8]*Frank Laboratory of Neutron Physics, Joint Institute of Nuclear Research, 141980 Dubna, Moscow Region, Russia*
(Received 26 November 2004; published 20 April 2005)

Radiative strength functions (RSFs) in $^{93-98}$Mo have been extracted using the (^{3}He,$\alpha\gamma$) and (^{3}He,^{3}He$'\gamma$) reactions. The RSFs are U shaped as function of γ energy with a minimum at around $E_\gamma = 3$ MeV. The minimum values increase with neutron number because of the increase in the low-energy tail of the giant electric dipole resonance with nuclear deformation. The unexpected strong increase in strength below $E_\gamma = 3$ MeV, here called soft pole, is established for all $^{93-98}$Mo isotopes. The soft pole is present at all initial excitation energies in the 5−8-MeV region.

DOI: 10.1103/PhysRevC.71.044307 PACS number(s): 24.30.Gd, 24.10.Pa, 25.55.Hp, 27.60.+j

I. INTRODUCTION

The γ decay of nuclei at high excitation energy tends to follow certain statistical rules. The dominating γ-transition driving factors are the number of accessible final states and the γ-ray transmission coefficient. The largest uncertainties are connected to the latter factor. In the description of this factor Blatt and Weisskopf [1] included an E_γ^{2L+1} dependency, where L is the angular momentum transfer in the transition. In their definition of the radiative strength function (RSF), this simple energy dependence was divided out. With such a definition, the single-particle RSF (Weisskopf) estimates become independent of γ-ray energy. Various concepts of RSFs and γ decay in the continuum are outlined in the reviews of Bartholomew *et al*. [2,3].

It has been well known that the RSF is not at all constant but shows an additional E_γ^x dependency with $x = 1-2$ for γ energies in the 4–8-MeV region. Axel [4] argued that this feature is because of the collective giant electric dipole resonance (GEDR), which represents the essential mechanism for the γ decay. However, the situation is more complex. Further studies [5–7] reveal fine structures in the RSF, which are commonly called pygmy resonances. This name does not refer to specific structures: the $E1$ pygmy resonance in the $E_\gamma = 5-7$ MeV region of gold to lead nuclei could be because of neutron skin oscillations [8], whereas bumps in the 3-MeV region of rare earth nuclei are now determined to be of $M1$ character [9,10]. The electromagnetic character and measured strength of the latter pygmy resonance is compatible with the scissors mode [11]. Recently [12,13], the RSF picture of iron isotopes has been further modified by the observation of an anomalous increase in strength at γ energies below 4 MeV. It is clear that in the present situation, new experimental results are urgently needed.

The stable molybdenum isotopes are well suited as targets for the study of nuclear properties when going from spherical to deformed shapes. In this work we perform a systematic analysis of the RSFs of the six $^{93-98}$Mo isotopes. The RSFs depend on the dynamic properties of electric charges present within these systems ($Z = 42$). Because the nuclear deformation varies from spherical shapes ($\beta \sim 0$) at $N = 51$ to deformed shapes ($\beta \sim 0.2$) at $N = 56$, we expect to observe effects because of shape changes. Furthermore, these nuclei reveal weak GEDR tails at low E_γ, making them interesting objects in the search for other weak structures in the RSF.

The Oslo Cyclotron group has developed a sensitive tool to investigate RSFs for E_γ below the neutron binding energy S_n. The method is based on the extraction of primary γ-ray spectra at various initial excitation energies E_i measured in particle reactions with one and only one charged ejectile. From such a set of primary γ spectra, nuclear level densities and RSFs can be extracted [14–16]. The level density reveals essential nuclear structure information such as thermodynamic properties and pair correlations as functions of temperature. These aspects of the molybdenum isotopes will be presented in a forthcoming work. Various applications of the Oslo method have been described in Refs. [17–21].

II. EXPERIMENTAL METHOD

The particle-γ coincidence experiments were carried out at the Oslo Cyclotron Laboratory for $^{93-98}$Mo using the CACTUS multidetector array. The charged ejectiles were detected with eight particle telescopes placed at an angle of 45° relative to the beam direction. An array of 28 NaI γ-ray detectors with

---

[*] Electronic address: magne.guttormsen@fys.uio.no

a total efficiency of ∼15% surrounded the target and particle detectors.

In the present work, results from eight different reactions on four different targets are discussed. Results from two of those reactions have been reported earlier. The beam energies for the different reactions are given in parentheses:

1. ^{94}Mo(^{3}He,$\alpha\gamma$)^{93}Mo (new, 30 MeV)
2. ^{94}Mo(^{3}He,^{3}He$'\gamma$)^{94}Mo (new, 30 MeV)
3. ^{96}Mo(^{3}He,$\alpha\gamma$)^{95}Mo (new, 30 MeV)
4. ^{96}Mo(^{3}He,^{3}He$'\gamma$)^{96}Mo (new, 30 MeV)
5. ^{97}Mo(^{3}He,$\alpha\gamma$)^{96}Mo (reported in [12,21], 45 MeV)
6. ^{97}Mo(^{3}He,^{3}He$'\gamma$)^{97}Mo (reported in [12,21], 45 MeV)
7. ^{98}Mo(^{3}He,$\alpha\gamma$)^{97}Mo (new, 45 MeV)
8. ^{98}Mo(^{3}He,^{3}He$'\gamma$)^{98}Mo (new, 45 MeV).

The targets were self-supporting metal foils enriched to ∼95% with thicknesses of ∼2 mg/cm^2 . The experiments were run with beam currents of ∼2 nA for 1–2 weeks. The reaction spin windows are typically $I \sim (2-6)\hbar$.

The experimental extraction procedure and the assumptions made are described in Refs. [14,16] and references therein. For each initial excitation energy E_i, determined from the ejectile energy and reaction Q value, γ-ray spectra are recorded. Then the spectra are unfolded using the known γ-ray response function of the CACTUS array [22]. These unfolded spectra are the basis for making the first-generation (or primary) γ-ray matrix [23], which is factorized according to the Brink-Axel hypothesis [4,24] as follows:

$$P(E_i, E_\gamma) \propto \rho(E_i - E_\gamma)\mathcal{T}(E_\gamma). \tag{1}$$

Here, ρ is the level density and $\mathcal{T}$ is the radiative transmission coefficient.

The ρ and $\mathcal{T}$ functions can be determined by an iterative procedure [16] through the adjustment of each data point of these two functions until a global χ^2 minimum of the fit to the experimental $P(E_i, E_\gamma)$ matrix is reached. It has been shown [16] that if one solution for the multiplicative functions ρ and $\mathcal{T}$ is known, one may construct an infinite number of other functions, which give identical fits to the P matrix by the following:

$$\tilde{\rho}(E_i - E_\gamma) = A\exp[\alpha(E_i - E_\gamma)]\,\rho(E_i - E_\gamma), \tag{2}$$

$$\tilde{\mathcal{T}}(E_\gamma) = B\exp(\alpha E_\gamma)\mathcal{T}(E_\gamma). \tag{3}$$

Consequently, neither the slope (α) nor the absolute values of the two functions (A and B) can be obtained through the fitting procedure.

The parameters A and α can be determined by normalizing the level density to the number of known discrete levels at low excitation energy [25] and to the level density estimated from neutron-resonance spacing data at the neutron binding energy S_n [26]. The procedure for extracting the total level density ρ from the resonance energy spacing D is described in Ref. [16]. Here, we will discuss only the determination of parameter B of Eq. (3), which gives the absolute normalization of $\mathcal{T}$. For this purpose we utilize experimental data on the average total radiative width of neutron resonances at S_n $\langle\Gamma_\gamma\rangle$.

We assume here that the γ decay in the continuum is dominated by $E1$ and $M1$ transitions. For initial spin I and parity π at S_n, the width can be written in terms of the transmission coefficient by the following [27]:

$$\langle\Gamma_\gamma\rangle = \frac{1}{2\rho(S_n, I, \pi)} \sum_{I_f} \int_0^{S_n} \mathrm{d}E_\gamma B\mathcal{T}(E_\gamma) \times \rho(S_n - E_\gamma, I_f), \tag{4}$$

where the summation and integration run over all final levels with spin I_f, which are accessible by γ radiation with energy E_γ and multipolarity $E1$ or $M1$.

A few considerations have to be made before B can be determined. Methodical difficulties in the primary γ-ray extraction prevents determination of the functions $\mathcal{T}(E_\gamma)$ in the interval $E_\gamma < 1$ MeV and $\rho(E)$ in the interval $E > S_n - 1$ MeV. In addition, $\mathcal{T}(E_\gamma)$ at the highest γ energies, above $E_\gamma \sim S_n - 1$ MeV, suffers from poor statistics. For the extrapolation of ρ we apply the back-shifted Fermi gas level density as demonstrated in Ref. [20]. For the extrapolations of $\mathcal{T}$ we use an exponential form. As a typical example, the extrapolations for ^{98}Mo are shown in Fig. 1. The contribution of the extrapolations of ρ and $\mathcal{T}$ to the calculated radiative width in Eq. (4) does not exceed 15% [18]. The experimental widths $\langle\Gamma_\gamma\rangle$ in Eq. (4) are listed in Table I. For ^{94}Mo, this width is unknown and is estimated by an extrapolation based on the ^{96}Mo and ^{98}Mo values.

The total radiative strength function for dipole radiation ($L = 1$) can be calculated from the normalized transmission coefficient $\mathcal{T}$ by the following:

$$f(E_\gamma) = \frac{1}{2\pi}\frac{\mathcal{T}(E_\gamma)}{E_\gamma^3}. \tag{5}$$

The RSFs extracted from the eight reactions are displayed in Fig. 2. As expected, the RSFs do not seem to show any odd-even mass differences. The results obtained for the (^{3}He,α) and (^{3}He,^{3}He$'$) reactions populating the same residual nucleus reveal very similar RSFs. Also for ^{96}Mo two different beam energies have been applied, giving very similar RSFs. Thus, the observed energy and reaction independency gives further confidence in the Oslo method.

III. DESCRIPTION OF THE RADIATIVE STRENGTH FUNCTIONS

An inspection of the experimental RSFs of Fig. 2 reveals that the RSFs are increasing functions of γ energy for $E_\gamma >$ 3 MeV. This indicates that the RSFs are influenced by the tails of the giant resonances. As follows from previous work, the main contribution (about 80%) is because of the electric dipole resonance (GEDR). The magnetic resonance (GMDR) and the isoscalar $E2$ resonance are also present in this region.

If the GEDR is described by a Lorentzian function, one will find that the strength function approaches zero in the limit $E_\gamma \to 0$. However, the ^{144}Nd(n,$\gamma\alpha$) reaction [29] strongly suggests that f_{E1} has a finite value in this limit. Kadmenskiĭ, Markushev, and Furman (KMF) have developed a model [30]

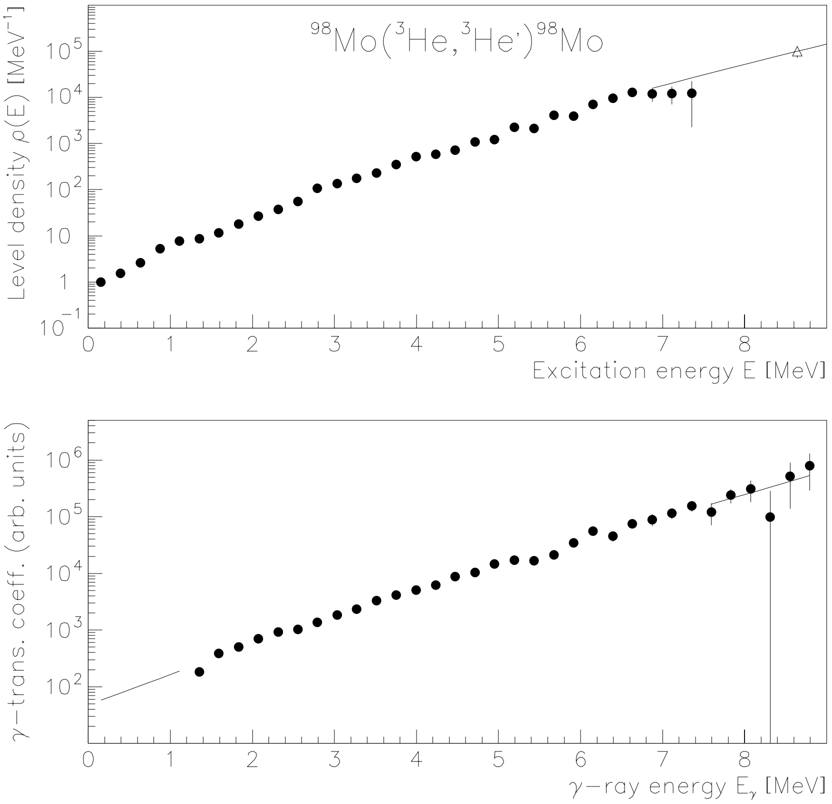

FIG. 1. Measured level density ρ (upper panel) and radiative transmission coefficient $\mathcal{T}$ (lower panel) for ^{98}Mo. The straight lines are extrapolations needed to calculate the normalization integral of Eq. (4). The triangle in the upper panel is based on resonance spacing data at S_n.

describing this feature for the electric dipole RSF:

$$f_{E1}(E_\gamma, T) = \frac{1}{3\pi^2\hbar^2c^2}\frac{0.7\sigma_{E1}\Gamma_{E1}^2\left(E_\gamma^2 + 4\pi^2T^2\right)}{E_{E1}\left(E_\gamma^2 - E_{E1}^2\right)^2}. \qquad (6)$$

The temperature T depends on the final state f and for simplicity we adapt the schematic form

$$T(E_f) = \sqrt{U_f/a}, \qquad (7)$$

where the level density parameter is parametrized as $a = 0.21A^{0.87}\,\mathrm{MeV}^{-1}$. The intrinsic energy is estimated by $U_f = E_f - C_1 - E_{\mathrm{pair}}$ with a back-shift parameter of $C_1 = -6.6A^{-0.32}$ MeV [31]. The pairing energy contribution E_{pair} is evaluated from the three-point mass formula of Ref. [33].

Although the KMF model has been developed for spherical nuclei, it has been successfully applied to ^{56,57}Fe and several rare earth nuclei [13,18–20] assuming a constant temperature parameter T in Eq. (6) (i.e., one that is independent of excitation energy). In this work we assume that the temperature depends on excitation energy according to Eq. (7), which gives an increase in the RSF at low γ energy [20].

The GMDR contribution to the total RSF is described by a Lorentzian. This approach is in accordance with numerous experimental data obtained so far [26]. However, the experimental data scatter and the resonance parameter values are uncertain. This is also true for the $E2$ resonance. The Lorentzian description of the $M1$ and $E2$ contributions are given in Ref. [17]. The resonance parameters for the $E1$, $M1$, and $E2$ resonances are taken from the compilations of Refs. [26,32] and are listed in Table I.

The enhanced RSF at low γ energies has at present no theoretical explanation. Recently, the same enhancement has

TABLE I. Parameters used for the radiative strength functions. The data are taken from Ref. [26]. The $E1$ resonance parameters for the even Mo isotopes are based on photo absorption experiments [32], and the parameters for the odd Mo isotopes are derived from interpolations.

Nucleus	E_{E1} (MeV)	σ_{E1} (mb)	Γ_{E1} (MeV)	E_{M1} (MeV)	σ_{M1} (mb)	Γ_{M1} (MeV)	E_{E2} (MeV)	σ_{E2} (mb)	Γ_{E2} (MeV)	$\langle\Gamma_\gamma\rangle$ (meV)
^{93}Mo	16.59	173.5	4.82	9.05	0.86	4.0	13.91	2.26	4.99	160(20)
^{94}Mo	16.36	185.0	5.50	9.02	1.26	4.0	13.86	2.24	4.98	170(40)[a]
^{95}Mo	16.28	185.0	5.76	8.99	1.38	4.0	13.81	2.22	4.97	135(20)
^{96}Mo	16.20	185.0	6.01	8.95	1.51	4.0	13.76	2.21	4.96	150(20)
^{97}Mo	16.00	187.0	5.98	8.92	1.58	4.0	13.71	2.19	4.95	110(15)
^{98}Mo	15.80	189.0	5.94	8.89	1.65	4.0	13.66	2.17	4.93	130(20)

[a] Estimated from systematics.

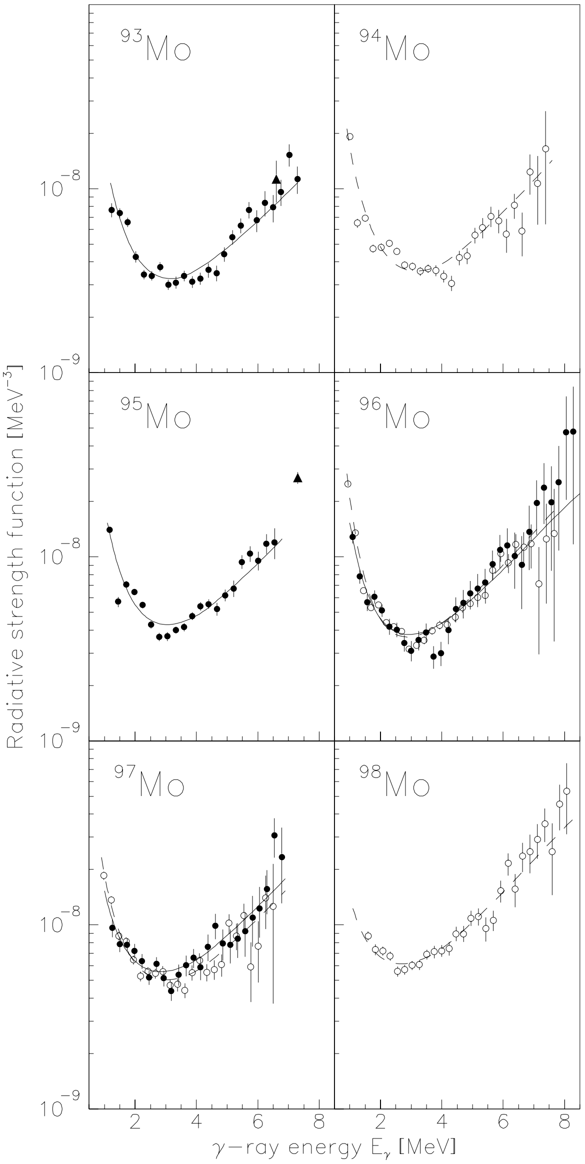

FIG. 2. Normalized RSFs for $^{93-98}$Mo. The filled and open circles represent data taken with the (^{3}He,α) and (^{3}He,^{3}He$'$) reactions, respectively. The filled triangles in ^{93,95}Mo are estimates of $E1$ RSF of hard primary γ rays [28] . The solid and dashed lines are fits to the RSF data from the two respective reactions (see text).

been observed in the iron isotopes [12,13]. We call this structure a soft pole in the RSF and choose a simple power law parametrization given by the following:

$$f_{\mathrm{softpole}} = \frac{1}{3\pi^2\hbar^2c^2}\mathcal{A}E_\gamma^{-b}, \tag{8}$$

where $\mathcal{A}$ and b are fit parameters and E_γ is given in MeV.

Previously, a pygmy resonance around $E_\gamma \sim 3$ MeV has been reported in several rare-earth nuclei [18–20]. The electromagnetic character of the corresponding RSF structure is now established to be of $M1$ type [9,10] and is interpreted as the scissors mode. Deformed nuclei can in principle possess this collective motion, and, for example, ^{98}Mo with a deformation of $\beta \sim 0.18$, could eventually show some reminiscence of the scissors mode. Data on ^{94}Mo [34] and ^{96}Mo [35] show a summed $M1$ strength to mixed symmetry 1^+ states around $\sim$3.2 MeV on the order of $\sim 0.6\mu_N^2$. This is about one order of magnitude lower than the $M1$ strength observed in well-deformed rare-earth nuclei using the present method. This $M1$ strength is deemed too weak to cause a visible bump in our RSFs above 3 MeV.

We conclude that a reasonable composition of the total RSF is as follows:

$$f = \kappa(f_{E1} + f_{M1} + f_{\mathrm{softpole}}) + E_\gamma^2 f_{E2}, \tag{9}$$

where κ is a normalization constant. Generally, its value deviates from unity for several reasons; the most important reasons are theoretical uncertainties in the KMF model and the evaluation of B in Eq. (4). We use κ, $\mathcal{A}$, and b as free parameters in the fitting procedure, and the results for the eight reactions are summarized in Table II.

In Fig. 3 the various contributions to the total RSF of ^{98}Mo are shown. The main components are the GEDR resonance and the unknown low-energy structure. We observe that the $E1$ component exhibits an increased yield for the lowest γ energies because of the increase in temperature T. However, this effect is not strong enough to explain the low-energy upbend.

Figure 2 shows the fit functions for all reactions and gives qualitative good agreements with the experimental data. The fitting parameters κ, $\mathcal{A}$, and b are all similar within the uncertainties. It should be noted that the soft pole parameters

TABLE II. Soft pole fitting parameters and integrated strenghts. The B values are only lower estimates (see text).

Reaction	κ	$\mathcal{A}$ (mb/MeV)	b	$B(E1\uparrow)$ (e^2 fm^2)	$B(M1\uparrow)$ (μ_N^2)	$B(E2\uparrow)$ (10^3e^2 fm^4)
(^{3}He,α)^{93}Mo	0.44(4)	0.37(7)	2.6(3)	0.021(5)	1.9(4)	14(3)
(^{3}He,^{3}He$'$)^{94}Mo	0.36(2)	0.48(5)	2.5(2)	0.023(3)	2.1(3)	16(2)
(^{3}He,α)^{95}Mo	0.39(2)	0.48(6)	2.6(2)	0.024(4)	2.2(3)	16(2)
(^{3}He,^{3}He$'$)^{96}Mo	0.36(1)	0.60(4)	3.2(2)	0.022(2)	2.0(2)	16(1)
(^{3}He,α)^{96}Mo	0.32(4)	0.47(14)	2.7(6)	0.019(7)	1.7(6)	13(4)
(^{3}He,^{3}He$'$)^{97}Mo	0.38(3)	0.47(7)	2.4(3)	0.025(5)	2.3(4)	16(3)
(^{3}He,α)^{97}Mo	0.45(5)	0.30(10)	2.2(5)	0.020(8)	1.9(7)	13(5)
(^{3}He,^{3}He$'$)^{98}Mo	0.52(4)	0.22(7)	2.1(5)	0.018(7)	1.6(6)	12(4)

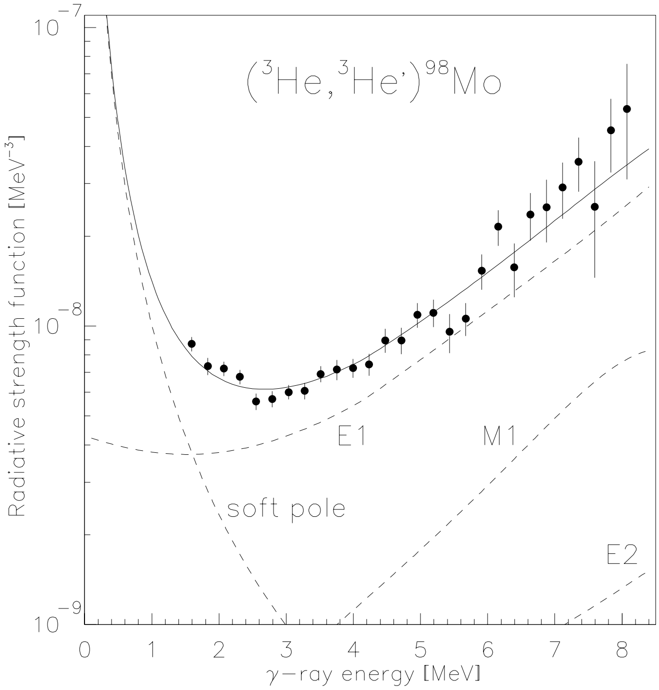

FIG. 3. Experimental radiative strength function of ^{98}Mo compared to a model description, including GEDR, GMDR, and the isoscalar $E2$ resonance. The empirical soft pole component is used to describe the low energy part of the RSF.

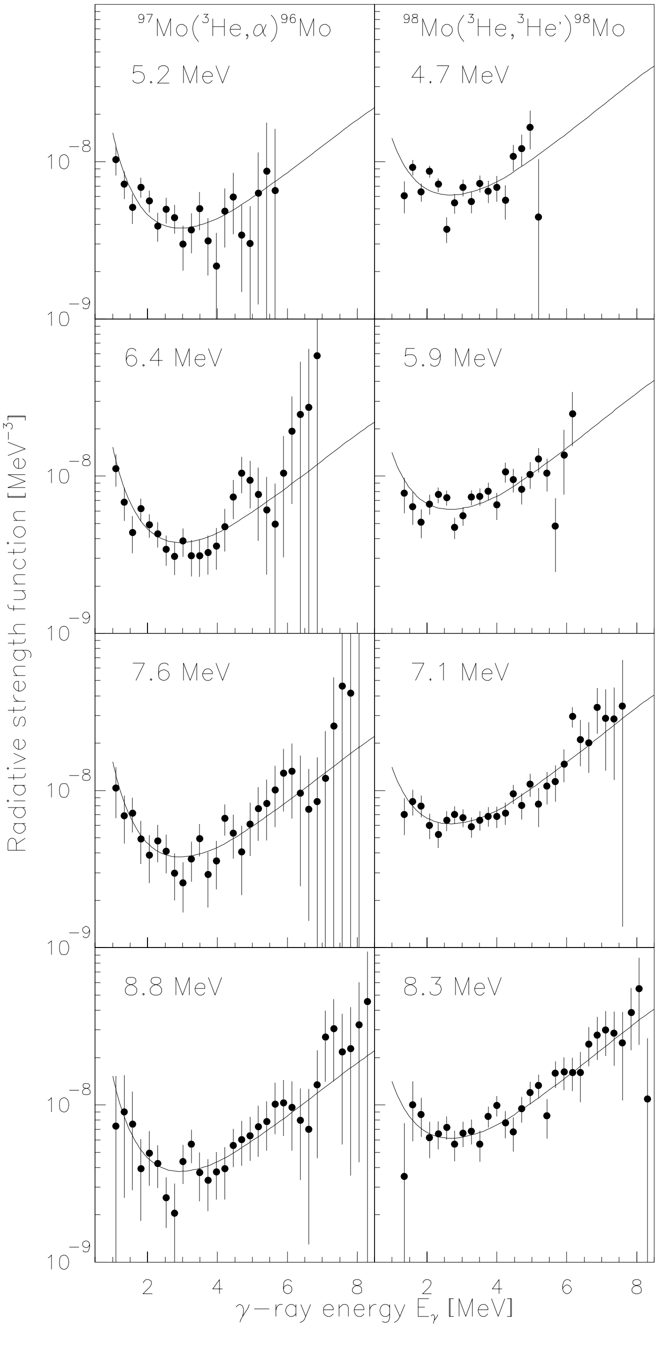

FIG. 4. RSFs for ^{96,98}Mo at various initial excitation energies. The soft pole is present for all E_i. The solid lines display the RSFs obtained in Fig. 2.

coincide with the description of the ^{57}Fe nucleus [13] having $\mathcal{A} = 0.47(7)$ mb/MeV and $b = 2.3(2)$.

The RSFs for $E_\gamma > 3$ MeV when going from $N = 51$ to 56 increase by almost a factor of 2 and this can be understood from the corresponding evolution of nuclear deformation. Following the onset of prolate deformation the GEDR will split into two parts, where 1/3 of its strength is shifted down in energy and 2/3 up. Photoneutron cross sections [32] show no splitting into two separate bumps; however, the observed increase in width Γ_{E1} as a function of neutron number (see Table I) supports the idea of a splitting, which is a well-known feature in other more deformed nuclei. Figure 2 demonstrates that the adopted widths describe very well the variation of the RSF strength as function of mass number.

To investigate whether the prominent soft pole structure is present in the whole excitation energy region, we have performed the following test. Assuming that the level density from Eq. (1) is correct, we can estimate the shape of the strength functions starting at various initial excitation energies using the following:

$$f(E_\gamma, E_i) = \frac{1}{2\pi}\frac{\mathcal{N}(E_i)P(E_i, E_\gamma)}{\rho(E_i - E_\gamma)E_\gamma^3}. \qquad (10)$$

Actually, $f(E_\gamma, E_f)$ would have been the proper expression to investigate, but because of technical reasons we chose $f(E_\gamma, E_i)$, which is equivalent to investigating $f(E_\gamma, E_f)$ because in our method E_f and E_i are uniquely related by $E_f = E_i - E_\gamma$. One problem is that the normalization constant is only roughly known through the following estimate:

$$\mathcal{N}(E_i) = \frac{\int_0^{E_i} dE_\gamma \rho(E_i - E_\gamma)\mathcal{T}(E_\gamma)}{\int_0^{E_i} dE_\gamma P(E_i, E_\gamma)}, \qquad (11)$$

with $E_i < S_n$. However, for the expression $f(E_\gamma, E_i)$ we are interested only in the shape of the RSFs, and an exact normalization is therefore not crucial. The evaluation assumes that eventual temperature-dependent behavior of the RSF is small compared to the soft pole structure.[1]

In Fig. 4, the RSFs for ^{96,98}Mo are shown at various initial energies E_i. For comparison, the figure also includes the global RSFs (solid lines) obtained with the Oslo method (Fig. 2). Within the error bars the data support that the soft pole is present in all the excitation bins studied.

The origin of the soft pole cannot be explained by any known theoretical model. One would therefore need to know the γ-ray multipolarity as guidance for theoretical approaches to this phenomenon. Rough estimates of the reduced strength can be obtained from the following:

$$B(XL\uparrow) = \frac{1}{8\pi}\frac{L(2L+1)[(2L+1)!!]^2}{L+1}(\hbar c)^{2L+1} \times \int_{1\,\text{MeV}}^{3\,\text{MeV}} dE_\gamma f_{XL}(E_\gamma). \tag{12}$$

In the evaluation, we have integrated the soft pole between 1 and 3 MeV. Thus, the estimates listed in Table II for the reactions studied give only a lower limit for the respective $B(XL\uparrow)$ values. The correct result will of course depend on the functional form of $f_{\text{softpole}}(E_\gamma)$ below 1 MeV; however, no experimental data exist in this region and any assumption here would be highly speculative. There seems to be no clear dependency of the B values on mass number or nuclear deformation.

With the assumptions above, we get in the case of an $E1$ soft pole an average $B(E1\uparrow)$ value of 0.02 e^2 fm^2, which is 0.07% of the sum rule for the GEDR. Assuming an $M1$ soft pole, we get roughly $B(M1\uparrow) \sim 2.0\mu_N^2$, which is 3–4 times larger than the observed strength to mixed symmetry 1^+ states around 3 MeV [34,35]. Provided the soft pole has $E2$ multipolarity we obtain finally a $B(E2\uparrow)$ value around 15000 e^2 fm^4, which is 5–15 times larger than the ones for the excitation to the first excited 2^+ states in the even molybdenum isotopes. Thus, we cannot exclude any of these multipolarities, since neither of them would yield unreasonably high transition strengths. Moreover, we would like to point out that the observed soft pole resides on top of the tails of giant resonances. Thus, the transition strength included in the soft pole has to be added to the strength in the giant resonance tail of the correct multipolarity to give the summed transition strength.

IV. SUMMARY AND CONCLUSIONS

As expected, the observed RSFs reveal very similar shapes because they all refer to isotopes with the same nuclear charge. When going from $N = 51$ to 56 the RSF increases by almost a factor of two for $E_\gamma > 3$ MeV, which can be understood from the change of nuclear deformation. With the onset of deformation, the increasing resonance GEDR width Γ_{E1} is responsible for the increasing strength.

An enhanced strength at low γ energies is observed, which is equally strong for all isotopes and excitation energies studied. A similar enhancement has also been seen in the iron isotopes. The multipolarity of the soft pole radiation is unknown and there is still no theoretical explanation for this very interesting phenomenon.

ACKNOWLEDGMENTS

Financial support from the Norwegian Research Council (NFR) is gratefully acknowledged. Part of this work was performed under the auspices of the U.S. Department of Energy by the University of California, Lawrence Livermore National Laboratory, under Contract W-7405-ENG-48. A.V. E.A, U.A, and G.E.M acknowledge support from the National Nuclear Security Administration under the Stewardship Science Academic Alliances program through Department of Energy Research Grants DE-FG03-03-NA00074 and DE-FG03-03-NA00076 and U.S. Department of Energy Grant DE-FG02-97-ER41042.

[1] J. M. Blatt and V. F. Weisskopf, *Theoretical Nuclear Physics* (Wiley, New York, 1952).

[2] G. A. Bartholomew, I. Bergqvist, E. D. Earle, and A. J. Ferguson, Can. J. Phys. **48**, 687 (1970).

[3] G. A. Bartholomew, E. D. Earle, A. J. Ferguson, J. W. Knowles, and M. A. Lone, Adv. Nucl. Phys. **7**, 229 (1973).

[4] P. Axel, Phys. Rev. **126**, 671 (1962).

[5] S. Joly, D. M. Drake, and L. Nilsson, Phys. Rev. C **20**, 2072 (1979).

[6] M. Guttormsen, J. Rekstad, A. Henriquez, F. Ingebretsen, and T. F. Thorsteinsen, Phys. Rev. Lett. **52**, 102 (1984).

[7] M. Igashira, H. Kitazawa, M. Shimizu, H. Komano, and N. Yamamuro, Nucl. Phys. **A457**, 301 (1986).

[8] N. Ryezayeva, T. Hartmann, Y. Kalmykov, H. Lenske, P. von Neumann-Cosel, V. Yu. Ponomarev, A. Richter, A. Shevchenko, S. Volz, and J. Wambach, Phys. Rev. Lett. **89**, 272502 (2002).

[9] A. Schiller, A. Voinov, E. Algin, J. A. Becker, L. A. Bernstein, P. E. Garrett, M. Guttormsen, R. O. Nelson, J. Rekstad, and S. Siem, preprint, nucl-ex/0401038.

[10] M. Krtička, F. Bečvář, J. Honzátko, I. Tomandl, M. Heil, F. Käppeler, R. Reifarth, F. Voss, and K. Wisshak, Phys. Rev. Lett. **92**, 172501 (2004).

[11] N. Pietralla, P. von Brentano, R.-D. Herzberg, U. Kneissl, N. Lo Iudice, H. Maser, H. H. Pitz, and A. Zilges, Phys. Rev. C **58**, 184 (1998).

[12] E. Tavukcu, Ph.D. thesis, North Carolina State University, 2002.

[13] A. Voinov, E. Algin, U. Agvaanluvsan, T. Belgya, R. Chankova, M. Guttormsen, G. E. Mitchell, J. Rekstad, A. Schiller, and S. Siem, Phys. Rev. Lett. **93**, 142504 (2004).

[14] L. Henden, L. Bergholt, M. Guttormsen, J. Rekstad, and T. S. Tveter, Nucl. Phys. **A589**, 249 (1995).

[15] E. Melby, L. Bergholt, M. Guttormsen, M. Hjorth-Jensen, F. Ingebretsen, S. Messelt, J. Rekstad, A. Schiller,

---

[1] Simulations using the KMF model with fixed temperature in the $T \sim 0.8$ MeV region indicate a maximum 20% effect from temperature dependence of the RSF.

S. Siem, and S. W. Ødegård, Phys. Rev. Lett. **83**, 3150 (1999).

[16] A. Schiller, L. Bergholt, M. Guttormsen, E. Melby, J. Rekstad, and S. Siem, Nucl. Instrum. Methods Phys. Res. A **447**, 498 (2000).

[17] U. Agvaanluvsan, *et al*., Phys. Rev. C **70**, 054611 (2004).

[18] A. Voinov, M. Guttormsen, E. Melby, J. Rekstad, A. Schiller, and S. Siem, Phys. Rev. C **63**, 044313 (2001).

[19] S. Siem, M. Guttormsen, K. Ingeberg, E. Melby, J. Rekstad, A. Schiller, and A. Voinov, Phys. Rev. C **65**, 044318 (2002).

[20] M. Guttormsen, A. Bagheri, R. Chankova, J. Rekstad, S. Siem, A. Schiller, and A. Voinov, Phys. Rev. C **68**, 064306 (2003).

[21] A. Schiller *et al*., Phys. Rev. C **68**, 054326 (2003).

[22] M. Guttormsen, T. S. Tveter, L. Bergholt, F. Ingebretsen, and J. Rekstad, Nucl. Instrum. Methods Phys. Res. A **374**, 371 (1996).

[23] M. Guttormsen, T. Ramsøy, and J. Rekstad, Nucl. Instrum. Methods Phys. Res. A **255**, 518 (1987).

[24] D. M. Brink, Ph.D. thesis, Oxford University, 1955.

[25] Data extracted using the NNDC On-Line Data Service from the ENSDF database.

[26] P. Obložinský, IAEA Report No. IAEA-TECDOC-1034, 1998.

[27] J. Kopecky and M. Uhl, Phys. Rev. C **41**, 1941 (1990).

[28] J. Kopecky and M. Uhl, in *Proceedings of a Specialists' Meeting on Measurement, Calculation and Evaluation of Photon Production Data, Bologna, Italy, 1994*, edited by C. Coceva, A. Mengoni, and A. Ventura [Report No. NEA/NSC/DOC(95)1], p. 119.

[29] Yu. P. Popov, in *Proceedings of the Europhysics Topical Conference, Smolenice, 1982*, edited by P. Obložinský (Institute of Physics, Bratislava, 1982), p. 121.

[30] S. G. Kadmenskiĭ, V. P. Markushev, and V. I. Furman, Yad. Fiz. **37**, 277 (1983) [Sov. J. Nucl. Phys. **37**, 165 (1983)].

[31] T. von Egidy, H. H. Schmidt, and A. N. Behkami, Nucl. Phys. **A481**, 189 (1988).

[32] Samuel S. Dietrich and Barry L. Berman, At. Data Nucl. Data Tables **38**, 199 (1988).

[33] J. Dobaczewski, P. Magierski, W. Nazarewicz, W. Satuła, and Z. Szymański, Phys. Rev. C **63**, 024308 (2001).

[34] C. Fransen *et al*., Phys. Rev. C **67**, 024307 (2003).

[35] C. Fransen *et al*., Phys. Rev. C **70**, 044317 (2004).

5.3 Paper 2: Level densities and thermodynamical quantities of heated $^{93-98}$Mo isotopes

PHYSICAL REVIEW C **73**, 034311 (2006)

Level densities and thermodynamical quantities of heated $^{93-98}$Mo isotopes

R. Chankova,[1,*] A. Schiller,[2] U. Agvaanluvsan,[2,3] E. Algin,[2,3,4,5] L. A. Bernstein,[2] M. Guttormsen,[1] F. Ingebretsen,[1]
T. Lönnroth,[6] S. Messelt,[1] G. E. Mitchell,[3,4] J. Rekstad,[1] S. Siem,[1] A. C. Larsen,[1] A. Voinov,[7,8] and S. Ødegård[1]
[1]*Department of Physics, University of Oslo, N-0316 Oslo, Norway*
[2]*Lawrence Livermore National Laboratory, L-414, 7000 East Avenue, Livermore, California 94551, USA*
[3]*North Carolina State University, Raleigh, North Carolina 27695, USA*
[4]*Triangle Universities Nuclear Laboratory, Durham, North Carolina 27708, USA*
[5]*Department of Physics, Osmangazi University, Meselik, Eskisehir, 26480 Turkey*
[6]*Department of Physics, Åbo Akademi, FIN-20500 Turku, Finland*
[7]*Department of Physics and Astronomy, Ohio University, Athens, Ohio 45701, USA*
[8]*Frank Laboratory of Neutron Physics, Joint Institute of Nuclear Research, RU-141980 Dubna, Moscow, Russia*

(Received 30 June 2005; published 16 March 2006)

Level densities for $^{93-98}$Mo have been extracted using the (^{3}He,$\alpha\gamma$) and (^{3}He,^{3}He$'\gamma$) reactions. From the level densities thermodynamical quantities such as temperature and heat capacity can be deduced. Data have been analyzed by utilizing both the microcanonical and the canonical ensemble. Structures in the microcanonical temperature are consistent with the breaking of nucleon Cooper pairs. The S shape of the heat capacity curves found within the canonical ensemble is interpreted as consistent with a pairing phase transition with a critical temperature for the quenching of pairing correlations at $T_c \sim 0.7-1.0$ MeV.

DOI: 10.1103/PhysRevC.73.034311 PACS number(s): 21.10.Ma, 24.10.Pa, 25.55.−e, 27.60.+j

I. INTRODUCTION

Level density is a characteristic property of many-body quantum mechanical systems. Its precise knowledge is often a key ingredient in the calculation of different processes, such as compound nuclear decay rates, yields of evaporation residues to populate exotic nuclei, or thermonuclear rates in astrophysical processes.

Measurements of experimental nuclear level density are an important prerequisite for thermodynamical studies of atomic nuclei. Level density is directly connected to the multiplicity of states, i.e., the number of physical realizations of the system at a certain excitation energy. The entropy is a fundamental quantity and a measure of the disorder of the many-body system. Within the microcanonical ensemble it is defined as the natural logarithm of the multiplicity of states. When the entropy is known, thermodynamic quantities such as temperature and heat capacity can be extracted. These quantities depend on the statistical properties of the nuclear many-body system and may reveal phase transitions.

Pairing correlations are one of the fundamental properties of nuclei and have been successfully described by the Bardeen-Cooper-Schrieffer (BCS) theory of superconductivity [1]. By using the BCS theory the thermodynamical properties of nuclear pairing were investigated in the study of warm nuclei [2–5]. In the case of a finite Fermi system such as the nucleus, statistical fluctuations beyond the mean field become important. The fluctuations smooth out the sharp phase transition, and then the pairing correlations do not vanish suddenly but decrease with increasing temperature. The quenching of pairing correlations has been obtained in recent theoretical approaches: the shell-model Monte-Carlo (SMMC) calculations [6–8], the finite-temperature Hartree-Fock-Bogoliubov theory [9], and the relativistic mean-field theory [10]. Experimental data on the quenching of pair correlations are important as a test for nuclear theories. A long-standing problem in experimental nuclear physics has been to observe the transition from strongly paired states at zero temperature to unpaired states at higher temperatures. A signature of the pairing transition at finite temperature might be a local increase in the heat capacity as a function of temperature [11]. Recently [12,13], fine structures in the level densities in the 1-to 7-MeV region were reported, which are probably because of the breaking of individual nucleon pairs and a gradual decrease of pair correlations.

The group at the Oslo Cyclotron Laboratory (OCL) has developed a method to extract simultaneously the level density and the radiative strength function from primary γ spectra [14]. The method is a further development of the sequential extraction method [15,16]. The Oslo method has been tested in the rare-earth mass region that led to many interesting applications [12,17–19]. To make quantitative judgments of the applicability of the method, the Oslo Cyclotron group has extracted the level density and radiative strength function (RSF) of the very light ^{27,28}Si nuclei, where these quantities are known. Excellent overall agreement was found [20]. Subsequently, another extension has been made to the intermediate nuclei ^{56,57}Fe and ^{96,97}Mo, and it has been shown that the method can be applied in this intermediate mass region where the level density is still relatively low [21,22]. All of these successful applications have motivated us to employ the Oslo method to study medium-heavy nuclei in the vicinity of closed shells.

The naturally occurring isotopes of molybdenum span one of the larger isotopic ranges and are well suited as targets for the study of nuclear properties, such as the effect of changing from spherical to deformed shapes. When approaching closed

---

[*] Electronic address: rositsa.chankova@fys.uio.no

shells, the nuclear structure changes significantly, and one expects this to influence the level densities and radiative strength functions.

The even-even ^{92}Mo has a filled $N = 50$ neutron shell [23]. It is essentially a spherical nucleus and vibrations are primarily governed by the proton core. As the mass increases from ^{94}Mo to ^{100}Mo, neutrons fill the $2d_{5/2}$ and $1g_{7/2}$ subshells. Moving away from the $N = 50$ shell closure, pairing and quadrupole interactions cause a more collective behavior in the heavier Mo isotopes. The character of the isotopes changes rapidly from that of the essentially spherical ^{92}Mo to nuclei making a transition from collective vibrators to the deformed rotors of the unstable ^{104}Mo and ^{106}Mo isotopes [24]. The transitional nature of molybdenum isotopes away from $N = 50$ has been the focus of several efforts as described in Ref. [25] and references therein.

Around closed shells, effects from the increasing single-particle energy spacings can be expected. These will also influence the entropy difference between odd-mass and even-even nuclei. Therefore, a statistical description of the transition from closed shells to deformed nuclei is of great interest.

In this work, a unique and consistent investigation of the six $^{93-98}$Mo isotopes is performed to determine experimentally the level density from the ground state to the neutron binding energy. The Oslo method also determines the RSFs of the molybdenum isotopes studied; these are presented in an earlier article [26].

II. EXPERIMENTAL METHODS

The experiments were carried out at the Oslo Cyclotron Laboratory by bombarding ^{94,96,97,98}Mo targets with ^{3}He ions. In the present work, results from eight different reactions on four different targets are discussed. These are the following six reactions that are the subject of the present investigation:

(i) ^{98}Mo(^{3}He,$\alpha\gamma$)^{97}Mo (45 MeV)
(ii) ^{98}Mo(^{3}He,^{3}He$'\gamma$)^{98}Mo (45 MeV)
(iii) ^{96}Mo(^{3}He,$\alpha\gamma$)^{95}Mo (30 MeV)
(iv) ^{96}Mo(^{3}He,^{3}He$'\gamma$)^{96}Mo (30 MeV)
(v) ^{94}Mo(^{3}He,$\alpha\gamma$)^{93}Mo (30 MeV)
(vi) ^{94}Mo(^{3}He,^{3}He$'\gamma$)^{94}Mo (30 MeV) together with the reactions
(vii) ^{97}Mo(^{3}He,$\alpha\gamma$)^{96}Mo (45 MeV)
(viii) ^{97}Mo(^{3}He,^{3}He$'\gamma$)^{97}Mo (45 MeV)

which have been reported earlier [21,22]. The self-supporting targets with thicknesses of ~2 mg/cm^2 are enriched to ~95%. The experiments were run with beam currents of ~2 nA for 1–2 weeks. The particle-γ coincidences were measured with the CACTUS multidetector array. The charged ejectiles were detected by eight particle telescopes placed at an angle of 45° relative to the beam direction. An array of 28 NaI γ-ray detectors with a total efficiency of ~15% surrounded the target and particle detectors.

For each initial excitation energy, the γ-ray spectra are recorded as a function of the initial excitation energy of the residual nucleus. This is accomplished by utilizing the known reaction Q values and kinematics. Using the particle-γ coincidence technique, each γ ray can be assigned to a cascade depopulating a certain initial excitation energy in the residual nucleus. The data are therefore sorted into total γ-ray spectra originating from different initial excitation-energy bins. Each spectrum is then unfolded with the NaI response function using a Compton-subtraction method which preserves the fluctuations in the original spectra and does not introduce further, spurious fluctuations [27]. From the unfolded spectra, a primary-γ matrix $P(E, E_\gamma)$ is constructed using the subtraction method of Ref. [28].

The basic assumption of this method is that the γ-ray energy distribution from any excitation energy bin is independent of whether states in this bin are populated directly via the (^{3}He,α) or (^{3}He,^{3}He$'$) reactions or indirectly via γ decay from higher excited levels following the initial nuclear reaction. This assumption is trivially fulfilled if one populates the same levels with the same weights within any excitation-energy bin, because the decay branchings are properties of the levels and do not depend on the population mechanisms. The assumptions behind this method have been tested extensively by the Oslo group and have been shown to work reasonably well [29].

The (^{3}He,^{3}He$'\gamma$) and (^{3}He,$\alpha\gamma$) reactions exhibit very different reaction mechanisms. This is demonstrated in Fig. 1, where the particle spectra in coincidence with γ rays show indeed very different yields and peak structures.

The (^{3}He,$\alpha\gamma$) pick-up reaction reveals a cross section dominated by high ℓ neutron transfer. Here, the direct population of the residual nucleus takes place through one-particle-one-hole components of the wave function. Such configurations are not eigenstates of the nucleus, but they are rather distributed over virtually all eigenstates in the neighboring excitation-energy region. Thus, the neutron-hole strength for single-particle levels away from the Fermi energy is distributed over a rather large range of background states.

However, the inelastic scattering (^{3}He,^{3}He$'\gamma$) reaction is known to populate mainly collective excitations with a slightly lower spin window. Collective excitations built on the ground state give rise to rather pure eigenfunctions and their strength is less spread over other eigenfunctions of the nucleus in the neighboring excitation-energy region.

To test if the number of γ rays per cascade depends on the two types of reactions, we have evaluated the average γ-ray multiplicity

$$\langle M_\gamma(E)\rangle = \frac{E}{\langle E_\gamma\rangle}, \tag{1}$$

as a function of excitation energy E. The average γ-ray energy $\langle E_\gamma\rangle$ is calculated from γ spectra selected at a certain energy E.

Figure 2 shows the γ-ray multiplicity versus excitation energy. Despite the different reaction mechanisms, the two reactions give similar results. In particular, the multiplicities (solid and dashed lines) of ^{96}Mo and ^{97}Mo are equal within their error bars, which gives support to the applicability of the Oslo method for both reactions.

The experimental extraction procedure and assumptions of the Oslo method are given in Refs. [14,29] and references therein. The first generation (or primary) γ-ray matrix that is obtained as described above can be factorized according to the

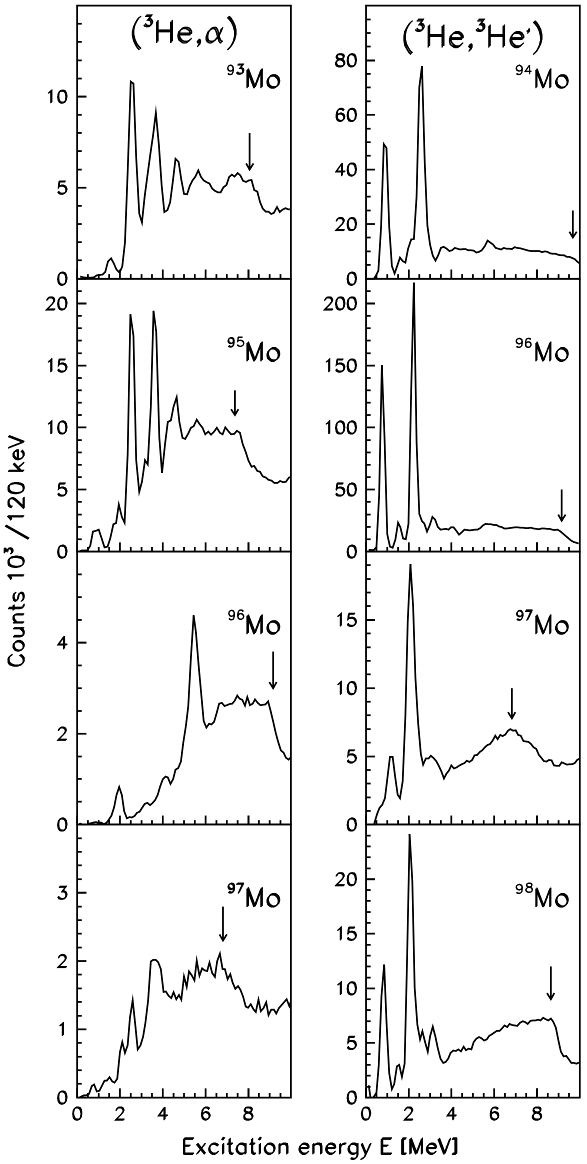

FIG. 1. Charged ejectile spectra for $^{93-98}$Mo in coincidence with γ-rays, labeled by the product nuclei. The arrows indicate the neutron-separation energy B_n.

Brink-Axel hypothesis [30,31] as

$$P(E, E_\gamma) \propto \rho(E - E_\gamma)\mathcal{T}(E_\gamma), \tag{2}$$

where ρ is the level density and $\mathcal{T}$ is the radiative transmission coefficient.

The ρ and $\mathcal{T}$ functions can be determined by an iterative procedure [14] through the adjustment of each data point of these two functions until a global χ^2 minimum with the experimental $P(E, E_\gamma)$ matrix is reached. It has been shown [14] that if one solution for the multiplicative functions ρ and $\mathcal{T}$ is known, one may construct an infinite number of other functions, which give identical fits to the P matrix by

$$\tilde{\rho}(E - E_\gamma) = A \exp[\alpha(E - E_\gamma)]\, \rho(E - E_\gamma), \tag{3}$$

$$\tilde{\mathcal{T}}(E_\gamma) = B \exp(\alpha E_\gamma)\mathcal{T}(E_\gamma). \tag{4}$$

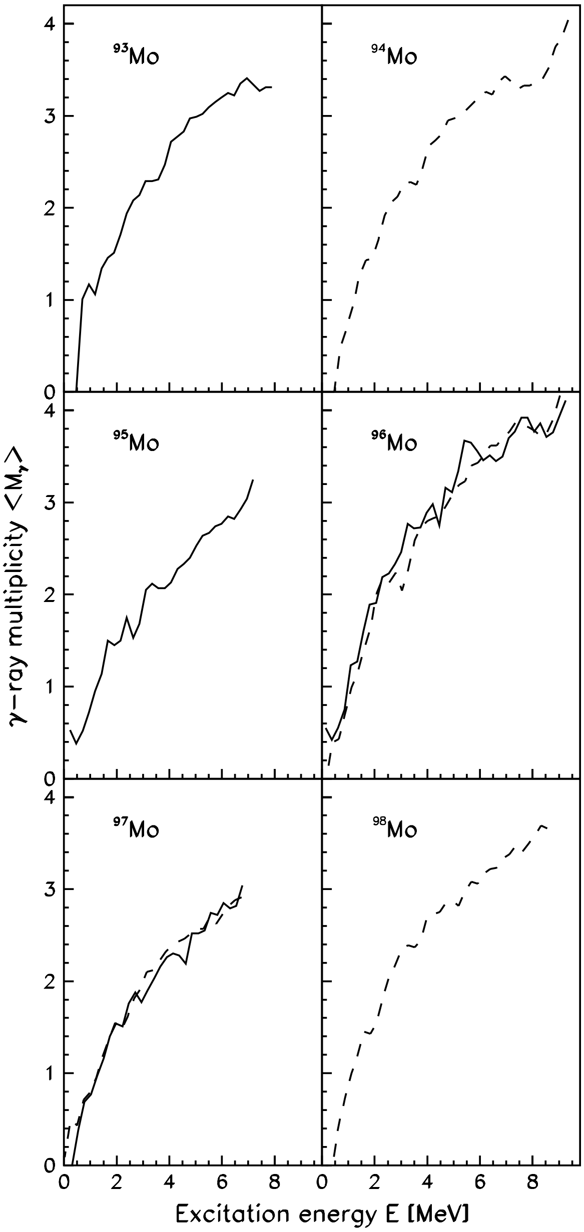

FIG. 2. γ-ray multiplicity evaluated by Eq. (1) versus excitation energy. The individual spectra are labeled by the product nuclei. Solid and dashed lines represent (^{3}He,α) and (^{3}He,^{3}He′) reactions, respectively.

Consequently, neither the slope nor the absolute values of the two functions can be obtained through the fitting procedure. Thus, the parameters α, A, and B remain to be determined.

The parameters A and α can be determined by normalizing the level density to the number of known discrete levels at low excitation energy [32] and to the level density estimated from neutron-resonance spacing data at the neutron-separation energy $E = B_n$ [33]. The procedure for extracting the total level density ρ from the resonance energy spacing D is described in Ref. [14]. Because our experimental level-density data points reach up to an excitation energy of only $E \sim B_n - 1$ MeV,

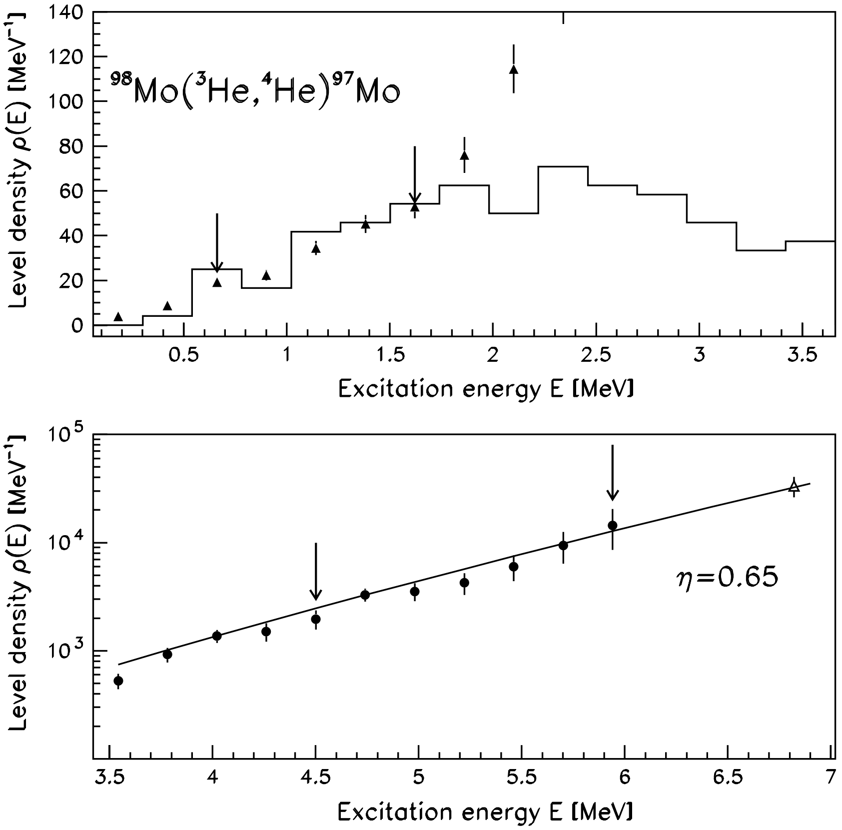

FIG. 3. Normalization procedure of the experimental level density (data points) of ^{97}Mo. The data points between the arrows in the upper panel are normalized to known levels at low excitation energy (histograms). In the lower panel they are normalized to the level density at the neutron-separation energy (open triangle) using a Fermi-gas extrapolation (line).

we extrapolate with the back-shifted Fermi-gas model [34,35]

$$\rho_{\mathrm{BSFG}}(E) = \eta \frac{\exp(2\sqrt{aU})}{12\sqrt{2}a^{1/4}U^{5/4}\sigma_I}, \tag{5}$$

where a constant η is introduced to adjust ρ_{BSFG} to the experimental level density at B_n. The intrinsic excitation energy is estimated by $U = E - C_1 - E_{\mathrm{pair}}$, where $C_1 = -6.6A^{-0.32}$ MeV and A are the back-shift parameter and mass number, respectively. The pairing energy E_{pair} is based on pairing-gap parameters Δ_p and Δ_n evaluated from even-odd mass differences [36] following the prescription of Dobaczewski *et al.* [37]. The level-density parameter is given by $a = 0.21A^{0.87}$ MeV^{-1}. The spin-cutoff parameter σ_I is given by $\sigma_I^2 = 0.0888aTA^{2/3}$, where the nuclear temperature is given by the following:

$$T = \sqrt{U/a}. \tag{6}$$

In cases where the intrinsic excitation energy U becomes negative, we set $U = 0$, $T = 0$, and $\sigma_I = 1$.

Figure 3 demonstrates the level-density normalization procedure for the ^{97}Mo case. The experimental data points are normalized according to Eq. (3) by adjusting the parameters A and α such that a least χ^2 fit is obtained in between the arrows. For the lower excitation region (see upper panel), one should take care only to include a fit region where it is likely that (almost) all levels are known. In practice, this means that the level density should not exceed ~50 levels per MeV. At the higher excitation region (lower panel), the Fermi-gas extrapolation connects seamlessly the highest-energy data points with the level-density value determined from neutron-resonance spacing at B_n. Generally, the resulting normalization is not very dependent on the choice of the theoretical extrapolation function (Fermi gas) or the chosen fit region (~4.5 to ~7 MeV).

Unfortunately, no information exists on the level density at $E = B_n$ for ^{94}Mo. Therefore, we estimate this value from a systematics of other Mo isotopes where information on the level density at B_n exists. In Fig. 4 we plot all the known data points from the Mo isotopic chain. The odd- and even-mass molybdenum nuclei fall into two groups, both showing a decreasing level density as function of excitation energy. This behavior is rather counterintuitive because in a given nucleus the level density increases exponentially with excitation energy, and for neighboring nuclei one would naively expect quite similar level-density curves. Two effects combine to result in the negative slope of the data points: (i) the decrease of single-particle level density when approaching the $N = 50$ shell gap resulting in a decrease of the level density in general and (ii) the increase of the neutron-separation energy with decreasing neutron number. For the negative slope to emerge, both effects have to be rather precisely of the same size for each step along the Mo isotopic chain. We have found no good physical explanation for this to happen, but we employ this fortuitous coincidence to estimate $\rho(B_n) = (6.2 \pm 1.0)10^4$ MeV^{-1} for ^{94}Mo from our phenomenological systematics.[1] The splitting of data points between even and odd Mo isotopes must not be interpreted solely as because

---

[1] This value also agrees within a factor of 2 with the systematics of Ref. [38].

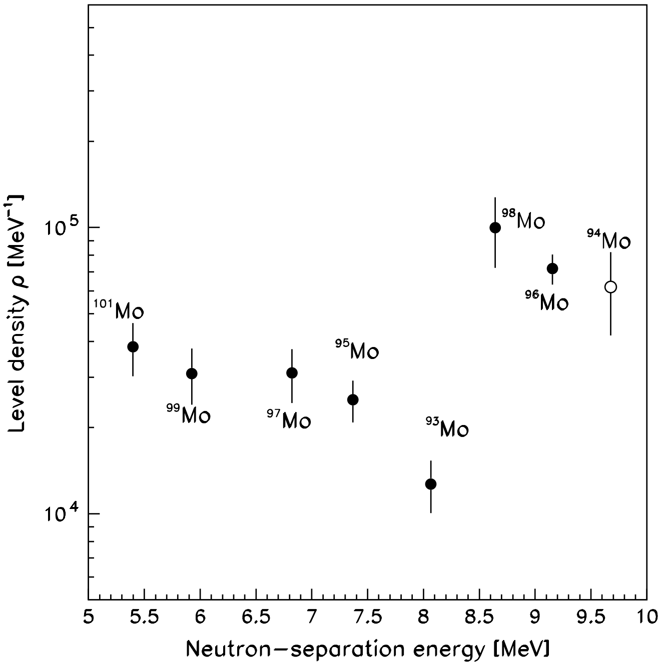

FIG. 4. Level densities at the neutron-separation energy. The unknown level density of ^{94}Mo (open circle) is estimated from the slope of the data points of the odd-mass molybdenum isotopes.

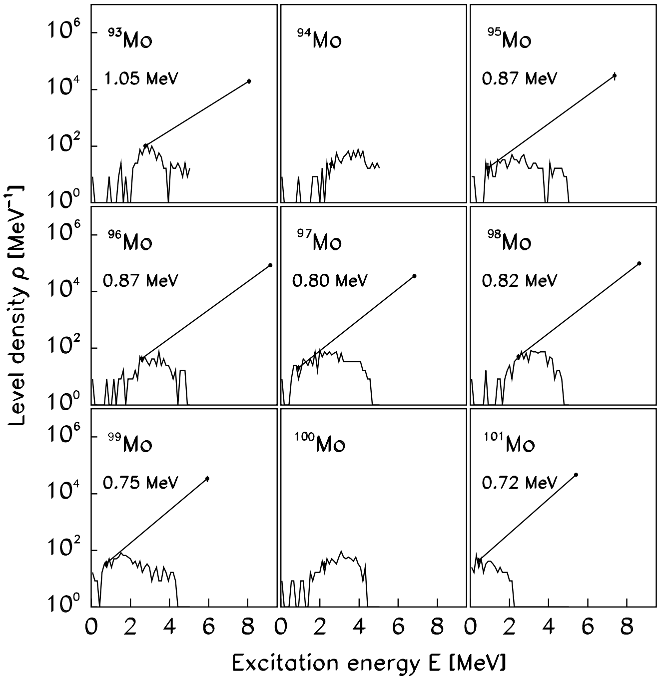

FIG. 5. Level density of nine molybdenum isotopes. The histograms represent levels from spectroscopy [39]. A straight line is drawn from these levels to the level density at the neutron-separation energy that is determined by average neutron-resonance spacings. The line represents the constant-temperature level-density formula (see text).

of the effect of the pairing-energy shift of the level-density curves; the difference in the magnitude of B_n between neutron-odd and -even isotopes also affects the magnitude of this splitting.

III. LEVEL DENSITY AND FINE STRUCTURES OF THE ENTROPY

The present knowledge on level density is concentrated in mainly two regions; the low-excitation region up to $\sim$2 MeV, studied in detail using spectroscopy and counting of known, discrete levels [39] and the region around the neutron-separation energy studied by experiments on neutron resonances [40]. Almost nothing is known of the level density in between the above-mentioned regions, but it is possible to determine quite reliably two anchor points of the level density.

Figure 5 shows the extracted anchor points (filled data points) for nine molybdenum isotopes together with the level density deduced from known discrete levels (solid lines). The upper anchor point is simply determined from neutron-resonance data. The lower anchor point, which is the average value of three data points, is determined such that a straight line on a logarithmic plot, going through the upper anchor point, provides an upper bound of the level-density distribution of known levels. The algorithm is iterative and treats all nuclei similarly to ensure that the results are comparable. The straight line connecting the lower and upper anchor points is defined by the constant temperature formula

$$\rho(E) = Ce^{E/\tau} \tag{7}$$

with $\tau^{-1} = (\ln \rho_2 - \ln \rho_1)/(E_2 - E_1)$ and $C = \rho_1 \exp(-E_1/\tau)$. Details are given in Ref. [41]. Provided that all the levels are measured at the excitation energy of the lower anchor point, we find from the plots of Fig. 5 that the temperature-like parameter τ drops from 1.05 MeV for the spherical ^{93}Mo to about 0.72 MeV for the well-deformed ^{101}Mo nucleus. This figure also illustrates the excitation energy where one would expect the appearance of missing levels in spectroscopic work, typically if the density of levels exceeds 50 MeV^{-1}.

The level densities $\rho(E)$ extracted from the eight reactions are displayed in Fig. 6. The data have been normalized as prescribed above, and the parameters used for $^{93-98}$Mo in Eq. (5) are listed in Table I. We find that the normalization constant η drops by one order of magnitude when going from deformed to spherical nuclei. This means that the spherical ^{93}Mo has about ten times lower level density than predicted by a global Fermi-gas model. As mentioned earlier, this effect is one of the reasons for the negative slope of the data points in Fig. 4.

Our experimental data interpolate between the previously known lower anchor point at $\sim$2 MeV and about 1 MeV below the upper anchor point at $\sim$7 MeV. For the energy interval between $\sim$6 and $\sim$7 MeV, we rely on models [34,35]. Despite the fact that the final extrapolation of the level density up to the nucleon-separation energy is model dependent, this affects only the average slope of the level density and does not affect the fine structure. This enables us to observe fine structures in the level density that are thought to reflect the breaking of individual pairs. In an earlier work, we showed how

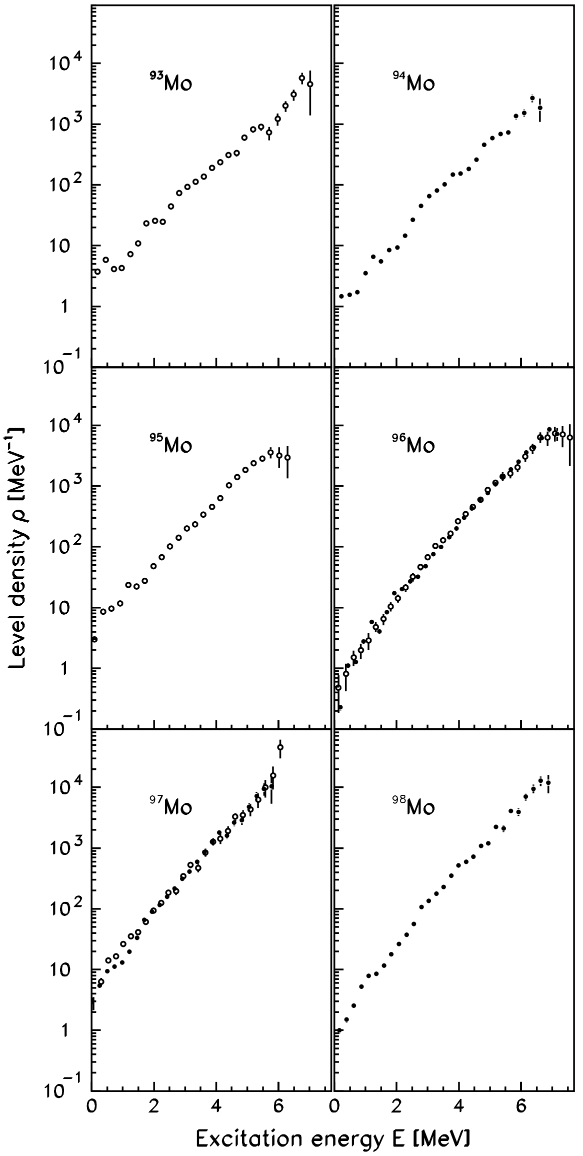

FIG. 6. Normalized level densities for $^{93-98}$Mo. The open and filled circles are data from the (^{3}He,α) and (^{3}He,^{3}He$'$) reactions, respectively.

a simple single-particle-plus-pairing model can qualitatively explain the emergence of such fine structures [21]. Moreover, we have in the past investigated how pairing correlations are weakened in the presence of already unpaired nucleons, but also how these unpaired nucleons around the Fermi energy can increase the cost in energy to break up further nucleon pairs because of the blocking effect of the Pauli principle [42]. Our goal in the present work is to obtain experimental values for the critical temperature of the pair-breaking process. On the way, we also investigate some other thermodynamical properties, in particular the entropy, when going from spherical to deformed nuclei. The generalization of the concept of temperature for a small system is not straightforward and has been discussed extensively in the literature (see, e.g., Ref. [42] and references therein). Traditionally, temperature is introduced in slightly different ways in the microcanonical statistical ensemble (as a property of the system itself) and in the canonical statistical ensemble (as imposed by a heat bath). The temperature-energy relations for rare-earth nuclei (the caloric curves) derived within the two statistical ensembles display in general a different behavior because the nuclei under discussion are essentially discrete systems [13].

To avoid the shortcomings imposed by the above-mentioned statistical ensembles, a new approach for the caloric curves based on the two-dimensional probability distribution $P(E, T)$ has been proposed [42,43]. This approach bypasses the well-known problem of spurious structures such as negative temperatures and heat capacities in the microcanonical ensemble. Conversely, more structures in the new caloric curve are evident than in the canonical caloric curve. However, this new method is still not well settled and we will defer the discussion of caloric curves to another occasion.

Within the microcanonical ensemble the experimentally obtained level density corresponds to the partition function that is simply the multiplicity Ω of accessible states. Thus, the entropy S of the system within the energy interval E and $E + \delta$ is determined by the following:

$$S(E) = k_B \ln \Omega(E), \tag{8}$$

where $\Omega(E) = \rho(E)/\rho_0$ and the Boltzmann constant is set to unity ($k_B \equiv 1$) for simplicity.[2] To fulfill the third law of thermodynamics; namely $S \rightarrow 0$ when $T \rightarrow 0$, the normalization denominator is set to $\rho_0 = 1.5\,\mathrm{MeV}^{-1}$. Entropy as a function of energy can be defined and measured for small and mesoscopic systems as well as for large systems. However, fluctuations in

TABLE I. Parameters used for the back-shifted Fermi-gas level density.

Nucleus	E_{pair} (MeV)	a (MeV^{-1})	C_1 (MeV)	B_n (MeV)	D (eV)	$\rho(B_n)\,(10^4\,\mathrm{MeV}^{-1})$	η
^{98}Mo	2.080	11.33	−1.521	8.642	75	9.99	0.87
^{97}Mo	0.995	11.23	−1.526	6.821	1050	3.10	0.65
^{96}Mo	2.138	11.13	−1.531	9.154	105	7.18	0.46
^{95}Mo	1.047	11.03	−1.537	7.367	1320	2.50	0.34
^{94}Mo	2.027	10.93	−1.542	9.678	—	6.20[a]	0.25
^{93}Mo	0.899	10.83	−1.547	8.067	2700	1.27	0.08

[a] Estimated from systematics (see text).

---

[2] More precisely, multiplicity $\Omega(E)$ is proportional to $\rho(E)(2\langle J(E)\rangle + 1)$, where $\langle J(E)\rangle$ is the average spin of levels with excitation energy E. However, in the present work, we neglect the weak excitation-energy dependence of $\langle J(E)\rangle$.

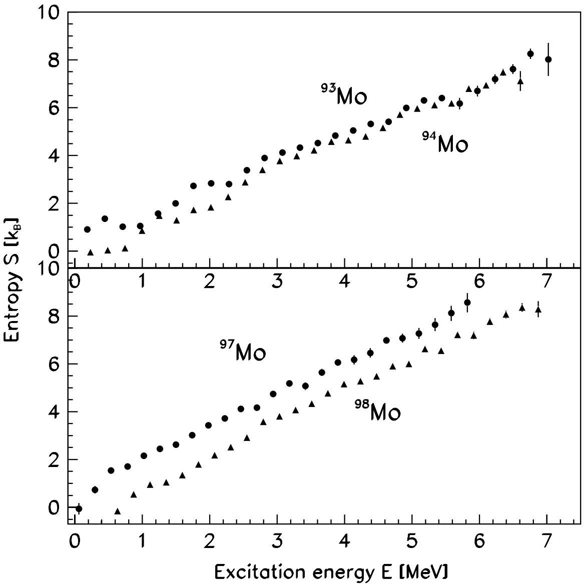

FIG. 7. Experimental entropy for ^{93,94}Mo (upper panel) and ^{97,98}Mo (lower panel) as function of excitation energy E.

level spacings that are typical for small systems will make the entropy sensitive to exactly how the energy interval between E and $E + \delta E$ is chosen. Thus, Eq. (8) is useful only if $\Omega(E)$ is a sufficiently smooth function, i.e., for the case that its first derivative exists. Small statistical fluctuations in the entropy S may give rise to large contributions to the temperature T, which is defined within the microcanonical ensemble as

$$T(E) = \left(\frac{\partial S}{\partial E}\right)^{-1}. \tag{9}$$

Figure 7 shows the entropy deduced within the microcanonical ensemble for ^{93,94}Mo (upper panel) and ^{97,98}Mo (lower panel). The entropy curve plotted on a linear scale is essentially identical to the level-density curve on a logarithmic scale. In general, the most efficient way to create additional states in atomic nuclei is to break $J = 0$ nucleon Cooper pairs from the core. The resulting two nucleons may thereby be thermally excited rather independently to the available single-particle levels around the Fermi surface. We therefore interpret, e.g., the steplike increases in entropy around 2–3 MeV excitation energy in Fig. 7 as because of the breaking of the first nucleon Cooper pair.

The entropies of odd-mass nuclei are higher than those of their even-even neighbors, even when their mass numbers are lower. It is interesting to compare entropies between neighboring nuclei. The difference in entropy

$$\Delta S(E) = S_{\text{odd-mass}} - S_{\text{even-even}} \tag{10}$$

is assumed to be a measure for the single-particle entropy. The entropies of the almost spherical ^{93}Mo and ^{94}Mo (upper panel of Fig. 7) follow each other closely above $E \sim 2.5$ MeV. Here, the odd valence nucleon behaves almost as a passive spectator. For ^{93,94}Mo, we find $\Delta S \gtrsim 0$ for $E > 2.5$ MeV. The deformed case, (lower panel of Fig. 7) exhibits an entropy difference of $\Delta S \gtrsim 1$. This is less than the value of $\Delta S \sim 2$ found for rare-earth nuclei [44,45].

These observations can be explained qualitatively by the fact that the single-particle entropy depends on the number of single-particle orbitals that are available for excitations at a certain temperature. For ^{93,94}Mo at low energies, the single neutron outside the closed shell can only occupy the two $d_{5/2}$ and $g_{7/2}$ orbitals giving an entropy of $\ln 2 \sim 0.7$. For the case of deformed nucleus ^{97,98}Mo, symmetry breaking results in a splitting of these two single-particle orbitals into seven Nilsson orbitals, giving a total entropy of $\ln 7 \sim 1.9$, i.e., about one unit more than for the ^{93,94}Mo case. In the rare-earth region strong deformation and intruder orbitals from other shells result in an even higher single-particle level density, giving rise to an even larger single-particle entropy. Although our simple argument somewhat overestimates the observed single-particle entropies, it provides a satisfactory explanation for the differences between the single-particle entropies in the different cases.

The entropy in atomic nuclei at low energies does not simply scale with the total number of nucleons. In the presence of pairing correlations, i.e., away from closed shells, the entropy scales rather with the number of unpaired nucleons at a certain excitation energy. When pairing correlations cannot form because of the large single-particle level spacings around closed shells, an unpaired nucleon will behave almost as a passive spectator without contributing significantly to the entropy of the system.

At excitations energies around 5.5 MeV, a bump is observed in the entropy curves for the lighter ^{93,94}Mo nuclei. In light of the discussion above, it is unlikely that such a bump can be interpreted as the breaking of a nucleon Cooper pair. We propose that this bump is related to the sudden onset of neutron excitations across the $N = 50$ shell gap. Because of the generally higher level density and the onset of deformation in the heavier Mo isotopes, the opening of the $g_{9/2}$ shell might be less significant, leading to the effect being spread out in energy. However, such an effect might become visible in the lighter ^{93,94}Mo nuclei. This interpretation is supported by the fact that the large transfer peak at 5.5 MeV excitation energy in the particle spectrum of the ^{97}Mo(^{3}He,$\alpha\gamma$)^{96}Mo reaction at a beam energy of 45 MeV (see Fig. 1) has been shown in an experiment at the Yale University Enge splitpole to be dominated by high ℓ transfer, most likely $\ell = 4\hbar$ [46].

IV. PHASE TRANSITIONS

A. Model

In this section we utilize a recently developed thermodynamic model [41,47,48] that allows the investigation and classification of the pairing phase transition. The model is based on the canonical ensemble theory where equilibrium is obtained at a certain given temperature T. It can describe level densities for midshell nuclei in the mass regions $A = 58$, 106, 162, and 234.

The basic idea of the model is the assumption of a reservoir of nucleon pairs. These nucleon pairs can be broken and the unpaired nucleons are thermally scattered into an infinite, equidistant, doubly degenerated single-particle level scheme. The nucleon pairs in the reservoir do not interact with each other and are thought to occupy an infinitely degenerated ground state. The nucleons in the single-particle level scheme do not interact with each other either, but they have to obey the Pauli principle.

The essential parameters of the model are the number of pairs n in the reservoir at zero temperature, the spacing of the single-particle level scheme $\epsilon = 30$ MeV/nucleon, and the energy necessary to break a nucleon pair $2\Delta = 24\ \mathrm{MeV}/\sqrt{A}$. Quenching of pairing correlations is introduced in this model by reducing the energy required to break a nucleon pair in the presence of unpaired nucleons. We assume that for every already broken nucleon pair, the energy to break a further nucleon pair is reduced by a factor of $r = 0.56$, which is suggested by theoretical calculations [49]. To simulate the effect of the $N = 50$ shell closure on the $A < 98$ isotopes, we depart from the global systematics for ϵ and replace it with $\epsilon' = \epsilon a(A = 98)/a(A < 98)$ using the experimentally deduced a values of Ref. [40]. We use the same parameters for both protons and neutrons, keeping the proton pairs fixed to seven because there are 14 more protons outside the $Z = 28$ shell closure.

The total partition function is written as a product of proton (Z_π), neutron (Z_ν), rotation (Z_{rot}), and vibration (Z_{vib}) partition functions where the parameters for the collective excitations are the rigid moment of inertia $A_{\mathrm{rig}} = 34$ MeV $A^{-5/3}$ and the energy of one-phonon vibrations $\hbar\omega_{\mathrm{vib}} = 1.5$ MeV taken from spectroscopic data [39]. Thermodynamical quantities of interest can be deduced from the Helmholtz free energy defined as

$$F(T) = -T\ln\left(Z_\pi Z_\nu Z_{\mathrm{rot}} Z_{\mathrm{vib}}\right). \tag{11}$$

This equation connects statistical mechanics and thermodynamics. Quantities such as entropy, average excitation energy, and heat capacity can be calculated by

$$S(T) = -\left(\frac{\partial F}{\partial T}\right)_V \tag{12}$$

$$\langle E(T)\rangle = F + ST \tag{13}$$

$$C_V(T) = \left(\frac{\partial\langle E\rangle}{\partial T}\right)_V, \tag{14}$$

respectively.

In Fig. 8, the Helmholtz free energy F, entropy S, average excitation energy $\langle E\rangle$, and heat capacity C_V are shown as functions of temperature for even-even, odd, and odd-odd systems in the ^{96}Mo mass region. The free energy F and the average excitation energy $\langle E\rangle$ are rather structureless as functions of temperature. The odd-even effects are small: The even-even, odd, and odd-odd systems have different excitation energies at the same temperature, where the even-even system requires the highest $\langle E\rangle$ to be heated to some given temperature T. Around $T_c \sim 0.9$–1.1 MeV the nuclei are excited to their respective nucleon-separation energies.

The entropy S and heat capacity C_V are more sensitive to thermal changes. The entropy difference ΔS between systems with A and $A \pm 1$ is a useful quantity. At moderate temperatures, it is approximately extensive (additive) and represents the single-particle entropy associated with the

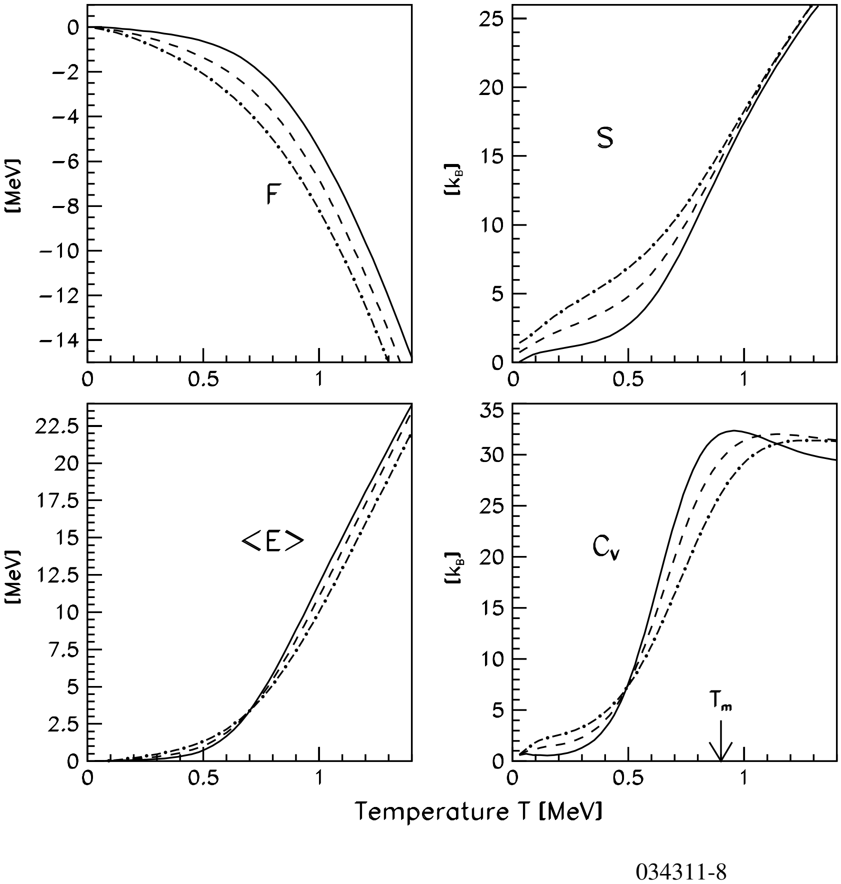

FIG. 8. Model calculation for nuclei around ^{96}Mo. The four panels show the free energy F, the entropy S, the thermal excitation energy $\langle E\rangle$, and the heat capacity C_V as a function of temperature T. The arrow at $T_m \sim 0.9$ MeV indicates the local maximum of C_V where the pair-breaking process takes place in the even-even system. The same parameter set is used for even-even (solid lines), odd (dashed lines), and odd-odd systems (dash-dotted lines).

valence particle (or hole) [41]. In the upper right panel, we find, e.g., that the nucleon carries a single-particle entropy of $\Delta S \sim 2.0$ at $T \sim 0.4$ MeV.

The shape of the heat-capacity curve is related to the level density. Traditionally, level-density curves have been described by the two-component model as proposed by Gilbert and Cameron [34]. Within this model, the low energetic part is a constant-temperature level density and the high energetic part is a Fermi-gas model. It has been shown in Ref. [12] that the inclusion of a constant-temperature part in the level-density formula creates a heat-capacity curve as function of temperature with a pronounced S shape similar to that shown in Fig. 8. With our model parameters, the maximum of the local increase in the C_V curve takes place at about $T \sim 0.9$ MeV. This temperature compares well with the temperature determined in the microcanonical ensemble from Eq. (9), giving a temperature of $T \sim 0.9$ MeV for ^{96}Mo (see also Fig. 5).

B. Comparison with experimental data

Our model is described within the canonical ensemble, whereas experimental data refer to the microcanonical ensemble. There are two ways to compare our model with experiments. Details are given in Ref. [41]. In this work we will make use of the saddle-point approximation [50]

$$\rho(\langle E\rangle) = \frac{\exp(S)}{T\sqrt{2\pi C_V}}, \tag{15}$$

which gives satisfactory results for the nuclear level density [41,48].

Figure 9 shows the theoretical level densities calculated using Eq. (15). The agreement with the anchor points and the experimental level densities for ^{97,98}Mo isotopes is satisfactory. Some of the model parameters could be adjusted more precisely, however, in this work we have chosen to use parameters taken from systematics.

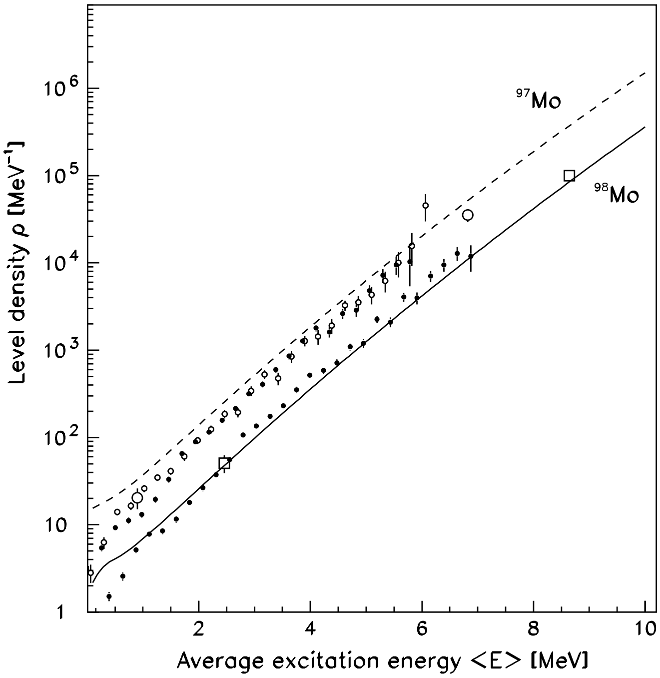

FIG. 9. Calculated level density of ^{98}Mo (solid line) and ^{97}Mo (dashed line) as function of average excitation energy $\langle E\rangle$. The big open circles and squares are experimental level-density anchor points from Ref. [41]. The small filled and open circles are experimental data points measured with the (^{3}He,α) and (^{3}He,^{3}He$'$) reactions, respectively for the two isotopes.

To investigate the behavior of the pairing correlations when approaching a major shell gap, we compare the canonical C_V curves that are based on the Laplace transforms of the experimental level densities. The curves are plotted in Fig. 10 for even ^{94,96,98}Mo (upper panel) and odd ^{93,95,97}Mo (lower panel) nuclei. The C_V curves resemble washed-out step structures and show an S shape as a function of temperature quite similar to the model calculation on the lower right panel of Fig. 8. Because of the averaging performed by the Laplace transformation discrete transitions between the different quasiparticle regimes, as observed within the microcanonical ensemble, are hidden. Only the phase transition related to the quenching of the pair correlations as a whole can be seen. Details are given in Ref. [17].

The canonical heat-capacity curves show local enhancements around $T \sim 0.5$–1.0 MeV. Such enhancements were predicted in the calculations of Fig. 8, and they are expected to be larger in the even-mass nuclei compared to the odd-mass neighbors. The experimental heat capacities show this feature for the ^{97,98}Mo pair, and up to a certain extend for the ^{93,94}Mo pair, but it is not very obvious for the ^{95,96}Mo pair, where ^{95}Mo shows a more pronounced enhancement than expected. Approaching the $N = 50$ closed shell, the local enhancements become less and less pronounced. The general behavior of pairing correlations is that at shell closure there are almost no pairing correlations and, as particles are added, the pairing correlations increase. Therefore the signature of a transition from a "paired phase" to an "unpaired phase" when approaching a major shell gap becomes less and less pronounced. We should note that very recently an alternative interpretation has been given [51]. These authors find that the S shape can be accounted for as an effect of the particle-number conservation, and it occurs even when assuming a constant gap in the BCS theory.

From the C_V curves, we have extracted the critical temperature for the quenching of pair correlations. The critical temperatures have been obtained by a fit of the canonical heat capacity of a constant-temperature level-density model to the data for the first 600 keV in temperature. The algorithm and its sensitivity are discussed in Ref. [12]. The values obtained are plotted in Fig. 11; there is a tendency for the critical temperature to be slightly higher for odd ^{93,95,97}Mo than for even ^{92,94,96}Mo nuclei, similar to the local enhancement of the heat-capacity curve in the model calculation (see the lower right panel of Fig. 8) that is observed at higher temperatures for odd-mass Mo isotopes. The higher critical temperature for odd-mass nuclei is because of the Pauli blocking effect of the unpaired quasiparticle that increases the distance to the Fermi surface for low-lying orbitals with coupled pairs and thus increases the cost in energy to break pairs into more

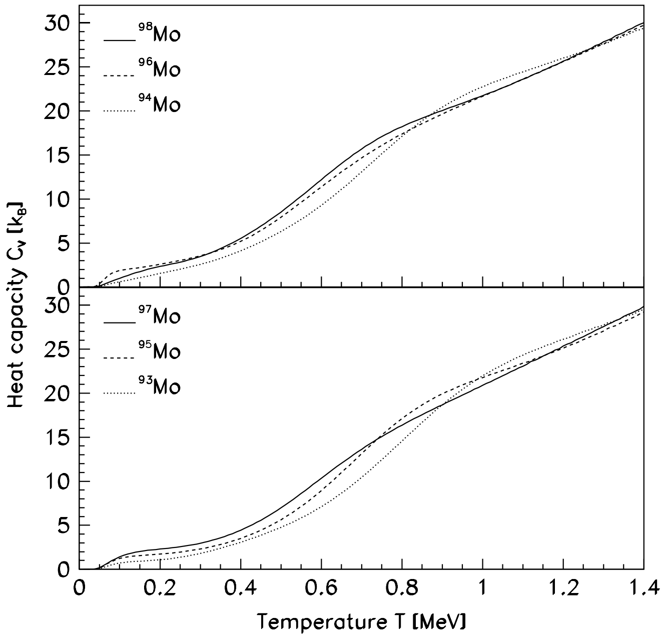

FIG. 10. Observed heat capacity as functions of temperature in the canonical ensemble for the even ^{94,96,98}Mo (upper panel) and odd ^{93,95,97}Mo (lower panel) nuclei.

quasiparticles. Incidentally, the critical temperature for the quenching of pairing correlations coincides (by construction) quite well with the temperature-like parameter τ of Fig. 5.

A discontinuity of the heat capacity in a macroscopic system indicates a second-order phase transition according to the Ehrenfest classification; this is observed in the transition of a paired Fermion system such as a low-temperature superconductor or superfluid ^{3}He to their normal phases. Thus, the experimentally observed local enhancement of the heat capacity is interpreted as a fingerprint of a phase transition from a phase with strong pairing correlations to a phase where the pairing correlations are quenched [12]. Shell-model Monte-Carlo calculations [7] have shown that the pairing phase transition is strongly correlated with the suppression of neutron pairs with increasing temperature. It has also been observed that the reduction of the neutron-pair content of the wave function is much stronger in the even-even than in the odd-mass isotopes, giving rise to the more pronounced S shape in the canonical heat-capacity curves in the even-even nuclei. The same odd-even difference in the heat capacity is also observed experimentally between ^{161}Dy and ^{162}Dy, as well as ^{171}Yb and ^{172}Yb [12].

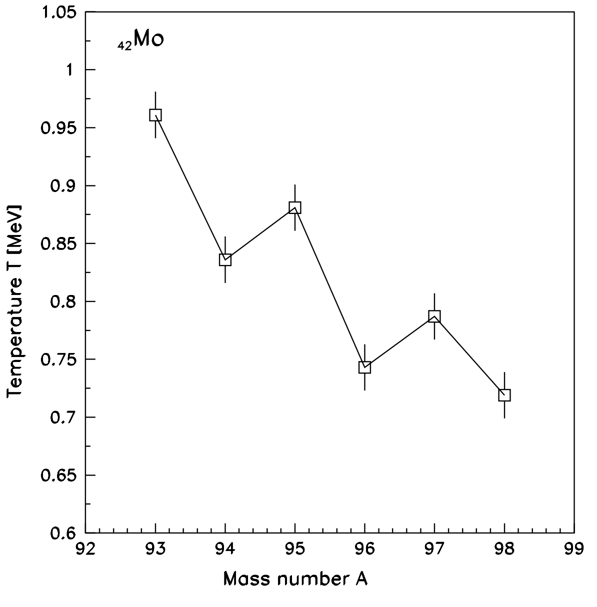

FIG. 11. Critical temperature for the quenching of pair correlations for $^{93-98}$Mo isotopes.

C. Entropy as function of neutron number

To study entropy as a function of neutron number, we compare the microcanonical entropy obtained by the saddle-point approximation of Eq. (15) to our experimental data. In Fig. 12 the data are plotted as a function of the neutron number N (left panel) and as a function of the number of available neutrons in the reservoir (right panel). Although only qualitative agreement is achieved, some simple conclusions can be drawn.

For the isotopes under investigation in this work, we see that the entropy at 1 MeV in both panels increases moderately as a function of the number of particles. The entropy at 7 MeV increases more rapidly and this is correlated to the evolution of the temperature-like parameter τ (see Fig. 5). Both theoretically and experimentally, the odd systems show $\Delta S = 1.0k_B$ higher entropy than their neighboring even-even systems.

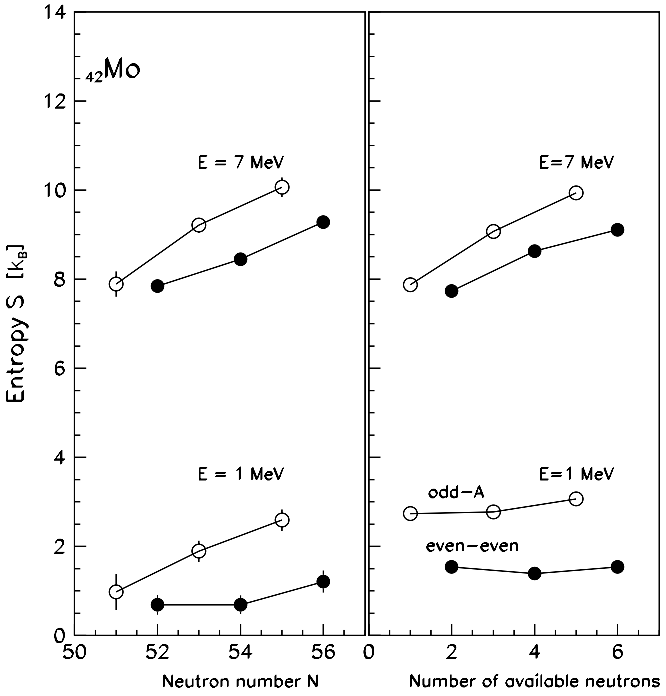

FIG. 12. Entropy extracted at excitation energies of 1 and 7 MeV as a function of neutron number N (left panel) and number of available neutrons in the model (right panel) for odd-even (open circles) and even-even (filled circles) molybdenum isotopes.

The slopes at 7 MeV in the left panel of Fig. 12 give $dS/dN = 0.5k_B$. Thus, going from ^{98}Mo to ^{93}Mo the level density drops when approaching the $N = 50$ shell gap by a factor of ∼0.03. This mechanism is also reflected in the η parameter of Eq. (5), which drops from 0.87 for ^{98}Mo to 0.08 for ^{93}Mo.

As we already mentioned, the less pronounced S shape shows that the pairing correlations decrease when approaching the $N = 50$ shell gap. At the same time, the critical temperature for the quenching of pair correlations increases, which is the opposite of what one might expect. This effect can be explained by the increase in single particle level spacing when approaching the $N = 50$ shell gap. We have already seen in the discussion in the previous section, that this increase, together with the weakening pairing correlations, which fail to push the nuclear ground state sufficiently down in energy, lead to a decrease in single-particle entropy, see Figs. 7 and 12.

Therefore, the increase in critical temperature for the quenching of pairing correlations when approaching the $N = 50$ shell gap is because of the competition between the weakening pairing correlations and the increasing single-particle level spacing. Just as the weakened pairing correlations in odd nuclei cannot compensate for the effect of Pauli blocking on T_c, they cannot compensate for the effect of an increase in single-particle level spacing on T_c when approaching a major shell gap.

V. CONCLUSIONS

Levels in $^{93-98}$Mo in the excitation-energy region up to the neutron-separation energy were populated using (^{3}He,$\alpha\gamma$) and (^{3}He,^{3}He$'\gamma$) reactions. The level densities of $^{93-98}$Mo were determined from their corresponding primary γ-ray spectra. Within the canonical ensemble, thermodynamical observables were deduced from the level density; they display features consistent with signatures of a phase transition from a strongly pair-correlated phase to a phase without strong pairing correlations. This conclusion is supported by recent theoretical calculations within shell-model Monte Carlo simulations by Alhassid *et al.* [7,8,50], where it is shown that the expectation value of the pair operator decreases strongly around the critical temperature. However, we would like to point out that other interpretations are not excluded. Different mechanisms governing the thermodynamic properties of odd and even systems were studied. A simple, recently developed model for the investigation and classification of the pairing phase transition in hot nuclei has been employed and qualitative agreement with experimental data achieved. Using the saddle-point approximation the experimental level densities of even-even and odd-even systems are reproduced. Estimates for the critical temperature of the pairing phase transition yield $T_c \sim 0.7$–1.0 MeV.

ACKNOWLEDGMENTS

Part of this work was performed under the auspices of the U.S. Department of Energy by the University of California, Lawrence Livermore National Laboratory under contract W-7405-ENG-48. U.A., E.A., G.E.M., and A.V. acknowledge support from U.S. Department of Energy grant DE-FG02-97-ER41042 and from the National Nuclear Security Administration under the Stockpile Stewardship Science Academic Alliances program through Department of Energy Research grant DE-FG03-03-NA00074 and DE-FG03-03-NA00076. M.G., F.I., S.M., J.R., S.S., A.C.L., and S.Ø acknowledge financial support from the Norwegian Research Council (NFR).

---

[1] J. Bardeen, L. N. Cooper, and J. R. Schrieffer, Phys. Rev. **108**, 1175 (1957).

[2] M. Sano and S. Yamasaki, Prog. Theor. Phys. **29**, 397 (1963).

[3] A. L. Goodman, Nucl. Phys. **A352**, 45 (1981).

[4] L. G. Moretto, Nucl. Phys. **A185**, 145 (1972).

[5] K. Tanabe and K. Sugawara-Tanabe, Phys. Lett. **B97**, 337 (1980).

[6] S. Rombouts, K. Heyde, and N. Jachowicz, Phys. Rev. C **58**, 3295 (1998).

[7] S. Liu and Y. Alhassid, Phys. Rev. Lett. **87**, 022501 (2001).

[8] Y. Alhassid, G. F. Bertsch, and L. Fang, Phys. Rev. C **68**, 044322 (2003).

[9] J. L. Egido, L. M. Robledo, and V. Martin, Phys. Rev. Lett. **85**, 26 (2000).

[10] B. K. Agrawal, Tapas Sil, S. K. Samaddar, and J. N. De, Phys. Rev. C **63**, 024002 (2001).

[11] R. Rossignoli, N. Canosa, and P. Ring, Phys. Rev. Lett. **80**, 1853 (1998).

[12] A. Schiller, A. Bjerve, M. Guttormsen, M. Hjorth-Jensen, F. Ingebretsen, E. Melby, S. Messelt, J. Rekstad, S. Siem, and S. W. Ødegård, Phys. Rev. C **63**, 021306(R) (2001).

[13] E. Melby, L. Bergholt, M. Guttormsen, M. Hjorth-Jensen, F. Ingebretsen, S. Messelt, J. Rekstad, A. Schiller, S. Siem, and S. W. Ødegård, Phys. Rev. Lett. **83**, 3150 (1999).

[14] A. Schiller, L. Bergholt, M. Guttormsen, E. Melby, J. Rekstad, and S. Siem, Nucl. Instrum. Methods A **447**, 498 (2000).

[15] G. A. Bartholomew, I. Bergqvist, E. D. Earle, and A. J. Ferguson, Can. J. Phys. **48**, 687 (1970).

[16] G. A. Bartholomew, E. D. Earle, A. J. Ferguson, J. W. Knowles, and M. A. Lone, Adv. Nucl. Phys. **7**, 229 (1973).

[17] E. Melby, M. Guttormsen, J. Rekstad, A. Schiller, S. Siem, and A. Voinov, Phys. Rev. C **63**, 044309 (2001).

[18] A. Voinov, M. Guttormsen, E. Melby, J. Rekstad, A. Schiller, and S. Siem, Phys. Rev. C **63**, 044313 (2001).

[19] S. Siem, M. Guttormsen, K. Ingeberg, E. Melby, J. Rekstad, A. Schiller, and A. Voinov, Phys. Rev. C **65**, 044318 (2002).

[20] M. Guttormsen, E. Melby, J. Rekstad, S. Siem, A. Schiller, T. Lönnroth, and A. Voinov, J. Phys. G **29**, 263 (2003).

[21] A. Schiller *et al.*, Phys. Rev. C **68**, 054326 (2003).

[22] E. Tavukcu, Ph.D. thesis, North Carolina State University, 2002.

[23] M. Mayer, *Elementary Theory of Nuclear Shell Structure* (John Wiley & Sons, New York, 1955).

[24] S. Burger and G. Heymann, Nucl. Phys. **A463**, 243 (1975).

[25] P. F. Mantica, A. E. Stuchbery, D. E. Groh, J. I. Prisciandaro, and M. P. Robinson, Phys. Rev. C **63**, 034312 (2001).

[26] M. Guttormsen *et al.*, Phys. Rev. C **71**, 044307 (2005).

[27] M. Guttormsen, T. Ramsøy, and J. Rekstad, Nucl. Instrum. Methods A **255**, 518 (1987).

[28] M. Guttormsen, T. S. Tveter, L. Bergholt, F. Ingebretsen, and J. Rekstad, Nucl. Instrum. Methods A **374**, 371 (1996).

[29] L. Henden, L. Bergholt, M. Guttormsen, J. Rekstad, and T. S. Tveter, Nucl. Phys. **A589**, 249 (1995).

[30] D. M. Brink, Ph.D. thesis, Oxford University, 1955.

[31] P. Axel, Phys. Rev. **126**, 671 (1962).

[32] Data extracted using the NNDC On-Line Data Service from the ENSDF database, file revised as of Jan. 21, 2000.

[33] *Handbook for Calculations of Nuclear Reaction Data* (IAEA, Vienna, 1998).

[34] A. Gilbert, A. G. W. Cameron, Can. J. Phys. **43**, 1446 (1965).

[35] T. von Egidy, H. H. Schmidt, and A. N. Behkami, Nucl. Phys. **A481**, 189 (1988).

[36] G. Audi and A. H. Wapstra, Nucl. Phys. **A729**, 337 (2003).

[37] J. Dobaczewski, P. Magierski, W. Nazarewicz, W. Satuła, and Z. Szymański, Phys. Rev. C **63**, 024308 (2001).

[38] D. Bucurescu, T. von Egidy, J. Phys. G: Nucl. Part. Phys. **31**, S1675 (2005).

[39] R. B. Firestone, and V. S. Shirley, *Table of Isotopes*, 8th ed. (John Wiley & Sons, New York, 1996), Vol. I.

[40] A. S. Iljinov, M. V. Mebel, N. Bianchi, E. De Sanctis, C. Guaraldo, V. Lucherini, V. Muccifora, E. Polli, A. R. Reolon, and P. Rossi, Nucl. Phys. **A543**, 517 (1992), and references therein.

[41] M. Guttormsen, M. Hjorth-Jensen, E. Melby, J. Rekstad, A. Schiller, and S. Siem, Phys. Rev. C **63**, 044301 (2001).

[42] A. Schiller *et al.*, AIP Conf. Proc. **777**, 216 (2005).

[43] A. Schiller, M. Guttormsen, M. Hjorth-Jensen, J. Rekstad, and S. Siem, nucl-th/0306082.

[44] M. Guttormsen, A. Bagheri, R. Chankova, J. Rekstad, S. Siem, A. Schiller, and A. Voinov, Phys. Rev. C **68**, 064306 (2003).

[45] U. Agvaanluvsan *et al.*, Phys. Rev. C **70**, 054611 (2004).

[46] T. F. Wang (private communication).

[47] M. Guttormsen, M. Hjorth-Jensen, E. Melby, J. Rekstad, A. Schiller, and S. Siem, Phys. Rev. C **64**, 034319 (2002).

[48] A. Schiller, M. Guttormsen, M. Hjorth-Jensen, J. Rekstad, and S. Siem, Phys. Rev. C **66**, 024322 (2002).

[49] T. Døssing *et al.*, Phys. Rev. Lett. **75**, 1276 (1995).

[50] H. Nakada and Y. Alhassid, Phys. Rev. Lett. **79**, 2939 (1997).

[51] K. Esashika, H. Nakada, and K. Tanabe, Phys. Rev. C **72**, 044303 (2005).

5.4 Paper 3: Microcanonical entropies and radiative strength functions of ^{50,51}V

PHYSICAL REVIEW C **73**, 064301 (2006)

Microcanonical entropies and radiative strength functions of ^{50,51}V

A. C. Larsen,* R. Chankova, M. Guttormsen, F. Ingebretsen, S. Messelt, J. Rekstad, S. Siem, N. U. H. Syed, and S. W. Ødegård
Department of Physics, University of Oslo, P.O. Box 1048, Blindern, N-0316 Oslo, Norway

T. Lönnroth
Department of Physics, Åbo Akademi University, FIN-20500 Åbo, Finland

A. Schiller
National Superconducting Cyclotron Laboratory, Michigan State University, East Lansing, Michigan 48824, USA

A. Voinov
Department of Physics and Astronomy, Ohio University, Athens, Ohio 45701, USA

(Received 23 November 2005; published 7 June 2006)

The level densities and radiative strength functions (RSFs) of ^{50,51}V have been extracted using the (^{3}He,$\alpha\gamma$) and (^{3}He,^{3}He$'\gamma$) reactions, respectively. From the level densities, microcanonical entropies are deduced. The high γ-energy part of the measured RSF fits well with the tail of the giant electric dipole resonance. A significant enhancement over the predicted strength in the region of $E_\gamma \lesssim 3$ MeV is seen, which at present has no theoretical explanation.

DOI: 10.1103/PhysRevC.73.064301 PACS number(s): 21.10.Ma, 24.10.Pa, 25.55.Hp, 27.40.+z

I. INTRODUCTION

The structure of the vanadium isotopes is based on simple shell-model configurations at low excitation energies. The valence protons and neutrons occupy the single-particle $\pi f_{7/2}$ and $\nu f_{7/2}$ orbitals, respectively. These shells are isolated from other orbitals by the $N, Z = 20$ and 28 shell gaps, making the vanadium isotopes interesting objects for studying various nuclear shell effects. In particular, it is well known that the number of available singe-particle levels is significantly reduced for nuclei at closed shells.

The density of states or, equivalently, the entropy in these systems depends on the number of broken Cooper pairs and single-particle orbitals made available by crossing the shell gaps. The ^{50,51}V nuclei are of special interest because the neutrons are strongly blocked in the process of creating entropy; ^{50}V and ^{51}V have seven and eight neutrons in the $\nu f_{7/2}$ orbital, respectively. Thus, the configuration space of the three protons in the $\pi f_{7/2}$ shell is of great importance.

These particular shell-model configurations are also expected to govern the γ-decay routes. Specifically, as within every major shell, the presence of only one parity for single-particle orbitals in the low-spin domain means that transitions of $E1$ type will be suppressed. The low mass of the investigated nuclei causes the centroid of the giant electric dipole resonance (GEDR) to be relatively high, while the integrated strength according to the Thomas-Reiche-Kuhn sum rule is low; both observations work together to produce a relatively weak low-energy tail when compared to heavier nuclei. Hence, possible nonstatistical effects in the radiative strength function (RSF) might stand out more in the present investigation.

The Oslo Cyclotron group has developed a method to extract first-generation (primary) γ-ray spectra at various initial excitation energies. From such a set of primary spectra, the nuclear level density and the RSF can be extracted simultaneously [1,2]. These two quantities reveal essential information on nuclear structure such as pair correlations and thermal and electromagnetic properties. In the last five years, the Oslo group has demonstrated several fruitful applications of the method [3–7].

In Sec. II an outline of the experimental procedure is given. The level densities and microcanonical entropies are discussed in Sec. III, and in Sec. IV the RSFs are presented. Finally, concluding remarks are given in Sec. V.

II. EXPERIMENTAL METHOD

The experiment was carried out at the Oslo Cyclotron Laboratory using a beam of 30-MeV ^{3}He ions. The self-supporting natural V target had a purity of 99.8% and a thickness of 2.3 mg/cm^2. Particle-γ coincidences for ^{50,51}V were measured with the CACTUS multidetector array [8]. The charged ejectiles were detected using eight Si particle telescopes placed at an angle of 45° relative to the beam direction. Each telescope consists of a front ΔE detector and a back E detector with thicknesses of 140 and 1500 μm, respectively. An array of 28 collimated NaI γ-ray detectors with a total efficiency of ~15% surrounded the target and the particle detectors. The reactions of interest were the pick-up reaction ^{51}V(^{3}He, $\alpha\gamma$)^{50}V, and the inelastic scattering ^{51}V(^{3}He,^{3}He$'\gamma$)^{51}V. The typical spin range is expected to be $I \sim 2$–$4\hbar$. The experiment ran for about one week, with beam currents of ~1 nA.

The experimental extraction procedure and the assumptions made are described in Refs. [1,2]. The data analysis is based

---

*Electronic address: a.c.larsen@fys.uio.no

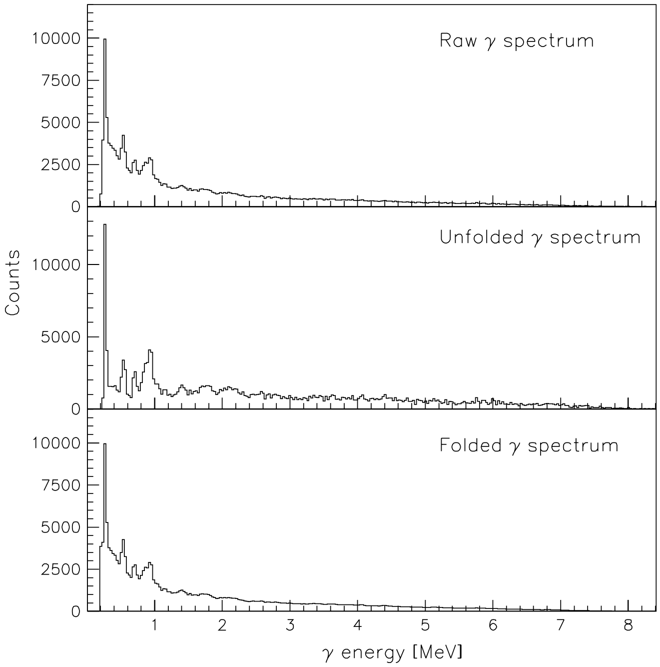

FIG. 1. γ spectra of ^{50}V for excitation energy $E = 6$–8 MeV.

on three main steps: (1) preparing the particle-γ coincidence matrix, (2) unfolding the γ-ray spectra, and (3) constructing the first-generation matrix.

In the first step, for each particle-energy bin, total spectra of the γ-ray cascades are obtained from the coincidence measurement. The particle energy measured in the telescopes is transformed to excitation energy of the residual nucleus, using the reaction kinematics. Then each row of the coincidence matrix corresponds to a certain excitation energy E, while each column corresponds to a certain γ energy E_γ.

In the next step, the γ-ray spectra are unfolded using the known response functions of the CACTUS array [9]. The Compton-subtraction method described in Ref. [9] preserves the fluctuations in the original spectra without introducing further spurious fluctuations. A typical raw γ spectrum is shown in the top panel of Fig. 1, taken from the ^{50}V coincidence matrix gating on the excitation energies between $E = 6$–8 MeV. The middle panel shows the unfolded spectrum, and in the bottom panel this spectrum has been folded with the response functions. The top and bottom panels are in excellent agreement, indicating that the unfolding method works very well.

The third step is to extract the γ-ray spectra containing only the first γ rays in a cascade. These spectra are obtained for each excitation-energy bin through a subtraction procedure as described in Ref. [10]. The main assumption of this method is that the γ-decay spectrum from any excitation-energy bin is independent of the method of formation, either directly by the nuclear reaction or populated by γ decay from higher-lying states following the initial reaction. This assumption is automatically fulfilled when the same states are equally populated by the two processes, since γ branching ratios are properties of the levels themselves. Even if different states are populated, the assumption is still valid for statistical γ decay,

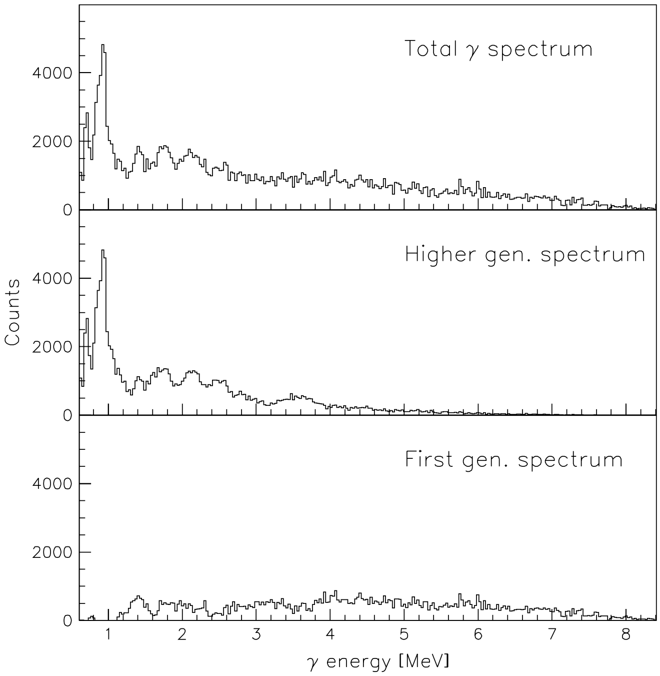

FIG. 2. Unfolded γ spectra of ^{50}V for excitation energy $E = 6$–8 MeV.

which only depends on the γ-ray energy and the number of accessible final states. In Fig. 2, the total unfolded γ spectrum, the γ spectrum of second and higher generations, and the first-generation spectrum of ^{50}V with excitation-energy gates $E = 6$–8 MeV are shown. The first-generation spectrum is obtained by subtracting the higher-generation γ rays from the total γ spectrum.

When the first-generation matrix is properly normalized [2], the entries of it are the probabilities $P(E, E_\gamma)$ that a γ ray of energy E_γ is emitted from an excitation energy E. The probability of γ decay is proportional to the product of the level density $\rho(E - E_\gamma)$ at the final energy $E_f = E - E_\gamma$ and the γ-ray transmission coefficient $\mathcal{T}(E_\gamma)$, that is,

$$P(E, E_\gamma) \propto \rho(E - E_\gamma)\mathcal{T}(E_\gamma). \qquad (1)$$

This factorization is the generalized form of the Brink-Axel hypothesis [11,12], which states that any excitation modes built on excited states have the same properties as those built on the ground state. This means that the γ-ray transmission coefficient is independent of excitation energy and thus of the nuclear temperature of the excited states. There is evidence that the width of the giant dipole resonance varies with the nuclear temperature of the state on which it is built [13,14]. However, the temperature corresponding to the excitation-energy range covered in this work is rather low and changes slowly with excitation energy ($T \sim \sqrt{E_f}$); thus, we assume that the temperature is constant and that the γ-ray transmission coefficient does not depend on the excitation energy in the energy interval under consideration.

The ρ and $\mathcal{T}$ functions can be determined by an iterative procedure [2], with which each data point of these two functions is simultaneously adjusted until a global χ^2 minimum with the experimental $P(E, E_\gamma)$ matrix is reached. No *a*

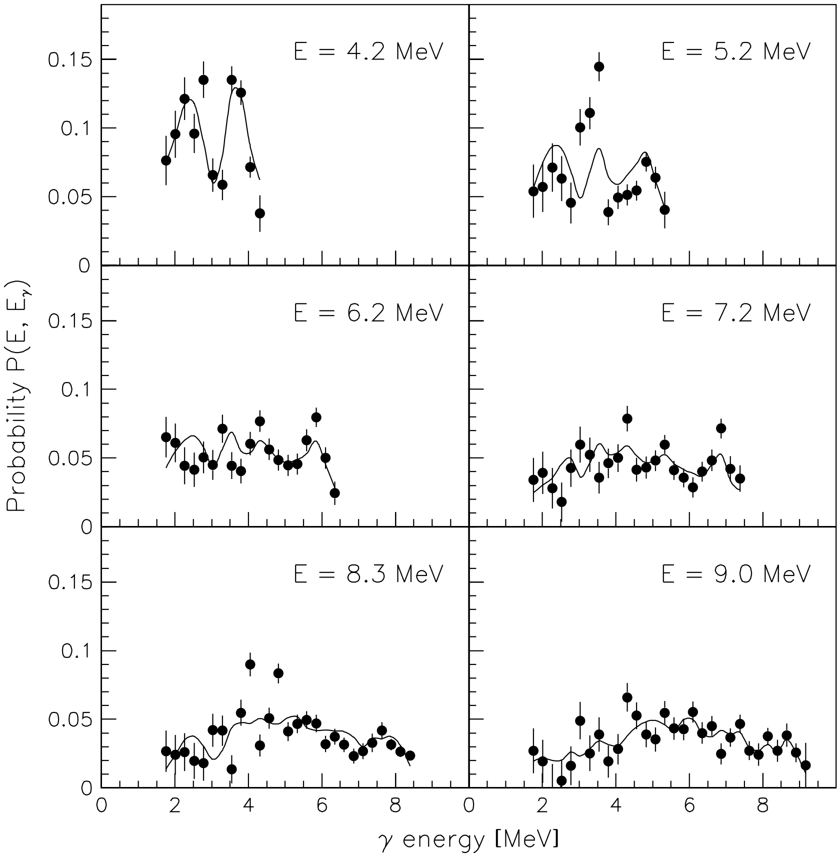

FIG. 3. Experimental first-generation γ spectra (data points with error bars) at six different initial excitation energies compared to the least-χ^2 fit (solid lines) for ^{50}V. The fit is performed simultaneously on the entire first-generation matrix of which the six displayed spectra are a fraction. The first-generation spectra are normalized to unity for each excitation-energy bin.

priori assumptions about the functional form of either the level density or the γ-ray transmission coefficient are used. An example to illustrate the quality of the fit is shown in Fig. 3, where we compare for the ^{51}V(^{3}He, $\alpha\gamma$)^{50}V reaction the experimental first-generation spectra to the least-χ^2 solution for six different initial excitation energies.

The globalized fitting to the data points determines the functional form of ρ and $\mathcal{T}$; however, it has been shown [2] that if one solution for the multiplicative functions ρ and $\mathcal{T}$ is known, one may construct an infinite number of other functions, which give identical fits to the P matrix by

$$\tilde{\rho}(E - E_\gamma) = A \exp[\alpha(E - E_\gamma)]\rho(E - E_\gamma), \qquad (2)$$

$$\mathcal{T}(E_\gamma) = B \exp(\alpha E_\gamma)\mathcal{T}(E_\gamma). \qquad (3)$$

Thus, the transformation parameters α, A, and B, which correspond to the physical solution, remain to be determined.

III. LEVEL DENSITY AND MICROCANONICAL ENTROPY

The parameters A and α can be obtained by normalizing the level density to the number of known discrete levels at low excitation energy [15] and to the level density estimated from neutron-resonance spacing data at the neutron binding energy $E = B_n$ [16]. The procedure for extracting the total level density ρ from the resonance energy spacing D is described in Ref. [2]. Since our experimental level-density data points only reach up to an excitation energy of $E \sim B_n - 1$ MeV, we extrapolate with the back-shifted Fermi-gas model with a global parametrization [17,18]

$$\rho_{\mathrm{BS}}(E) = \eta \frac{\exp(2\sqrt{aU})}{12\sqrt{2}a^{1/4}U^{5/4}\sigma_I}, \qquad (4)$$

where a constant attenuation coefficient η is introduced to adjust ρ_{BS} to the experimental level density at B_n. The intrinsic excitation energy is estimated by $U = E - C_1 - E_{\mathrm{pair}}$, where $C_1 = -6.6A^{-0.32}$ MeV is the back-shift parameter and A is the mass number. The pairing energy E_{pair} is based on pairing gap parameters Δ_p and Δ_n evaluated from even-odd mass differences [19] according to [20]. The level-density parameter a and the spin-cutoff parameter σ_I are given by $a = 0.21A^{0.87}\mathrm{MeV}^{-1}$ and $\sigma_I^2 = 0.0888TA^{2/3}$, respectively. The nuclear temperature T is described by $T = \sqrt{U/a}$. The parameters used for ^{50,51}V in Eq. (4) are listed in Table I.

Unfortunately, ^{49}V is unstable, and no information exists on the level density at $E = B_n$ for ^{50}V. Therefore, we estimate the values from the systematics of other nuclei in the same mass region. In order to put these data on the same footing, we plot the level densities as a function of intrinsic energy U. Due to the strongly scattered data of Fig. 4, the estimate is rather uncertain. We chose a rough estimate of $\rho(B_n) = 5400 \pm 2700$ MeV^{-1} for ^{50}V. This value gives an attenuation $\eta = 0.46$, which is in good agreement with the obtained value of $\eta = 0.51$ for the ^{51}V nucleus. Figure 5 demonstrates the level-density normalization procedure for the ^{50}V case, i.e., how parameters A and α of Eq. (3) are determined to obtain a level-density function consistent with known experimental data.

TABLE I. Parameters used for the back-shifted Fermi-gas level density.

Nucleus	E_{pair} (MeV)	a (MeV^{-1})	C_1 (MeV)	B_n (MeV)	D (keV)	$\rho(B_n)$ (10^3 MeV^{-1})	η
^{50}V	0	6.31	-1.89	9.33	-	5.4(16)[a]	0.46
^{51}V	1.36	6.42	-1.88	11.05	2.3(6)	8.4(26)	0.51

[a] Estimated from systematics.

The experimentally extracted and normalized level densities of ^{50}V and ^{51}V are shown in Fig. 6 for excitation energies up to ~8 and 9 MeV, respectively. The level density of ^{50}V is relatively high and has a rather smooth behavior due to the effect of the unpaired proton and neutron, while the level density of ^{51}V displays distinct structures for excitation energies up to ~4.5 MeV. This effect is probably caused by the closed $f_{7/2}$ neutron shell in this nucleus.

The level densities of ^{50,51}V obtained with the Oslo method are compared to the number of levels from spectroscopic experiments [21]. The ^{51}V nucleus has relatively few levels per energy bin because of its closed neutron shell, so using spectroscopic methods to count the levels seems to be reliable up to ~4 MeV excitation energy in this case. For higher excitations, the spectroscopic data are significantly lower compared to the level density obtained with the Oslo method. This means that many levels are not accounted for in this excitation region by using standard methods. The same can be concluded for ^{50}V, and in this case the spectroscopic level density drops off at an excitation energy of about 2.5 MeV.

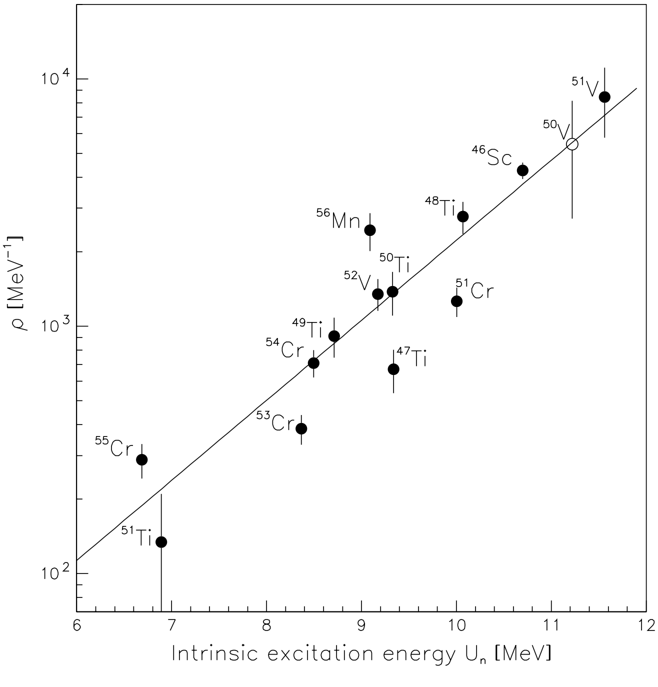

FIG. 4. Level densities estimated from neutron resonance level spacings at B_n and plotted as a function of intrinsic excitation energy $U_n = B_n - C_1 - E_{\text{pair}}$. The unknown level density for ^{50}V (open circle) is estimated from the line determined by a least-χ^2 fit to the data points.

The level densities of ^{50,51}V are also compared to the constant-temperature formula

$$\rho_{\text{fit}} = C\exp(E/T), \tag{5}$$

which is drawn as a solid line in Fig. 6. Here the parameters C and T are the level density at about zero excitation energy and the average temperature, respectively; both are estimated from the fit of the exponential to the region of the experimental level density indicated by arrows. From this model, a constant temperature of about 1.3 MeV is found for both nuclei.

The level density of a system can give detailed insight into its thermal properties. The multiplicity of states $\Omega_s(E)$, which is the number of physically obtainable realizations available at a given energy, is directly proportional to the level density and a spin-dependent factor $(2\langle J(E)\rangle + 1)$, thus

$$\Omega_s(E) \propto \rho(E)(2\langle J(E)\rangle + 1), \tag{6}$$

where $\langle J(E)\rangle$ is the average spin at excitation energy E. Unfortunately, the experimentally measured level density in this work does not correspond to the true multiplicity of states, since the $(2J + 1)$ degeneracy of magnetic substates

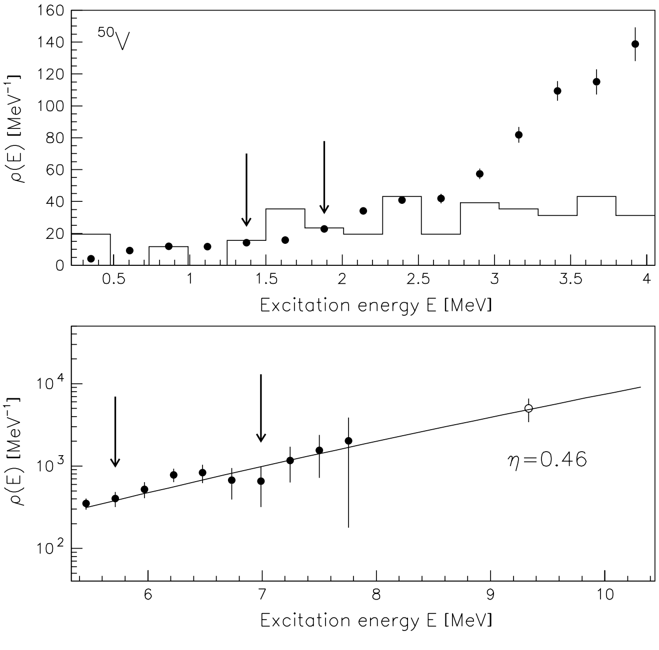

FIG. 5. Normalization procedure of the experimental level density (data points) of ^{50}V. The data points between the arrows are normalized to known levels at low excitation energy (histograms) and to the level density at the neutron-separation energy (open circle) using a Fermi-gas level-density extrapolation (solid line).

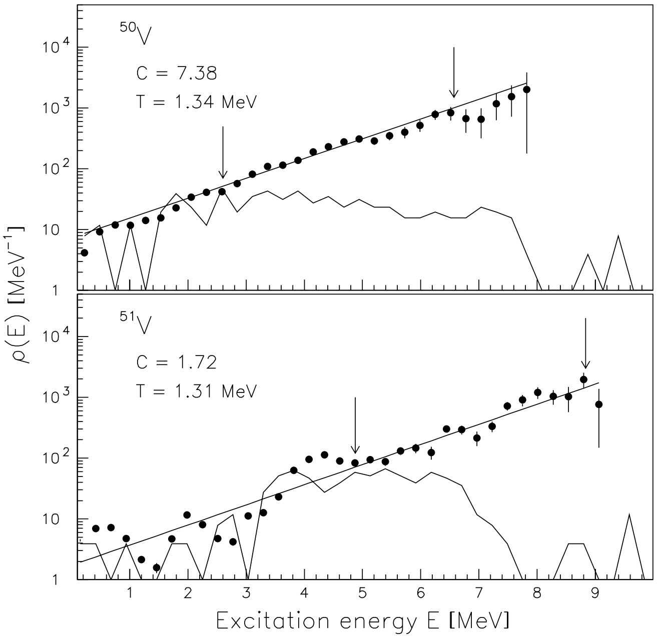

FIG. 6. Normalized level density of ^{50,51}V compared to known discrete levels (jagged line) and a constant temperature model (straight line). The fits are performed in the region between the arrows.

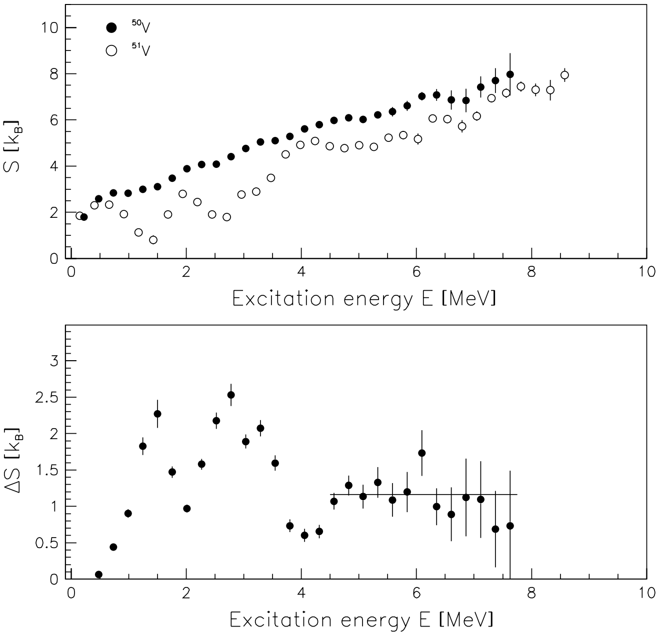

FIG. 7. Entropies of ^{50,51}V (upper panel), and entropy difference between the two vanadium isotopes (lower panel).

is not included. If the average spin of levels $\langle J\rangle$ at any excitation energy were known, this problem could be solved by multiplying an energy-dependent factor $(2\langle J(E)\rangle + 1)$ by the experimental level density. However, little experimental data exist on the spin distribution. Therefore, we choose in this work to use a multiplicity $\Omega_l(E)$ based on the experimental level density alone:

$$\Omega_l(E) \propto \rho(E). \tag{7}$$

The entropy $S(E)$ is a measure of the degree of disorder of a system at a specific energy. The microcanonical ensemble in which the system is completely isolated from any exchange with its surroundings, is often considered as the appropriate one for the atomic nucleus since the strong force has such a short range, and because the nucleus normally does not share its excitation energy with the external environment.

According to our definition of the multiplicity of levels $\Omega_l(E)$ obtained from the experimental level density, we define a "pseudo" entropy

$$S(E) = k_{\mathrm{B}} \ln \Omega_l(E), \tag{8}$$

which is utilized in the following discussion. For convenience, Boltzmann's constant k_B can be set to unity.

In order to normalize the entropy, the multiplicity is written as $\Omega_l(E) = \rho(E)/\rho_0$. The normalization denominator ρ_0 is to be adjusted such that the entropy approaches a constant value when the temperature approaches zero in order to fullfill the third law of thermodynamics: $S(T \to 0) = S_0$. In the case of even-even nuclei, the ground state represents a completely ordered system with only one possible configuration. This means that the entropy in the ground state is $S = \ln 1 = 0$, and the normalization factor $1/\rho_0$ is chosen such that this is the case. Since the vanadium nuclei have an odd number of protons, a ρ_0 which is typical for even-even nuclei in this mass region is used for both the ^{50}V and the ^{51}V nucleus. The normalization factor ρ_0 used is 0.7 MeV^{-1}, found from averaging data on ^{50}Ti and ^{52}Cr.

The entropies of ^{50,51}V extracted from the experimental level densities are shown in the upper panel of Fig. 7. Naturally, they show the same features as the level-density plot, with the odd-odd ^{50}V displaying higher entropy than the odd-even ^{51}V. Since the neutrons are almost (^{50}V) or totally (^{51}V) blocked at low excitation energy, the multiplicity and thus the entropy is made primarily by the protons in this region.

At 4 MeV of excitation energy, a relatively large increase in entropy is found in the case of ^{51}V. This is probably because the excitation energy is large enough to excite a nucleon across the $N, Z = 28$ shell gap to other orbitals.

In the excitation region above ∼4.5 MeV, the entropies show similar behavior, which is also expressed by the entropy difference ΔS displayed in the lower panel of Fig. 7. We assume here that the two systems have an approximately statistical behavior and that the neutron hole in ^{50}V acts as a spectator to the ^{51}V core. The entropy of the hole can be estimated from the entropy difference $\Delta S = S(^{50}\mathrm{V}) - S(^{51}\mathrm{V})$. From the lower panel of Fig. 7, we find $\Delta S \sim 1.2 k_B$ for $E > 4.5$ MeV. This is slightly less than the quasiparticle entropy found in rare-earth nuclei, which is estimated to be $\Delta S \sim 1.7 k_B$ [5]. This is not unexpected since the single-particle levels are more closely spaced for these nuclei; they have therefore more entropy.

The naive configurations of ^{50,51}V at low excitations are $\pi f_{7/2}^3 \nu f_{7/2}^7$ and $\pi f_{7/2}^3 \nu f_{7/2}^8$, respectively. Thus, by counting the possible configurations within the framework of the BCS model [22] in the nearly degenerate $f_{7/2}$ shell, one can estimate the multiplicity of levels and thus the entropy when no Cooper pairs are broken in the nucleus, one pair is broken, and so on. We assume a small deformation that gives four energy levels with Nilsson quantum numbers $\Omega = 1/2, 3/2, 5/2, 7/2$. Furthermore, we neglect the proton-neutron coupling and hence assume that the protons and neutrons can be considered as two separate systems; the total entropy based on the number of energy levels can then be written as $S = S_p + S_n$. This gives $S = 2.8k_B$ for the nucleus ^{50}V, and $S = 1.4k_B$ for ^{51}V when two protons are coupled in a Cooper pair. These values are in fair agreement with the data of Fig. 7 at an excitation energy below ~2 MeV. It is gratifying that these crude estimates give an entropy of the neutron hole in ^{50}V of $\Delta S = 1.4k_B$, in good agreement with the experimental value for the entropy difference of $1.2k_B$ found from Fig. 7.

With the three $f_{7/2}$ protons unpaired, we obtain a total entropy of $S = 3.5$ and $2.1k_B$ for ^{50,51}V, respectively. This means that the process of just breaking a proton pair within the same shell does not contribute much to the total entropy, but when a nucleon has enough energy to cross the shell gap a significant increase of the entropy is expected. As already mentioned, at excitation energies above ~4 MeV, it is very likely that configurations from other shells will participate in building the total entropy.

IV. RADIATIVE STRENGTH FUNCTIONS

The γ-ray transmission coefficient $\mathcal{T}$ in Eq. (1) is expressed as a sum of all the RSFs f_{XL} of electromagnetic character X and multipolarity L:

$$\mathcal{T}(E_\gamma) = 2\pi \sum_{XL} E_\gamma^{2L+1} f_{XL}(E_\gamma). \tag{9}$$

The slope of the experimental γ-ray transmission coefficient $\mathcal{T}$ has been determined through the normalization of the level densities, as described in Sec. III. The remaining constant B in Eq. (3) is determined using information from neutron resonance decay, which gives the absolute normalization of $\mathcal{T}$. For this purpose, we utilize experimental data [16] on the average total radiative width $\langle\Gamma_\gamma\rangle$ at $E = B_n$.

We assume here that the γ decay taking place in the quasicontinuum is dominated by $E1$ and $M1$ transitions and that the number of positive and negative parity states is equal. For initial spin I and parity π at $E = B_n$, the expression of the width [23] reduces to

$$\langle\Gamma_\gamma\rangle = \frac{1}{4\pi\rho(B_n, I, \pi)} \sum_{I_f} \int_0^{B_n} dE_\gamma B\mathcal{T}(E_\gamma) \times \rho(B_n - E_\gamma, I_f), \tag{10}$$

where $D_i = 1/\rho(B_n, I, \pi)$ is the average spacing of s-wave neutron resonances. The summation and integration run over all final levels with spin I_f, which are accessible by dipole ($L = 1$) γ radiation with energy E_γ. From this expression, the normalization constant B can be determined as described in Ref. [6]. However, some considerations have to be made before normalizing according to Eq. (10).

Methodical difficulties in the primary γ-ray extraction prevent determination of the function $\mathcal{T}(E_\gamma)$ in the interval $E_\gamma < 1$ MeV. In addition, the data at the highest γ energies, above $E_\gamma \sim B_n - 1$ MeV, suffer from poor statistics. We therefore extrapolate $\mathcal{T}$ with an exponential form, as demonstrated for ^{51}V in Fig. 8. The contribution of the extrapolation to the total radiative width given by Eq. (10) does not exceed 15%, thus the errors due to a possibly poor extrapolation are expected to be of minor importance [6].

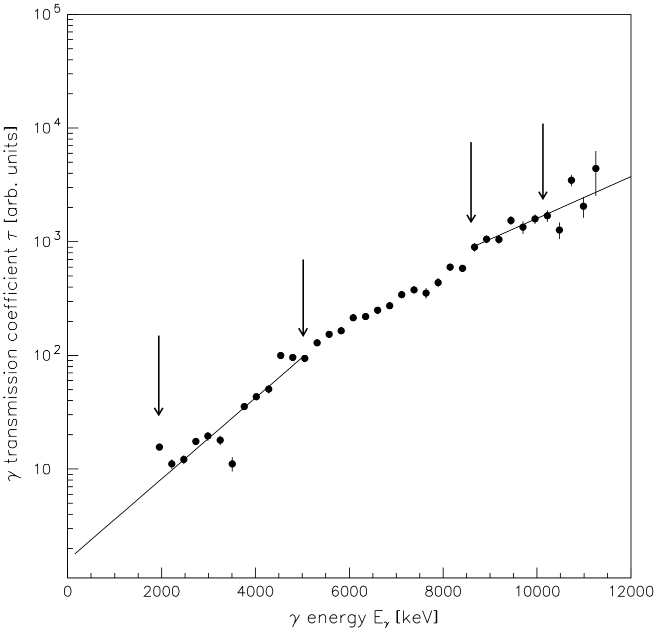

FIG. 8. Unnormalized γ-ray transmission coefficient for ^{51}V. Lines are extrapolations needed to calculate the normalization integral of Eq. (10). Arrows indicate the lower and upper fitting regions for the extrapolations.

Again, difficulties occur when normalizing the γ-ray transmission coefficient in the case of ^{50}V because of the lack of neutron resonance data. Since the average total radiative width $\langle\Gamma_\gamma\rangle$ at $E = B_n$ does not seem to show any clear systematics for nuclei in this mass region, we choose the same absolute value of the GEDR tail for ^{50}V as the one found for ^{51}V from photoabsorption experiments. The argument for this choice is that the GEDR should be similar for equal number of protons provided that the two nuclei have the same shapes.

Since it is assumed that the radiative strength is dominated by dipole transitions, the RSF can be calculated from the normalized transmission coefficient by

$$f(E_\gamma) = \frac{1}{2\pi} \frac{\mathcal{T}(E_\gamma)}{E_\gamma^3}. \tag{11}$$

We would now like to decompose the RSF into its components from different multipolarities to investigate how the $E1$ and $M1$ radiation contribute to the total strength.

The Kadmenskiĭ, Markushev, and Furman (KMF) model [13] is employed for the $E1$ strength. In this model, the Lorentzian GEDR is modified in order to reproduce the nonzero limit of the GEDR for $E_\gamma \to 0$ by means of a temperature-dependent width of the GEDR. The $E1$ strength

TABLE II. Parameters used for the radiative strength functions.

Nucleus	$E_{E1,1}$ (MeV)	$\sigma_{E1,1}$ (mb)	$\Gamma_{E1,1}$ (MeV)	$E_{E1,2}$ (MeV)	$\sigma_{E1,2}$ (mb)	$\Gamma;_{E1,2}$ (MeV)	E_{M1} (MeV)	σ_{M1} (mb)	Γ_{M1} (MeV)	$\langle\Gamma_\gamma\rangle$ (meV)	T (MeV)	κ
^{50}V	17.93	53.3	3.62	20.95	40.7	7.15	11.1	0.532	4.0	–	1.34	0.75
^{51}V	17.93	53.3	3.62	20.95	40.7	7.15	11.1	0.563	4.0	600(80)	1.31	0.74

in the KMF model is given by

$$f_{E1}(E_\gamma) = \frac{1}{3\pi^2\hbar^2c^2}\frac{0.7\sigma_{E1}\Gamma_{E1}^2\left(E_\gamma^2+4\pi^2T^2\right)}{E_{E1}\left(E_\gamma^2-E_{E1}^2\right)^2}, \quad (12)$$

where σ_{E1} is the cross section, Γ_{E1} is the width, and E_{E1} is the centroid of the GEDR determined from photoabsorption experiments.

We adopt the KMF model with temperature T taken as a constant to be consistent with our assumption that the RSF is independent of excitation energy. The possible systematic uncertainty caused by this assumption is estimated to have a maximum effect of 20% on the RSF [24]. The values used for T are the ones extracted from the constant-temperature model in Eq. (5).

The GEDR is split into two parts for deformed nuclei. Data of ^{51}V from photoabsorption experiments show that the GEDR is best fitted with two Lorentzians, indicating a splitting of the resonance and a non-zero ground-state deformation of this nucleus. Indeed, $B(E2)$ values [16] suggest a deformation of $\beta \sim 0.1$ for ^{50,51}V. Therefore, a sum of two modified Lorentzians each described by Eq. (12) is used (see Table II).

For f_{M1}, which is supposed to be governed by the spin-flip $M1$ resonance [6], the Lorentzian giant magnetic dipole resonance (GMDR)

$$f_{M1}(E_\gamma) = \frac{1}{3\pi^2\hbar^2c^2}\frac{\sigma_{M1}E_\gamma\Gamma_{M1}^2}{\left(E_\gamma^2-E_{M1}^2\right)^2+E_\gamma^2\Gamma_{M1}^2} \quad (13)$$

is adopted.

The GEDR and GMDR parameters are taken from the systematics of Ref. [16] and are listed in Table II. Thus, we fit the total RSF given by

$$f = \kappa(f_{E1,1}+f_{E1,2}+f_{M1}) \quad (14)$$

to the experimental data using the normalization constant κ as a free parameter. The value of κ generally deviates from unity because of theoretical uncertainties in the KMF model and the evaluation of the absolute normalization in Eq. (10). The resulting RSFs extracted from the two reactions are displayed in Fig. 9, where the data have been normalized with parameters from Tables I and II.

The γ-decay probability is governed by the number and character of available final states and by the RSF. A rough inspection of the experimental data of Fig. 9 indicates that the RSFs are increasing functions of γ energy, generally following the tails of the GEDR and GMDR resonances in this region.

At low γ energies ($E_\gamma \lesssim 3$ MeV), an enhancement of a factor of ~5 over the KMF estimate of the strength appears in the RSFs. This increase has also been seen in some Fe [25] and Mo [24] isotopes, where it has been shown to be present in the whole excitation-energy region. In the case of the ^{57}Fe RSF, the feature has been confirmed by an $(n, 2\gamma)$ experiment [25]. However, it has not appeared in the RSFs of the rare-earth nuclei investigated earlier by the Oslo group. The physical origin of the enhancement has not, at present, any satisfying explanation, as none of the known theoretical models can account for this behavior.

So far, we have not been able to detect any technical problems with the Oslo method. The unfolding procedure with the NaI response functions gives reliable results, as demonstrated in Fig. 1. Also, Fig. 2 indicates that the low-energy γ intensity

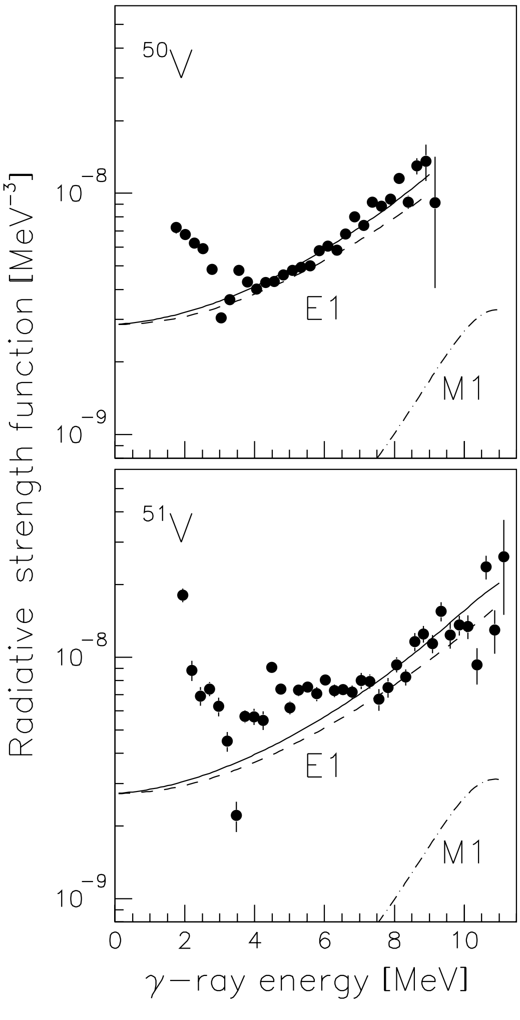

FIG. 9. Normalized RSFs of ^{50,51}V. Dashed and dash-dotted lines show the extrapolated tails of the giant electric and giant magnetic dipole resonances, respectively. Solid line is the summed strength for the giant dipole resonances.

is subtracted correctly; if not, one would find less intensity in the higher-generation spectrum at these γ energies. Figure 3 shows the final test, where the result from the least-χ^2 fit nicely reproduces the experimental data. In addition, investigations in ^{27,28}Si [26] showed that our method produced γ-transition coefficients in excellent agreement with average decay widths of known, discrete transitions. Hence, we do not believe that the enhancement is caused by some technical or methodical problems. Still, independent confirmation of the increasing RSF from, e.g., $(n, 2\gamma)$ experiments on the V and Mo isotopes, is highly desirable.

V. SUMMARY AND CONCLUSIONS

The Oslo method has been applied to extract level densities and RSFs of the vanadium isotopes ^{50,51}V. From the measured level densities, microcanonical entropies have been derived. The entropy carried by the neutron hole in ^{50}V is estimated to be $\sim 1.2\ k_B$, which is less than the quasiparticle entropy of $\sim 1.7\ k_B$ found in rare-earth nuclei.

The experimental RSFs are generally increasing functions of γ energy. The main contribution to the RSFs is the GEDR; also the GMDR is present. At low γ energies, an increase in the strength functions is apparent. A similar enhancement has also been seen in iron and molybdenum isotopes. There is still no explanation for the physics behind this very interesting behavior.

ACKNOWLEDGMENTS

A.V. acknowledges support from a NATO Science Fellowship under Project Number 150027/432 given by the Norwegian-Research Council (NFR) and from the Stewardship Science Academic Alliances, Grant Number DE-FG03-03-NA0074. Financial support from the NFR is gratefully acknowledged.

---

[1] L. Henden, L. Bergholt, M. Guttormsen, J. Rekstad, and T. S. Tveter, Nucl. Phys. **A589**, 249 (1995).

[2] A. Schiller, L. Bergholt, M. Guttormsen, E. Melby, J. Rekstad, and S. Siem, Nucl. Instrum. Methods Phys. Res. A **447**, 498 (2000).

[3] E. Melby, L. Bergholt, M. Guttormsen, M. Hjorth-Jensen, F. Ingebretsen, S. Messelt, J. Rekstad, A. Schiller, S. Siem, and S. W. Ødegård, Phys. Rev. Lett. **83**, 3150 (1999).

[4] A. Schiller, A. Bjerve, M. Guttormsen, M. Hjorth-Jensen, F. Ingebretsen, E. Melby, S. Messelt, J. Rekstad, S. Siem, and S. W. Ødegård, Phys. Rev. C **63**, 021306(R) (2001).

[5] M. Guttormsen, M. Hjorth-Jensen, E. Melby, J. Rekstad, A. Schiller, and S. Siem, Phys. Rev. C **63**, 044301 (2001).

[6] A. Voinov, M. Guttormsen, E. Melby, J. Rekstad, A. Schiller, and S. Siem, Phys. Rev. C **63**, 044313 (2001).

[7] S. Siem, M. Guttormsen, K. Ingeberg, E. Melby, J. Rekstad, A. Schiller, and A. Voinov, Phys. Rev. C **65**, 044318 (2002).

[8] M. Guttormsen, A. Atac, G. Løvhøiden, S. Messelt, T. Ramsøy, J. Rekstad, T. F. Thorsteinsen, T. S. Tveter, and Z. Zelazny, Phys. Script. T **32**, 54 (1990).

[9] M. Guttormsen, T. S. Tveter, L. Bergholt, F. Ingebretsen, and J. Rekstad, Nucl. Instrum. Methods Phys. Res. A **374**, 371 (1996).

[10] M. Guttormsen, T. Ramsøy, and J. Rekstad, Nucl. Instrum. Methods Phys. Res. A **255**, 518 (1987).

[11] D. M. Brink, Ph.D. thesis, Oxford University, 1955.

[12] P. Axel, Phys. Rev. **126**, 671 (1962).

[13] S. G. Kadmenskiĭ, V. P. Markushev, and V. I. Furman, Yad. Fiz. **37**, 277 (1983) [Sov. J. Nucl. Phys. **37**, 165 (1983)].

[14] G. Gervais, M. Thoennessen, and W. E. Ormand, Phys. Rev. C **58**, R1377 (1998).

[15] Data extracted using the NNDC On-Line Data Service from the ENSDF database, www.nndc.bnl.gov/ensdf.

[16] Data extracted using the Reference Input Parameter Library, http://www-nds.iaea.org/RIPL-2/

[17] A. Gilbert and A. G. W. Cameron, Can. J. Phys. **43**, 1446 (1965).

[18] T. von Egidy, H. H. Schmidt, and A. N. Behkami, Nucl. Phys. **A481**, 189 (1988).

[19] G. Audi and A. H. Wapstra, Nucl. Phys. **A595**, 409 (1995).

[20] A. Bohr and B. Mottelson, *Nuclear Structure* (Benjamin, New York, 1969), Vol. I, p. 169.

[21] R. Firestone and V. S. Shirley, *Table of Isotopes*, 8th ed. (Wiley, New York, 1996), Vol. II.

[22] J. Bardeen, L. N. Cooper, and J. R. Schrieffer, Phys. Rev. **108**, 1175 (1957).

[23] J. Kopecky and M. Uhl, Phys. Rev. C **41**, 1941 (1990).

[24] M. Guttormsen, R. Chankova, U. Agvaanluvsan, E. Algin, L. A. Bernstein, F. Ingebretsen, T. Lönnroth, S. Messelt, G. E. Mitchell, J. Rekstad, A. Schiller, S. Siem, A. C. Sunde, A. Voinov, and S. Ødegård, Phys. Rev. C **71**, 044307 (2005).

[25] A. Voinov, E. Algin, U. Agvaanluvsan, T. Belgya, R. Chankova, M. Guttormsen, G. E. Mitchell, J. Rekstad, A. Schiller, and S. Siem, Phys. Rev. Lett. **93**, 142504 (2004).

[26] M. Guttormsen, E. Melby, J. Rekstad, A. Schiller, S. Siem, T. Lönnroth, and A. Voinov, J. Phys. G **29**, 263 (2003).

5.5 Paper 4: Nuclear level densities and γ-ray strength functions in ^{44,45}Sc

PHYSICAL REVIEW C **76**, 044303 (2007)

Nuclear level densities and γ-ray strength functions in ^{44,45}Sc

A. C. Larsen,[1,*] M. Guttormsen,[1] R. Chankova,[2] F. Ingebretsen,[1] T. Lönnroth,[3] S. Messelt,[1] J. Rekstad,[1]
A. Schiller,[4] S. Siem,[1] N. U. H. Syed,[1] and A. Voinov[5]
[1]*Department of Physics, University of Oslo, P. O. Box 1048 Blindern, N-0316 Oslo, Norway*
[2]*North Carolina State University, Raleigh, North Carolina 27695, USA and*
Triangle Universities Nuclear Laboratory, Durham, North Carolina 27708, USA
[3]*Department of Physics, Åbo Akademi University, FIN-20500 Åbo, Finland*
[4]*National Superconducting Cyclotron Laboratory, Michigan State University, East Lansing, Michigan 48824, USA*
[5]*Department of Physics and Astronomy, Ohio University, Athens, Ohio 45701, USA and Frank Laboratory of Neutron Physics,*
Joint Institute for Nuclear Research, RU-141980 Dubna, Moscow region, Russia
(Received 29 May 2007; published 4 October 2007)

The scandium isotopes ^{44,45}Sc were studied with the ^{45}Sc(^{3}He, $\alpha\gamma$)^{44}Sc and ^{45}Sc(^{3}He, ^{3}He$'\gamma$)^{45}Sc reactions, respectively. The nuclear level densities and γ-ray strength functions have been extracted using the Oslo method. The experimental level densities are compared to calculated level densities obtained from a microscopic model based on BCS quasiparticles within the Nilsson level scheme. This model also gives information about the parity distribution and the number of broken Cooper pairs as a function of excitation energy. The experimental γ-ray strength functions are compared to theoretical models of the $E1$, $M1$, and $E2$ strength and to data from (γ, n) and (γ, p) experiments. The strength functions show an enhancement at low γ energies that cannot be explained by the present standard models.

DOI: 10.1103/PhysRevC.76.044303 PACS number(s): 21.10.Ma, 24.10.Pa, 25.55.Hp, 27.40.+z

I. INTRODUCTION

The energy levels of an atomic nucleus and the decay probability of each level contain essential information on the nuclear structure. When the nucleus is excited to levels just above the ground state, spectroscopic measurements are able to give accurate information on the energy, spin, parity, and transition rates of the levels. However, as the excitation energy increases, the number of levels quickly becomes so high that all levels cannot be found with present state-of-the art spectroscopy methods. The nucleus leaves the discrete region and enters the region of quasicontinuum and continuum, where it is regarded as more appropriate to use average quantities to describe the behavior of the nucleus.

The nuclear level density and the γ-ray strength function give a measure of the gross properties of the nucleus. These average quantities are indispensable in practical applications of nuclear physics, such as calculations of nuclear reaction rates in astrophysical processes, the design and operation of fission reactors, and transmutation of nuclear waste. When it comes to fundamental nuclear structure, the level density can reveal information on, e.g., pair correlations and thermodynamic quantities such as entropy and temperature [1,2], whereas the average electromagnetic properties are characterized by the γ-ray strength function [3].

Neutron (and proton) resonance experiments provide data on the level density at or above the nucleon binding energy [4], and fluctuation analysis of total neutron cross sections [5] gives level density at excitation energies well above the nucleon binding energy. However, in the intermediate region between the nucleon binding energy and the discrete regime (the quasicontinuum) relatively little is known. To fill in this gap, the Oslo Cyclotron group has developed the so-called Oslo method, which enables the extraction of both level density and γ-ray strength function from the distribution of primary γ rays at various initial excitation energies. The method has been thoroughly tested on nuclei in the rare-earth region [6–8] and has also been successfully extended to other mass regions [9–12].

The present work reports on new results from an experiment on the scandium isotopes ^{44,45}Sc. The ^{45}Sc nucleus has one unpaired proton in the $\pi f_{7/2}$ orbital, whereas ^{44}Sc has an unpaired proton and a neutron in the $\pi f_{7/2}$, $\nu f_{7/2}$ orbitals. If one naively assumes that only the $f_{7/2}$ orbital is dominant in the model space, one would expect a majority of positive-parity states in the case of ^{44}Sc and negative-parity states for ^{45}Sc. However, it is well known that states with different parity appear already at very low excitation energy in these nuclei. Early attempts on reproducing the states both with particle-plus-rotor models [13] and shell-model calculations [14] had relatively little success. More recent works have shown that these nuclei exhibit both collective and single-particle character even at low excitation energy, and they have been considered as a good case for studying the interplay between the single-particle and the collective degrees of freedom in medium-mass nuclei near the closed shell [15,16]. These scandium isotopes are therefore of special interest to test the Oslo method further.

In Sec. II an outline of the experimental procedure and the Oslo method is given. The level densities and the γ-ray strength functions are discussed in Secs. III and IV, respectively. Finally, concluding remarks are given in Sec. V.

---

[*] a.c.larsen@fys.uio.no

II. EXPERIMENTAL DETAILS AND THE OSLO METHOD

The experiment was performed at the Oslo Cyclotron Laboratory (OCL) using a beam of ^{3}He ions with energy 38 MeV. The self-supporting natural target of 99.9% ^{45}Sc had a thickness of 3.4 mg/cm^2. Eight Si ΔE-E telescopes were arranged close to the target at an angle of 45° relative to the beam. The γ-detector array CACTUS [17], consisting of 28 collimated NaI crystals with a total efficiency of $\sim$15%, surrounded the target and the particle detectors. The experimental setup enabled particle-γ coincidence measurements of the reactions (^{3}He, $\alpha\gamma$) and (^{3}He, ^{3}He$'\gamma$). These reactions populate states with spin range $I \sim 2$–$6\hbar$, which means that most of the energy transferred to the target nucleus is intrinsic excitation energy. The experiment ran for about 5 days, with a typical beam current of $\sim$1 nA.

The recorded coincidences were sorted into two-dimensional particle-γ matrices. From the reaction kinematics, the measured energy of the outgoing ^{3}He or α particle were converted into excitation energy of the residual nucleus. With particle-energy bins of 240 keV/channel, total γ-ray spectra were obtained for each bin. These γ spectra were then unfolded using a well-tested unfolding procedure based on the known response functions of the CACTUS array [18]. The unfolding method described in Ref. [18] preserves the fluctuations in the original spectra without introducing further, spurious fluctuations. In Fig. 1 an original γ spectrum, an unfolded spectrum, and the unfolded spectrum convoluted with the response functions are shown for ^{44}Sc with gate on the excitation-energy bins between 5.5 and 6.5 MeV. The original and the convoluted spectrum show excellent agreement, giving strong confidence in the unfolding method. The unfolded particle-γ matrix of the ^{45}Sc(^{3}He, $\alpha\gamma$)^{44}Sc data is displayed in Fig. 2, where the sharp diagonal $E = E_\gamma$ is clearly seen. Apart from the prominent peak at $E \sim 1$ MeV and $E_\gamma \sim 0.75$ MeV, the matrix is without outstanding structures.

The energy distribution of the first emitted γ rays from the decay cascades reveals essential information on the nuclear structure. To extract these primary γ rays from the total γ spectra, a subtraction procedure described in Ref. [19] is applied for each excitation-energy bin. The main assumption of this method is that the γ decay from any excitation-energy bin is independent on how the nucleus was excited to this bin. In other words, the decay routes are the same whether they were initiated directly by the nuclear reaction or by γ decay from higher-lying states. This assumption is automatically fulfilled when the same states are equally populated by the two processes, because γ branching ratios are properties of the levels themselves. Even if different states are populated, the assumption is still valid for statistical γ decay, which depends only on the γ-ray energy and the number of accessible final states. Figure 3 shows the total, unfolded γ spectrum, the second and higher generations γ spectrum and the first-generation spectrum of ^{45}Sc for excitation energy between $E = 5.5$ and 6.5 MeV. The first-generation spectrum is obtained by subtracting the higher-generation γ rays from the total γ spectrum. By looking at the lower panel of Fig. 3, it is clear that the main assumption of the subtraction method is

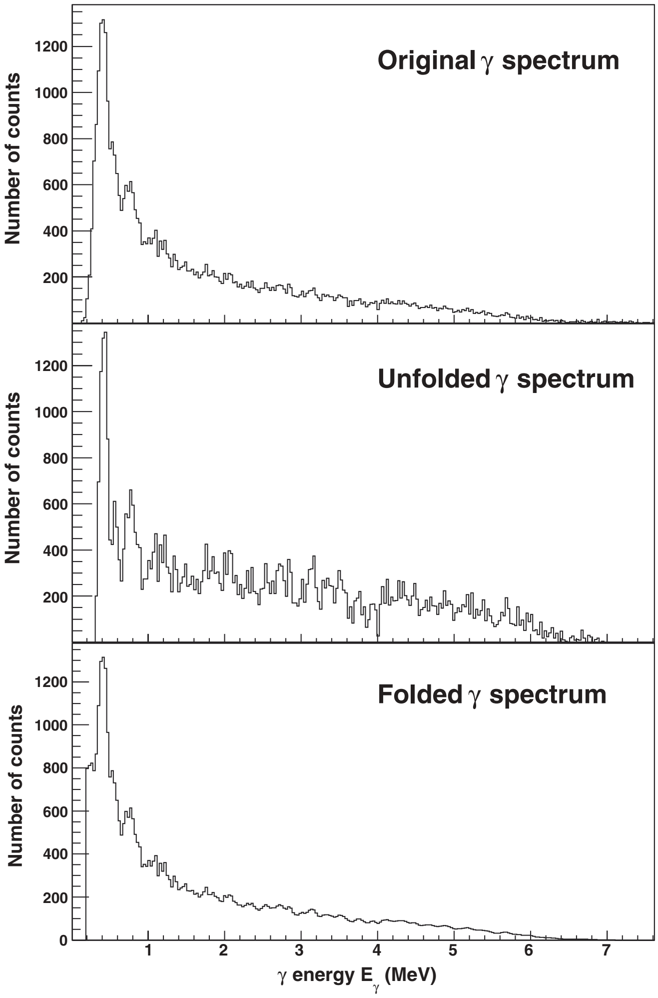

FIG. 1. Original (top), unfolded (middle) and folded γ spectrum of ^{44}Sc for excitation energy between 5.5 and 6.5 MeV.

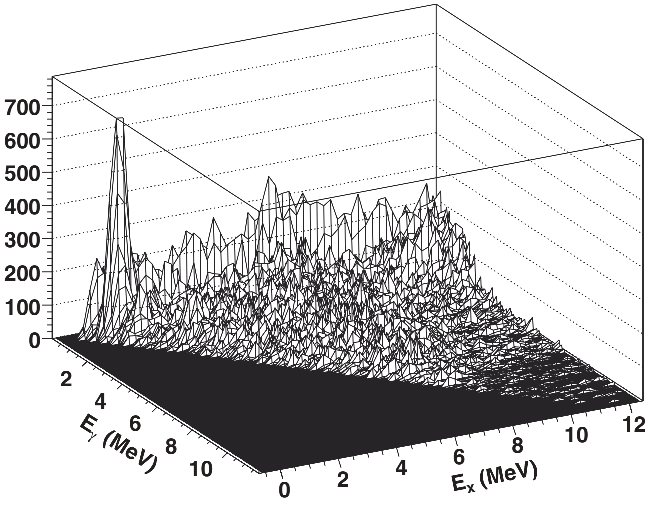

FIG. 2. Unfolded particle-γ matrix for the ^{45}Sc(^{3}He, α)^{44}Sc reaction.

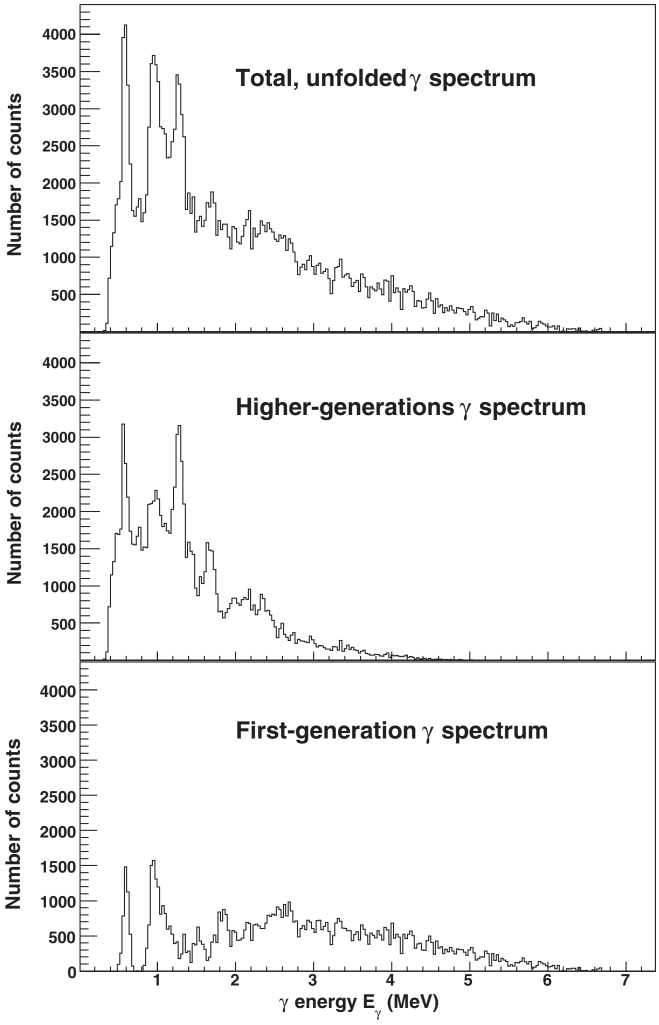

FIG. 3. Unfolded, total γ spectrum, second and higher-generation γ spectrum and first-generation γ spectrum of ^{45}Sc for excitation energy between 5.5 and 6.5 MeV.

not fulfilled for $E_\gamma \lesssim 1.4$ MeV. In this region, some strong, low-energy transitions were not subtracted correctly. This means that the levels from which these transitions originate are populated more strongly from higher excited levels through γ emission than directly by inelastic ^{3}He scattering. Therefore, only data for $E_\gamma > 1.6$ MeV are used in the further analysis. Similar considerations were done for ^{44}Sc.

The experimental matrix of first-generation γ rays is then normalized [20] such that for every excitation-energy bin E, the sum over all γ energies E_γ from some minimum value $E_\gamma^{\min}$ to the maximum value $E_\gamma^{\max} = E$ at this excitation-energy bin is unity:

$$\sum_{E_\gamma=E_\gamma^{\min}}^{E} P(E, E_\gamma) = 1. \tag{1}$$

For statistical γ decay in the continuum region, the γ-decay probability from an excitation energy E to $E_f = E - E_\gamma$ is proportional to the γ-ray transmission coefficient $\mathcal{T}(E_\gamma)$ and the level density at the final excitation energy $\rho(E_f)$:

$$P(E, E_\gamma) \propto \rho(E - E_\gamma)\mathcal{T}(E_\gamma). \tag{2}$$

The essential assumption underlying the above relation is that the reaction can be described as a two-stage process, where a compound state is first formed, before it decays in a manner that is independent of the mode of formation [21,22]. Equation (2) could also be regarded as a generalization[1] of Fermi's golden rule, where the decay rate is proportional to the density of final states and the square of the matrix element between the initial state and the final state.

The experimental normalized first-generation γ matrix can theoretically be approximated by

$$P_{\text{th}}(E, E_\gamma) = \frac{\rho(E - E_\gamma)\mathcal{T}(E_\gamma)}{\sum_{E_\gamma=E_\gamma^{\min}}^{E} \rho(E - E_\gamma)\mathcal{T}(E_\gamma)}. \tag{3}$$

The γ-ray transmission coefficient $\mathcal{T}$ is independent of excitation energy according to the generalized Brink-Axel hypothesis [23,24], which states that collective excitation modes built on excited states have the same properties as those built on the ground state. There is evidence that the width of the giant dipole resonance (GDR) varies with the nuclear temperature of the state on which it is built [25,26]. However, the temperature corresponding to the excitation-energy range covered in this work is rather low and changes slowly with excitation energy ($T \sim \sqrt{E_f}$). The temperature is therefore assumed to be approximately constant, and the Brink-Axel hypothesis is recovered in the energy region of interest.

To extract the level density and the γ-ray transmission coefficient, an iterative procedure [20] is applied to the first-generation γ matrix $P(E, E_\gamma)$. The basic idea of this method is to minimize

$$\chi^2 = \frac{1}{N_{\text{free}}} \sum_{E=E^{\min}}^{E^{\max}} \sum_{E_\gamma=E_\gamma^{\min}}^{E} \left[\frac{P_{\text{th}}(E, E_\gamma) - P(E, E_\gamma)}{\Delta P(E, E_\gamma)} \right]^2, \tag{4}$$

where N_{free} is the number of degrees of freedom and $\Delta P(E, E_\gamma)$ is the uncertainty in the experimental first-generation γ matrix. Every point of the ρ and $\mathcal{T}$ functions is assumed as an independent variable, so the reduced χ^2 is minimized for every argument $E - E_\gamma$ and E. The quality of the procedure when applied to the ^{44}Sc data is shown in Fig. 4, where the experimental first-generation spectra for various initial excitation energies are compared to the least-χ^2 solution. In general, the agreement between the experimental data and the fit is very good.

The globalized fitting to the data points only gives the functional form of ρ and $\mathcal{T}$. In fact, it has been shown [20] that if one solution for the multiplicative functions ρ and $\mathcal{T}$ is known, one may construct an infinite number of other

---

[1] A generalization in the sense that the present work deals with an ensemble of initial and final states and therefore considers the average decay properties in each excitation-energy bin.

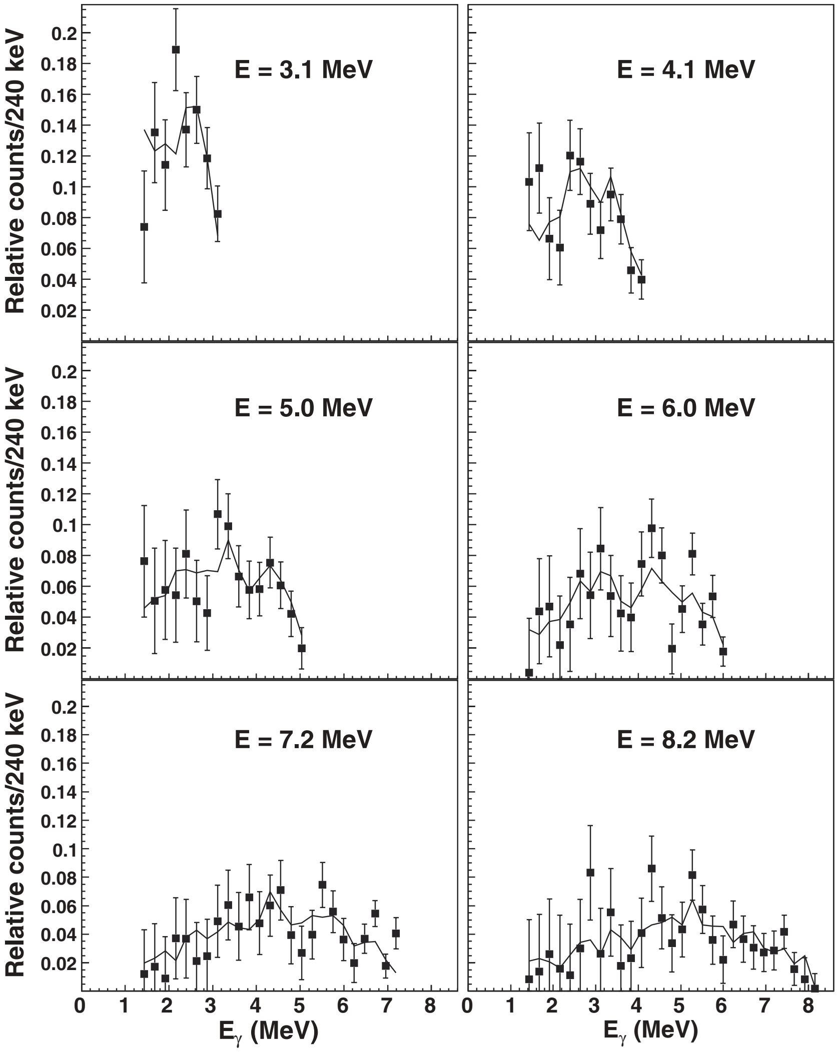

FIG. 4. A sample of the experimental first-generation spectra of ^{44}Sc (data points with error bars) are plotted with the least-χ^2 fit (lines).

functions, which give identical fits to the $P(E, E_\gamma)$ matrix by

$$\tilde{\rho}(E - E_\gamma) = A \exp[\alpha(E - E_\gamma)]\, \rho(E - E_\gamma), \tag{5}$$

$$\tilde{\mathcal{T}}(E_\gamma) = B \exp(\alpha E_\gamma)\mathcal{T}(E_\gamma). \tag{6}$$

Therefore the transformation parameters α, A, and B, which correspond to the physical solution, remain to be found.

III. THE LEVEL DENSITIES

A. Normalization

As described in the previous section, only the shape of the level density is found through the least χ^2 procedure of Ref. [20]. To determine the slope α and the absolute value A in Eq. (5), the ρ function is adjusted to match the number of known discrete levels at low excitation energy [27] and proton-resonance data [28,29] at high excitation energy. The procedure for extracting the total level density ρ from the resonance spacing D is described in Ref. [20]. Because the proton beam energy had a range of $E_p(^{44}\mathrm{Sc})$ = 0.90–1.50 MeV and $E_p(^{45}\mathrm{Sc})$ = 2.50–3.53 MeV in Refs. [28,29], respectively, the level density estimated from the proton resonances is not at the proton binding energy B_p, but rather at approximately $B_p + (\Delta E)/2$, where ΔE is the energy range of the proton beam, assuming that the resonances are approximately equally distributed over ΔE. Also, the authors of Ref. [28] do not distinguish between s- and p-wave resonances, so the calculation of the total level density is rather uncertain in the case of ^{44}Sc. However, by comparing with preliminary level-density data from an experiment done on ^{44}Sc at Ohio University, the slope α seems to be correct [30].

Because our experimental data points of the level density only reach up to an excitation energy of ~7.2 and ~8.0 MeV for ^{44,45}Sc, respectively, we extrapolate with the back-shifted Fermi gas model [31,32]

$$\rho_{\mathrm{BS}}(E) = \eta \frac{\exp(2\sqrt{aU})}{12\sqrt{2}a^{1/4}U^{5/4}\sigma}, \tag{7}$$

where a constant η is introduced to ensure that ρ_{BS} has the same value as the level density calculated from the proton-resonance experiments. The intrinsic excitation energy is estimated by $U = E - E_1$, where E_1 is the back-shift parameter.

TABLE I. Parameters used for the back-shifted Fermi gas level density and the parameters from Ref. [32].

Nucleus	E_1 (MeV)	a (MeV^{-1})	σ	E_1^{a} (MeV)	a^{a} (MeV^{-1})	σ^{a}	B_p (MeV)	$B_p + (\Delta E)/2$ (MeV)	D^{b} (eV)	ρ (proton res.) (MeV^{-1})	η
^{44}Sc	−2.91	5.13	3.53	−2.06	5.68	3.37	6.696	7.896	3243(324)	1855(392)	1.12
^{45}Sc	−2.55	4.94	3.75	−0.61	6.07	3.41	6.889	9.904	7874(496)	3701(760)	1.26

[a] Calculated with the method of Ref. [32].

[b] Calculated from proton-resonance data.

The spin-cutoff parameter is given by[2]

$$\sigma^2 = 0.0146A^{5/3}\frac{1+\sqrt{1+4aU}}{2a}, \tag{8}$$

where A is the mass number. Because the level-density parameter a and the back-shift parameter E_1 calculated with the method of Ref. [32] did not seem to give reliable results for ^{45}Sc, these parameters were extracted by fitting the Fermi gas to the known levels at $\sim$1.75 MeV and $\sim$2 MeV for ^{44,45}Sc, respectively, and to the known resonance-spacing data at $B_p + (\Delta E)/2$. The parameters used for ^{44,45}Sc in Eq. (7) are listed in Table I, where also the Fermi-gas parameters from Ref. [32] are shown. As the authors demonstrate in Fig. 5 in Ref. [32], the difference between the calculated parameters and the empirically extracted ones might be large in the mass region $A \leqslant 50$. The normalization procedure is pictured in Fig. 5; note that only statistical errors are shown. Above $\sim$2 MeV, there are more than 30 levels per MeV, giving the present limit to make complete spectroscopy in these nuclei.

The normalized level densities of ^{44}Sc and ^{45}Sc are displayed in Fig. 6. As one would expect, the odd-odd nucleus ^{44}Sc has an overall higher level density than its odd-even neighbor ^{45}Sc due to its two unpaired nucleons. The difference in level density between the odd-odd (^{44}Sc) and the odd-even (^{45}Sc) nucleus is seen to be approximately constant, except in the area between $E \sim$ 4–5 MeV, where the level densities are almost the same. This is in agreement with earlier findings in the rare-earth region. However, here the odd-odd system has approximately a factor of 2 higher level density compared to the odd-even nucleus, whereas for rare-earth nuclei the difference was found to be a factor of 5.

Bump structures in the level densities of the scandium nuclei are observed. Standard models such as the back-shifted Fermi gas give a smooth ρ function and are unable to describe the structures that appear in the experimental level density in this excitation-energy region.

B. Comparison with microscopic model

To further investigate the level density at high excitation energy, a microscopic model has been developed. The model is based on combining all possible proton and neutron configurations within the Nilsson energy scheme, and the concept of Bardeen-Cooper-Schrieffer (BCS) quasiparticles [33] is utilized.

The model is described within the microcanonical ensemble, where the excitation energy E is well defined. The single-particle energies e_{sp} are taken from the Nilsson model for an axially deformed core described by the quadrupole deformation parameter ϵ_2. Furthermore, the model depends on the spin-orbit and centrifugal parameters κ and μ. The oscillator quantum energy $\hbar\omega_0 = 41A^{-1/3}$ MeV between the harmonic oscillator shells is also input to the code. Within the BCS model, the single-quasiparticle energies are defined by

$$e_{\text{qp}} = \sqrt{(e_{\text{sp}} - \lambda)^2 + \Delta^2}, \tag{9}$$

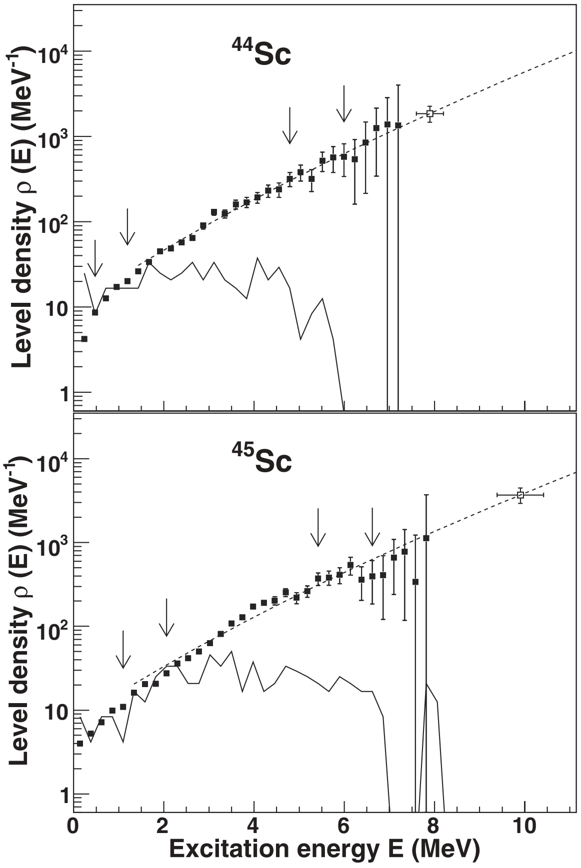

FIG. 5. Normalization procedure of the experimental level density (data points) of ^{44,45}Sc. The data points between the arrows are normalized to known levels at low excitation energy (solid line) and to the level density at the proton-separation energy (open square) using the Fermi-gas level density (dashed line).

---

[2] The authors of Ref. [32] found this expression to be the most adequate in the low-energy region, even though it is connected to the (mathematically incorrect) relation $U = aT^2 - T$ and not the standard one $U = aT^2$ (see Ref. [31] for more details).

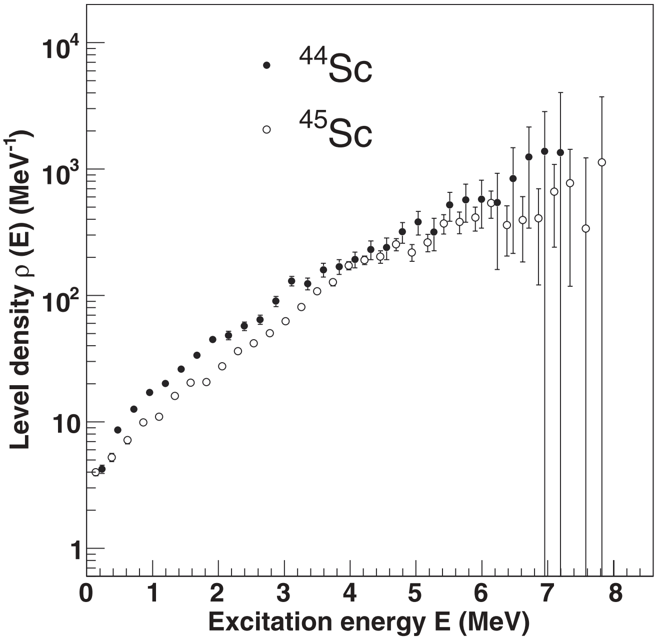

FIG. 6. Normalized level densities for ^{44,45}Sc.

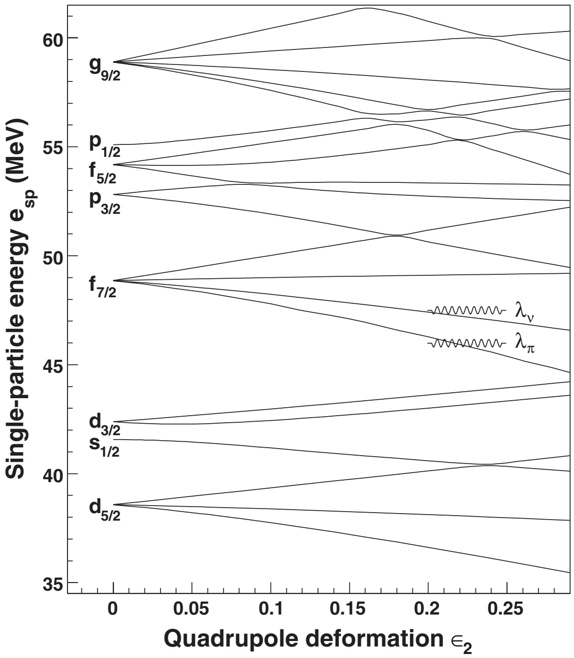

FIG. 7. The Nilsson level scheme for ^{45}Sc with parameters $\kappa = 0.066$ and $\mu = 0.32$.

where the Fermi level λ is adjusted to reproduce the number of particles in the system and Δ is the pair-gap parameter, which is kept constant.

The double-degenerated proton and neutron quasiparticle orbitals are characterized by their spin projections on the symmetry axis Ω_π and Ω_ν, respectively. The energy due to quasiparticle excitations is given by

$$E_{\mathrm{qp}}(\Omega_\pi, \Omega_\nu) = \sum_{\{\Omega'_\pi \Omega'_\nu\}} [e_{\mathrm{qp}}(\Omega'_\pi) + e_{\mathrm{qp}}(\Omega'_\nu) + V(\Omega'_\pi, \Omega'_\nu)]. \tag{10}$$

Between the aligned and antialigned levels of the proton and neutron projections, i.e., $\Omega_\pi + \Omega_\nu$ and $|\Omega_\pi - \Omega_\nu|$, a residual interaction V is defined as a random Gaussian distribution centered at zero energy with a width of 50 keV. The sets of proton and neutron orbitals $\{\Omega'_\pi \Omega'_\nu\}$ are picked out by using a random generator. The total number of broken Cooper pairs are set to 3, making a maximum number of 8 participating quasiparticles for odd-odd nuclear systems. Technically, this process is repeated until all possible energies $E_{\mathrm{qp}}(\Omega_\pi, \Omega_\nu)$ have been obtained. An indicator that this saturation is reached, is that all energies are reproduced at least ten times in the simulation.

Collective energy terms are schematically added by

$$E = E_{\mathrm{qp}}(\Omega_\pi, \Omega_\nu) + A_{\mathrm{rot}} R(R+1) + \hbar\omega_{\mathrm{vib}}\nu, \tag{11}$$

where $A_{\mathrm{rot}} = \hbar^2/2\mathcal{J}$ is the rotational parameter and $R = 0, 1, 2, 3 \ldots$ is the rotational quantum number. The vibrational motion is described by the phonon number $\nu = 0, 1, 2, \ldots$ and the oscillator quantum energy $\hbar\omega_{\mathrm{vib}}$.

The advantage of the present model is a fast algorithm that may include a large model space of single-particle states. Because level density is a gross property, the detailed knowledge of the many-particle matrix elements through large diagonalizing algorithms is not necessary. No level inversion is observed, as frequently seen for microscopic models with single-particle orbital truncations. In the sum of Eq. (10), all orbitals with energy up to the maximum energy ($e_{\mathrm{qp}} < E$) are included. Typically, for excitation energies up to ∼10 MeV, about 20 proton and 20 neutron orbitals are taken into account (∼10 orbitals below the Fermi level and ∼10 orbitals above).

In the calculation we adopted the Nilsson parameters $\kappa = 0.066$ and $\mu = 0.32$ from Ref. [34] with oscillator quantum energy of $\hbar\omega_{\mathrm{vib}} = 1.904$ MeV, found from the 0^+ vibrational state in ^{44}Ti [35]. The Nilsson levels used in the calculations for ^{45}Sc are shown in Fig. 7, with the Fermi levels for the protons and neutrons. The value of the deformation parameter ϵ_2 was set to 0.23, which is in agreement with values suggested in Ref. [15]. The rotational and vibrational terms contribute only significantly to the total level density in the lower excitation region. To reproduce the transition energy from the $11/2^- \to 7/2^-$ transition in the ground-state rotational band of ^{45}Sc [35], the rotational parameter A_{rot} was set to 0.135 MeV. The adopted pairing gap parameters Δ_π and Δ_ν are taken from the calculations of Dobaczewski *et al.* [36] for the even-even ^{42}Ca for ^{44}Sc and ^{44}Ca for ^{45}Sc. A list of the input data for the model calculations can be found in Table II.

The experimental and calculated level densities are shown in Fig. 8. The result is satisfactory, especially for the nucleus

TABLE II. Model parameters.

Nucleus	ϵ_2	Δ_π (MeV)	Δ_ν (MeV)	A_{rot} (MeV)	$\hbar\omega_0$ (MeV)	$\hbar\omega_{\mathrm{vib}}$ (MeV)	λ_π (MeV)	λ_ν (MeV)
^{44}Sc	0.23	1.234	1.559	0.135	11.61	1.904	45.96	47.47
^{45}Sc	0.23	1.353	1.599	0.135	11.53	1.904	45.60	47.91

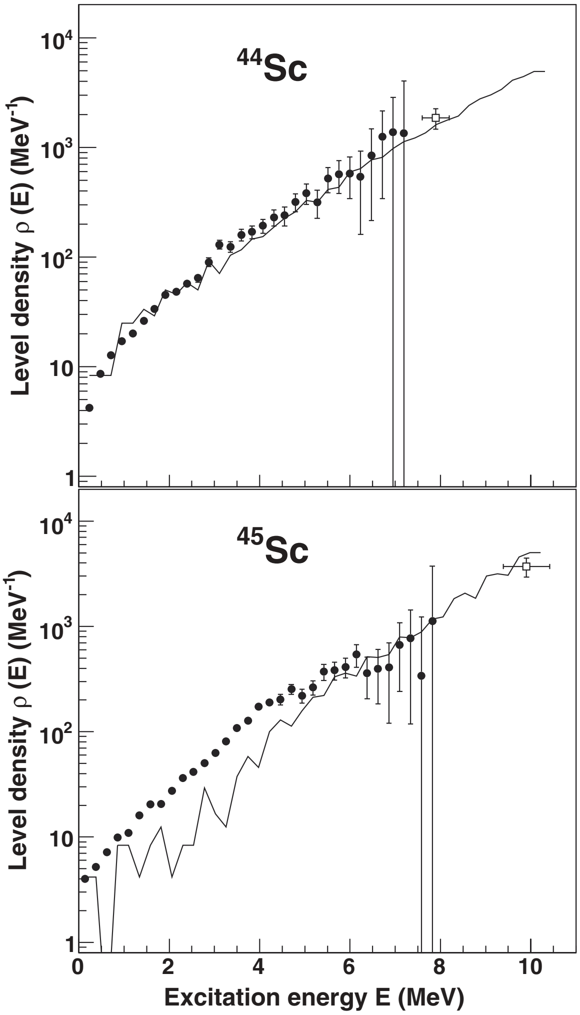

FIG. 8. Calculated level densities (solid lines) compared with the experimental ones (data points with error bars) for ^{44,45}Sc.

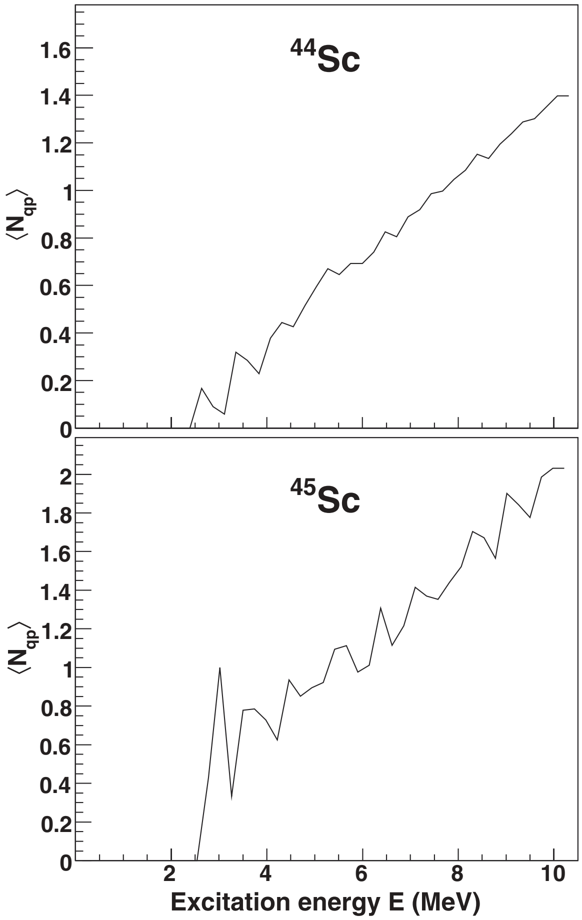

FIG. 9. The average number of broken Cooper pairs as function of excitation energy for ^{44,45}Sc.

^{44}Sc where there is a good agreement between the model calculation and the experimental level density. The general decrease in level density for the odd-even system compared to the odd-odd nucleus as well as the level densities found from the proton-resonance experiments are well reproduced. However, it is seen that the model misses many low-lying levels in the excitation-energy region $E = 1$–5 MeV for ^{45}Sc. This can, at least partially, be explained by the well-established shape coexistence determined from the negative-parity and positive-parity bands in this nucleus [15]. Only one shape is included in our model, and thus only one potential, which results in an undershoot of bandheads of about a factor of 2.

The pairing parameters Δ_π and Δ_ν are important inputs of the model, because the slope of the level density (in log scale) increases with decreasing pairing parameters in the energy region considered here. It can be seen from Fig. 8 that the adopted values give a nice agreement of the log slope of the level densities for both isotopes.

Figure 9 shows the average number of broken Cooper pairs $\langle N_{\mathrm{qp}}\rangle$ as a function of excitation energy. This is calculated by looking at all configurations obtained in each 240-keV excitation-energy bin, and finding the number of configurations with one broken pair, two broken pairs and so on. Both neutron and proton pairs are taken into account. From this information the average number of broken Cooper pairs is calculated. From Fig. 9, the pair-breaking process is seen to start at $E \sim 2.5$ MeV for both nuclei, in accordance with the values used for Δ_π (see Table II). The average number of broken pairs seems to have a relatively linear increase, giving an exponential growth in the level density. This behavior also indicates that there is no abrupt change in seniority as a function of excitation energy. For example, in the region $E = 9$–10 MeV, the model predicts 1% states with no pairs broken, 34% states with one broken pair, 61% states with two broken pairs, and 4% of the states have three pairs broken.

The location of the proton and neutron Fermi levels of ^{44,45}Sc in the Nilsson level scheme gives, roughly speaking, mostly positive-parity orbitals below and negative-parity states above the Fermi levels. Knowing this, one would expect a relatively homogeneous mixture of positive and negative parity states in the whole excitation-energy region covered by the calculations. In order to investigate this feature, we utilize the parity asymmetry defined in Ref. [37] by

$$\alpha = \frac{\rho_+ - \rho_-}{\rho_+ + \rho_-}, \tag{12}$$

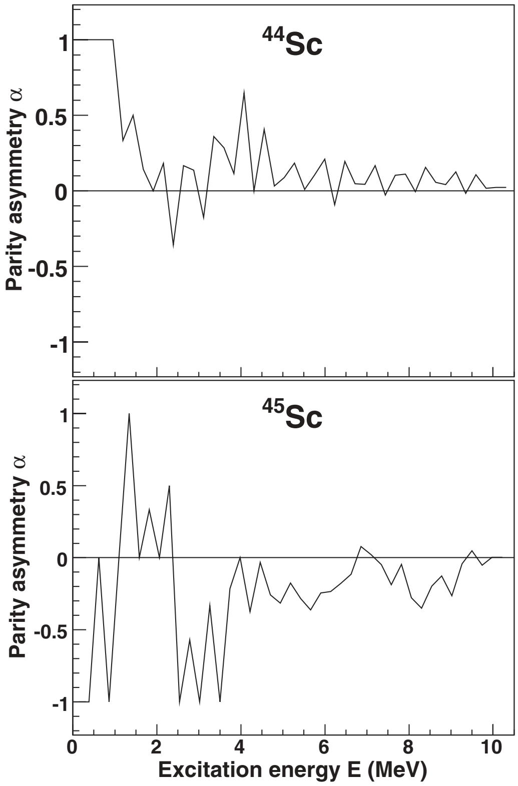

FIG. 10. The parity asymmetry as function of excitation energy for ^{44,45}Sc.

which gives -1 and 1 for only negative and positive parities, respectively, and 0 when both parities are equally represented. In Fig. 10 the parity asymmetry α is shown as a function of excitation energy. On the average, for $E > 4$ MeV, there seems to be a slight excess of positive- and negative-parity states in ^{44}Sc and ^{45}Sc, respectively. However, as the excitation energy increases, the model predicts that the parity asymmetry becomes smaller and smaller for both nuclei. The proton-resonance data in Ref. [37] from the reaction ^{44}Ca+p (compound nucleus ^{45}Sc, with excitation-energy region 9.77–10.53 MeV), gives an asymmetry parameter $\alpha = -0.18^{+0.07}_{-0.06}$ for $J = 1/2$ resonances, and $\alpha = 0.23 \pm 0.07$ for $J = 3/2$ resonances. Given the level densities of $J = 1/2$ and $J = 3/2$ resonances (see Table III in Ref. [37]), the parity asymmetry for $\rho(J = 1/2, J = 3/2)$ can be estimated to $\alpha \sim 0.02$, in good agreement with the model's result in this excitation-energy region.

IV. THE γ-RAY STRENGTH FUNCTIONS

As mentioned in Sec. II, the γ-decay process in the (quasi-)continuum is governed by the level density and the γ-ray transmission coefficient. By using the Oslo method, also the γ-ray transmission coefficient can be extracted from the experimental data.

The slope of the γ-ray transmission coefficient $\mathcal{T}(E_\gamma)$ has already been determined through the normalization of the level densities (Sec. III A). However, the constant B in Eq. (6) remains to be determined. If there was data on the average total radiative width $\langle \Gamma_\gamma \rangle$ for these nuclei, this data could be utilized for the absolute normalization of $\mathcal{T}$ as described in, e.g, Refs. [38,39]. Because such data does not exist for ^{44,45}Sc, other considerations had to be made to obtain the absolute value of the strength function.

The experimental $\mathcal{T}$ contains components from all electromagnetic characters X and multipolarities L. It is closely connected to the total γ-ray strength function through the relation [40]

$$\mathcal{T}(E_\gamma) = 2\pi \sum_{XL} E_\gamma^{2L+1} f_{XL}(E_\gamma), \tag{13}$$

where f_{XL} is the γ-ray strength function for electromagnetic character X and multipolarity L. Assuming that the γ-decay taking place in the continuum is dominated by $E1$ and $M1$ transitions, the total γ-ray strength function can be approximated by

$$f(E_\gamma) \simeq \frac{1}{2\pi} \frac{\mathcal{T}(E_\gamma)}{E_\gamma^3}. \tag{14}$$

The resulting γ-ray strength functions of ^{44,45}Sc are then scaled to agree with data from Ref. [41]. Based on two resonances from the reaction ^{45}Sc(n,γ) and on the observation of 13 $E1$ transitions and 9 $M1$ transitions of average energy 7.0 and 7.2 MeV, respectively, the strength functions are found to be $f_{E1} = 1.61(59) \times 10^{-8}$ MeV^{-3} and $f_{M1} = 1.17(59) \times 10^{-8}$ MeV^{-3} [41]. By adding these values together, the absolute normalization is given at this specific γ energy. The experimental γ-ray strength functions of ^{44,45}Sc are displayed in Fig. 11, together with the data point from Ref. [41] used for the normalization.

Several interesting features can be seen in Fig. 11. In general, for $E_\gamma \geqslant 3.5$ MeV, the data show that the γ-ray strength functions of ^{44,45}Sc are slowly increasing with γ energy. For γ energies below $\sim$3 MeV, the γ-ray strength functions of both nuclei have an increase of a factor $\sim$3 relative to their minimum.

To investigate the experimental strength functions further, they are compared to theoretical predictions. For the $E1$ part of the total γ-strength function, the Kadmenskiĭ, Markushev, and Furman (KMF) model [26] described by

$$f_{E1}(E_\gamma) = \frac{1}{3\pi^2\hbar^2c^2} \frac{0.7\sigma_{E1}\Gamma_{E1}^2\left(E_\gamma^2 + 4\pi^2T^2\right)}{E_{E1}\left(E_\gamma^2 - E_{E1}^2\right)^2} \tag{15}$$

is applied. Here, σ_{E1} is the cross section, Γ_{E1} is the width, and E_{E1} is the centroid of the giant electric dipole resonance (GEDR). The Lorentzian parameters are taken from Ref. [42] (see Table III). The nuclear temperature on the final state, introduced to ensure a nonvanishing GEDR for $E_\gamma \to 0$, is given by $T(E_f) = \sqrt{U_f/a}$.

For f_{M1}, which is supposed to be governed by the spin-flip $M1$ resonance [38], the Lorentzian giant magnetic dipole resonance (GMDR)

$$f_{M1}(E_\gamma) = \frac{1}{3\pi^2\hbar^2c^2} \frac{\sigma_{M1}E_\gamma\Gamma_{M1}^2}{\left(E_\gamma^2 - E_{M1}^2\right)^2 + E_\gamma^2\Gamma_{M1}^2} \tag{16}$$

is adopted.

TABLE III. Parameters used for the theoretical γ-ray strength functions.

Nucleus	κ	A	b	E_{E1} (MeV)	σ_{E1} (mb)	Γ_{E1} (MeV)	E_{M1} (MeV)	σ_{M1} (mb)	Γ_{M1} (MeV)	E_{E2} (MeV)	σ_{E2} (mb)	Γ_{E2} (MeV)
^{44}Sc	1.11(3)	0.52(10)	2.57(23)	19.44	39.40	8.0	11.61	1.239	4.0	17.85	1.069	5.58
^{45}Sc	1.20(1)	1.62(9)	2.93(5)	19.44	39.40	8.0	11.53	1.214	4.0	17.71	1.047	5.57

The contribution from $E2$ radiation to the total strength function is assumed to be very small. However, for the sake of completeness, the $E2$ isoscalar reconance described by

$$f_{E2}(E_\gamma) = \frac{1}{5\pi^2\hbar^2c^2E_\gamma^2}\frac{\sigma_{E2}E_\gamma\Gamma_{E2}^2}{\left(E_\gamma^2 - E_{E2}^2\right)^2 + E_\gamma^2\Gamma_{E2}^2} \qquad (17)$$

is included in the total, theoretical strength function.

In lack of any established theoretical prediction of the observed increase at low γ energy, this phenomenon is modelled by a simple power law as

$$f_{\mathrm{upbend}}(E_\gamma) = \frac{1}{3\pi^2\hbar^2c^2}AE_\gamma^{-b}, \qquad (18)$$

where A and b are fit parameters.

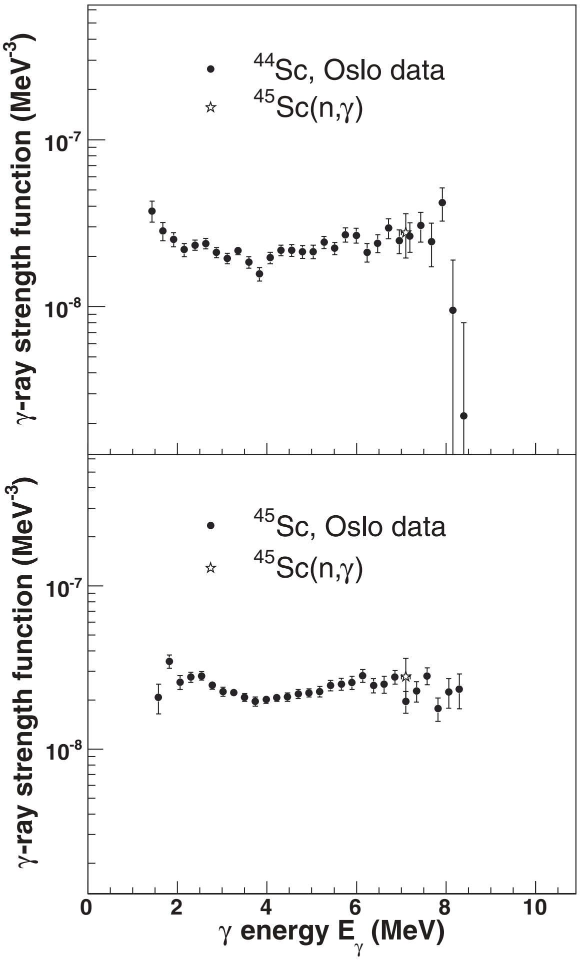

FIG. 11. Normalized γ-strength functions of ^{44,45}Sc (black dots), and $f_{E1} + f_{M1}$ from Ref. [41] (star).

The total, theoretical γ-ray strength function is then given by

$$f_{\mathrm{total}} = \kappa(f_{E1} + f_{M1} + f_{\mathrm{upbend}}) + E_\gamma^2 f_{E2}, \qquad (19)$$

where κ is a renormalization factor that should be close to unity. All parameters employed are listed in Table III, and the result for ^{44}Sc is displayed in Fig. 12. It is seen that the theoretical strength function fits the data well. From Fig. 12, one would also conclude that the data points below ~3 MeV are not described by the standard models.

In Fig. 12 also the photoneutron cross-section data from the reaction ^{45}Sc$(\gamma,n)^{44}$Sc [43] and the photoproton cross-section data from the reaction ^{45}Sc$(\gamma,p)^{44}$Ca [44] are shown. The photoabsorbtion cross-section $\sigma(E_\gamma)$ is converted into strength function through the relation

$$f(E_\gamma) = \frac{1}{3\pi^2\hbar^2c^2}\left[\frac{\sigma(E_\gamma)}{E_\gamma}\right]. \qquad (20)$$

The (γ,n) and (γ,p) data exhaust ~57% and ~25% of the Thomas-Reiche-Kuhn sum rule, respectively [42]. The summed strength of the two photoabsorption experiments for

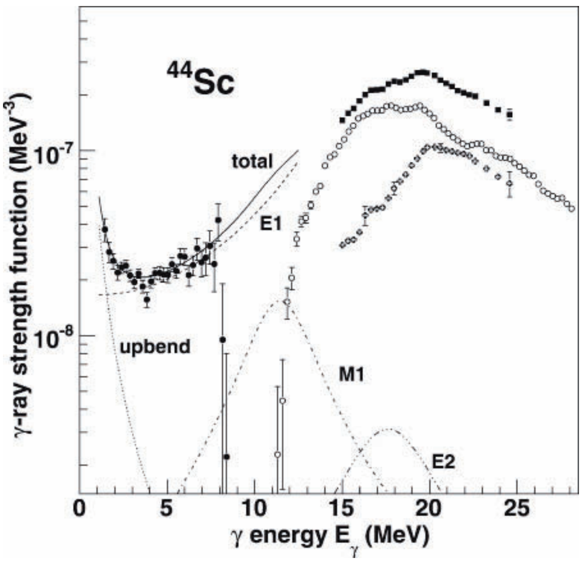

FIG. 12. The γ-strength functions of ^{44,45}Sc from Oslo experiments (black dots) and GDR data from (γ,n) (white dots) and (γ,p) (white crosses) experiments [43,44]. The black squares represent the summed strength from the (γ,n) and (γ,p) experiments for $E_\gamma = 15.0$–24.6 MeV. Also the total, theoretical strength function (solid line), the $E1$ tail from the KMF model (dashed line), the spin-flip $M1$ resonance (dashed-dotted line), the $E2$ isoscalar resonance (dashed-dotted line), and a fit to the upbend structure (dotted line) are shown.

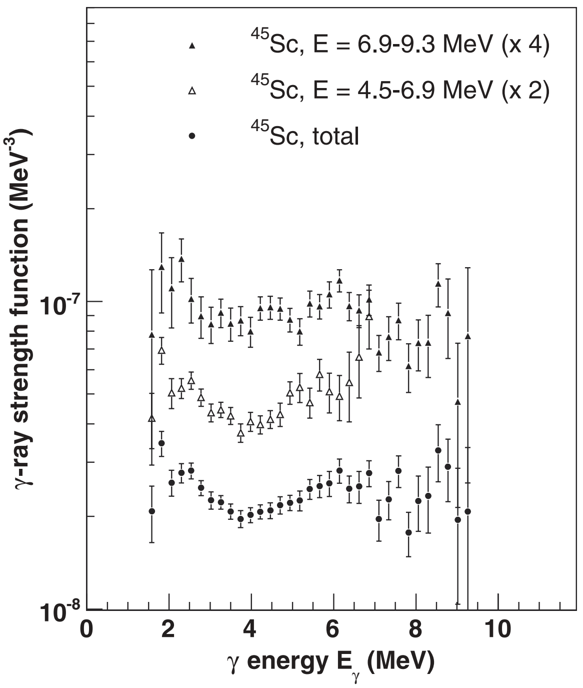

FIG. 13. The γ-strength function of ^{45}Sc extracted from different excitation-energy regions together with the strength function obtained from the total excitation-energy region considered.

$E_\gamma = 15.0$–24.6 MeV is also displayed in Fig. 12, and it seems to fit reasonably well with the theoretical expectation and the Oslo data. Note that the photoabsorption cross sections from the (γ, n) and (γ, p) reactions may have some overlap in strength in the energy region where the (γ, pn) channel is opened.

For γ energies below ~3 MeV, the γ-ray strength functions of ^{44,45}Sc display an increase of a factor ~3 relative to their minimum. This behavior has been observed in several medium-mass nuclei; first in ^{56,57}Fe [45], then recently in $^{93-98}$Mo [39] and ^{50,51}V [12]. For the iron and molybdenum isotopes, the upbend structure has been shown to be independent of excitation energy. This has also been tested for the Sc isotopes, as demonstrated in Fig. 13. Here, the γ-ray strength function of ^{45}Sc has been extracted from two different excitation-energy regions (the intervals 4.5–6.9 MeV and 6.9–9.3 MeV), representing two independent sets of data. As seen in Fig. 13, the result is quite convincing. The general trends are very similar, and the enhancement at low γ energies appears in both data sets.

The physical origin of this low-energy enhancement in strength is not yet understood. To check if the upbend feature could be due to peculiarities of the nuclear reactions or the Oslo method, a two-step cascade $(n, 2\gamma)$ experiment was carried out with ^{56}Fe as a target [45]. This experiment confirmed the large increase in γ-ray strength observed in the Oslo data but was unable to establish the character and multipolarity of the enhancement. To pin down the physical reason behind these observations, it is necessary to design and carry out experiments that have the possibility to determine the electromagnetic nature of this low-energy structure. Also, it would give better confidence to the findings to have independent confirmation of the increase from, e.g, $(n, 2\gamma)$ experiments on the Mo, V, and Sc isotopes as well.

V. SUMMARY AND CONCLUSIONS

The nuclear level densities and the γ-ray strength functions of the scandium isotopes ^{44,45}Sc were measured from primary γ rays using the Oslo method. The level densities display bump structures that cannot be obtained from standard statistical level-density models. A new, microscopic model to calculate the level density has been developed and applied on both nuclei, giving an overall good agreement with the experimental data. From the model, information on the average number of broken pairs and the parity asymmetry can also be extracted.

The γ-ray strength functions are in general found to be increasing functions of γ energy in the energy region examined in this work. The new data sets from the Oslo experiment are compared to theoretical models of the strength function and photoabsorbtion data, and the agreement seems to be good. At low γ energies a substantial enhancement of the total γ-ray strength is observed that is not accounted for in any of the standard theories. As of today, this puzzling feature has no satisfying, physical explanation.

ACKNOWLEDGMENTS

Financial support from the Norwegian Research Council (NFR) is gratefully acknowledged. A. Schiller acknowledges support from the U.S. National Science Foundation, grant number PHY-06-06007.

---

[1] E. Melby, L. Bergholt, M. Guttormsen, M. Hjorth-Jensen, F. Ingebretsen, S. Messelt, J. Rekstad, A. Schiller, S. Siem, and S. W. Ødegård, Phys. Rev. Lett. **83**, 3150 (1999).
[2] M. Guttormsen, M. Hjorth-Jensen, E. Melby, J. Rekstad, A. Schiller, and S. Siem, Phys. Rev. C **63**, 044301 (2001).
[3] J. M. Blatt and V. F. Weisskopf, *Theoretical Nuclear Physics* (John Wiley & Sons, New York, 1952).
[4] T. von Egidy, H. H. Schmidt, and A. N. Behkami, Nucl. Phys. **A481**, 189 (1988).
[5] W. P. Abfalterer, R. W. Finlay, and S. M. Grimes, Phys. Rev. C **62**, 064312 (2000).
[6] S. Siem, M. Guttormsen, K. Ingeberg, E. Melby, J. Rekstad, A. Schiller, and A. Voinov, Phys. Rev. C **65**, 044318 (2002).
[7] M. Guttormsen, A. Bagheri, R. Chankova, J. Rekstad, S. Siem, A. Schiller, and A. Voinov, Phys. Rev. C **68**, 064306 (2003).
[8] U. Agvaanluvsan *et al.*, Phys. Rev. C **70**, 054611 (2004).
[9] M. Guttormsen, E. Melby, J. Rekstad, A. Schiller, S. Siem, T. Lönnroth, and A. Voinov, J. Phys. G **29**, 263 (2003).
[10] A. Schiller *et al.*, Phys. Rev. C **68**, 054326 (2003).
[11] R. Chankova *et al.*, Phys. Rev. C **73**, 034311 (2006).
[12] A. C. Larsen *et al.*, Phys. Rev. C **73**, 064301 (2006).

[13] F. B. Malik and W. Scholz, Phys. Rev. **150**, 919 (1966).

[14] B. J. Cole, Nucl. Phys. **11**, 953 (1985).

[15] P. Bednarczyk *et al.*, Phys. Lett. **B393**, 285 (1997).

[16] E. Caurier, G. Martinez-Pinedo, F. Nowacki, A. Poves, and A. P. Zuker, Rev. Mod. Phys. **77**, 427 (2005).

[17] M. Guttormsen, A. Atac, G. Løvhøiden, S. Messelt, T. Ramsøy, J. Rekstad, T. F. Thorsteinsen, T. S. Tveter, and Z. Zelazny, Phys. Scr. **T32**, 54 (1990).

[18] M. Guttormsen, T. S. Tveter, L. Bergholt, F. Ingebretsen, and J. Rekstad, Nucl. Instrum. Methods Phys. Res., Sect. A **374**, 371 (1996).

[19] M. Guttormsen, T. Ramsøy, and J. Rekstad, Nucl. Instrum. Methods A **255**, 518 (1987).

[20] A. Schiller, L. Bergholt, M. Guttormsen, E. Melby, J. Rekstad, and S. Siem, Nucl. Instrum. Methods Phys. Res., Sect. A **447**, 498 (2000).

[21] A. Bohr and B. Mottelson, *Nuclear Structure* (Benjamin, New York, 1969), Vol. I, p. 169, pp. 184–185.

[22] L. Henden, L. Bergholt, M. Guttormsen, J. Rekstad, and T. S. Tveter, Nucl. Phys. **A589**, 249 (1995).

[23] D. M. Brink, Ph.D. thesis, Oxford University, 1955.

[24] P. Axel, Phys. Rev. **126**, 671 (1962).

[25] G. Gervais, M. Thoennessen, and W. E. Ormand, Phys. Rev. C **58**, R1377 (1998).

[26] S. G. Kadmenskiĭ, V. P. Markushev, and V. I. Furman, Yad. Fiz. **37**, 277 (1983); [Sov. J. Nucl. Phys. **37**, 165 (1983)].

[27] Data extracted using the NNDC On-Line Data Service from the ENSDF database (http://www.nndc.bnl.gov/ensdf/).

[28] C. P. Poirier and J. C. Manthuruthil, *Proceedings from Topical Conference on the Structure of* $1f_{7/2}$ *Nuclei, Legnaro (Padova)*, Editrice Compositori, Bologna (1971).

[29] S. J. Lokitz, G. E. Mitchell, and J. F. Shriner, Jr., Phys. Rev. C **71**, 064315 (2005).

[30] A. Voinov (private communication).

[31] A. Gilbert and A. G. W. Cameron, Can. J. Phys. **43**, 1446 (1965).

[32] T. von Egidy and D. Bucurescu, Phys. Rev. C **72**, 044311 (2005); **73**, 049901(E) (2006).

[33] J. Bardeen, L. N. Cooper, and J. R. Schrieffer, Phys. Rev. **108**, 1175 (1957).

[34] D. C. S. White, W. J. McDonald, D. A. Hutcheon, and G. C. Neilson, Nucl. Phys. **A260**, 189 (1976).

[35] R. Firestone and V. S. Shirley, *Table of Isotopes*, 8th ed. (Wiley, New York, 1996), vol. II.

[36] J. Dobaczewski, P. Magierski, W. Nazarewicz, W. Satuła, and Z. Szymański, Phys. Rev. C **63**, 024308 (2001).

[37] U. Agvaanluvsan, G. E. Mitchell, J. F. Shriner Jr., and M. Pato, Phys. Rev. C **67**, 064608 (2003).

[38] A. Voinov, M. Guttormsen, E. Melby, J. Rekstad, A. Schiller, and S. Siem, Phys. Rev. C **63**, 044313 (2001).

[39] M. Guttormsen, R. Chankova, U. Agvaanluvsan, E. Algin, L. A. Bernstein, F. Ingebretsen, T. Lönnroth, S. Messelt, G. E. Mitchell, J. Rekstad, A. Schiller, S. Siem, A. C. Sunde, A. Voinov, and S. Ødegård, Phys. Rev. C **71**, 044307 (2005).

[40] J. Kopecky and M. Uhl, Phys. Rev. C **41**, 1941 (1990).

[41] J. Kopecky and M. Uhl, *Proceedings of a Specialists' Meeting on Measurement, Calculation and Evaluation of Photon Production Data, Bologna, Italy, 1994,* edited by C. Coceva, A. Mengoni, and A. Ventura [Report No. NEA/NSC/DOC(95)1].

[42] Centre for Photonuclear Experiments Data, http://cdfe.sinp.msu.ru

[43] A. Veyssiere, H. Beil, R. Bergere, P. Carlos, A. Lepretre, and A. de Miniac, Nucl. Phys. **A227**, 513 (1974).

[44] S. Oikawa and K. Shoda, Nucl. Phys. **A277**, 301 (1977).

[45] A. Voinov, E. Algin, U. Agvaanluvsan, T. Belgya, R. Chankova, M. Guttormsen, G. E. Mitchell, J. Rekstad, A. Schiller, and S. Siem, Phys. Rev. Lett. **93**, 142504 (2004).

5.6 Paper 5: Level densities of ^{44}Sc and ^{47}Ti from different experimental techniques

PHYSICAL REVIEW C **77**, 034613 (2008)

Level densities of ^{44}Sc and ^{47}Ti from different experimental techniques

A. V. Voinov,[1,*] S. M. Grimes,[1] A. C. Larsen,[2] C. R. Brune,[1] M. Guttormsen,[2] T. Massey,[1] A. Schiller,[1] S. Siem,[2] and N. U. H. Syed[2]

[1]*Department of Physics and Astronomy, Ohio University, Athens, Ohio 45701, USA*

[2]*Department of Physics, University of Oslo, N-0316 Oslo, Norway*

(Received 18 December 2007; published 31 March 2008)

The level densities of ^{44}Sc and ^{47}Ti have been determined from measurements of particle evaporation spectra from the compound nuclear reaction ^{3}He + ^{45}Sc with an 11 MeV ^{3}He beam. The level density of ^{44}Sc has been compared to the level density obtained from an independent experimental method based on an analysis of α-γ coincidences from the transfer reaction ^{45}Sc(^{3}He,$\alpha\gamma$)^{44}Sc. The good agreement between the two experiments indicates the reliability of the level density obtained. Some level density systematics have been tested against the experimental data. New Fermi-gas level density parameters have been derived.

DOI: 10.1103/PhysRevC.77.034613 PACS number(s): 21.10.Ma, 24.60.Dr, 27.40.+z

I. INTRODUCTION

The nuclear level density is difficult to measure precisely because of the lack of reliable experimental techniques. The counting of discrete levels is restricted to excitation energies below about 3–5 MeV for medium mass nuclei because above this limit the levels become too close in energy to resolve. Above these energies more sophisticated methods need to be applied (see Ref. [1]). The main approach for estimating the level density above the discrete level region is to use some model-based function with parameters fitted to the density of discrete low-lying levels and the density of neutron resonances. For nuclei for which information about the neutron resonance spacing is not available, parameter systematics must be used. There are several systematics of level density parameters (mainly related to either Fermi-gas or constant temperature models) that modern computer codes utilize to calculate reaction cross sections. However, because neutron resonances are known only for a very narrow spin interval, and because the shape of the level density function is not well established, it is not yet clear how well available systematics reproduce total level densities above the discrete level region.

At this time, two experimental techniques appear to be good candidates for the systematic investigation of the total level density in nuclei above the region of discrete levels. The first one was developed at the Oslo Cyclotron Laboratory (hereafter referred to as the “Oslo method”) to extract both level density and γ-strength functions from the particle-γ coincidence matrix measured from inelastic scattering (^{3}He,^{3}He$'\gamma$) and transfer (^{3}He,$\alpha\gamma$) reactions [2]. The second method uses particle evaporation spectra from compound nuclear reactions [3]. The problem is that both methods might contain intrinsic systematic uncertainties, which are difficult to estimate while remaining inside of these methods. Particularly the Oslo method suffers from normalization uncertainties because it produces only a level density function with an uncertainty factor of $A\exp(BE_x)$, where E_x is the excitation energy. The coefficients (A, B) then have to be determined from auxiliary experimental information such as neutron resonance spacing (when available) and the density of discrete levels. The Oslo method is also based on assumptions discussed below, which are possible sources of systematic uncertainties as well. The main problem with the particle evaporation technique is possible contaminations of the evaporation spectra due to multistep and/or direct reaction contributions. It could result in an incorrect slope of the obtained level density function and could cause an absolute normalization problem.

The consistency of these two experimental techniques has been confirmed in Ref. [4], where the level density of ^{56}Fe was investigated with the reaction ^{57}Fe(^{3}He,$\alpha\gamma$)^{56}Fe by the Oslo method and with the neutron evaporation spectrum from the ^{55}Mn(d,n)^{56}Fe reaction. Neutron spectra are most suitable for level density studies because neutron transmission coefficients are better known than proton and α-transmission coefficients. Moreover, the neutron channel is a preferred decay channel for the compound nucleus. This means that it is more likely that compound reactions dominate the neutron spectrum. On the other hand, it would be highly desirable to study different types of reactions for these purposes. In this work we have studied the level density from the evaporation spectra of α particles from the ^{45}Sc(^{3}He,α)^{44}Sc reaction and compared it to the level density obtained recently from the ^{45}Sc(^{3}He,$\alpha\gamma$)^{44}Sc reaction using the Oslo method. The level density of ^{47}Ti populated by the ^{45}Sc(^{3}He,p)^{47}Ti reaction has been obtained as well. Different available level density systematics have been tested.

II. EXPERIMENTS AND METHODS

A. The Oslo method

At the Oslo Cyclotron Laboratory, a measurement of the ^{45}Sc(^{3}He,$\alpha\gamma$)^{44}Sc reaction with a 38 MeV ^{3}He beam was performed. The self-supporting natural target of 99.9% ^{45}Sc had a thickness of 3.4 mg/cm^2. Eight Si ΔE-E telescopes were arranged close to the target at an angle of 45° relative to the beam. The γ-ray detector CACTUS [5], consisting of 28 collimated NaI crystals with a total efficiency of 15%

---

[*] voinov@ohio.edu

surrounded the target and particle detectors. The experimental setup enabled particle-γ coincidence measurements of the reaction ^{45}Sc(^{3}He,$\alpha\gamma$)^{44}Sc. The experiment ran for about 5 days, with a typical beam current of ∼1 nA.

The essential part of the analysis of particle-γ coincidences is the extraction of first-generation spectra $P(E_x, E_\gamma)$ at each excitation energy bin E_x, which is the initial excitation energy of the γ transitions. The corresponding technique is described in Ref. [6]. The first generation matrix $P(E_x, E_\gamma)$ can be decomposed into a level density $\rho(E_x - E_\gamma)$ and γ-transmission function $T(E_\gamma)$ as

$$P(E_x, E_\gamma) \propto \rho(E_x - E_\gamma) T(E_\gamma). \tag{1}$$

The details of this particular experiment and its analysis are described in Ref. [7]. Here we would like to outline the important assumptions behind this decomposition.

(i) The γ decay from each excitation energy bin and the spin population within the bin are independent of how the levels were populated; whether directly by the reaction or by γ decay from higher-lying states.

(ii) The γ-strength function does not depend on the excitation energies of either initial or final states, it depends only on the γ energy.

It is difficult to estimate how large the possible violations of the assumptions are and how they affect the final results. Special concern is caused by the possible temperature dependence of the γ-strength function suggested in theoretical work [8] which would mean a violation of the second assumption.

B. Level density from evaporation spectra

To obtain an independent result on the level density of ^{44}Sc, we measured the α-particle evaporation spectrum from the ^{45}Sc(^{3}He,α)^{44}Sc reaction. The proton spectrum was also studied, which allowed us to investigate the level density of the residual ^{47}Ti nucleus. The experiment was performed with an 11-MeV ^{3}He beam from the tandem accelerator of the Ohio University Edwards Accelerator Laboratory. Proton and α-particle spectra were measured with a charged-particle spectrometer [1]. Seven 2-m time-of-flight tubes with Si detectors placed at the end were set up at angles ranging from 22.5° up to 157.5°. The masses of the charged particles were determined by measuring both the energy deposited in the Si detectors and the time of flight. The mass resolution was sufficient to resolve protons, deuterons, ^{3}He/^{3}H, and α particles.

The cross section of outgoing particles resulting from compound nucleus decay can be calculated in the framework of the Hauser-Feshbach (HF) model [9], according to which

$$\frac{d\sigma}{d\varepsilon_b}(\varepsilon_a, \varepsilon_b) = \sum_{J\pi^c} \sigma^{\mathrm{CN}}(\varepsilon_a) \frac{\sum_{I\pi^r} \Gamma_b(U, J, \pi^c, E, I, \pi^r) \rho_b(E, I, \pi^r)}{\Gamma(U, J, \pi^c)}, \tag{2}$$

with

$$\Gamma(U, J, \pi^c) = \sum_{b'} \left(\sum_k \Gamma_{b'}(U, J, \pi^c, E_k, I_k, \pi_k^r) + \sum_{I'\pi^{r'}} \int_{E_c}^{U-B_{b'}} dE' \, \Gamma_{b'} \times (U, J, \pi^c, E', I', \pi^{r'}) \, \rho_{b'}(E', I', \pi^{r'}) \right). \tag{3}$$

Here $\sigma^{\mathrm{CN}}(\varepsilon_a)$ is the fusion cross section, ε_a and ε_b are energies of relative motion for incoming and outgoing channels ($\varepsilon_b = U - E_k - B_b$, where B_b is the separation energy of particle b from the compound nucleus), Γ_b is the transmission coefficient of outgoing particles, and the quantities (U, J, π^c) and (E, I, π^r) are the energy, angular momentum, and parity of the compound and residual nuclei, respectively. The energy E_c is the continuum edge, above which levels are modeled using a level density parametrization. For energies below E_c, the known excitation energies, spins, and parities of discrete levels are used. In practice E_c is determined by the available spectroscopic data in the literature. It follows from Eq. (3) that the cross section is determined by both transmission coefficients of outgoing particles and the level density of the residual nucleus $\rho_b(E, I, \pi)$. It is believed that transmission coefficients are known with sufficient accuracy near the line of stability because they can be obtained from optical model potentials, which are usually based on experimental data for elastic scattering and total cross sections in the corresponding outgoing channel. Transmission coefficients obtained from different systematics of optical model parameters do not differ by more that 15–20 % from each other in our region of interest (1–15 MeV of outgoing particles). The uncertainties in level densities are much larger. Therefore, the HF model can be used to improve level densities by comparing experimental and calculated particle evaporation spectra. Details and assumptions of this procedure are described in Refs. [3] and [10]. The code HF2002 [11] was used for calculations of spectra from compound nuclear reactions.

The main uncertainty of this method comes from contributions of noncompound mechanisms of a nuclear reaction including direct, multistep direct, and multistep compound. They correspond to different stages of nucleon-nucleon interactions inside the projectile + target nuclear system until complete equilibrium is achieved. The measurement of the energy distribution of outgoing particles at backward angles reduces considerably the contribution from noncompound reactions, but does not guarantee their complete elimination. Therefore, the systematic uncertainties connected to the presence of noncompound reaction contributions can be estimated only by applying different experimental techniques directed to measure the level density of the same nucleus.

By comparing data obtained from the Oslo method with data extracted from particle evaporation spectra one can estimate possible systematic uncertainties pertaining to these methods.

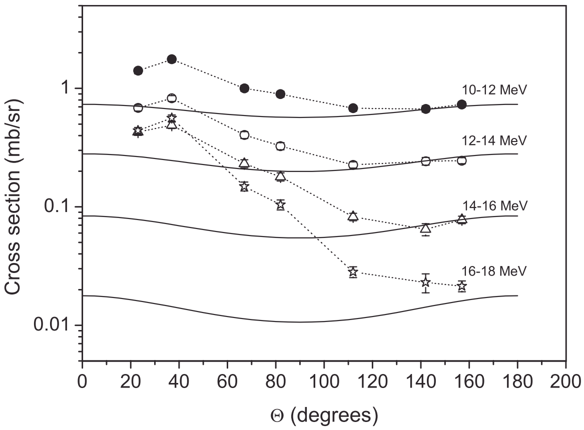

FIG. 1. Angular distributions of α particles in the c.m. system for different energy intervals. The points are experimental data and the solid lines are HF calculations normalized to match the experimental points at backward angles for low energy particles.

III. RESULTS

To investigate the reaction mechanism, the proton and α-particle angular distributions were measured (Figs. 1 and 2). In the figures the particle energies are restricted to ensure that only first stage particles emitted immediately from the compound nucleus ^{48}V can contribute. For compound nuclear reactions the HF calculation predicts a symmetric angular distribution of the cross section with respect to 90° in the center of mass system. The present measurement exhibits forward-peaked distributions for both protons and α particles. However, it is important to note that for lower energy α particles, the angular distribution starts to follow the calculated curve at $\approx$115° and beyond. For higher energy particles the asymmetry is stronger. For α particles in the energy interval 16–18 MeV, i.e., for those populating the discrete levels of ^{44}Sc, the angular distribution does not agree with calculations even at backward angles. This means that high energy α particles contain contributions from noncompound reactions even at backward angles. From this analysis, it is possible to conclude that the α-particle spectra measured at backward angles can be used for extracting level densities but only in the energy region 10–16 MeV, which corresponds to excitation energies of the residual ^{44}Sc nucleus between 2 and 8 MeV. We could not make a similar analysis for protons because the thickness of our detectors (1000 and 1500 μm) was not sufficient to stop protons with energies greater than 10 and 15 MeV, respectively (note that the maximum proton energy from this reaction is 21 MeV). Therefore, the proton angular distribution is integrated over all energies and is presented in Fig. 2 along with integrated distribution for α particles. The similarity of these distributions indicates that the compound mechanism is the main mechanism determining both proton and α-particle spectra measured at backward angles.

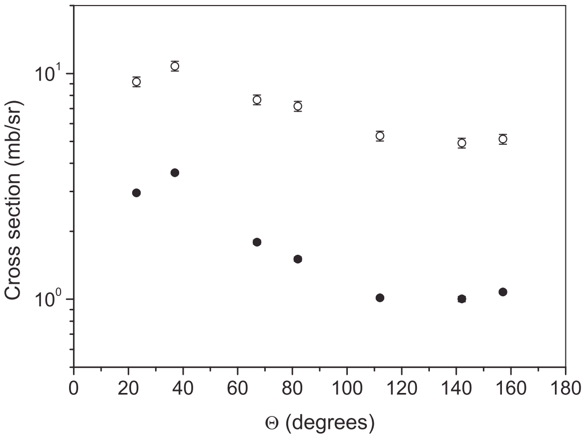

FIG. 2. Angular distributions of protons (open circles) and α particles (solid circles) in the c.m. system.

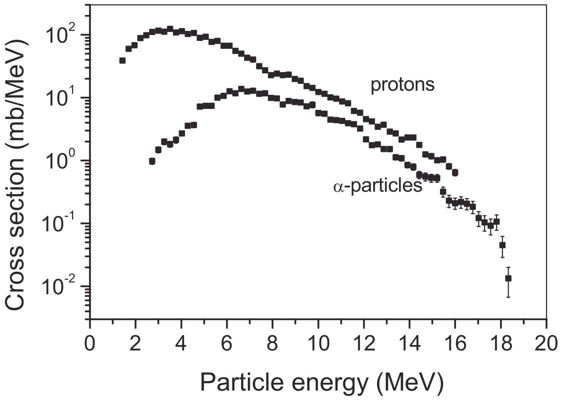

FIG. 3. Experimental energy spectra of protons and α particles measured at 157° with respect to the beam line.

The energy dependence of proton and α-particle cross sections measured at 157° with respect to the beam axis are shown in Fig. 3. The level densities for both ^{44}Sc (populated by α particles) and ^{47}Ti (populated by protons) nuclei were obtained by the method described in Ref. [3] and in our previous article [1]: a level density model is chosen for the calculation of the differential cross section of Eq. (3). The parameters of the model are then adjusted to reproduce the experimental spectra as closely as possible. The input level density is improved by binwise renormalization according to the expression

$$\rho_b(E, I, \pi) = \rho_b(E, I, \pi)_{\text{input}} \frac{(d\sigma/d\varepsilon_b)_{\text{meas}}}{(d\sigma/d\varepsilon_b)_{\text{calc}}}. \qquad (4)$$

To get the absolute normalization, information about the level density of discrete levels is used.

The level densities of ^{47}Ti and ^{44}Sc extracted from proton and α-particle evaporation spectra are shown in Fig. 4. The level density of ^{44}Sc extracted from the Oslo experiment is presented for comparison.

The absolute normalization of the level density for ^{44}Sc has been obtained by matching the Oslo level density to the density of discrete levels in the low energy region and by matching the slope of the Oslo level density to the slope of the level density obtained from the particle evaporation spectrum. One can see the good agreement between the shapes of the level densities from two types of experiments. The absolute normalization of the level density for ^{47}Ti was obtained from the ratio of α/proton cross sections of the ^{3}He + ^{45}Sc reaction.

TABLE I. Ratio of experimental and model level densities at different excitation energies E_x. The bottom line shows the comparison of the experimental and calculated ratios of α-particle and proton cross sections.

Nucleus	E_x (MeV)	$\rho^{\text{exp}}/\rho^{\text{model}}$			
		FG [12]	HFBCS [15]	GC [14]	CT [12]
^{47}Ti	5.5	0.78(16)	0.92(19)	1.52(31)	1.19(24)
	6.5	0.83(17)	1.14(23)	1.73(35)	1.18(24)
	7.5	0.69(14)	1.12(23)	1.53(31)	0.92(19)
	8.5	0.58(12)	1.10(22)	1.34(27)	0.70(14)
	9.5	0.60(12)	1.30(26)	1.40(28)	0.63(12)
	10.5	0.53(10)	1.29(26)	1.20(24)	0.45(9)
	11.5	0.49(10)	1.35(27)	1.06(21)	0.36(7)
^{44}Sc	2.5	1.41(30)	0.67(14)	1.50(31)	1.53(32)
	3.5	1.16(24)	0.61(13)	1.46(30)	1.27(26)
	4.5	1.00(20)	0.56(11)	1.42(29)	1.04(21)
	5.5	0.91(18)	0.56(11)	1.43(29)	0.88(18)
	6.5	0.93(19)	0.60(12)	1.55(31)	0.81(16)
		$\frac{\sigma_\alpha^{\text{exp}}/\sigma_p^{\text{exp}}}{\sigma_\alpha^{\text{cal}}/\sigma_p^{\text{cal}}}$			
		1.6(2)	0.5(2)	1.1(2)	1.2(2)

The experimental level densities have been compared to some level density models widely used in modern HF computer codes. These prescriptions are based on the Fermi gas (FG) model, the constant temperature (CT) model with parameters from the recent compilation of Ref. [12], and the Gilbert-Cameron (GC) formula [13]. Parameter systematics are obtained mainly on the basis of available information about the level density in the region of discrete levels and neutron resonances. For the GC model the Fermi-gas level density parameter a was calculated according to the Ignatyuk systematics [14] while parameters of the constant temperature part of the GC formula were obtained from the fit to discrete levels. We also tested the level density calculations based on the Hartree-Fock-BCS approach (HFBCS) [15] recommended by the RIPL data base [16]. Table I shows the ratio between experimental and model level densities at different excitation energies. It shows also how well HF calculations reproduce the ratio of α and proton cross sections. This is an important issue because this ratio gives an additional constraint on level densities of residual nuclei. The conclusion is that the level density of ^{47}Ti is best reproduced with the HFBCS model but the FG systematics fit better for ^{44}Sc. No single model with parameters from systematics reproduces level densities of both nuclei equally well. However, HF calculations with GC and CT models reproduce well the ratio of α and proton cross sections.

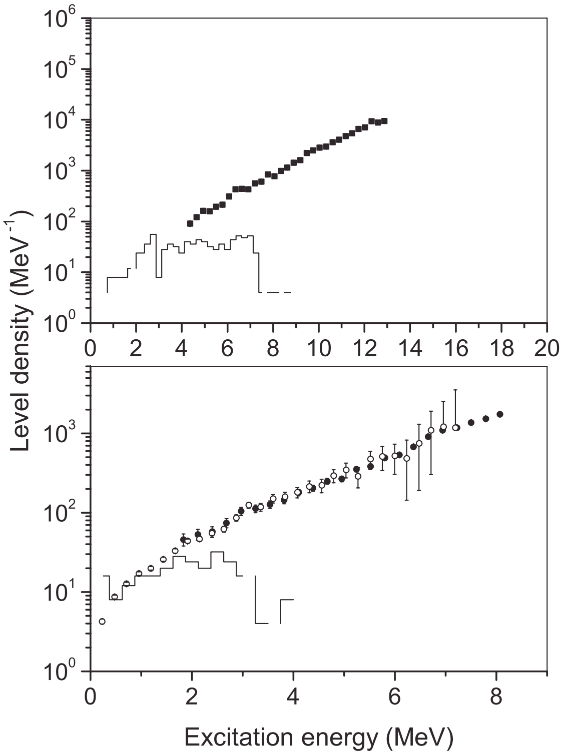

FIG. 4. Level densities of ^{47}Ti (upper panel) and ^{44}Sc (lower panel) nuclei obtained from proton and α-particle energy spectra, respectively. Black points are data from particle evaporation spectra. Open points are data from the Oslo experiment [7]. The histograms represent level densities from the counting of discrete levels.

To improve the level density prescription for these nuclei, we used the FG model with free parameters a and δ to fit the experimental level densities. The rigid-body spin cutoff parameter was adopted for this fit. The parameters we obtained are $a = 5.13$ MeV^{-1} and $\delta = -2.91$ MeV for ^{44}Sc and $a = 5.06$ MeV^{-1} and $\delta = -1.95$ MeV for ^{47}Ti. These parameters can be compared to parameters from systematics [12]: $a = 5.68$ MeV^{-1} and $\delta = -2.064$ MeV for ^{44}Sc and $a = 5.99$ MeV^{-1} and $\delta = -0.738$ MeV for ^{47}Ti. Discrepancies in corresponding level densities are shown in Table I. The systematics of Ref. [12] agree with the experimental level density of the ^{44}Sc nucleus but are off by a factor of 1.3–2 for ^{47}Ti. However, in the case of ^{47}Ti, level density parameters from our experiment agree better with ones determined in Ref. [12] on the basis of a fit to low-lying discrete levels and neutron resonance spacings ($a = 5.14(30)$ MeV^{-1} and $\delta = -1.35(74)$ MeV).

It should be noted that the drawback of all available level density systematics is that all of them use the neutron resonance spacing as a main source for the experimental level density at the neutron binding energy. The problem is that the neutron resonances are known within a narrow spin interval and the spin cutoff parameter must be used to calculate the total level density, which actually affects the reaction cross section calculations. The lack of experimental information on the spin cutoff parameter above the discrete level region introduces additional uncertainties in the calculation of reaction cross sections and can cause deviations from our experimental data (see Table I). An alternative option would be to establish a level density systematic based on experimental data on total level densities. There was an attempt [17] to establish the systematic based on particle evaporation spectra. About 50 nuclei from the $A = 10$–70 region have been analyzed. However, because of large discrepancies in level density parameters from different experiments, no good systematic regularity has been found.

The consistency between experimental level densities obtained from the Oslo method and particle evaporation spectra supports the underlying assumption of the Oslo method. It shows that the statistical mechanism is the major mechanism of γ decay following α-particle emission in the ^{45}Sc(^{3}He,$\alpha\gamma$) reaction. The spin of levels populated by either α particles or γ transitions does not seem to be much different. Also, the uncertainties due to the possible temperature dependence of the γ-strength function are small enough to not affect the final level density obtained by the Oslo method. All of these results indicate that the Oslo method, within its limitations, is a reliable tool for studying nuclear level densities.

The method based on particle energy spectra may suffer from systematic uncertainties connected to contributions of noncompound reaction mechanisms. These contributions depend on the type of reaction used as well as on the angle at which the spectra are measured. Backward angles allow one to reduce the contribution from noncompound reactions considerably but do not eliminate completely this effect, especially for high energy particles. The measurement of the angular distribution is an important tool in the analysis helping to determine the angle and energy ranges to be used for the level density determination.

IV. CONCLUSION

The level density of ^{44}Sc has been obtained from two independent experiments by using two different methods. These are the Oslo method based on the analysis of particle-γ coincidences from the ^{45}Sc(^{3}He,$\alpha\gamma$) reaction and the method based on the analysis of particle spectra from the compound nuclear reaction ^{45}Sc(^{3}He,α). Both methods produce the level densities that are in good agreement with each other. It has been shown that possible systematic uncertainties of the Oslo method resulting from underlying assumptions are negligible and do not cause any serious problems. The α particles from the ^{45}Sc(^{3}He,α) compound reaction measured at backward angles can be used to extract the level density of the corresponding residual nucleus. The angular distribution is an important factor in determining the range of energies of outgoing particles where the compound reaction mechanism is dominant.

The level density of ^{47}Ti has been obtained from the proton evaporation spectrum of the ^{45}Sc(^{3}He,p) reaction. Both ^{44}Sc and ^{47}Ti experimental level densities have been compared to several level density models. Despite the fact that some of these models reproduce experimental data well for one of these nuclei, none of the models seem to fit experimental data for both of them. The deviation from the best fit can be as large as 50%. New Fermi-gas level density parameters have been obtained.

ACKNOWLEDGMENTS

We are grateful to J. E. O'Donnell and D. Carter for computer and electronic support during the experiment and to A. Adekola, C. Matei, B. Oginni, and Z. Heinen for taking shifts. We also acknowledge financial support from the Department of Energy, Grant N DE-FG52-06NA26187/A000.

---

[1] A. V. Voinov, S. M. Grimes, C. R. Brune, M. J. Hornish, T. N. Massey, and A. Salas, Phys. Rev. C **76**, 044602 (2007).

[2] A. Schiller, L. Bergholt, M. Guttormsen, E. Melby, J. Rekstad, and S. Siem, Nucl. Instrum. Methods Phys. Res. A **447**, 498 (2000).

[3] H. Vonach, in *Proceedings of the IAEA Advisory Group Meeting on Basic and Applied Problems of Nuclear Level Densities, Upton, NY, 1983, BNL Report No. BNL-NCS-51694, 1983*, edited by M. R. Bhat (Brookhaven National Laboratory, New York, 1983) p. 247.

[4] A. V. Voinov, S. M. Grimes, U. Agvaanluvsan, E. Algin, T. Belgya, C. R. Brune, M. Guttormsen, M. J. Hornish, T. Massey, G. E. Mitchell, J. Rekstad, A. Schiller, and S. Siem, Phys. Rev. C **74**, 014314 (2006).

[5] M. Guttormsen, A. Atac, G. Løvhøiden, S. Messelt, T. Ramsøy, J. Rekstad, T. F. Thorsteinsen, T. S. Tveter, and Z. Zelazny, Phys. Scr., T **32**, 54 (1990).

[6] M. Guttormsen, T. Ramsøy, and J. Rekstad, Nucl. Instrum. Methods Phys. Res. A **255**, 518 (1987).

[7] A. C. Larsen, M. Guttormsen, R. Chankova, T. L Lönnroth, S. Messelt, F. Ingebretsen, J. Reckstad, A. Schiller, S. Siem, N. U. H. Syed, and A. Voinov, Phys. Rev. C **76**, 044303 (2007).

[8] S. G. Kadmenski, V. P. Markushev, and V. I. Furman, Yad. Fiz. **37**, 277 (1983) [Sov. J. Nucl. Phys. **37**, 165 (1983)].

[9] W. Hauser and H. Feshbach, Phys. Rev. **87**, 366 (1952).

[10] A. Wallner, B. Strohmaier, and H. Vonach, Phys. Rev. C **51**, 614 (1995).

[11] S. M. Grimes, Ohio University Report INPP-04-03, 2004 (unpublished).

[12] T. von Egidy and D. Bucurescu, Phys. Rev. C **72**, 044311 (2005); **73**, 049901(E) (2006).

[13] A. Gilbert and A. G. W. Cameron, Can. J. Phys. **43**, 1446 (1965).

[14] A. V. Ignatyuk, G. N. Smirenkin, and A. S. Tishin, Sov. J. Nucl. Phys. **21**, 255 (1975).
[15] P. Demetriou and S. Goriely, Nucl. Phys. **A695**, 95 (2001).
[16] T. Belgya, O. Bersillon, R. Capote, T. Fukahori, G. Zhigang, S. Goriely, M. Herman, A. V. Ignatyuk, S. Kailas, A. Koning, P. Oblozinsky, V. Plujko, and P. Young, Handbook for Calculations of Nuclear Reaction Data: Reference Input Parameter Library. Available online at http://www-nds.iaea.org/RIPL-2/, IAEA, Vienna, 2005.
[17] E. Gadioli and L. Zetta, Phys. Rev. **167**, 1016 (1968).

Chapter 6

Conclusions and outlook

6.1 Summary of the results

The quasi-continuum properties of the nuclei ^{44,45}Sc, ^{50,51}V, and $^{93-98}$Mo have been investigated by performing a statistical analysis of primary γ-ray spectra with the so-called Oslo method, thereby extracting the level density and γ-ray strength function. For all nuclei, the odd system displays an overall larger level density than the corresponding even system, with an approximately constant entropy difference in the quasi-continuum region. This odd-even effect is thought to be due to the valence nucleon behaving as a spectator to the underlying even-even or odd-even system. More pronounced structures are seen in the level density of nuclei near shell closure except for the Sc isotopes. An independent measurement of the level density of ^{44}Sc through Hauser-Feshbach modeling of α-evaporation spectra at Ohio University has confirmed the Oslo results with great accuracy, giving further confidence in the Oslo method.

From the level density, thermodynamic quantities such as entropy, temperature, and heat capacity have been extracted for the Mo isotopes. The results derived within the canonical ensemble indicate that a pairing phase transition takes place at $T_C \approx 0.7 - 1.0$ MeV, which is higher than the critical temperature observed in rare-earth nuclei [79]. The difference in the microcanonical entropies of ^{50,51}V and ^{97,98}Mo was found to be about $1k_B$, while for ^{93,94}Mo the difference was close to zero. These values are smaller than the result of $\approx 2k_B$ seen in mid-shell [80], which can be interpreted as effects of approaching shell closure.

In general, the γ-ray strength functions agree well with theoretical descriptions of the GEDR tail, and for the Sc isotopes also with experimental photoneutron and photoproton data. The low-energy enhancement first discovered in the γ-ray strength functions of ^{56,57}Fe was later also found in $^{93-98}$Mo, and is now confirmed to be present in ^{44,45}Sc and ^{50,51}V also. These findings suggest that this increase at low γ-ray energies is probably not due to peculiar structures that are specific for the Fe isotopes, but rather caused by some sort of collective mode(s) in a certain mass region.

6.2 Future upgrades of the experimental setup

6.2.1 New particle telescopes: the SiRi array

The nuclear physics group has been granted money for developing a new, highly efficient system of particle telescopes called the Silicon Ring (SiRi). Each particle telescope is designed as a trapeze, with an eight-fold segmented ΔE detector (see Fig. 6.1) in front of one E detector serving all eight front pads. There are in total eight such telescopes that arranged in a ring that can be placed at forward or backward angles, covering a solid angle fraction 6% of 4π. This is about 30 times the solid-angle coverage of the setup previously used in the Sc, V, and Mo experiments, and will thus give much better statistics. Also, the energy resolution is expected to improve, as the segmented ΔE detector allows for a better angular resolution. The new SiRi setup is developed by the company SINTEF (URL: `http://www.sintef.no/`) and Microcomponent (URL: `http://www.microcomponent.no/`), and is expected to be operational during fall 2008.

6.2.2 New γ-ray detectors: BrilLanCe

As described in Chapter 3, the CACTUS array consists mainly of NaI(Tl) scintillation detectors, which are preferred over Ge detectors in Oslo-type experiments due to their rather good and constant efficiency as a function of γ-ray energy. With the development of new scintillation materials such as LaBr$_3$(Ce), a better energy resolution can also be obtained without loss of efficiency, because these crystals have a resolution of about 2% (at $E_\gamma =$ 1.33 MeV) instead of 6% for NaI(Tl)s. The LaBr$_3$(Ce) crystals are actually superior to NaI(Tl)s when it comes to efficiency; from Fig. 6.2 it is seen that at $E_\gamma = 2.6$ MeV, the LaBr$_3$(Ce) detector has a 65% better efficiency than the NaI(Tl), and the resolution is almost three times better. In addition, the LaBr$_3$(Ce) detectors have excellent timing properties and temperature stability. The future prospect is therefore to replace all the NaI(Tl)s of the CACTUS array with LaBr$_3$(Ce) detectors. As the large LaBr$_3$(Ce) crystals

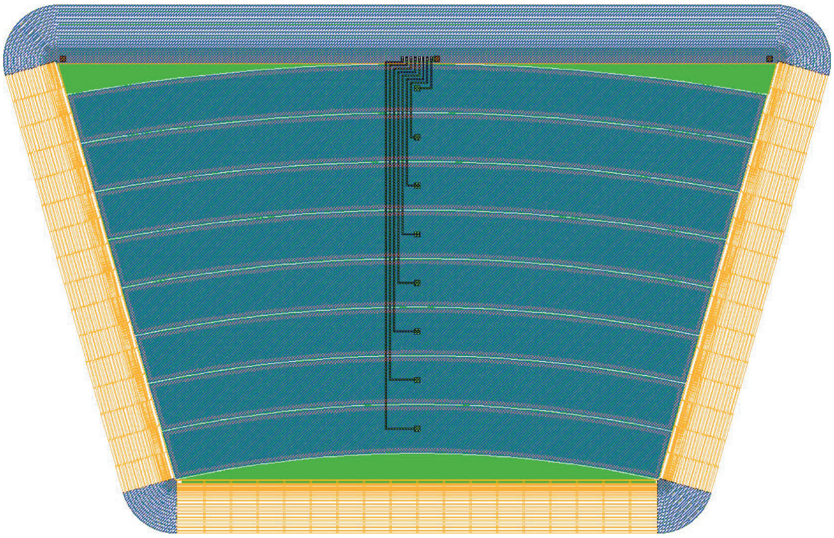

Figure 6.1: Layout of the Si ΔE detector that will be used in the new particle-telescope system SiRi. The eight strips and the guard ring are seen.

are still expensive, the replacement will be done stepwise. Several grant applications have been submitted for the purpose of raising money for the purchase of $4'' \times 5''$ $LaBr_3$(Ce) BrilLanCe®380 detectors. The time line of the new-generation CACTUS is however uncertain.

6.3 Outlook

Perhaps the most important task for future experiments is to determine the electromagnetic character and the multipolarity of the low-energy enhancement in order to be able to understand the underlying physics of this phenomenon. The multipolarity could in principle be found by measuring the γ-ray angular distribution with CACTUS; however, good statistics and experimental conditions are necessary. When it comes to the electromagnetic character, other experimental techniques must be utilized such as, e.g., the (n,2γ) two-step-cascade method, preferably with ARC neutrons to avoid peculiarities in the decay from thermal neutron capture states.

Another important aspect is to determine for which mass region and nuclei the low-energy enhancement disappears. It has not been seen in the rare-earth region [5, 77, 78], and preliminary OCL data on ^{116,117}Sn show no indication for any such behavior in these nuclei either. During fall 2008, an experimental campaign will start at OCL to study the $^{89-92}$Zr isotopes. Also, $^{105-108}$Pd will be investigated in the near future. The Pd isotopes

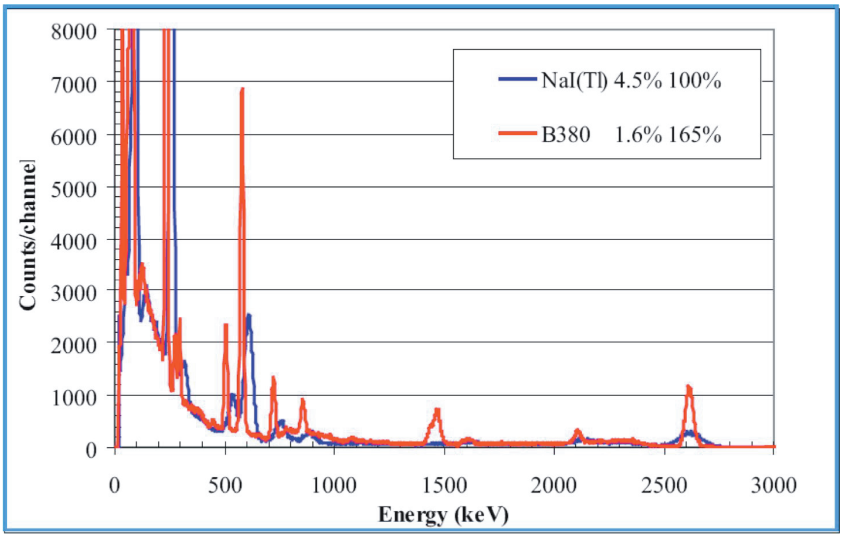

Figure 6.2: The γ-ray spectrum of the ^{228}Th decay chain measured with a $3'' \times 3''$ NaI(Tl) detector (blue line) and a $3'' \times 3''$ LaBr$_3$(Ce) BrilLanCe®380 detector (red line). The figure is taken from [81].

have $Z = 46$, right in between the Mo ($Z = 42$) and Sn ($Z = 50$) nuclei, and it is therefore an open question whether these nuclei will exhibit an upbend structure in their γ-ray strength functions.

The new SiRi particle-detector system will make it possible to measure evaporation ejectiles in backward angles. Thus, a comprehensive analysis with both the Oslo method and Hauser-Feshbach modeling of the particle spectra can be performed on the same data set. In parallell with the upgrade of the experimental setup, refinements of the Oslo method should be implemented. In this way, the nuclear physics group at OCL will be able to continue and improve the ongoing high-quality research in the fascinating field of quasi-continuum nuclear physics.

Appendices

Appendix A

Thermodynamics in nuclear systems

Thermodynamics and statistical mechanics have been effective tools to study macroscopic systems in equilibrium. In thermodynamics, the system is described from a macroscopic point of view by introducing appropriate quantities such as volume, pressure, and temperature. A large number of particles makes it possible to treat the microscopic description through statistical methods. In this appendix, some general thermodynamic concepts and quantities will briefly be described for the microcanonical and canonical ensemble theory, and their applicability to mesoscopic systems such as the nucleus will be discussed. For a thorough presentation of thermal physics, see the text book of C. Kittel and H. Kroemer [82].

A.1 General concepts

The *fundamental assumption* of thermal physics in general is that a closed system is equally likely to be in any of the quantum states accessible to it [82]. All accessible quantum states are thus assumed to be equally probable – there is no reason to prefer some accessible states over other accessible states. Suppose we have a closed system with g accessible states, and let s denote a general, accessible state. Then, the probability $P(s)$ of finding the system in this state is

$$P(s) = \frac{1}{g} \tag{A.1}$$

where

$$\sum_s P(s) = 1 \tag{A.2}$$

according to the fundamental assumption. For systems that are not closed, the energy U and the particle number N may vary. For such systems $P(s)$ will not be constant as in Eq. (A.1), but will have a functional dependence on U and N.

The average value of any observable physical property X when the system is in a quantum state s is given by

$$\langle X \rangle = \sum_s X(s)P(s). \tag{A.3}$$

For a closed system, we have

$$\langle X \rangle = \sum_s X(s)(1/g). \tag{A.4}$$

This is an example of an *ensemble average*: g similar systems are constructed, one in each accessible quantum state. The average of any property over the group is then called the ensemble average of that property. An *ensemble of systems* is composed of many systems, all constructed alike.

Let two systems $\mathcal{S}_1$ and $\mathcal{S}_2$ with energies E_1 and E_2 be brought in thermal contact with each other, that is, energy can be transferred freely from one to the other. The total, constant energy of the two systems is then $E = E_1 + E_2$. The total number of states accessible to the combined system is given by [82]

$$g(N, E) = \sum_{E_1 \leq E} g_1(N_1, E_1) g_2(N_2, E - E_1). \tag{A.5}$$

Here $g_1(N_1, E_1)$ is the number of accessible states of system 1 at energy E_1, and $g_2(N_2, E - E_1)$ is the number of accessible states of system 2 at energy $E_2 = E - E_1$. The *entropy* S of the total system is defined as

$$S \equiv k_B \ln g(N, E) \tag{A.6}$$

where k_B is the Boltzmann constant.

Taking the differential at extremum of $g(N, E)$ and E for an infinitesimal exchange of energy, we get:

$$\mathrm{d}g = \left(\frac{\partial g_1}{\partial E_1}\right)_{N_1} g_2 \mathrm{d}E_1 + \left(\frac{\partial g_2}{\partial E_2}\right)_{N_2} g_2 \mathrm{d}E_2 = 0, \tag{A.7}$$

$$\mathrm{d}E = \mathrm{d}E_1 + \mathrm{d}E_2 = 0, \tag{A.8}$$

which corresponds to thermal equilibrium of the two systems. Further, dividing Eq. (A.7) by $g_1 g_2$ and using the result of Eq. (A.8), we get

$$\frac{1}{g_1}\left(\frac{\partial g_1}{\partial E_1}\right)_{N_1} = \frac{1}{g_2}\left(\frac{\partial g_2}{\partial E_2}\right)_{N_2}, \tag{A.9}$$

which can be written as

$$\left(\frac{\partial \ln g_1}{\partial E_1}\right)_{N_1} = \left(\frac{\partial \ln g_2}{\partial E_2}\right)_{N_2}, \tag{A.10}$$

or, from the definition of entropy,

$$\left(\frac{\partial S_1}{\partial E_1}\right)_{N_1} = \left(\frac{\partial S_2}{\partial E_2}\right)_{N_2}. \tag{A.11}$$

For macroscopic systems in thermal equilibrium, this corresponds to the temperatures of the two systems being equal.

A.2 Microcanonical ensemble

A *microcanonical ensemble* consists of isolated physical systems with fixed particle number N and a well-defined (sharp) energy E within a small uncertainty $\delta E \ll E$. The quantum states are distributed according to the fundamental assumption of thermal physics. The number of accessible states $\Omega(E, N)$ is proportional to the density of states $\omega(E, N)$ per energy unit so that

$$\Omega(E, N) = \omega(E, N) \cdot \Delta E, \tag{A.12}$$

where ΔE is the energy bin.

The so-called *partition function* Z, which makes the connection between the microcanonical ensemble and thermodynamics, is simply given by the entropy:

$$Z(E, N) = S(E, N) = k_B \ln \Omega(E, N). \tag{A.13}$$

All thermodynamic quantities can be derived from Eq. (A.13), such as the temperature T given by the caloric curve

$$\frac{1}{T} = \left(\frac{\partial S(E, N)}{\partial E}\right)_N, \tag{A.14}$$

which defines the relationship between the temperature and energy of the system. The microcanonical heat capacity can then be expressed by

$$C_V = T\left(\frac{\partial S(E,N)}{\partial T}\right)_V, \tag{A.15}$$

where the volume V is held fixed.

When dealing with atomic nuclei, the microcanonical ensemble theory seems most appealing since the nucleus is a completely isolated system with no thermal contact with its surroundings. Therefore, it is probably the most appropriate ensemble to use as it corresponds to the actual, physical case when a nucleus is given a well-defined excitation energy in a very short time interval through a direct reaction. However, complications might arise when applying the above relations to the experimental nuclear entropy, that can be estimated through

$$S_{\mathrm{exp}}(E) = k_B \ln(\rho(E)/\rho_0), \tag{A.16}$$

where $\rho(E)$ is the measured level density at an excitation energy E, and ρ_0 is a constant set to ensure the fulfillment of the third law of thermodynamics: $S(T \to 0) = S_0$ for a constant S_0[1]. Here, we have neglected the spin-projection factor $(2\langle J(E)\rangle + 1)$ (see Ref. [12] for more details). Now, consider the bin size ΔE in Eq. (A.12). If it is too small, one can in principle have bins with no quantum states in it, especially at low excitation energy where the level spacing can be large. One therefore ends up with δ functions in the entropy. To ensure that the experimental entropy will have a sufficiently smooth behavior, the energy bin ΔE must be large enough so that more than one state is contained within each bin. On the other hand, the energy bin and thus the applied smoothing should not be too large, so that significant structures in the entropy are preserved. Ideally, the energy bin should be dependent on excitation energy to ensure an appropriate bin size in the various level-density regions.

Another peculiarity of the microcanonical ensemble when applied to nuclear level densities, is the appearance of negative branches in the temperature and the heat capacity as a direct consequence of the entropy not being a monotonic increasing function of excitation energy. The interpretation of these features is not straightforward. According to the Ehrenfest classification of phase transitions in macroscopic systems, a discontinuity of the temperature indicates a first-order phase transition, and discontinuity of the heat capacity indicates a second-order phase transition. It is

---

[1] For even-even nuclei the ground state represents a completely ordered system with only one possible configuration, and $S_0 = 0$ in this case.

however unclear whether this classification is valid for small systems such as the nucleus.

A.3 Canonical ensemble

An ensemble of physical systems that are in thermal equilibrium with a heat reservoir $\mathcal{R}$ at constant temperature T and can exchange energy (but not particles) with the reservoir, is called a *canonical ensemble*. The heat reservoir is assumed to be very large compared to the system, so that the reservoir temperature T is also the temperature of the system. As discussed for the microcanonical ensemble, the nucleus is not in contact with a heat reservoir, so the temperature will just be a control parameter related to the excitation energy when applying the canonical ensemble theory to a nuclear system.

The partition function in the canonical ensemble is given by

$$Z(T) = \sum_s \exp(-\varepsilon_s/k_B T). \tag{A.17}$$

The summation goes over the *Boltzmann factor* $\exp(-\varepsilon_s/k_B T)$ for all states s of the system. The probability $P(\varepsilon_s)$ for the system to be in state s with energy ε_s can be written as

$$P(\varepsilon_s) = \frac{\exp(-\varepsilon_s/k_B T)}{Z}, \tag{A.18}$$

with normalization $\sum P(\varepsilon_s) = Z/Z = 1$.

The average energy of the system for a given reservoir temperature can now be obtained from Eqs. (A.3) and (A.18):

$$\langle E \rangle = \langle \varepsilon \rangle = \sum \varepsilon_s P(\varepsilon_s) = \frac{\sum \varepsilon_s \exp(-\varepsilon_s/k_B T)}{Z}. \tag{A.19}$$

The energy E refers to those states of the system that can exchange energy with the reservoir. In contrast to the microcanonical ensemble, where the energy is a sharp quantity, the energy in the canonical ensemble is fluctuating around the mean value $\langle E \rangle$.

A useful quantity in the canonical ensemble is the *Helmholtz free energy* given by the function

$$F = \langle E \rangle - TS, \tag{A.20}$$

or, expressed through the partition function,

$$F = -k_B T \ln Z. \tag{A.21}$$

Taking the differential of Eq. (A.20) and using the *thermodynamic identity*

$$\mathrm{d}\langle E\rangle = T\mathrm{d}S - p\mathrm{d}V \tag{A.22}$$

where p is the pressure, we find that the entropy can be written as

$$S(T) = -\left(\frac{\partial F}{\partial T}\right)_V, \tag{A.23}$$

for a constant volume, and the average energy can then be expressed as

$$\langle E\rangle = -T^2\left(\frac{\partial(F/T)}{\partial T}\right)_V. \tag{A.24}$$

The canonical heat capacity is given by

$$C_V(T) = \left(\frac{\partial\langle E\rangle}{\partial T}\right)_V. \tag{A.25}$$

When applying the canonical ensemble theory to the experimental level density, one must take into account the energy bin for which the level density is defined in the partition function. This can be done in the following way:

$$Z(T) = \sum_i \rho(E_i)\Delta E_i \exp(-E_i/k_BT), \tag{A.26}$$

where the summation goes over all energy bins i. Equation (A.26) represents the Laplace transform of the multiplicity of levels $\rho(E_i)\Delta E_i$ within the energy bin ΔE_i. Due to the summation the Laplace transform performs a significant averaging and smoothing of eventual structural changes in the experimental $\rho(E)$. However, a bump in the heat capacity at $T \approx 0.5$ MeV has been observed in rare-earth nuclei [79]. One possible interpretation of this S-shaped curve is that a transition from a phase with strong pair correlations to a phase with weak or no pair correlations takes place at this temperature.

Appendix B

Connection between reduced transition probability and γ-ray strength function

This Appendix explains briefly the relations between reduced transition probabilities, γ-ray strength functions, and photoabsorption cross sections. In addition, it is shown how to calculate the fraction of the energy-weighted sum rule for E1 radiation that is filled by the summed E1 transition strengths.

B.1 Basic relations

In the general theory of photon radiation, the decay rate λ (in units of s^{-1}) can be expressed by the reduced transition probability $B(XL)$, where X denotes the electric or magnetic character, and L is the multipolarity of the radiation. The reduced transition probability for a transition from an initial state i to a final state f is given by [83]

$$B(XL, J_i \rightarrow J_f) = \frac{1}{2J_i + 1} \sum_{M_i, M_f} |\langle f|\mathcal{O}_{LM_L}|i\rangle|^2, \tag{B.1}$$

where $\mathcal{O}$ is the electric ($X = \mathrm{E}$) or the magnetic ($X = \mathrm{M}$) transition operator. We note here that B is defined as an average over the substates M_i (by the factor in front of the sum), and a sum over M_f. It is common to distinguish between excitation ($E_i < E_f$) and decay (de-excitation, $E_i > E_f$) with the notations $B\uparrow$ and $B\downarrow$, respectively. From Eq. (B.1), we find that

$$\frac{B\uparrow}{B\downarrow} = \frac{B(i \rightarrow f)}{B(f \rightarrow i)} = \frac{2J_f + 1}{2J_i + 1}. \tag{B.2}$$

We will use the notation

$$g = \frac{2J_f + 1}{2J_i + 1} \tag{B.3}$$

in the following.

The left-hand side of Eq. (B.1) is directly connected to the decay rate λ, which leads to a relation between λ and $B\!\downarrow$ [83]:

$$\lambda(XL) = \frac{8\,\pi\,(L+1)}{L\,[(2L+1)!!]^2}\frac{1}{\hbar}\left(\frac{E_\gamma}{\hbar\, c}\right)^{2L+1} B\!\downarrow(XL). \tag{B.4}$$

The decay width Γ and the decay rate λ of a specific energy level are connected by

$$\Gamma = \hbar\lambda, \tag{B.5}$$

and the expressions for dipole (E1, M1) and quadrupole (E2, M2) transitions thus become

$$\Gamma(X1) = \frac{16\,\pi}{9}\left(\frac{E_\gamma}{\hbar c}\right)^3 B\!\downarrow(X1) \tag{B.6}$$

and

$$\Gamma(X2) = \frac{4\,\pi}{75}\left(\frac{E_\gamma}{\hbar c}\right)^5 B\!\downarrow(X2), \tag{B.7}$$

respectively.

In general, we have the following relation between the reduced transition probability $B(XL)$ and the γ-ray strength function $f_{XL}(E_\gamma)$ (Chapter 2):

$$\frac{\mathrm{d}B\!\uparrow(XL)}{\mathrm{d}E_\gamma} = \frac{L\,[(2L+1)!!]^2(2L+1)}{8\,\pi\,(L+1)}\cdot(\hbar c)^{(2L+1)} f_{XL}(E_\gamma). \tag{B.8}$$

Similarly, the photoabsorption cross section $\sigma_{XL}(E_\gamma)$ (next section) is connected to $B(XL)$ by

$$\frac{\mathrm{d}B\!\uparrow(XL)}{\mathrm{d}E_\gamma} = \frac{L\,[(2L+1)!!]^2}{8\,\pi^3\,(L+1)}\cdot\left(\frac{\hbar c}{E_\gamma}\right)^{(2L+1)} \sigma_{XL}(E_\gamma)\,. \tag{B.9}$$

B.2 Photoabsorption cross section

In the semiclassical theory of the interaction of photons with nuclei [84, 85], the shape of the resonance in the absorption cross section is described by the Lorentzian shape

$$\sigma(E_\gamma) = \frac{\sigma_r}{1 + [(E_\gamma^2 - E_r^2)^2/E_\gamma^2\Gamma_r^2]}, \tag{B.10}$$

where E_γ is the photon energy. The resonance is described by the resonance parameters as discussed in Chapter 2: the energy centroid E_r, the peak cross section σ_r and the width Γ_r.

The area under $\sigma(E_\gamma)$ is called the energy-integrated cross section and is given by

$$\sigma = \int_0^\infty \sigma(E_\gamma)\, dE_\gamma = \frac{\pi}{2}\sigma_r\Gamma_r. \tag{B.11}$$

Despite of the name, this is actually no cross section, but is found to be a fruitful concept. In particular, the energy-weighted sum rule for E1 photoabsorption in the absence of exchange forces is given by [35]

$$\sigma_{\mathrm{E1}} = \int_0^\infty \sigma(E_\gamma)\, dE_\gamma = \frac{2\pi^2 e^2\hbar}{mc}\frac{NZ}{A} \simeq 60\frac{NZ}{A}\ [\mathrm{MeV}\cdot\mathrm{mb}]\,. \tag{B.12}$$

B.3 Photon scattering cross section

The total cross section of resonance-scattered photons with energy E_γ to a final level f is described by the Breit-Wigner shape [86, 87]

$$\sigma_f(E_\gamma) = \pi\left(\frac{\hbar c}{E_r}\right)^2 \frac{g}{2}\frac{\Gamma_0\Gamma_f}{(E_\gamma - E_r)^2 + \Gamma^2/4}. \tag{B.13}$$

Here, the cross section depends on

- Γ_0, the decay width of the ground state transition
- Γ_f, the decay width of the outgoing channel
- Γ, the total decay width

We calculate the energy-integrated cross section and find

$$\sigma_f = \int_0^\infty \sigma_f(E_\gamma)\, dE_\gamma = \pi^2 g\left(\frac{\hbar c}{E_r}\right)^2 \frac{\Gamma_f}{\Gamma}\Gamma_0. \tag{B.14}$$

Summing over all possible final states ($\sum_f \Gamma_f = \Gamma$), we obtain for the absorption cross-section:

$$\sigma = \pi^2 g\left(\frac{\hbar c}{E_r}\right)^2 \Gamma_0. \tag{B.15}$$

B.4 Putting things together

We now set σ from Eq. (B.11) equal σ from Eq. (B.15) and replace Γ_0 with Eqs. (B.6) and (B.7) for dipole and quadrupole transitions, respectively. Then we find

$$g\,B\!\downarrow(X1) = \frac{9\,\sigma_r\Gamma_r}{32\,\pi^2}\left(\frac{\hbar c}{E_r}\right) \tag{B.16}$$

and

$$g\,B\!\downarrow(X2) = \frac{75\,\sigma_r\Gamma_r}{8\,\pi^2}\left(\frac{\hbar c}{E_r}\right)^3, \tag{B.17}$$

for dipole and quadrupole transitions, respectively.

B.5 Summed B↑(E1) strength and its fraction of the energy-weighted sum rule

For electric dipole radiation, Eq. (B.9) gives

$$\frac{\mathrm{d}B\!\uparrow(\mathrm{E1})}{\mathrm{d}E_\gamma} = \frac{9}{16\pi^3}\cdot\frac{\hbar c}{E_\gamma}\,\sigma_{\mathrm{E1}}(E_\gamma)\,, \tag{B.18}$$

and solving for the cross section σ_{E1}, we get

$$\sigma_{\mathrm{E1}}(E_\gamma) = \frac{16\pi^3}{9\hbar c}\frac{\mathrm{d}B\!\uparrow(\mathrm{E1})}{\mathrm{d}E_\gamma}E_\gamma\,. \tag{B.19}$$

Assuming that $\sigma_{\mathrm{E1}}(E_\gamma)$ can be described by the Lorentzian shape given in Eq. (B.10) and integrating over all γ-ray energies, we get the result of Eq. (B.11) on the left-hand side. Integrating the right-hand side, we must solve

$$\frac{16\pi^3}{9\hbar c}\int_0^\infty \frac{\mathrm{d}B\!\uparrow(\mathrm{E1})}{\mathrm{d}E_\gamma}E_\gamma \mathrm{d}E_\gamma\,. \tag{B.20}$$

Let us assume that $\mathrm{d}B\uparrow/\mathrm{d}E_\gamma$ can be described by a sum of δ functions with coefficients B_i, i.e.,

$$\frac{\mathrm{d}B\!\uparrow(\mathrm{E1})}{\mathrm{d}E_\gamma} = \sum_i B_i\delta(E_{i\gamma}-E_\gamma) \tag{B.21}$$

where the summation goes over all states i. Using this in Eq. (B.20), we obtain for the integral

$$\sum_i B_i\int_0^\infty \delta(E_{i\gamma}-E_\gamma)E_\gamma\mathrm{d}E_\gamma = \sum_i B_i\cdot E_{\gamma,i}. \tag{B.22}$$

Noting that the average γ-ray energy $\langle E_\gamma \rangle$ of all discrete states is given by

$$\langle E_\gamma \rangle = \frac{\sum_i B_i E_{\gamma,i}}{\sum_i B_i}, \tag{B.23}$$

we find

$$\langle E_\gamma \rangle \sum_i B_i = \sum_i B_i E_{\gamma,i} \,. \tag{B.24}$$

Finally, inserting the above into Eq. (B.20), we obtain

$$\frac{16\pi^3}{9\hbar c} \cdot \langle E_\gamma \rangle \sum_i B_i = \frac{\pi}{2} \sigma_r \Gamma_r . \tag{B.25}$$

We can then find the fraction η of the energy-weighted sum rule:

$$\eta = \frac{\frac{16\pi^3}{9\hbar c} \cdot \langle E_\gamma \rangle \sum_i B_i}{60 \frac{NZ}{A}} \,. \tag{B.26}$$

Note that $\sum_i B_i$ is often given in units of $e^2\mathrm{fm}^2$ (the CGS system) in the literature, while the energy-integrated cross section (Eq. (B.11) and the energy-weighted sum rule (Eq. (B.12) are given in SI units. We have the following relations between CGS and SI units for the summed strength of E1 radiation:

$$\left(e^2\mathrm{fm}^2\right)_{\mathrm{CGS}} = \left(\frac{e^2\mathrm{fm}^2}{4\pi\epsilon_0}\right)_{\mathrm{SI}}, \tag{B.27}$$

and for M1 radiation:

$$\left(\mu_N^2\right)_{\mathrm{CGS}} = \left(\frac{e\hbar}{2mc}\right)^2_{\mathrm{CGS}} = \left(\frac{e\hbar}{2mc}\right)^2_{\mathrm{SI}} \cdot \frac{1}{4\pi\epsilon_0} = \frac{e^2\hbar^2\mu_0}{16\pi m^2}, \tag{B.28}$$

Here, μ_N is the nuclear magneton. We have used the relation $c = 1/\sqrt{\epsilon_0\mu_0}$, where ϵ_0 is the electric vacuum permittivity, and μ_0 is the magnetic vacuum permeability.

Appendix C

Details of E1, M1 and E2 strength-function models

C.1 Global systematics of GEDR parameters

For nuclei close to the β-stability line and where the GEDR parameters are unknown, the following global parameterization is recommended in RIPL-2 [19] for *spherical nuclei*:

$$E_r \equiv E_0 = 31.2A^{-1/3} + 20.6A^{-1/6} \ \text{[MeV]}, \tag{C.1}$$

$$\Gamma_r = 0.026E_r^{1.91} \ \text{[MeV]}, \tag{C.2}$$

$$\sigma_r \equiv \sigma_0 = 1.2 \times 120\,\frac{NZ}{A\pi\Gamma_r} \ \text{[mb]}. \tag{C.3}$$

The factor of 1.2 in the expression for σ_r is the value of the experimental energy-weighted sum in units of the classical dipole Thomas-Reiche-Kuhn sum rule $\sigma_{\text{TRK}} \simeq 60(NZ/A)$ [MeV mb], see [35] for more details.

For *deformed nuclei*, which are usually considered axially symmetric with a radius defined by

$$R(\theta) = R_0'(1 + \alpha_2 P_2 \cos\theta) = R_0'(1 + \beta_2 Y_{20}), \tag{C.4}$$

$$R_0' = R_0/\lambda,\ \lambda^3 = 1 + \frac{3}{5}\alpha_2^2 + \frac{2}{35}\alpha_2^3, \tag{C.5}$$

where R_0 is the radius of a spherical nucleus of equal volume, $P_2 \cos\theta$ is the Legendre polynomial, and $Y_{20} = (5/4\pi)^{1/2}P_2$ is the spherical harmonic. The constant α_2 is related to the ground-state quadrupole deformation β_2 by

$$\alpha_2 = \sqrt{\frac{5}{4\pi}}\beta_2. \tag{C.6}$$

The E1 strength function in deformed nuclei is defined as the sum of two components, each with the corresponding centroid energy $E_{r,j}$, damping width $\Gamma_{r,j}$ and peak value of the photo-absorption cross section $\sigma_{r,j}$ where $j = 1$ and $j = 2$ correspond to collective vibrations along and perpendicular to the symmetry axis. The global parameterization gives [19]

$$E_{r1} = E_{r2} / \left[0.911 \frac{a_0}{b_0} + 0.089 \right], \quad E_{r2} = E_0 \frac{1}{b_0} \left[1 - 1.51 \cdot 10^{-2} \cdot (a_0^2 - b_0^2) \right], \tag{C.7}$$

$$\Gamma_{r1} = 0.026 E_{r1}^{1.91}, \qquad \Gamma_{r2} = 0.026 E_{r2}^{1.91}, \tag{C.8}$$

$$\sigma_{r1} = \frac{2}{3} \sigma_0, \qquad \sigma_{r2} = \frac{1}{3} \sigma_0, \tag{C.9}$$

with relative semi-axes of a spheroid a_0, b_0 defined as

$$a_0 \equiv R(\theta = 0)/R_0 = (1 + \alpha_2)/\lambda, \tag{C.10}$$

$$b_0 \equiv R(\theta = \pi/2)/R_0 = (1 - 0.5\alpha_2)/\lambda. \tag{C.11}$$

C.2 Enhanced Generalized Lorentzian model

As described in Chapter 2, the Enhanced Generalized Lorentzian (EGLO) model for the E1 strength function is given as

$$f_{\mathrm{E1}}^{\mathrm{EGLO}}(E_\gamma, T_f) = \frac{1}{3\pi^2 \hbar^2 c^2} \sigma_r \Gamma_r \left[E_\gamma \frac{\Gamma_{\mathcal{K}}(E_\gamma, T_f)}{(E_\gamma^2 - E_r^2)^2 + E_\gamma^2 \Gamma_{\mathcal{K}}^2(E_\gamma, T_f)} + 0.7 \frac{\Gamma_{\mathcal{K}}(E_\gamma = 0, T_f)}{E_r^3} \right] \; [\mathrm{MeV}^{-3}]. \tag{C.12}$$

Again, the Lorentzian parameters σ_r (in mb), Γ_r (in MeV) and E_r (in MeV) are the peak cross section, width and centroid energy of the GEDR, respectively, and T_f is the nuclear temperature of the final states. The expression for the temperature-dependent width $\Gamma_{\mathcal{K}}$ is

$$\Gamma_{\mathcal{K}}(E_\gamma, T_f) = \mathcal{K}(E_\gamma) \frac{\Gamma_r}{E_r^2} (E_\gamma^2 + 4\pi^2 T_f^2), \tag{C.13}$$

where the empirical function $\mathcal{K}(E_\gamma)$ is given by

$$\mathcal{K}(E_\gamma) = \kappa + (1 - \kappa) \frac{E_\gamma - E_0}{E_r - E_0}. \tag{C.14}$$

The factor κ depends on the model adopted for the level density, while the constant reference energy E_0 is set to 4.5 MeV. If the BSFG model is used, κ is defined by:

$$\kappa = \begin{cases} 1, & \text{if } A < 148, \\ 1 + 0.09(A-148)^2 \exp(-0.18(A-148)), & \text{if } A \geq 148. \end{cases} \tag{C.15}$$

The equations (C.13) − (C.15) provide an enhanced E1 strength function for nuclei between $A = 150 - 170$, so that the EGLO model is able to give reasonable agreement with experimental data in the mass region $A = 50 - 200$ [19].

C.3 Modified Lorentzian model

The Modified Lorentzian (MLO) model for the E1 strength function is given by

$$f_{\mathrm{E1}}^{\mathrm{MLO}}(E_\gamma, T_f) = \frac{1}{3\pi^2\hbar^2c^2}\mathcal{L}(E_\gamma, T_f)\sigma_r\Gamma_r\frac{E_\gamma\Gamma(E_\gamma, T_f)}{(E_\gamma^2 - E_r^2)^2 + E_\gamma^2\Gamma^2(E_\gamma, T_f)} \ [\mathrm{MeV}^{-3}], \tag{C.16}$$

where

$$\mathcal{L}(E_\gamma, T_f) = \frac{1}{1 - \exp(-E_\gamma/T_f)} \tag{C.17}$$

is a scaling factor that determines the enhancement of the γ-ray strength function in a heated nucleus as compared to a cold nucleus. The damping width is expressed as

$$\Gamma(E_\gamma, T_f) = \Gamma_C(E_\gamma, T_f) + \Gamma_F(E_\gamma), \tag{C.18}$$

where Γ_C represents the collisional damping width and Γ_F simulates the fragmentation component of the total damping width. The component Γ_C is inversely proportional to the collision relaxation time τ in the isovector channel of dipole distortion of the Fermi surface [19], and depends linearly on the γ energy within the doorway-state relaxation mechanism of heated nuclei:

$$\Gamma_C = \frac{\hbar}{\tau(E_\gamma, T_f)} = C_{\mathrm{coll}}E_r(E_\gamma + U), \tag{C.19}$$

where $U = aT_f^2$ is the thermal excitation energy within the Fermi-gas model. The collision parameter C_{coll} is determined from the in-medium cross section $\sigma(\mathrm{np})$ of neutron-proton scattering near the Fermi surface:

$$C_{\mathrm{coll}} = \frac{1}{4\pi^2}\frac{16m}{9\hbar^2}\sigma(\mathrm{np}) = c_f \cdot F, \tag{C.20}$$

$$c_f = \frac{1}{4\pi^2}\frac{16m}{9\hbar^2}\sigma_f(\mathrm{np}) = 5.39 \cdot 10^{-3}\,[\mathrm{MeV}^{-1}],\; F = \frac{\sigma(\mathrm{np})}{\sigma_f(\mathrm{np})}, \tag{C.21}$$

in which m is the nucleon mass, and the in-medium cross section $\sigma(\mathrm{np})$ is assumed to be proportional with a factor F to the free-space cross section $\sigma_f(\mathrm{np}) = 5\,\mathrm{fm}^2$ near the Fermi surface. This relationship for C_{coll} ensures agreement between the relaxation time given in Eq. (C.19) and the relaxation time calculated from the collision integral within the Fermi-liquid approach at $E_\gamma = E_r$ and $T_f = 0$. Note that the value given here for c_f is the updated value from V. Plujko [88]. The factor F is found to be equal to unity ($F = 1.0$) by fitting the MLO model to experimental γ-decay strengths.

The fragmentation width Γ_F is imitated by the one-body ("wall") relaxation component Γ_W scaled with a factor k_s as discussed in [19, 41, 42]:

$$\Gamma_F(E_\gamma) = k_s(E_\gamma)\Gamma_W,\; \Gamma_W = \frac{3\hbar v_F}{4R_0} \tag{C.22}$$

at the Fermi energy $\epsilon_F = mv_F^2/2 = 37$ MeV. There is a misprint in [19], where it is stated that $\Gamma_W = 36.43 \cdot A^{-1/3}$. However, using the average nucleon mass $m = (m_p + m_n)/2 = 938.9265\,\mathrm{MeV}/c^2$, and $(\hbar c)^2 = (197.329)^2$ $\mathrm{MeV}^2\,\mathrm{fm}^2/c^2$, we get $\hbar^2/m = 41.4715\,\mathrm{MeV\,fm}^2$. Further,

$$(\hbar v_F)^2 = \hbar^2 \cdot \frac{2\epsilon_F}{m} = \frac{\hbar^2}{m} \cdot 2\epsilon_F, \tag{C.23}$$

and finally,

$$\Gamma_W = \frac{3\hbar v_F}{4R_0} = \frac{3}{4} \cdot \frac{\sqrt{\frac{\hbar^2}{m} \cdot 2\epsilon_F}}{r_0 \cdot A^{-1/3}} = 32.72 \cdot A^{-1/3} \tag{C.24}$$

where the (spherical) nuclear radius R_0 is given by the standard relationship $R_0 = r_0 \cdot A^{1/3}$, and $r_0 = 1.27$ fm is used.

For simplicity, an energy-dependent power approximation is adopted for the factor k_s:

$$k_s(E_\gamma) = \begin{cases} k_r + (k_0 - k_r)\,|(E_\gamma - E_r)|^{n_s} & \text{for } E_\gamma < 2E_r, \\ k_0 & \text{for } E_\gamma \geq 2E_r, \end{cases} \tag{C.25}$$

where the quantities $k_0 \equiv k_s(E_\gamma = 0)$ and $k_r \equiv k_s(E_\gamma = E_r)$ determine the contribution of the "wall" component to the width at zero energy and the

GDR energy, respectively. The constant k_r is determined from the condition $\Gamma(E_\gamma = E_r, T_f = 0) = \Gamma_r$ in cold nuclei. According to this condition and Eqs. (C.18)– (C.25), the following relationship is obtained:

$$\Gamma_r = \Gamma_C(E_r, T_f = 0) + k_s(E_r)\Gamma_W = C_{\text{coll}}E_r^2 + k_r\Gamma_W, \tag{C.26}$$

whence it follows that

$$k_r = \frac{\Gamma_r - C_{\text{coll}}E_r^2}{\Gamma_W}. \tag{C.27}$$

By fitting the predictions of the MLO model to experimental γ-decay strengths, the values for k_0 and n_s were found to be $k_0 = 0.3,\ n_s = 1$.

For deformed nuclei, the fragmentation damping widths Γ_{F1}, Γ_{F2} of the collective vibrations along two principal axes of a spheroid are assumed to be proportional to the dipole widths Γ_{s1}, Γ_{s2} of the surface dissipative model [89]:

$$\Gamma_{Fj}(E_\gamma) = k_s(E_\gamma)\Gamma_{sj},\ \Gamma_{s1} = \Gamma_W/a_0^\delta,\ \Gamma_{s2} = \Gamma_W/b_0^\delta,\ \delta = 1.6, \tag{C.28}$$

where $j = 1, 2$ corresponds to collective vibrations along and perpendicular to the axis of symmetry, and a_0 and b_0 are relative semi-axes of a spheroid as given in Sect. C.1.

C.4 Generalized Fermi Liquid model

The Generalized Fermi Liquid (GFL) model [43, 19] is given in Chapter 2 as

$$f_{\text{E1}}^{\text{GFL}}(E_\gamma, T_f, \beta_2) = \frac{1}{3\pi^2\hbar^2c^2}\sigma_r\Gamma_r\frac{\mathcal{K}_{\text{GFL}}E_\gamma\Gamma_m(E_\gamma, T_f)}{(E_\gamma^2 - E_r^2)^2 + \mathcal{K}_{\text{GFL}}E_\gamma^2\Gamma_m^2(E_\gamma, T_f)}. \tag{C.29}$$

The factor $\mathcal{K}_{\text{GFL}}$ is expressed through the Landau-Migdal parameters F_0', F_1' of the quasi-particle interaction in the isovector channel of the Fermi system:

$$\mathcal{K}_{\text{GFL}} = \sqrt{E_r/E_0} = \sqrt{\frac{1 + F_1'/3}{1 + F_0'}} = 0.63, \tag{C.30}$$

with $F_0' = 1.49$ and $F_1' = -0.04$ according to [43], and E_0 is the average energy for one-particle one-hole states forming the GEDR. Following [19], the term $\mathcal{K}_{\text{GFL}}E_\gamma^2\Gamma_m^2(E_\gamma, T_f)$ is added in the denominator to avoid singularity at the resonance centroid energy. Also, $\mathcal{K}_{\text{GFL}}$ is included in the nominator to preserve the standard relationship between the strength function at the resonance energy E_r and peak value σ_r of the photo-absorption cross section.

The GFL model takes into account a dipole-quadrupole interaction term so that Γ_m is given by a sum of a collisional damping width Γ_C and the term Γ_{dq} that simulates the fragmentation width:

$$\Gamma_m(E_\gamma, T_f) = \Gamma_C(E_\gamma, T_f) + \Gamma_{\mathrm{dq}}(E_\gamma, \beta_2). \tag{C.31}$$

The width Γ_{dq} results from spreading of the GEDR over surface quadrupole vibrations as a consequence of the dipole-quadrupole interaction, and is expressed as

$$\Gamma_{\mathrm{dq}}(E_\gamma, \beta_2) = \sqrt{\frac{5\ln 2}{\pi}}\,|\beta_2|\,\sqrt{1+\frac{E_2}{E_\gamma}} = C_{\mathrm{dq}}\sqrt{E_\gamma^2\beta_2^2 + E_\gamma s_2},\ s_2 = E_2\beta_2^2. \tag{C.32}$$

Here, the constant $C_{\mathrm{dq}} = \sqrt{5\ln 2/\pi} = 1.05$, β_2 is the deformation parameter , and E_2 is the energy of the first excited 2^+ state (in MeV). If E_2 is not known, s_2 can be estimated from global parameterization by

$$s_2 = 217.16/A^2. \tag{C.33}$$

The collisional component corresponds to the damping width in the infinite Fermi-liquid model:

$$\Gamma_C = C_f(E_\gamma^2 + 4\pi^2 T_f^2). \tag{C.34}$$

The constant C_f is determined by defining the total GFL damping width at the GEDR energy E_r in cold nuclei to be equal to Γ_r:

$$\Gamma_m(E_\gamma = E_r, T_f = 0) = \Gamma_C(E_r, 0) + \Gamma_{\mathrm{dq}}(E_r) = C_f E_r^2 + C_{\mathrm{dq}}\sqrt{E_r^2\beta_2^2 + E_r s_2}, \tag{C.35}$$

which leads to

$$C_f = \frac{\Gamma_r - C_{\mathrm{dq}}\sqrt{E_r^2\beta_2^2 + E_r s_2}}{E_r^2}. \tag{C.36}$$

C.5 Giant magnetic dipole resonance

To describe the distribution of the M1 strength, two prescriptions are usually used; either the single-particle model [34] where the fragmented strength is adjusted to experimental data on primary M1 transitions to correct for a global overestimation by this model, or a giant resonance model based on the existence of an M1 giant resonance assumed to be related to shell-model spin-flip transitions between $\ell \pm 1/2$ single-particle states (see A. Bohr and B. Mottelson [75]).

An expression for the magnetic spin-flip giant resonance is recommended in [19] for the M1 strength function. Its functional form can be described by, e.g., a standard Lorentzian,

$$f_{\mathrm{M1}}(E_\gamma) = \frac{1}{3\pi^2\hbar^2c^2}\frac{\sigma_{\mathrm{M1}}\Gamma_{\mathrm{M1}}^2 E_\gamma}{(E_\gamma^2 - E_{\mathrm{M1}}^2)^2 + \Gamma_{\mathrm{M1}}^2 E_\gamma^2}\ [\mathrm{MeV}^{-3}], \tag{C.37}$$

with global parameterization

$$E_{\mathrm{M1}} = 41 \cdot A^{-1/3}\,[\mathrm{MeV}],\ \Gamma_{\mathrm{M1}} = 4\,[\mathrm{MeV}]. \tag{C.38}$$

To determine the peak cross section σ_{M1} of the M1 spin-flip resonance if it is not known experimentally, one of the following relations are used:

$$f_{\mathrm{M1}} = 1.58 \cdot A^{0.47} \qquad \text{at} \simeq 7\,\mathrm{MeV}, \tag{C.39}$$

$$\frac{f_{\mathrm{E1}}}{f_{\mathrm{M1}}} = 0.0588 \cdot A^{0.878} \qquad \text{at} \simeq 7\,\mathrm{MeV}. \tag{C.40}$$

Note that since there is still a very limited amount of experimental information on the M1 giant resonance parameters, the global systematics is quite uncertain [90].

C.6 Giant electric quadrupole resonance

Radiation of E2 type is linked to the excitation of the giant quadrupole isoscalar resonance, and a standard Lorentzian is recommended to describe the E2 strength [19]:

$$f_{\mathrm{E2}}(E_\gamma) = \frac{1}{3\pi^2\hbar^2c^2}\frac{\sigma_{\mathrm{E2}}\Gamma_{\mathrm{E2}}^2 E_\gamma}{(E_\gamma^2 - E_{\mathrm{E2}}^2)^2 + \Gamma_{\mathrm{E2}}^2 E_\gamma^2}\ [\mathrm{MeV}^{-3}]. \tag{C.41}$$

A global parameterization is given by [19, 90]:

$$E_{\mathrm{E2}} = 63 \cdot A^{-1/3} \qquad [\mathrm{MeV}], \tag{C.42}$$

$$\Gamma_{\mathrm{E2}} = 6.11 - 0.012A \qquad [\mathrm{MeV}], \tag{C.43}$$

$$\sigma_{E2} = \frac{0.00015 \cdot Z^2 E_{\mathrm{E2}}^2}{A^{1/3}\Gamma_{\mathrm{E2}}} \qquad [\mathrm{mb}]. \tag{C.44}$$

Bibliography

[1] K. S. Krane, *Introductory Nuclear Physics*, John Wiley& Sons, Inc., 1988, pp. 416-419.

[2] M. Guttormsen, T.S. Tveter, L. Bergholt, F. Ingebretsen, and J. Rekstad, Nucl. Instrum. Methods Phys. Res. A **374**, 371 (1996).

[3] M. Guttormsen, T. Ramsøy, and J. Rekstad, Nucl. Instrum. Methods Phys. Res. A **255**, 518 (1987).

[4] A. Schiller, L. Bergholt, M. Guttormsen, E. Melby, J. Rekstad, and S. Siem, Nucl. Instrum. Methods Phys. Res. A **447**, 498 (2000).

[5] E. Melby, L. Bergholt, M. Guttormsen, M. Hjorth-Jensen, F. Ingebretsen, S. Messelt, J. Rekstad, A. Schiller, S. Siem, and S. W. Ødegård, Phys. Rev. Lett. **83**, 3150 (1999).

[6] A. Schiller, A. Voinov, E. Algin, J. A. Becker, L. A. Bernstein, P. E. Garrett, M. Guttormsen, R. O. Nelson, J. Rekstad, S. Siem, Phys. Lett. B **633** 225 (2006).

[7] A. Schiller, M. Guttormsen, E. Melby, J. Rekstad, S. Siem, and A. Voinov, nucl-ex/0011018; Los Alamos preprint server: `http://xxx.lanl.gov/abs/nucl-ex/0011018`.

[8] A. Voinov, E. Algin, U. Agvaanluvsan, T. Belgya, R. Chankova, M. Guttormsen, G.E. Mitchell, J. Rekstad, A. Schiller and S. Siem, Phys. Rev. Lett **93**, 142504 (2004).

[9] M. Guttormsen, R. Chankova, U. Agvaanluvsan, E. Algin, L.A. Bernstein, F. Ingebretsen, T. Lönnroth, S. Messelt, G.E. Mitchell, J. Rekstad, A. Schiller, S. Siem, A.C. Sunde, A. Voinov and S. Ødegård, Phys. Rev. C **71**, 044307 (2005).

[10] A. C. Larsen, M. Guttormsen, R. Chankova, F. Ingebretsen, T. Lönnroth, S. Messelt, J. Rekstad, A. Schiller, S. Siem, N. U. H. Syed, and A. Voinov, Phys. Rev. C **76**, 044303 (2007).

[11] A. V. Voinov, S. M. Grimes, A. C. Larsen, C. R. Brune, M. Guttormsen, T. Massey, A. Schiller, S. Siem, and N. U. H. Syed, Phys. Rev. C **77**, 034613 (2008).

[12] A. C. Larsen, R. Chankova, M. Guttormsen, F. Ingebretsen, T. Lönnroth, S. Messelt, J. Rekstad, A. Schiller, S. Siem, N. U. H. Syed, A. Voinov, and S. W. Ødegård, Phys. Rev. C **73**, 064301 (2006).

[13] R. Chankova, A. Schiller, U. Agvaanluvsan, E. Algin, L. A. Bernstein, M. Guttormsen, F. Ingebretsen, T. Lönnroth, S. Messelt, G. E. Mitchell, J. Rekstad, S. Siem, A. C. Larsen, A. Voinov, and S. W. Ødegård, Phys. Rev. C **73**, 034311 (2006).

[14] S. Siem, M. Guttormsen, K. Ingeberg, E. Melby, J. Rekstad, A. Schiller, and A. Voinov, Phys. Rev. C **65**, 044318 (2002).

[15] H. A. Bethe, Phys. Rev. **50**, 332 (1936).

[16] A. Gilbert and A. G. W. Cameron, Can. J. Phys. **43**, 1446 (1965).

[17] T. von Egidy, H. H. Schmidt og A. N. Behkami, Nucl. Phys. **A 481** (1988) 189.

[18] T. von Egidy and D. Bucurescu, Phys. Rev. C **72**, 044311 (2005); Phys. Rev. C **73**, 049901(E) (2006).

[19] RIPL-1: Handbook for calculations of nuclear reaction data, IAEA, Vienna, Report No. IAEA-TECDOC-1024 (1998); RIPL-2: Handbook for calculations of nuclear reaction data, IAEA, Vienna, Report No. IAEA-TECDOC-1506 (2006).
URL: `http://www-nds.iaea.org/RIPL-2/`

[20] H. Nakada, and Y. Alhassid, Phys. Rev. Lett. **79**, 2939 (1997).

[21] Y. Alhassid, S. Liu, and H. Nakada, Phys. Rev. Lett. **83**, 4265 (1999).

[22] Y. Alhassid, S. Liu, and H. Nakada, Phys. Rev. Lett. **99**, 162504 (2007).

[23] P. Demetriou and S. Goriely, Nucl. Phys. **A 695**, 95 (2001).

[24] S. Hilaire, J. P. Delaroche, M. Girod, Eur. Phys. J. A 12, 169 (2001).

[25] S. Hilaire and S. Goriely, Nucl. Phys. **A 779**, 63 (2006).
URL: `http://www-astro.ulb.ac.be/Html/nld_comb.html`

[26] R. Firestone and V. S. Shirley, *Table of Isotopes*, 8th ed. (Wiley, New York, 1996), Vol. II.

[27] Data extracted using the NNDC On-Line Data Service from the ENSDF database.
URL: `http://www.nndc.bnl.gov/ensdf/`

[28] A. V. Voinov, S. M. Grimes, U. Agvaanluvsan, E. Algin, T. Belgya, C. R. Brune, M. Guttormsen, M. J. Hornish, T. Massey, G. E. Mitchell, J. Rekstad, A. Schiller, and S.Siem, Phys. Rev. C **74**, 014314 (2006).

[29] V. Mishra, N.Boukharouba, S. M. Grimes, K. Doctor, R. S. Pedroni, and R. C. Haight, Phys. Rev. C **44**, 2419 (1991);V. Mishra, N.Boukharouba, S. M. Grimes, K. Doctor, R. S. Pedroni, and R. C. Haight, Phys. Rev. C **47**, 2426(E) (1993).

[30] P. Axel, Phys. Rev. **126**, 671 (1962).

[31] F. Bečvář, P. Cejnar, R. E. Chrien, and J. Kopecky, Phys. Rev. C **46**, 1276 (1992).

[32] G. A. Bartholomew, E. D. Earle, A. J. Fergusson, J. W. Knowles, and M. A. Lone, Adv. Nucl. Phys. **7**, 229 (1972/73).

[33] M. A. Lone,*"Neutron induced reactions"*, Proc. 4th. Int. Symp., Smolenice, Czechoslovakia, 1985; Eds.: J. Kristiak, E. Betak, D. Reidel, Publ. Comp. Dordrecht, Holland, 238 (1986).

[34] J. M. Blatt and V. F. Weisskopf, *Theoretical Nuclear Physics* (John Wiley & Sons, New York, 1952).

[35] M. N. Harakeh and A. van der Woude, *Giant Resonances; Fundamental High-Frequency Modes of Nuclear Excitation*, Oxford University Press, 2001, pages 57-58 and 222-224.

[36] D. M. Brink, Ph.D. thesis, Oxford University, 1955.

[37] S.G. Kadmenskiĭ, V.P. Markushev, and V.I. Furman, Yad. Fiz. **37**, 277 (1983) [Sov. J. Nucl. Phys. **37**, 165 (1983)].

[38] Y. P. Popov,*"Neutron induced reactions"*, Proc. Europhys. Topical Conf., Smolenice, 1982, Physics and Applications, Vol. 10, Ed.: P. Oblozinsky, 121 (1982).

[39] J. Kopecky and R. E. Chrien, Nucl. Phys. **A 468**, 285 (1987).

[40] J. Kopecky, M. Uhl and R. E. Chrien, Phys. Rev. C**47**, 312 (1993).

[41] V. M. Kolomietz, V. A. Plujko, and S. Shlomo, Phys. Rev. C**54**, 3014 (1996).

[42] V. A. Plujko, Nucl. Phys. **A 649**, 209 (1999).

[43] S. F. Mughabghab and C. L. Dunford, Phys. Lett. **B 487**, 155 (2000).

[44] S. Goriely, Phys. Lett. **B 436**, 10 (1998).

[45] S. Goriely and E. Khan, Nucl. Phys. **A 706**, 217 (2002).

[46] P. Ring and P. Schuck, *The Nuclear Many-Body Problem*, Springer Verlag, New York, 1980.

[47] F. Andreozzi, F. Knapp, N. Lo Iudice, A. Porrino, and J. Kvasil, Phys. Rev. C **75**, 044312 (2007).

[48] S. S. Dietrich and B. L. Berman, At. Data Nucl. Data Tables 38, 199 (1988).

[49] Centre for Photonuclear Experiments Data.
URL: `http://cdfe.sinp.msu.ru`

[50] B. L. Berman and S. C. Fultz, Rev. Mod. Phys. **47**, 713 (1975)

[51] B. S. Ishkhanov and V. V. Varlamov, Phys. At. Nucl. **67**, 1664 (2004).

[52] H. Utsunomiya, H. Akimune, S. Goko, M. Ohta, H. Ueda, T. Yamagata, and K. Yamasaki, Phys. Rev. C **67**, 015807 (2003).

[53] U. Kneissl, H. H. Pitz and A. Zilges, Prog. Part. Nucl. Phys. **37**, 349 (1996).

[54] J. Margraf, T. Eckert, M. Rittner, I. Bauske, O. Beck, U. Kneissl, H. Maser, H. H. Pitz, A. Schiller, P. von Brentano, R. Fischer, R.-D. Herzberg, N. Pietralla, A. Zilges, and H. Friedrichs, Phys. Rev. C **52**, 2429 (1995).

[55] M. Krtička, F. Bečvář, J. Honzátko, I. Tomandl, M. Heil, F. Käppeler, R. Reifarth, F. Voss, K. Wisshak, Phys. Rev. Lett. **92**, 172501 (2004).

[56] D. Bohle, A. Richter, W. Steffen, A. E. L. Dieperink, N. Lo Iudice, F. Palumbo and O. Scholten, Phys. Lett. **B 137**, 27 (1984).

[57] A. Zilges, M. Babilon, T. Hartmann, D. Savran, and S. Volz, Prog. Part. Nucl. Phys. **55**, 408 (2005).

[58] W.V. Prestwich, M.A. Islam, and T.J. Kennett, Z. Phys. 315, 103 (1984).

[59] J. Kopecky and M. Uhl, Phys. Rev. C**41**, 1941 (1990).

[60] A. Schiller and M. Thoennessen, At. Data Nucl. Data Tables 93, 549 (2007).

[61] A. Voinov, M. Guttormsen, E. Melby, J. Rekstad, A. Schiller, and S. Siem, Phys. Rev. C **63**, 044313 (2001).

[62] M. Guttormsen, A. Atac, G. Løvhøiden, S. Messelt, T. Ramsøy, J. Rekstad, T.F. Thorsteinsen, T.S. Tveter, and Z. Zelazny, Phys. Scr. **T 32**, 54 (1990).

[63] A. Schiller, L. Bergholt, M. Guttormsen, E. Melby, S. Messelt, E. A. Olsen, J. Rekstad, S. Rezazadeh, S. Siem, T. S. Tveter, P. H. Vreim, and J. Wikne, *Recent Upgrades and Performance of the CACTUS-Detector Array*, Tech. Rep. 98-02, Department of Physics, University of Oslo (1998), p. 3, 5.

[64] M. Guttormsen, *Eventbuilder for the RTPC 8067 Single Board Computer*, Tech. Rep. 98-08, Department of Physics, University of Oslo (1998).

[65] M. Guttormsen, *Offline sorting program Offline+*,
URL: `http://ocl.uio.no/offline/`.

[66] P. D. Kunz, DWBA code DWUCK (1971), University of Colorado, Boulder, Colorado, unpublished.

[67] R. F. Casten, P. Kleinheinz, P. J. Daly, and B. Elbek, Mat. Fys. Medd. Dan. Vid. Selsk. **38**, no. 13 (1972).

[68] B. Elbek and P. O. Tjøm, Adv. Nucl. Phys. **3**(1969).

[69] W. R. Leo, *Techniques for Nuclear and Particle Physics Experiments* (Springer-Verlag, 1994), 24.

[70] J. Rekstad, A. Henriquez, F. Ingebretsen, G. Midttun, B. Skaali, R. Øyan, J. Wikne, and T. Engeland, Phys. Scr. **T 5**, 45 (1983).

[71] U. Agvaanluvsan, G. E. Mitchell, J. F. Shriner Jr., and M. Pato, Phys. Rev. C **67**, 064608 (2003).

[72] A. Richter, invited talk at the *Workshop on Level Density and Gamma Strength in Continuum*, Oslo, May 21-24, 2007;
URL: `http://ocl.uio.no/workshop07/talks.htm`

[73] D. Mocelj, T. Rauscher, G. Martínez-Pinedo, K. Langanke, L. Pacearescu, A. Faessler, F.-K. Thielemann, and Y. Alhassid, Phys. Rev. C **75**, 045805 (2007).

[74] M. Guttormsen, R. Chankova, U. Agvaanluvsan, E. Algin, L.A. Bernstein, F. Ingebretsen, T. Lönnroth, S. Messelt, G.E. Mitchell, J. Rekstad, A. Schiller, S. Siem, A.C. Larsen, A. Voinov and S. Ødegård, Los Alamos preprint server:
`http://xxx.lanl.gov/abs/0801.4667`

[75] A. Bohr and B. Mottelson, *Nuclear Structure*, Benjamin, New York, 1969, Vol. I.

[76] L. Henden, L. Bergholt, M. Guttormsen, J. Rekstad, and T.S. Tveter, Nucl. Phys. **A589**, 249 (1995).

[77] M. Guttormsen, A. Bagheri, R. Chankova, J. Rekstad, A. Schiller, S. Siem, and A. Voinov, Phys. Rev. C **68**, 064306 (2003).

[78] U. Agvaanluvsan, A. Schiller, J. A. Becker, L. A. Bernstein, P. E. Garrett, M. Guttormsen, G. E. Mitchell, J. Rekstad, S. Siem, A. Voinov, and W. Younes, Phys. Rev. C **70**, 054611 (2004).

[79] A. Schiller, A. Bjerve, M. Guttormsen, M. Hjorth-Jensen, F. Ingebretsen, E. Melby, S. Messelt, J. Rekstad, S. Siem, and S. W. Ødegård, Phys. Rev. C **63**, 021306(R) (2001).

[80] M. Guttormsen, M. Hjorth-Jensen, E. Melby, J. Rekstad, A. Schiller, and S. Siem, Phys. Rev. C **63**, 044301 (2001).

[81] BrilLanCe®380 documentation, Saint-Gobain Crystals and Scintillation Products.
URL: `www.detectors.saint-gobain.com/`

[82] C. Kittel and H. Kroemer, *Thermal physics*, W. H. Freeman and Company, New York, 2000.

[83] M. A. Preston, *Physics of the Nucleus*, Addison-Wesley Publishing Company, Massachusetts, 1962.

[84] H. Steinwedel and J. H. Jensen, Z. Naturforsch. A, 413 (1950).

[85] M. Danos, Nucl. Phys. 5, 23 (1958).

[86] G. Breit and E. Wigner, Phys. Rev. 49, 519 (1936).

[87] A. Schiller, Diplomarbeit 1995, University of Stuttgart.

[88] V. Plujko, private communication.

[89] B. Bush and Y. Alhassid, Nucl. Phys. **A 531**, 27 (1991).

[90] J. Kopecky and M. Uhl, Phys. Rev. C**41**, 1941 (1990).